



Fitches, James (2023) *Analysis of unpolarised $\pi^+\pi^-$ photoproduction with the GlueX Experiment*. PhD thesis.

<http://theses.gla.ac.uk/83716/>

Copyright and moral rights for this work are retained by the author

A copy can be downloaded for personal non-commercial research or study, without prior permission or charge

This work cannot be reproduced or quoted extensively from without first obtaining permission in writing from the author

The content must not be changed in any way or sold commercially in any format or medium without the formal permission of the author

When referring to this work, full bibliographic details including the author, title, awarding institution and date of the thesis must be given

Enlighten: Theses

<https://theses.gla.ac.uk/>
research-enlighten@glasgow.ac.uk

Analysis of Unpolarised $\pi^+\pi^-$ Photoproduction with the GlueX Experiment

James Fitches

Submitted in fulfilment of the requirements for the
Degree of Doctor of Philosophy

School of Physics and Astronomy
College of Science and Engineering
University of Glasgow



University
of Glasgow

April 2023

Abstract

This thesis presents measurements of spin-density matrix elements in unpolarised $\pi^+\pi^-$ photoproduction on a proton target. The dominant resonance contribution to the dipion system is the $\rho(770)$ meson. Due to the large production cross section for this resonance, a valid comparison can be made between the obtained final results and $\rho(770)$ spin-density matrix elements measured previously with other experiments. The measurement was performed over the 3.0 – 11.6 GeV beam energy regime, which is a more extensive energy range than has ever been studied previously for the $\rho(770)$. Results were obtained by analysing data from the GlueX experiment based at Jefferson Lab.

Extended maximum likelihood fits were applied to extract three spin-density matrix elements using Markov chain Monte Carlo based parameter estimations. This was performed using various binning configurations to probe the energy, mass, and four-momentum transfer dependence of the determined physics observables. Spin-density matrix elements are shown to be consistent with the model of s-channel helicity conservation at low $-t$. The effects of pomeron and f_2 exchanges are clearly visible in the energy dependence of the measured observables. These observations provide valuable insights into the relative strengths of both processes as a function of the photon energy, and may enable theorists to disentangle the f_2/\mathbb{P} coupling ratio. Spin-density matrix elements are seen to be highly dependent on the reconstructed resonance mass. This observation is likely to be a result of non-resonant S-wave background processes, and emphasises the need for a more detailed model of the $\pi^+\pi^-$ angular distribution that considers all of the competing angular momentum components that contribute to the measured final state.

The statistical precision of measurements performed for this thesis surpass what was achievable in previous studies of the $\rho(770)$ by several orders of magnitude. Studies of the energy and four-momentum transfer dependence, and insights into the effects of non $\rho(770)$ background contributions provide valuable input for production models. This will help inform the choice of wave-sets used for partial wave analyses, supporting GlueX in its search for exotic hybrid meson states.

Contents

Abstract	i
Acknowledgements	ix
Declaration	x
1 Introduction	1
2 $\pi^+\pi^-$ photoproduction theory	7
2.1 The $\rho(770)$ meson resonance	7
2.2 Spin-density matrix elements	11
2.3 Baryonic contributions to the $\pi^+\pi^-$ final state	18
2.4 Summary	19
3 Review of previous results and theoretical model	20
3.1 Previous measurements	20
3.2 Current theoretical model	23
3.3 Summary	25
4 Experimental setup	26
4.1 CEBAF	27
4.2 Photon Beam	28
4.3 Target	33
4.4 Solenoid magnet	33
4.5 Start Counter	34
4.6 Tracking	34
4.7 Calorimetry	36
4.8 Time-of-Flight Detector	38
4.9 Data acquisition and trigger	40
4.10 Summary	41

5	Event selection and analysis	42
5.1	Dataset	42
5.2	Calibrations	43
5.3	Event reconstruction	47
5.4	Skimming and kinematic fitting	48
5.5	Detector simulations	49
5.6	Additional corrections	50
5.7	Final selection	55
5.8	Binning	61
5.9	Summary	64
6	Observable extraction	66
6.1	Extended maximum likelihood fit	66
6.2	Markov chain Monte Carlo	68
6.3	Results	73
6.4	Summary	75
7	Determination of systematic uncertainties	76
7.1	Event selection	76
7.2	Validation of results	90
7.3	Summary	94
8	Results	96
8.1	$-t$ dependence	96
8.2	$\pi^+\pi^-$ invariant mass dependence	105
9	Conclusion	111
A	Additional Barlow significance plots	113
A.1	Kinematic fit χ^2/NDF cut	113
A.2	Missing energy cut	118
A.3	π^+p invariant mass cut	122

List of Tables

- 4.1 Summary of trigger conditions for the Spring 2017 beam time 40
- 5.1 Number of recorded triggers for each radiator setting 43
- 5.2 Summary of particle identification cuts applied during the data skim. Note that
in the final column, p denotes the measured particle momentum along the x axis. 49
- 5.3 Summary of cuts applied in the final selection. 64
- 7.1 Modifications to the event selection that were used for cut stability studies . . . 77

List of Figures

1.1	Table of the elementary particles defined in the standard model	2
1.2	The running QCD coupling constant	3
2.1	$\pi^+\pi^-$ invariant mass distribution	8
2.2	Feynman diagrams showing possible Drell processes	8
2.3	Prediction of the $\rho(770)$ line shape	9
2.4	Feynman diagram showing $\rho(770)$ photoproduction mechanisms	9
2.5	Definition of the helicity frame	12
2.6	Photoproduction cross sections as a function of photon energy	18
2.7	Feynman diagrams showing t-channel production of baryon resonances	19
3.1	$\rho(770)$ SDMEs measured by SLAC	22
3.2	P-wave SDMEs in unpolarised photoproduction reported by CLAS	22
3.3	Vector meson SDMEs predicted by JPAC	23
4.1	Schematic diagram of the GlueX detector	26
4.2	Schematic view of CEBAF	27
4.3	Diagram showing bremsstrahlung production	28
4.4	Dominant bremsstrahlung Feynman diagrams	28
4.5	Photon energy spectra obtained with diamond and amorphous radiators	29
4.6	Schematic view of the GlueX beam line	30
4.7	Diagram of the tagger hodoscope and microscope	31
4.8	Schematic view of the GlueX pair spectrometer	33
4.9	Schematic view of the GlueX Start Counter and target	34
4.10	Straw tube arrangement visible in the CDC	35
4.11	CDC $\frac{dE}{dx}$ plotted versus the momenta of positively charged particles	36
4.12	Schematics of the BCAL detector	37
4.13	Photo of the FCAL detector in hall D	38
4.14	Photo of the TOF wall in hall D	39
4.15	Lorentz factor β plotted against momentum for various particles	39

5.1	Plots of the timing signal measured relative to the RF clock	45
5.2	Plots of the $\gamma\gamma$ invariant mass measured in the BCAL	46
5.3	Missing energy distributions	51
5.4	Tagger correction plots	51
5.5	Missing energy distributions after applying tagger correction	52
5.6	Transverse beam momentum versus photon energy	53
5.7	Missing p_x distributions	53
5.8	Beam correction plots	54
5.9	Missing p_x distributions after applying beam correction	55
5.10	Photon timing distribution	56
5.11	z vertex distribution	57
5.12	Missing mass squared distribution	58
5.13	Missing energy distribution	59
5.14	dE/dx measured for particle tracks in the CDC	60
5.15	Invariant mass distributions showing the effects of various kinematic fit cuts	60
5.16	π^+p invariant mass distribution at $E_\gamma < 4.25$ GeV	61
5.17	$-t$ distribution	62
5.18	Photon energy spectrum with binning scheme denoted	63
5.19	$\pi^+\pi^-$ invariant mass distribution with binning scheme denoted	63
5.20	Flowchart showing sequence of analysis steps	65
6.1	Illustration of the Metropolis-Hastings algorithm	70
6.2	Comparison of SDMEs measured using Minuit and MCMC	72
6.3	MCMC step timeline plots	73
6.4	MCMC corner plot	74
6.5	Angular distributions from experimental data and weighted Monte Carlo	74
7.1	SDMEs measured using various kinematic fit χ^2/NDF cuts	78
7.2	Barlow test results for χ^2/NDF cut studies in the 3.00 – 4.25 GeV E_γ range	79
7.3	Comparison of χ^2/NDF distributions in simulated and experimental data	79
7.4	Barlow test results for χ^2/NDF cut studies in the 9.5 – 11.6 GeV E_γ range	80
7.5	Barlow test results for χ^2/NDF cut studies in the 3.00 – 4.25 GeV E_γ range using a modified significance definition	81
7.6	Barlow test results binned in $M_{\pi^+\pi^-}$ for χ^2/NDF cut studies at low $-t$	81
7.7	Barlow test results binned in $M_{\pi^+\pi^-}$ for χ^2/NDF cut studies at high $-t$	82
7.8	Barlow test results for missing mass squared cut studies in the 3.00 – 4.25 GeV E_γ range	82
7.9	Barlow test results binned in $M_{\pi^+\pi^-}$ for missing mass squared cut studies at low $-t$	83

7.10	Barlow test results for missing energy cut studies in the 3.00 – 4.25 GeV E_γ range	83
7.11	Barlow test results for missing energy cut studies in the 9.5 – 11.6 GeV E_γ range	83
7.12	Barlow test results binned in $M_{\pi^+\pi^-}$ for missing energy cut studies at low $-t$	84
7.13	Barlow test results binned in $M_{\pi^+\pi^-}$ for missing energy cut studies at high $-t$	84
7.14	Barlow test results for π^+p invariant mass cut studies in the 3.00 – 4.25 GeV E_γ range	85
7.15	Distributions showing the π^+p invariant mass over the 3.00 – 4.25 GeV E_γ range	86
7.16	Barlow test results for π^+p invariant mass cut studies in the 9.5 – 11.6 GeV E_γ range	86
7.17	Barlow test results binned in $M_{\pi^+\pi^-}$ for π^+p invariant mass cut studies at low $-t$	87
7.18	Barlow test results binned in $M_{\pi^+\pi^-}$ for π^+p invariant mass cut studies at intermediate $-t$	87
7.19	Barlow test results binned in $M_{\pi^+\pi^-}$ for π^+p invariant mass cut studies at high $-t$	87
7.20	Barlow test results for a single particle ID cut study	88
7.21	SDMEs measured over five different regions in the reaction vertex z	89
7.22	Summary of vertex z binning study	90
7.23	Barlow test results for vertex z cut studies in the 3.00 – 4.25 GeV E_γ range	90
7.24	Comparison of $-t$ distributions in reconstructed and experimental data	91
7.25	Comparison of toy angular distributions with experimental data	92
7.26	Pull distributions from toy studies of the 0.28 – 0.32 GeV ² / c^2 range in $-t$	93
7.27	Means extracted from pull distributions for each SDME and each $-t$ bin	94
7.28	Widths extracted from pull distributions for each SDME and each $-t$ bin	94
8.1	ρ_{00}^0 measured in various E_γ ranges as a function of $-t$	97
8.2	$\text{Re}\rho_{10}^0$ measured in various E_γ ranges as a function of $-t$	98
8.3	ρ_{1-1}^0 measured in various E_γ ranges as a function of $-t$	98
8.4	ρ_{00}^0 plotted versus $-t$ with systematic uncertainties	99
8.5	$\text{Re}\rho_{10}^0$ plotted versus $-t$ with systematic uncertainties	99
8.6	ρ_{1-1}^0 plotted versus $-t$ with systematic uncertainties	100
8.7	SDMEs measured over the 3.00 – 4.25 GeV E_γ range and various ranges in $M_{\pi^+\pi^-}$	101
8.8	SDMEs measured over the 4.25 – 5.50 GeV E_γ range and various ranges in $M_{\pi^+\pi^-}$	101
8.9	SDMEs measured over the 5.5 – 6.5 GeV E_γ range and various ranges in $M_{\pi^+\pi^-}$	102
8.10	SDMEs measured over the 6.5 – 7.5 GeV E_γ range and various ranges in $M_{\pi^+\pi^-}$	102
8.11	SDMEs measured over the 7.5 – 8.5 GeV E_γ range and various ranges in $M_{\pi^+\pi^-}$	103
8.12	SDMEs measured over the 8.5 – 9.5 GeV E_γ range and various ranges in $M_{\pi^+\pi^-}$	103
8.13	SDMEs measured over the 9.5 – 11.6 GeV E_γ range and various ranges in $M_{\pi^+\pi^-}$	104
8.14	Polarised and unpolarised SDMEs measured over the coherent peak	105
8.15	$\pi^+\pi^-$ invariant mass distribution with binning scheme annotated	106
8.16	ρ_{00}^0 plotted versus $M_{\pi^+\pi^-}$ in various $-t$ and E_γ regimes	107

8.17	$\text{Re}\rho_{10}^0$ plotted versus $M_{\pi^+\pi^-}$ in various $-t$ and E_γ regimes	107
8.18	ρ_{1-1}^0 plotted versus $M_{\pi^+\pi^-}$ in various $-t$ and E_γ regimes	108
8.19	Comparison with CLAS results in the $0.4 - 0.5 \text{ GeV}^2/c^2$ $-t$ range	108
8.20	Comparison with CLAS results in the $0.5 - 0.6 \text{ GeV}^2/c^2$ $-t$ range	109
8.21	Comparison with CLAS results in the $0.6 - 0.7 \text{ GeV}^2/c^2$ $-t$ range	109
8.22	Comparison with CLAS results in the $0.7 - 0.8 \text{ GeV}^2/c^2$ $-t$ range	109
8.23	Comparison with CLAS results in the $0.8 - 0.9 \text{ GeV}^2/c^2$ $-t$ range	110
8.24	Comparison with CLAS results in the $0.9 - 1.0 \text{ GeV}^2/c^2$ $-t$ range	110

Acknowledgements

This PhD has been one of the most challenging experiences of my life. It only seems right to thank the people who helped me along the way, and without whom this work would not have been possible.

First of all, I would like to thank Ken Livingston for his unfaltering guidance and support, and for being an all-round nice guy. It's fair to say I hit the jackpot as far as supervision is concerned, and I will sincerely miss our weekly catch-ups. Thanks to Dave Ireland for giving me the opportunity to study hadron physics at PhD level. It really has been a fantastic experience, and one I will never forget. I would also like to thank Peter Hurck and Derek Glazier for helping me in more ways than I could ever possibly list. The Glasgow Nuclear and Hadron Physics group is truly a special thing to be a part of, and I extend my gratitude to all of you for making our department such a stimulating and enjoyable place to work.

I would also like to thank the GlueX collaboration, without which this analysis would not have been possible. Special thanks to Alex Austregesilo for his technical assistance and for providing a great template analysis, and to Dave Mack for encouraging me to focus on unpolarised SDMEs in the first place.

I want to thank my friends for leading me astray every once in a while. Postgraduate study can be stressful at times, and you were always there to encourage me to let loose (not that I needed much encouragement). Also a big thank you to my parents for their continuous support throughout my university studies. I will get a real job one day, I promise...

Last but not least to my long suffering girlfriend Becky, who put up with my incoherent ramblings about mesons, detectors, and other physics-related nonsense every night for more than three and a half years. Through the thick and thin you were always there for me, and I can't thank you enough.

Declaration

The work in this thesis is based on research carried out at the Nuclear and Hadron Physics Group, School of Physics Astronomy, University of Glasgow, UK. No part of this thesis has been submitted elsewhere for any other degree or qualification and it is all my own work unless referenced to the contrary in the text.

Chapter 1

Introduction

In this thesis, measurements of spin-density matrix elements in unpolarised $\pi^+\pi^-$ photoproduction on a proton target are presented, where the reaction of interest is given by $\gamma p \longrightarrow p\pi^+\pi^-$. The measurement was performed by analysing data obtained with the GlueX experiment based at Jefferson lab. The dominant resonance contribution to the $\pi^+\pi^-$ final state is the $\rho(770)$ meson, which is produced abundantly with GlueX. Since the signal from $\rho(770)$ production is so large, the final results describe $\rho(770)$ spin-density matrix elements to a first approximation. The statistics available in this channel with GlueX are excellent, making it possible to explore the mass, energy and momentum transfer dependence of the extracted results more extensively than any previous measurement. This will aid the development of production models, ultimately helping GlueX to achieve its primary physics objective of measuring exotic hybrid meson states.

The standard model of particle physics is widely considered to be one of the most successful scientific theories of all time. It predicted the existence of particles such as the W and Z bosons [1–3], gluon [4], and Higgs boson [5] years before the first experimental observations, and predicted a value for the electron magnetic moment that agreed with experimental measurements at the level of 7.7×10^{-10} [6]. The standard model describes three of the four known fundamental forces of nature within a self-consistent quantum field theory. These three forces are electromagnetism, weak and strong interactions, while gravity does not currently fit into the model. The standard model describes twelve elementary particles with half integer spin known as fermions, where the three fundamental interactions encapsulated by the theory are mediated by integer spin bosons.

Within the standard model, the strong interaction is described by a quantum field theory known as Quantum Chromodynamics (QCD). In this theory, interactions between fermionic quarks are governed by exchanges of gluons, the force mediating bosons of the strong force. The standard model defines six quarks which are classified into three generations of ascending mass. The

Standard Model of Elementary Particles

three generations of matter (fermions)			interactions / force carriers (bosons)		
	I	II	III		
mass	$\approx 2.2 \text{ MeV}/c^2$	$\approx 1.28 \text{ GeV}/c^2$	$\approx 173.1 \text{ GeV}/c^2$	0	$\approx 124.97 \text{ GeV}/c^2$
charge	$\frac{2}{3}$	$\frac{2}{3}$	$\frac{2}{3}$	0	0
spin	$\frac{1}{2}$	$\frac{1}{2}$	$\frac{1}{2}$	1	0
	u up	c charm	t top	g gluon	H higgs
	d down	s strange	b bottom	γ photon	
	e electron	μ muon	τ tau	Z Z boson	
	ν_e electron neutrino	ν_μ muon neutrino	ν_τ tau neutrino	W W boson	
	$\approx 0.511 \text{ MeV}/c^2$	$\approx 105.66 \text{ MeV}/c^2$	$\approx 1.7768 \text{ GeV}/c^2$	$\approx 91.19 \text{ GeV}/c^2$	
	-1	-1	-1	0	
	$\frac{1}{2}$	$\frac{1}{2}$	$\frac{1}{2}$	1	
	$< 2.2 \text{ eV}/c^2$	$< 0.17 \text{ MeV}/c^2$	$< 18.2 \text{ MeV}/c^2$	$\approx 80.39 \text{ GeV}/c^2$	
	0	0	0	± 1	
	$\frac{1}{2}$	$\frac{1}{2}$	$\frac{1}{2}$	1	

QUARKS (left side of quark section)
LEPTONS (left side of lepton section)
GAUGE BOSONS VECTOR BOSONS (left side of boson section)
SCALAR BOSONS (right side of boson section)

Figure 1.1: Table of the elementary particles defined in the standard model. Figure taken from [7].

lightest quarks are labelled *up* and *down*, carrying electric charges of $+\frac{2}{3}$ and $-\frac{1}{3}$ respectively. The second and third generations of charge $+\frac{2}{3}$ quarks are given by *charm* and *top* quarks, while the corresponding charge $-\frac{1}{3}$ quarks consist of *strange* and *bottom* quarks. Since quarks carry electric charge, they are also subject to electromagnetic interactions via photon exchanges, where the photon is the force mediating boson of the electromagnetic force. The standard model also includes six particles that do not interact through the strong force, known as leptons. These are also classified into three generations. Three leptons carry a charge of -1 , called the electron, muon and tau in order of ascending mass. Each lepton has a chargeless and nearly massless neutrino counterpart. Since neutrinos carry zero electric charge, they are only able to interact via the weak force, mediated by the Z^0 and W^\pm gauge bosons. The table of elementary particles defined in the standard model is completed by the Higgs boson. This boson is responsible for the Higgs mechanism, which plays an important role in the generation of particle mass. Note that the full set of fundamental particles defined in the standard model is visualised in Figure 1.1.

While the electromagnetic force is governed by photon exchanges, where photons couple to positive and negative electric charge, the situation in QCD is a little more complex. The force mediating gluon couples to three colour charges, called *red*, *green* and *blue*, where each charge also has an associated anti-colour charge. Moreover, while the photon is electrically neutral, gluons themselves carry colour charge in QCD, meaning they can self-interact. This property of QCD results in a phenomenon known as *colour confinement*, meaning only colour neutral bound states of quarks and gluons are observed in nature. The colour field between two strongly

interacting objects can be approximated by a *flux tube* of self-interacting gluons. This results in a coupling constant, α_s , which becomes larger with increasing separation distance. Since the binding energy increases with separation distance, eventually the energy required to stretch the flux tube any further will be sufficient to produce a quark anti-quark pair from the vacuum in a process known as *hadronisation*. This limits the range of the strong force to within the order of the nucleon size. Since the coupling constant of the strong force is directly proportional to the distance between two colour charges, quarks demonstrate *asymptotic freedom* for distances approaching zero. At small separation distances, quarks are approximately free with minimal interaction between particles, and the field theory of QCD becomes perturbative.

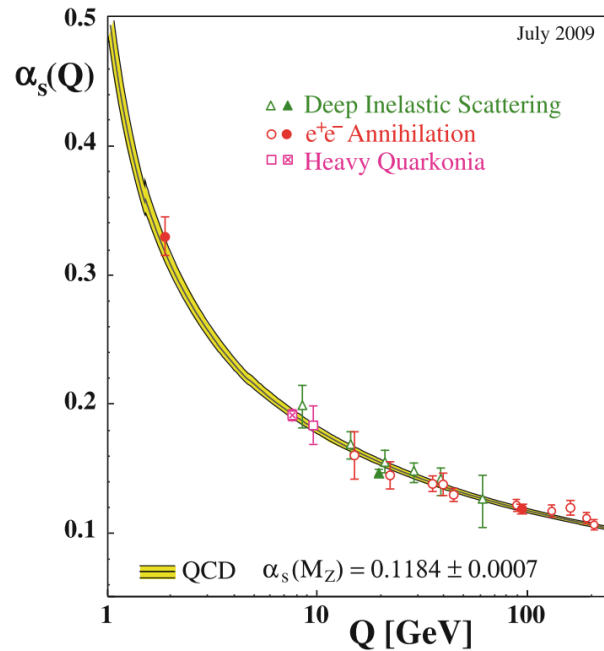


Figure 1.2: Plot showing the dependence of the QCD coupling constant on the momentum transfer Q^2 . Note that Q^2 is inversely proportional to the quark separation distance. Figure taken from [8].

As a result of confinement, only colour neutral bound states of quarks and anti-quarks are observed in nature. A colour neutral state can be obtained by combining a colour charge with its anti-colour charge, or by combining all three colour or anti-colour charges. A bound state must therefore always consist of two or more quarks. Quarks combine to form colourless, composite particles called *hadrons*. Hadrons can generally be divided into two sub-categories called *mesons* and *baryons*. A meson consists of a quark anti-quark pair, while a baryon comprises three bound quarks to form a colour neutral system. The proton and neutron are the constituent particles of the atomic nucleus. These particles constitute the vast majority of observable matter, and are perhaps the two most famous baryons. They were also the first two baryons to be discovered, by Rutherford and Chadwick in 1919 [9] and 1932 [10, 11] respectively. The pion was the first meson to be discovered in 1947 [12] following theoretical predictions of the existence

of mesons by Yukawa in 1935 [13]. The pion is a particularly important meson in QCD. Due to quantum confinement, the range of the gluon exchange is within the order of the nucleon size. At larger distance scales, the strong force is effectively mediated by the pion exchange, which governs the inter-nucleon forces holding the nucleus together. The 1950s saw an explosion in the discovery of new hadronic particles following the construction of the worlds first particle accelerators. In 1964, Gell-Mann and Zweig proposed the *Eightfold Way* [14] to describe the observed pattern of particle masses. This scheme laid the early foundations of the quark model framework, describing baryons and mesons as bound states of three and two constituents respectively.

Although QCD is largely a well tested and well understood quantum field theory, there are still many aspects of the theory that would benefit from further study. For hadrons composed of light quarks such as the proton and neutron, the masses of constituent valence quarks are seen to only account for around 1 % of the overall particle mass. The remaining 99 % is attributable to contributions from *sea* quarks (quarks originating from the hadronisation of quark anti-quark pairs from the vacuum), the gluon clouds surrounding valence quarks, and the interactions between gluons, sea quarks and valence quarks within the hadron. The dynamics of this mass generation process are currently poorly understood. The so-called *proton spin crisis* is another unresolved problem in QCD. Experimental results published by the European Muon Collaboration in 1988 [15] demonstrated that the sum of the spins of quarks and anti-quarks within the proton only accounts for around $\frac{1}{3}$ of the total proton spin. The origin of the remaining spin contribution is still unknown. Furthermore, the experimental evidence for many non-conventional hadron states remains scarce. Although the simple quark model describes mesons and baryons as $q\bar{q}$ and qqq states, more complicated configurations of bound quarks are not forbidden by QCD. Recent years have seen mounting evidence for $qq\bar{q}\bar{q}$ (tetraquark) and $qqq\bar{q}q$ (pentaquark) candidate states [16–19]. Since gluons also carry colour charge, bound states consisting purely of glue termed *glueballs* are also possible. Although there exists some experimental evidence for glueballs [20, 21], glueball identification is a challenging task, and there are currently no definitive observations of such states.

QCD also permits meson states called *hybrid mesons*, where excitations of the gluonic field binding the $q\bar{q}$ system can also contribute to the J^{PC} quantum numbers of the meson. The eightfold way groups mesons into nonets, where the values of spin (J), parity (P) and charge conjugation (C) associated with each nonet are unique. The spin is given by

$$\vec{J} = \vec{L} + \vec{S}, \quad (1.1)$$

where \vec{L} is the orbital angular momentum and \vec{S} is the intrinsic spin. The parity and charge conjugation are given by

$$P = (-1)^{L+1} \quad (1.2)$$

and

$$C = (-1)^{L+S} \quad (1.3)$$

respectively. Collectively, this means that only certain J^{PC} quantum numbers are consistent with a pure $q\bar{q}$ system, while combinations such as 1^{-+} are forbidden. In a hybrid meson state, certain forbidden quantum numbers become accessible due to the additional degrees of freedom introduced by the gluonic component. Non-conventional states with J^{PC} numbers that are incompatible with the simple quark picture are termed *exotic*. The identification of a state with forbidden quantum numbers would provide unambiguous proof for the existence of an exotic state. Although several observations of states with exotic J^{PC} numbers 1^{-+} have been reported in recent years [22–26], many of the states predicted by lattice QCD calculations are yet to be observed.

Ever since the search began, various challenges have curtailed the discovery of hybrid mesons. These states are concealed by complex backgrounds consisting of numerous broad, overlapping resonances with non-exotic quantum numbers. Moreover, the determination of these quantum numbers is only possible using a technique called *partial wave analysis*. Partial wave analysis is a complicated and computationally challenging procedure, and requires a detailed understanding of the production mechanisms involved. The GlueX experiment was designed for the specific purpose of identifying exotic hybrid mesons. The basic working principle underlying this experiment can be summarised as follows; a stable proton target is elevated to an excited state by a high energy photon beam. The target then de-excites when unstable particles called *resonances* are formed, which subsequently decay into stable final state particle configurations. Hybrid mesons are expected to decay to both charged and neutral final states, and the GlueX detector was designed to measure both with excellent momentum and energy resolution. A unique feature of the GlueX experiment is the linearly polarised photon beam which it incorporates. Photoproduction experiments are capable of producing resonances with a range of different quantum numbers, while experiments studying alternative processes such as e^+e^- annihilation are often only capable of producing resonances with a single J^{PC} combination. The linear polarisation of the beam imposes constraints on the J^{PC} numbers of the photoproduced mesons, acting as a filter to reduce the contribution from resonances which are not of interest. Moreover, the energy of the GlueX photon beam is sufficiently high to produce an exotic state in a t-channel exchange process rather than through s-channel production, which proceeds via the exchange of an intermediate baryon resonance. This also simplifies the identification of exotic hybrid states.

Future generations of analysers will perform partial wave analyses of GlueX data to try and identify resonances with exotic quantum numbers. As mentioned previously, a detailed understanding of the production mechanisms involved is required for this. Spin-density matrix elements provide a complete description of the angular distribution of a resonance's decay

products. Studying the dependence of their values on the momentum transfer $-t$, in addition to the impinging photon energy and reconstructed resonance mass provide valuable constraints on theoretical models describing the production process. The $\rho(770)$ is produced abundantly with GlueX over a large kinematic region, and the results presented in this work probe the mass and energy dependence of the photoproduced $\pi^+\pi^-$ angular distribution in more detail than has ever been attempted previously. Spin-density matrix elements were extracted over an extensive range of beam energies, where the background of non- ρ contributions varies significantly. This will improve our understanding of the non- ρ background, contributing valuable input to partial wave analyses. Moreover, the measurements presented here were performed with unrivaled statistical precision. This will make it possible to implement a stringent test of the ability of partial wave analyses to discriminate between the decays of the dominant $\rho(770)$ resonance and smaller contributions from non- ρ events. Systematic effects also become more apparent when studying the $\rho(770)$ with GlueX since the associated statistical uncertainties are so small. This will help in developing a more detailed understanding of the GlueX detector performance.

In the next chapter, a summary of the important theoretical concepts is provided, including a detailed introduction to the spin-density matrix formalism. Previous measurements of spin-density matrix elements in $\pi^+\pi^-$ photoproduction are reviewed in Chapter 3. Chapter 4 describes the working principles of the important GlueX detector and beamline components. Chapter 5 explains how the raw data measured with the GlueX detector is prepared to obtain a sample of events corresponding to the exclusive $p\pi^+\pi^-$ final state, and Chapter 6 describes how SDMEs are extracted from the resulting data using Markov chain Monte Carlo based parameter estimates and MINUIT fits. Chapter 7 details the systematic studies that were performed to determine systematic uncertainties. The final results are presented in Chapter 8.

Chapter 2

$\pi^+ \pi^-$ photoproduction theory

The following chapter presents a formalism for describing the decay distributions of vector mesons in terms of *spin-density matrix elements* (SDMEs). This formalism applies specifically to photoproduction reactions. Properties of the dominant resonance decay contribution to the dipion final state from the $\rho(770)$ meson are also discussed. Furthermore, a discussion of baryonic contributions to the measured final state is provided.

2.1 The $\rho(770)$ meson resonance

The dominant resonance contribution over the $0.60 - 0.88 \text{ GeV}/c^2$ dipion mass range in high energy photoproduction is the $\rho(770)$, which decays to $\pi^+ \pi^-$ with a branching fraction approaching 100 % [27]. The $\rho(770)$ is a *vector meson*, meaning it has quantum numbers $J^P = 1^-$. The quark content of the resonance is given by

$$\frac{u\bar{u} - d\bar{d}}{\sqrt{2}}. \quad (2.1)$$

The most recent values published by the Particle Data Group [27] for the $\rho(770)$ mass and width are $775.26 \pm 0.23 \text{ MeV}$ and $149.10 \pm 0.80 \text{ MeV}$ respectively. The $\rho(770)$ peak observed in the $\pi^+ \pi^-$ invariant mass spectrum with GlueX is shown in Figure 2.1.

The broad resonance width makes the $\rho(770)$ difficult to analyse. There is a significant contribution from non-resonant S-wave production over the $\rho(770)$ invariant mass range. The three possible non-resonant production mechanisms are shown schematically in Figure 2.2. These processes exhibit interference with the $\rho(770)$ photoproduction mechanism. This gives a rapidly changing interference contribution in the vicinity of the $\rho(770)$ peak, as shown in Figure 2.3. As a result of this, the $\rho(770)$ mass observed in photoproduction is about 25 MeV less than that measured for other production processes [28].

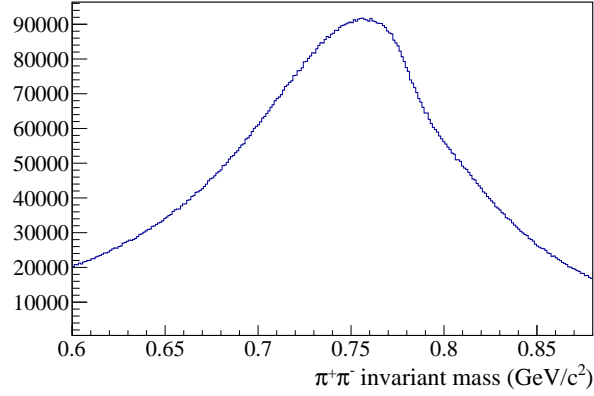


Figure 2.1: Histogram of the $\pi^+\pi^-$ invariant mass measured with GlueX in the Spring 2017 beam time, where the $\rho(770)$ peak is seen to be the dominant feature.

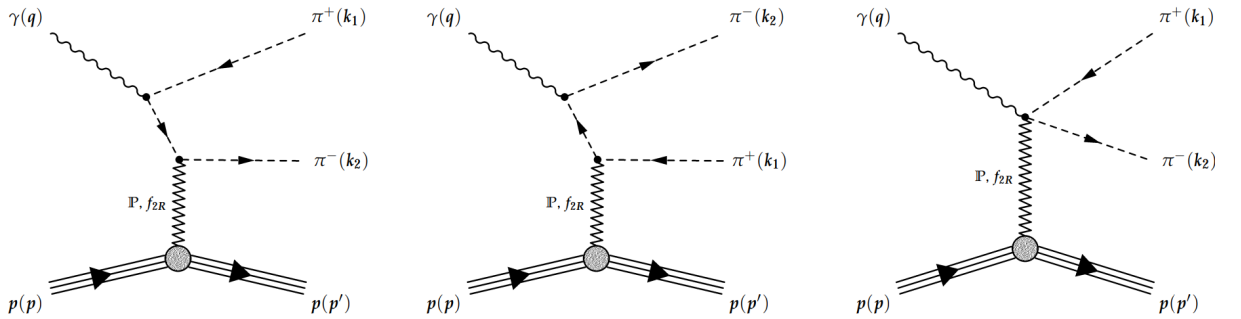


Figure 2.2: Feynman diagrams for the three possible Drell background processes under the $\rho(770)$ invariant mass peak. Each reaction proceeds via the exchange of a virtual particle such as a pomeron, \mathbb{P} , or f_2 meson. For the f_{2R} , the 'R' subscript indicates that we are referring to an f_2 reggeon. For a detailed discussion of Regge theory, see [29]. Figure taken from [30].

Since the line shape of the $\rho(770)$ is dependent on the production process, it can not be described by a relativistic Breit-Wigner function. An additional shape parameter is required to account for the dependence on the production mechanism. Following from these complications, it is worth noting that the work presented in this thesis is an analysis of SDMEs in $\pi^+\pi^-$ photoproduction over the $\rho(770)$ invariant mass range, rather than of the SDMEs for the $\rho(770)$ itself. Although the SDME formalism presented in Section 2.2 is only valid for vector mesons, the measurements presented in this work are still valuable input for future theoretical models that may incorporate backgrounds from Drell processes and baryonic contributions. Furthermore, the background fraction is still relatively low compared with the $\rho(770)$ yield.

2.1.1 Production mechanisms

The three main processes for vector meson photoproduction off the proton over the $\rho(770)$ invariant mass range are shown in Figure 2.4. The dominant production mechanism for the $\rho(770)$ over a wide range of photon energies is the t-channel exchange process shown in Figure 2.4b.

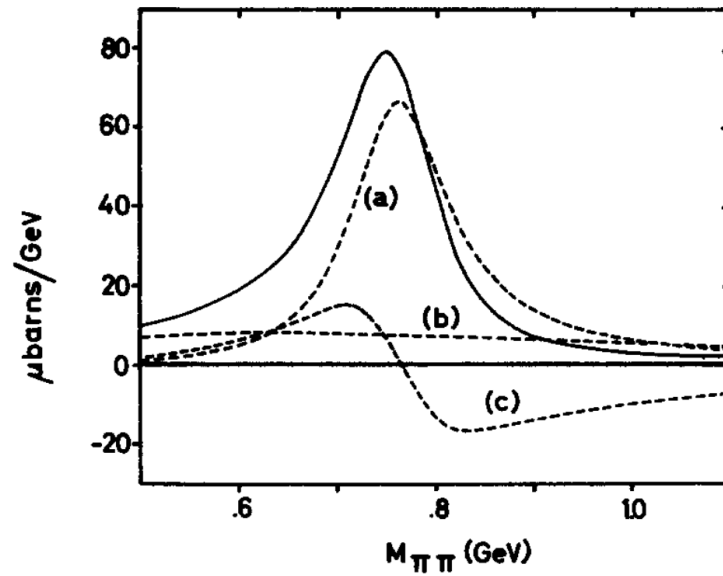


Figure 2.3: Prediction of the $\rho(770)$ line shape where the contribution from Drell backgrounds has been taken into account. The curve (a) shows the $\rho(770)$ line shape in the absence of non-resonant background processes. The Drell mechanisms shown in Figure 2.2 produce a smooth background given by curve (b). Curve (c) is the contribution from the interference term between $\rho(770)$ production and each of the Drell processes shown in Figure 2.2. Figure taken from [28].

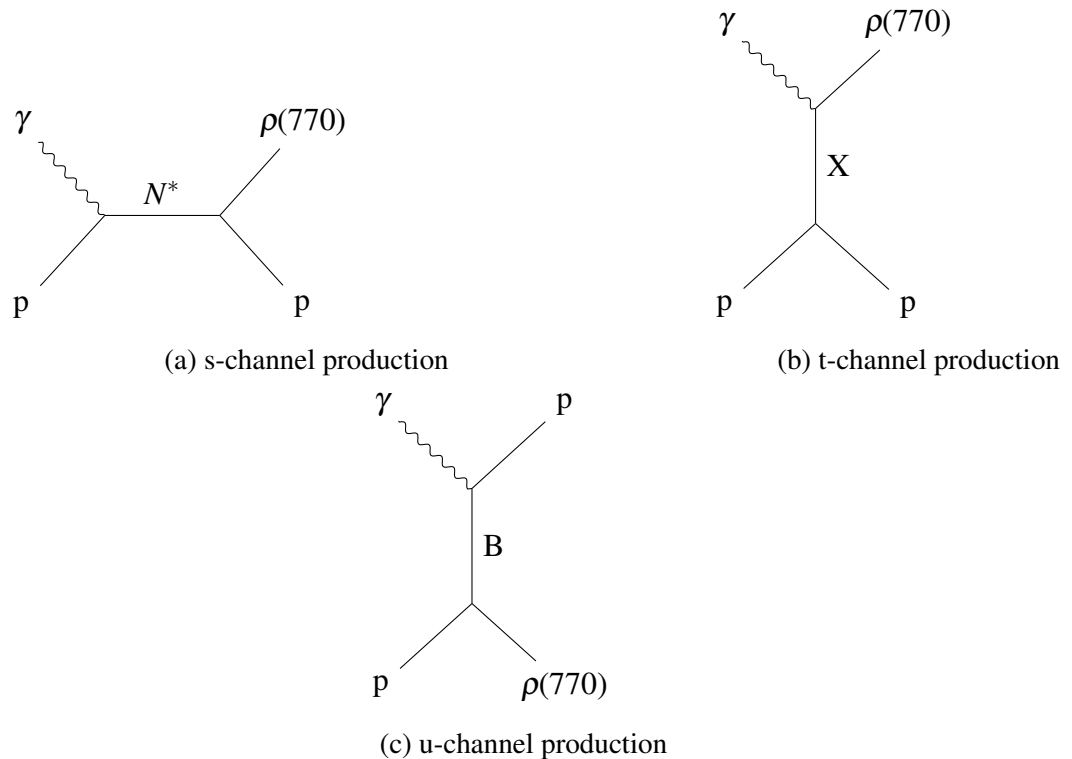


Figure 2.4: Production mechanisms for the $\rho(770)$. (a) in s-channel production a nucleon resonance N^* decays into a proton and a $\rho(770)$. (b) The $\rho(770)$ is produced via the exchange of a virtual meson X in t-channel production. (c) The u-channel production process involves the exchange of a virtual baryon, B.

This reaction is known to dominate because of the vector meson dominance model (VMD) [31], which describes the photon as a superposition of the electromagnetic photon and one of the lightest vector mesons (ρ, ω, ϕ). The photon couples directly to the ρ , which then scatters diffractively from the target proton via the exchange of a virtual meson. This process dominates since the photon has the same spin alignment as a vector meson ($J^{PC} = 1^{--}$). It can therefore be approximated as a virtual vector meson that hadronises readily in the field of the proton.

At high photon energies, the reaction typically proceeds via the exchange of a pomeron, \mathbb{P} [32]. The pomeron is a hypothetical particle carrying zero electric or colour charge. For lower energies the contribution from f_2 exchanges becomes more significant. The f_2 is a tensor meson resonance with quantum numbers $J^{PC} = 2^{++}$. Measuring vector meson SDMEs over a wide photon energy range provides insights into the relative contribution of both exchanges as a function of photon energy. This is made possible by studying the conservation of helicity in the s-channel. Helicity is defined as the projection of the spin of a state, \bar{s} , onto the direction of its momentum vector, \bar{p} ,

$$\lambda = \frac{\bar{s} \cdot \bar{p}}{|\bar{p}|}. \quad (2.2)$$

In the s-channel, helicity is transferred between the $\rho(770)$ meson and the beam photon. In the centre-of-mass frame, the net helicity transfer in this channel can be 0, 1 or 2, defined as helicity conserving, single, and double helicity flip respectively. The f_2 exchange results in a helicity flip, inducing deviations from s-channel helicity conservation. The pomeron exchange is helicity non-flip, which counteracts these deviations. The extent to which helicity is conserved in the s-channel can be studied experimentally by measuring SDMEs as a function of the four-momentum transfer squared $-t$ in the s-channel helicity system (c.f. Section 2.2.1). The measured SDMEs should follow a straight line centred on zero when s-channel helicity is conserved. Note that the s-channel helicity conservation model is discussed in detail in Section 2.2.6.

In s-channel production, an intermediate nucleon excitation decays into a $\rho(770)$ and a proton. The required mass of the intermediate nucleon resonance scales with the incoming photon energy. For example, in the 8 – 9 GeV photon energy regime, the intermediate state would require a mass of about 5 GeV. Although this is not impossible, no such N^* states have ever been observed, making this production mechanism unlikely for higher photon energies. For lower energy regimes however, the contribution from this production mode is likely to become more significant. Another possible production mode is the u-channel mechanism shown in Figure 2.4c. In this reaction, a virtual baryon is exchanged with the target proton, resulting in a transition of the photon into a proton. The exchanged virtual baryon would then result in the target proton transitioning to a $\rho(770)$. This is far less probable than the t-channel mode shown in Figure 2.4b, and no significant contribution from u-channel production is expected in any photon energy regime.

2.2 Spin-density matrix elements

The quantum state of a physical system is described by a density matrix. Density matrices can be used to describe both pure and mixed quantum states. For an ensemble of n pure states, $|\psi\rangle$, the density matrix is given by

$$\rho = \sum_{i,j}^n a_{ij} |\psi_j\rangle \langle \psi_i|, \quad (2.3)$$

where a_{ij} are the eigenvalues of the matrix and the probability of occupying a state i is given by the diagonal element a_{ii} . Density matrices are constrained to be Hermitian, with a trace of one. A more detailed description of density matrices can be found in [33].

The spin polarisation of a state is described by a spin-density matrix. Consider a real, linearly polarised photon striking an unpolarised nucleon target to produce a vector meson resonance,

$$\gamma N \longrightarrow VN, \quad (2.4)$$

where the polarisation of the recoil nucleon is unknown. The angular distribution of vector meson decay products can be parameterised in terms of spin-density matrix elements. This distribution can be measured experimentally, making it possible to determine the elements of the spin-density matrix. In doing so, spin properties of the virtual particle exchange become accessible. This is valuable input for production models, which need to be well understood in the search for hybrid mesons.

2.2.1 Notations

The polarisation state of the vector meson is expressed as a spin-density matrix, $\rho(V)$, which is related to the photon spin-density matrix (c.f. Section 2.2.3), $\rho(\gamma)$, and production amplitudes, T [34]

$$\rho(V) = T\rho(\gamma)T^\dagger. \quad (2.5)$$

Using the centre of mass helicity representation of Jacob and Wick [35], this expression becomes

$$\rho(V)_{\lambda_V \lambda'_V} = \frac{1}{n} \sum_{\lambda_{N'} \lambda_\gamma \lambda_N \lambda'_\gamma} T_{\lambda_V \lambda_{N'}, \lambda_\gamma \lambda_N} \rho(\gamma)_{\lambda_\gamma \lambda'_\gamma} T_{\lambda'_V \lambda_{N'}, \lambda'_\gamma \lambda_N}^* \quad (2.6)$$

The λ terms denote the helicities of particles from Reaction (2.4), where $\lambda_\gamma = \pm\frac{1}{2}$ and $\lambda_N, \lambda_{N'} = +1, 0$ or -1 . The normalisation factor, n , is given by

$$n = \frac{1}{2} \sum_{\lambda_V \lambda_{N'} \lambda_\gamma \lambda_N} |T_{\lambda_V \lambda_{N'}, \lambda_\gamma \lambda_N}|^2. \quad (2.7)$$

The helicity system

For the remainder of this section, the vector meson decay distribution is described in its helicity rest frame [34], which is a convenient system for studying helicity conservation in the s -channel. The system is constructed such that the z direction is given by the direction of the target recoil in the vector meson rest frame. This is equivalent to the direction of the vector meson in the overall centre of mass frame. The y direction is chosen to be orthogonal to the production plane defined by the cross product $\mathbf{k} \times \mathbf{q}$, where \mathbf{k} and \mathbf{q} are the three-momentum vectors of the incident photon and photoproduced vector meson respectively. The x direction is then given by $\mathbf{y} \times \mathbf{z}$. An illustration of the helicity frame is shown in Figure 2.5. The decay angles θ and ϕ are defined as the polar and azimuthal angles of one of the decay products in the vector meson rest frame, assuming the reaction is described by a two body decay. Note that for the analysis presented in this thesis, the π^+ was chosen to define θ and ϕ . The direction of the decay particle is denoted by the unit vector $\boldsymbol{\pi}$.

$$\cos(\theta) = \boldsymbol{\pi} \cdot \mathbf{z}, \quad \cos\phi = \frac{\mathbf{y} \cdot (\mathbf{z} \times \boldsymbol{\pi})}{|\mathbf{z} \times \boldsymbol{\pi}|}, \quad \sin(\phi) = -\frac{\mathbf{x} \cdot (\mathbf{z} \times \boldsymbol{\pi})}{|\mathbf{z} \times \boldsymbol{\pi}|}. \quad (2.8)$$

Note that the conversions from the helicity system to the Adair or Gottfried-Jackson systems are trivial, and only require a rotation with a small Wigner matrix. This is possible since these frames only differ from the helicity system in their choice of z axis. In the Gottfried-Jackson frame, the z direction is defined as the direction on the incoming photon in the vector meson rest frame. In the Adair frame the z axis is chosen as the direction of the incoming photon in the centre of mass frame.

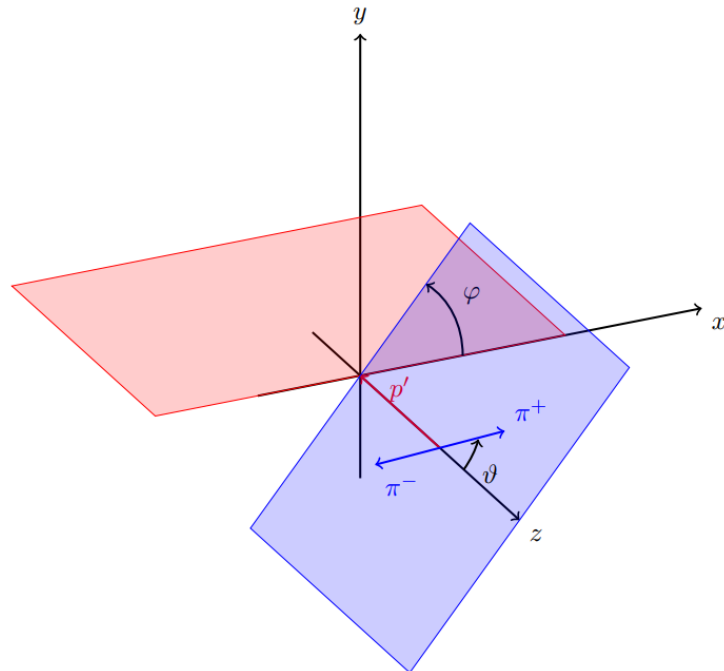


Figure 2.5: Diagram showing the helicity frame. Figure taken from [36]

2.2.2 Generalised form of the decay angular distribution

The angular distribution of decay products in the rest frame of the vector meson is given by

$$\frac{dN}{d\cos\theta d\phi} = W(\cos\theta, \phi) = M\rho(V)M^\dagger = \sum_{\lambda_V\lambda'_V} \langle\theta, \phi|M|\lambda_V\rangle \rho(V)_{\lambda_V\lambda'_V} \langle\lambda'_V|M^\dagger|\theta, \phi\rangle \quad (2.9)$$

Where M is the decay amplitude and

$$\langle\theta, \phi|M|\lambda_V\rangle = C\sqrt{\frac{3}{4\pi}}D_{\lambda_V 0}^{1*}(\phi, \theta, -\phi) \quad (2.10)$$

for a vector meson decaying into spinless particles [34]. $|C|^2$ is proportional to the vector meson decay width [37]. C is independent of λ_V due to rotational invariance, and is set to equal one since a normalised decay angular distribution is being considered. The Wigner rotation functions [38] $D_{\lambda_V 0}^1$ are given by

$$\begin{aligned} D_{10}^1(\phi, \theta, -\phi) &= -\frac{1}{\sqrt{2}}\sin\theta e^{-i\phi}, \\ D_{00}^1(\phi, \theta, -\phi) &= \cos\theta, \\ D_{-10}^1(\phi, \theta, -\phi) &= \frac{1}{\sqrt{2}}\sin\theta e^{i\phi}. \end{aligned} \quad (2.11)$$

Equation (2.9) can be written as

$$W(\cos\theta, \phi) = \frac{3}{4\pi} \sum_{\lambda_V\lambda'_V} D_{\lambda_V 0}^1(\phi, \theta, -\phi)^* \rho(V)_{\lambda_V\lambda'_V} D_{\lambda'_V 0}^1(\phi, \theta, -\phi) \quad (2.12)$$

using Equation (2.10). Since $\rho(V)$ is hermitian ($\rho(V)_{\lambda_V\lambda'_V} = \rho^*(V)_{\lambda'_V\lambda_V}$, see Equations (2.6) and (2.16)), Equation (2.12) can be expressed as

$$\begin{aligned} W(\cos\theta, \phi, \rho(V)) &= \frac{3}{4\pi} \left(\frac{1}{2}(\rho_{11} + \rho_{-1-1}) \sin^2\theta + \rho_{00} \cos^2\theta + \right. \\ &\frac{1}{\sqrt{2}}(-\text{Re}\rho_{10} + \text{Re}\rho_{-10}) \sin\theta \cos\phi + \frac{1}{\sqrt{2}}(\text{Im}\rho_{10} + \text{Im}\rho_{-10}) \sin 2\theta \sin\phi \\ &\left. - \text{Re}\rho_{1-1} \sin^2\theta \cos 2\phi + \text{Im}\rho_{1-1} \sin^2\theta \sin 2\phi \right). \end{aligned} \quad (2.13)$$

This expression is simplified in Section 2.2.5 using symmetries of $\rho(V)$ following from the properties of $\rho(\gamma)$ and the production amplitude, T .

2.2.3 Photon density matrix

The photon wave function $|\gamma\rangle$ in the helicity basis for a pure photon state is given by

$$|\gamma\rangle = a_+ |\lambda_\gamma = +1\rangle + a_- |\lambda_\gamma = -1\rangle \quad (2.14)$$

where

$$||\lambda_\gamma = \pm 1\rangle|^2 = 1, \quad |a_+|^2 + |a_-|^2 = 1. \quad (2.15)$$

The photon density matrix can then be written as

$$\rho^{pure}(\gamma) = |\gamma\rangle \langle \gamma| = \begin{bmatrix} |a_+|^2 & a_+ a_-^* \\ a_- a_+^* & |a_-|^2 \end{bmatrix} \quad (2.16)$$

For linearly polarised photons, Equation (2.14) is written as [34]

$$|\gamma\rangle = -\frac{1}{\sqrt{2}}(e^{-i\Phi} |\lambda_\gamma = +1\rangle - e^{i\Phi} |\lambda_\gamma = -1\rangle) \quad (2.17)$$

where Φ is the angle between the polarisation vector of the photon, $\varepsilon = (\cos \Phi, \sin \Phi, 0)$, and the production plane, as shown in Figure 2.5. The resulting density matrix is

$$\rho^{pure}(\gamma) = \frac{1}{2} \begin{bmatrix} 1 & -e^{2i\Phi} \\ e^{2i\Phi} & 1 \end{bmatrix}. \quad (2.18)$$

For partially polarised photons, the density matrix can be expressed as a linear combination of the 2×2 unit matrix, I , and the three Pauli matrices, σ_i ($i = 1, 2, 3$) [34]

$$\rho(\gamma) = \frac{1}{2}I + \frac{1}{2}\mathbf{P}_\gamma \cdot \boldsymbol{\sigma}. \quad (2.19)$$

I and σ_i form a complete set in the space of 2×2 hermitian matrices. \mathbf{P}_γ is given by

$$\mathbf{P}_\gamma = P_\gamma(-\cos 2\Phi, -\sin 2\Phi, 0) \quad (2.20)$$

where P_γ defines the degree of linear polarisation of the photon.

2.2.4 Symmetry properties of helicity amplitudes

When working in the helicity frame, parity conservation gives the following relation for Reaction (2.4) [35]

$$T(\Theta^*)_{-\lambda_V - \lambda_{N'}, -\lambda_\gamma - \lambda_N} = (-1)^{(\lambda_V - \lambda_{N'}) - (\lambda_\gamma - \lambda_N)} T(\Theta^*)_{\lambda_V \lambda_{N'}, \lambda_\gamma \lambda_N}, \quad (2.21)$$

where Θ^* is the production angle in the centre of mass frame [34]. If only natural ($P = (-1)^J$) or only unnatural ($P = -(-1)^J$) t-channel parity exchanges contribute, then to leading order in photon energy an additional symmetry [39] holds,

$$\begin{aligned} T(\Theta^*)_{-\lambda_V-\lambda_{N'},-\lambda_\gamma-\lambda_N} &= \pm(-1)^{\lambda_V-\lambda_\gamma} T(\Theta^*)_{\lambda_V\lambda_{N'},\lambda_\gamma\lambda_N} \\ &= \mp(-1)^{\lambda_V} T(\Theta^*)_{\lambda_V\lambda_{N'},\lambda_\gamma\lambda_N}, \end{aligned} \quad (2.22)$$

where the upper and lower signs apply for natural and unnatural parity exchanges respectively.

The production amplitude can be split into natural and unnatural components as

$$T = T^N + T^U \quad (2.23)$$

T^N and T^U can then be projected out using Equation (2.21),

$$T^{\overset{N}{U}}(\Theta^*)_{\lambda_V\lambda_{N'},\lambda_\gamma\lambda_N} = \frac{1}{2} \left(T(\Theta^*)_{\lambda_V\lambda_{N'},\lambda_\gamma\lambda_N} \mp (-1)^{\lambda_V} T(\Theta^*)_{-\lambda_V\lambda_{N'},-\lambda_\gamma\lambda_N} \right) \quad (2.24)$$

2.2.5 Decomposition of $\rho(\mathbf{V})$

Using Equations (2.5) and (2.19), the density matrix $\rho(V)$ can be expressed as

$$\rho(V) = \rho^0 + \sum_{i=1}^3 P_\gamma^\alpha \rho^\alpha, \quad (2.25)$$

where

$$(\rho^0, \rho^\alpha) = T \left(\frac{1}{2} I, \frac{1}{2} \sigma^\alpha \right) T^\dagger, \quad \alpha = 1, 2, 3. \quad (2.26)$$

The form of this relation now explicitly shows the dependence on the polarisation vector \mathbf{P}_γ .

The ρ^α matrices are given by

$$\rho_{\lambda_V\lambda_V'}^0 = \frac{1}{2n} \sum_{\lambda_\gamma\lambda_{N'}\lambda_N} T_{\lambda_V\lambda_{N'},\lambda_\gamma\lambda_N} T_{\lambda_V'\lambda_{N'},\lambda_\gamma\lambda_N}^* \quad (2.27a)$$

$$\rho_{\lambda_V\lambda_V'}^1 = \frac{1}{2n} \sum_{\lambda_\gamma\lambda_{N'}\lambda_N} T_{\lambda_V\lambda_{N'},-\lambda_\gamma\lambda_N} T_{\lambda_V'\lambda_{N'},\lambda_\gamma\lambda_N}^* \quad (2.27b)$$

$$\rho_{\lambda_V\lambda_V'}^2 = \frac{i}{2n} \sum_{\lambda_\gamma\lambda_{N'}\lambda_N} \lambda_\gamma T_{\lambda_V\lambda_{N'},-\lambda_\gamma\lambda_N} T_{\lambda_V'\lambda_{N'},\lambda_\gamma\lambda_N}^* \quad (2.27c)$$

$$\rho_{\lambda_V\lambda_V'}^3 = \frac{1}{2n} \sum_{\lambda_\gamma\lambda_{N'}\lambda_N} \lambda_\gamma T_{\lambda_V\lambda_{N'},\lambda_\gamma\lambda_N} T_{\lambda_V'\lambda_{N'},\lambda_\gamma\lambda_N}^* \quad (2.27d)$$

The parity conservation relation given by Equation (2.21) limits the number of linearly independent matrix elements

$$\rho_{\lambda\lambda'}^\alpha = (-1)^{\lambda-\lambda'} \rho_{-\lambda-\lambda'}^\alpha, \quad \alpha = 0, 1 \quad (2.28a)$$

$$\rho_{\lambda\lambda'}^\alpha = -(-1)^{\lambda-\lambda'} \rho_{-\lambda-\lambda'}^\alpha, \quad \alpha = 2, 3. \quad (2.28b)$$

Note that these symmetries hold in any reference frame that can be reached from the helicity system by a rotation about the normal to the production plane. Since the ρ^α matrices are hermitian, Equations (2.28a) and (2.28b) imply that ρ_{1-1}^0 and ρ_{1-1}^1 are real while ρ_{1-1}^2 and ρ_{1-1}^3 are purely imaginary. The decay distribution W from Equation (2.13) scales linearly with $\rho(V)$. This means Equation (2.25) can also be used to decompose the decay distribution W

$$W(\cos\theta, \phi, \rho) = W^0(\cos\theta, \phi) + \sum_{\alpha=1}^3 P_\gamma^\alpha W^\alpha(\cos\theta, \phi), \quad (2.29)$$

where

$$W^\alpha(\cos\theta, \phi) = W(\cos\theta, \phi, \rho^\alpha), \quad \alpha = 0, 1, 2, 3 \quad (2.30)$$

The symmetries of ρ^α matrices given by Equations (2.28a) and (2.28b) are used to express W^α as

$$\begin{aligned} W^0(\cos\theta, \phi) &= \frac{3}{4\pi} \left(\frac{1}{2}(1 - \rho_{00}^0) + \frac{1}{2}(3\rho_{00}^0 - 1)\cos^2\theta - \sqrt{2}\operatorname{Re}\rho_{10}^0\sin 2\theta\cos\phi - \rho_{1-1}^0\sin^2\theta\cos 2\phi \right), \\ W^1(\cos\theta, \phi) &= \frac{3}{4\pi} \left(\rho_{11}^1\sin^2\theta + \rho_{00}^1\cos^2\theta - \sqrt{2}\operatorname{Re}\rho_{10}^1\sin 2\theta\cos\phi - \rho_{1-1}^1\sin^2\theta\cos 2\phi \right), \\ W^2(\cos\theta, \phi) &= \frac{3}{4\pi} \left(\sqrt{2}\operatorname{Im}\rho_{10}^2\sin 2\theta\sin\phi + \operatorname{Im}\rho_{1-1}^2\sin^2\theta\sin 2\phi \right), \\ W^3(\cos\theta, \phi) &= \frac{3}{4\pi} \left(\sqrt{2}\operatorname{Im}\rho_{10}^3\sin 2\theta\sin\phi + \operatorname{Im}\rho_{1-1}^3\sin^2\theta\sin 2\phi \right). \end{aligned} \quad (2.31)$$

For linearly polarised photons,

$$W(\cos\theta, \phi) = W^0(\cos\theta, \phi) - P_\gamma\cos 2\Phi W^1(\cos\theta, \phi) - P_\gamma\sin 2\Phi W^2(\cos\theta, \phi). \quad (2.32)$$

A majority of the work presented in this thesis concerns unpolarised $\pi^+\pi^-$ photoproduction. In the case of unpolarised photons, Equation (2.32) is simplified to

$$W(\cos\theta, \phi) = W^0(\cos\theta, \phi). \quad (2.33)$$

2.2.6 The helicity conservation model

By considering parity conservation and hermiticity, the density matrices ρ^μ are constructed as follows [34]

$$\begin{aligned}
 \rho^0 &= \begin{bmatrix} \frac{1}{2}(1 - \rho_{00}^0) & \text{Re} \rho_{10}^0 + i \text{Im} \rho_{10}^0 & \text{Re} \rho_{1-1}^0 \\ & \rho_{00}^0 & -(\text{Re} \rho_{10}^0 - i \text{Im} \rho_{10}^0) \\ & & \frac{1}{2}(1 - \rho_{00}^0) \end{bmatrix}, \\
 \rho^1 &= \begin{bmatrix} \rho_{11}^1 & \text{Re} \rho_{10}^1 + i \text{Im} \rho_{10}^1 & \text{Re} \rho_{1-1}^1 \\ & \rho_{00}^1 & -(\text{Re} \rho_{10}^1 - i \text{Im} \rho_{10}^1) \\ & & \rho_{11}^1 \end{bmatrix}, \\
 \rho^2 &= \begin{bmatrix} \rho_{11}^2 & \text{Re} \rho_{10}^2 + i \text{Im} \rho_{10}^2 & i \text{Im} \rho_{1-1}^2 \\ & 0 & (\text{Re} \rho_{10}^2 - i \text{Im} \rho_{10}^2) \\ & & -\rho_{11}^2 \end{bmatrix}, \\
 \rho^3 &= \begin{bmatrix} \rho_{11}^3 & \text{Re} \rho_{10}^3 + i \text{Im} \rho_{10}^3 & i \text{Im} \rho_{1-1}^3 \\ & 0 & (\text{Re} \rho_{10}^3 - i \text{Im} \rho_{10}^3) \\ & & -\rho_{11}^3 \end{bmatrix},
 \end{aligned} \tag{2.34}$$

where the lower half of the matrices are completed by hermitian conjugation. The s-channel helicity conservation model predicts vector meson photoproduction to proceed via diffraction. In this model, the ρ matrices do not depend on the incoming photon energy or the production angle. It also predicts that ρ^0 and ρ^3 are diagonal while ρ^1 and ρ^2 are anti-diagonal. This would imply that the helicity system density matrices are

$$\begin{aligned}
 \rho^0 &= \begin{bmatrix} \frac{1}{2} & 0 & 0 \\ 0 & 0 & 0 \\ 0 & 0 & \frac{1}{2} \end{bmatrix}, & \rho^1 &= \begin{bmatrix} 0 & 0 & \frac{1}{2} \\ 0 & 0 & 0 \\ \frac{1}{2} & 0 & 0 \end{bmatrix}, \\
 \rho^2 &= \begin{bmatrix} 0 & 0 & -\frac{i}{2} \\ 0 & 0 & 0 \\ \frac{i}{2} & 0 & 0 \end{bmatrix}, & \rho^3 &= \begin{bmatrix} \frac{1}{2} & 0 & 0 \\ 0 & 0 & 0 \\ 0 & 0 & -\frac{1}{2} \end{bmatrix},
 \end{aligned} \tag{2.35}$$

assuming the parity exchange is purely natural ($P = (-1)^J$). Experimental measurements of SDMEs in unpolarised vector meson photoproduction test the validity of the model, which if true would suggest that $\rho_{00}^0 = \text{Re} \rho_{10}^0 = \rho_{1-1}^0 = 0$. Any observed deviations from s-channel helicity conservation would either imply that the production process is not purely diffractive, or that the parity exchange is not purely natural. For a more detailed discussion of the helicity conservation model, see [40].

2.3 Baryonic contributions to the $\pi^+\pi^-$ final state

Although vector mesons are produced abundantly in photoproduction due to vector meson dominance, it is possible to produce various other hadronic states. This is illustrated in Figure 2.6, which shows the photoproduction cross section for several reactions as a function of beam energy. The 100 MeV to 1 GeV energy range for photoproduction is known as the *resonance*

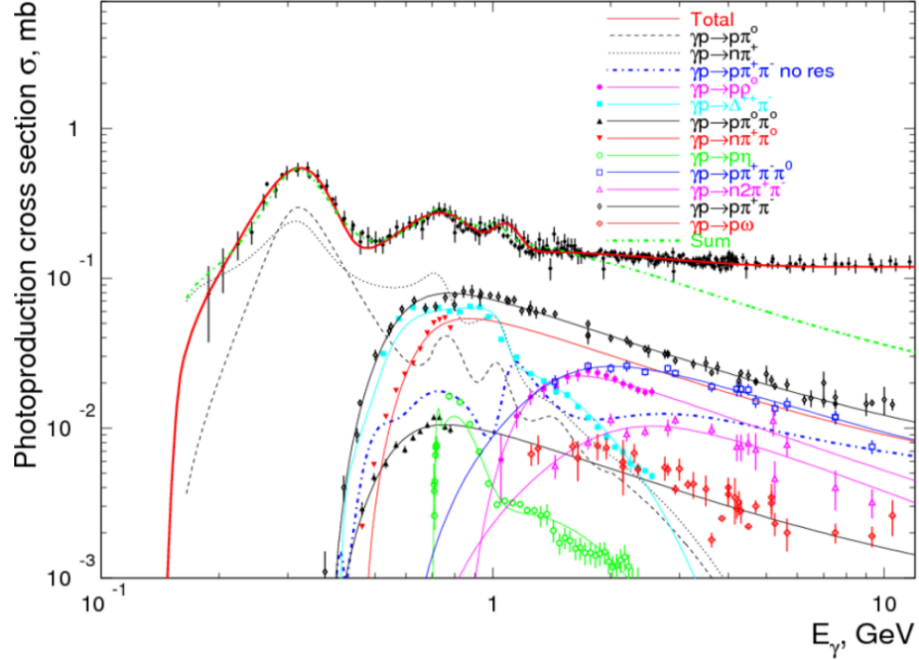


Figure 2.6: Photoproduction cross sections for various final states as a function of beam energy. The cross section can be thought of as a measure of the probability for a specific reaction to occur. Figure taken from [41]

region. Over this energy regime, the photon is more likely to induce excited baryon states such as N^* and Δ resonances in the target nucleon. More hadronic channels become accessible in the GlueX photon energy regime of 3.0 – 11.6 GeV, and the overall baryonic contribution becomes less important. Nevertheless, these resonances produce final states which are indistinguishable from that expected from the $\rho(770)$ resonance. The most prominent contribution comes from the Δ^{++} , which decays via the $p\pi^+$ subsystem. Although both N^* and Δ^0 resonances can decay to $p\pi^-$, they do so with lower branching fractions. The production mechanisms for Δ^{++} , Δ^0 and N^* resonances are illustrated in Figure 2.7. Equation (2.32) explicitly relates to vector mesons decaying to a pseudoscalar ($J^P = 0^-$) meson pair, and can not describe the measured $\pi^+\pi^-$ angular distribution resulting from baryon production. In the low GlueX beam energy region, the kinematic separation between baryon resonances and the $\rho(770)$ is poorer. Removing these backgrounds is often not possible, and the only way in which they can be properly accounted for is by performing a partial wave analysis of the full $p\pi^+\pi^-$ final state. A cleaner separation is obtained at higher energies, and contamination from baryons becomes less significant.

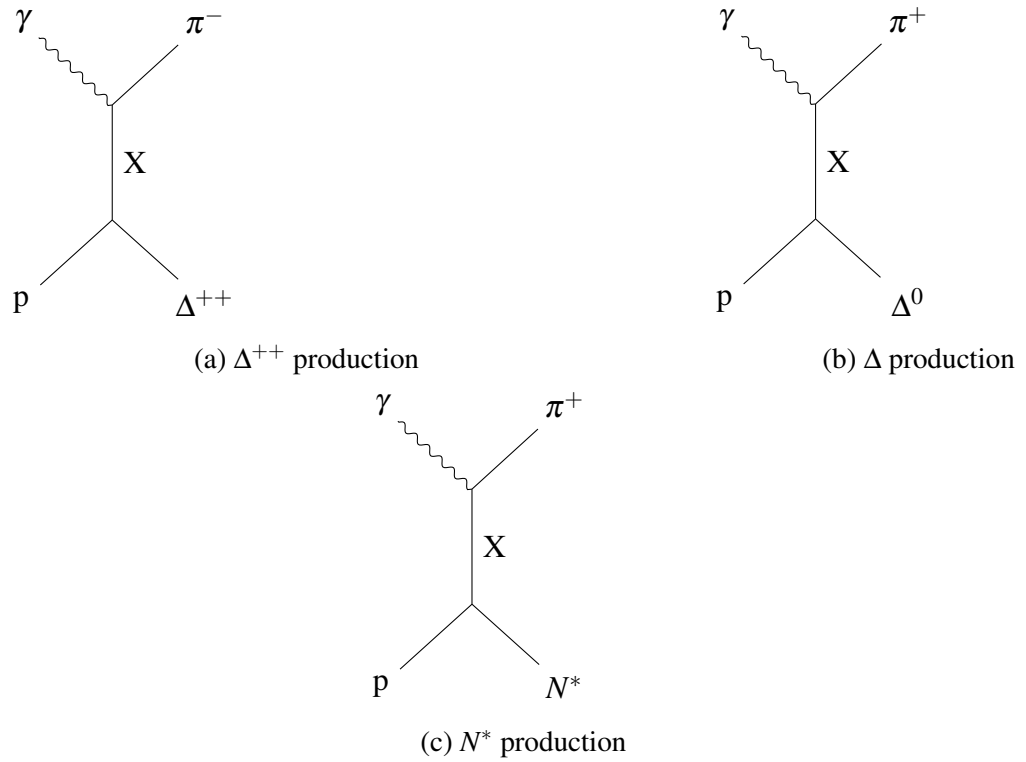


Figure 2.7: Diagrams showing the t-channel production of (a) Δ^{++} , (b) Δ^0 and (c) N^* baryon resonances.

2.4 Summary

In this chapter, a formalism for parameterising the angular distribution of vector meson decay products as SDMEs has been presented. Chapter 6 demonstrates that the formalism makes it possible to extract SDMEs from experimental data using an extended maximum likelihood fit. SDMEs are valuable input for production models, since they allow access to properties of the underlying production exchange mechanism. Although the analysed decay distribution is dominated by the $\rho(770)$ vector meson resonance, there is also a non-negligible contribution from Drell-type, non-resonant processes. Currently, there is no way of distinguishing these from $\rho(770)$ decays. Moreover, there are baryonic contributions to the $\pi^+\pi^-$ final state that can not be described by the vector meson SDME model. These contributions become especially important at low photon energies, where the kinematic separation between the $\rho(770)$ and baryon resonances is not as clean. For these reasons, it is worth re-iterating that the measurements presented in Chapter 8.1 describe $\pi^+\pi^-$ production, rather than the production of the $\rho(770)$ resonance alone. It is likely that a model for $\pi^+\pi^-$ photoproduction that incorporates non-resonant s-wave processes and baryonic contributions will be developed in the future. In the following chapter, previous measurements of SDMEs in $\pi^+\pi^-$ photoproduction are summarised. The theoretical model for vector meson photoproduction formulated by the JPAC theory group is also introduced.

Chapter 3

Review of previous results and theoretical model

The following chapter gives an overview of the results published by other experimental collaborations, along with a summary of the most detailed existing photoproduction model for vector mesons. Although the $\rho(770)$ has been studied extensively over the years, limited photoproduction data exists in the GlueX energy regime. The best available photoproduction data was measured by the CLAS collaboration over the 3.0 – 3.8 GeV energy range, and also with SLAC over a range of energies with limited statistics. These analyses are summarised in the sections that follow.

3.1 Previous measurements

The earliest predictions of vector mesons were based on nuclear form factor data. In 1957, Nambu [42] postulated the existence of an isovector meson, called the ρ^0 , to account for the nucleon charge distributions observed in electron scattering experiments [43]. Fraser and Fulco [44] supported this claim in 1959, predicting that the existence of the ρ^0 was required to explain the behavior of the electromagnetic structure of the nucleons. In 1960, Sakurai [45] developed a theory which included an isovector and two isoscalar vector mesons based on conserved currents and universality. The theory was extended to include the full set of vector mesons by Salam and Ward [46] in 1961, and later by both Gell-Mann [4] and Neeman [47] in independently developed formalisms.

The $\rho(770)$ was the first vector meson to be observed experimentally in bubble chamber studies of $\pi^- p$ scattering at Brookhaven National Laboratory in 1961 [48]. They observed a peak at low momentum transfer in the $\pi^+ \pi^-$ cross section at an invariant mass of 750 MeV with a width of 150 – 200 MeV, which they identified as a J=1 resonance state. Soon thereafter, Brookhaven

reported another observation of the $\rho(770)$ in π^+p scattering [49]. The formulation of the vector meson dominance model [31] sparked interest in vector meson photoproduction. Following the development of the spin-density matrix formalism for vector mesons in photoproduction by Schilling et al [34], the first measurements of neutral vector meson SDMEs were performed at the Stanford Linear Accelerator Center (SLAC) in 1973 [50]. These measurements are summarised in the following.

3.1.1 SLAC

In 1973, Ballam et al used linearly polarised bremsstrahlung photons to study vector meson photoproduction with a hydrogen bubble chamber at SLAC [50]. Data were obtained using photon energies of 2.8 GeV, 4.7 GeV and 9.3 GeV. This allowed the analysers to extract differential cross sections and SDMEs for the $\rho(770)$, ω and ϕ vector meson resonances. The linear polarisation of the beam made it possible to measure six polarised SDMEs for the $\rho(770)$, in addition to the three unpolarised SDMEs in seven bins in the momentum transfer squared $-t$. The parity asymmetry P_σ was also determined, where

$$P_\sigma = 2\rho_{11}^1 - \rho_{00}^1. \quad (3.1)$$

The results measured with 9.3 GeV photons are presented in Figure 3.1. Although measurements were performed with limited statistics, the data were sufficient to demonstrate that the natural exchanges contributing to $\rho(770)$ production generally conserve helicity, and that the unnatural parity contributions are negligible.

3.1.2 CLAS

In 2009, Battaglieri et al published an analysis of the exclusive reaction $\gamma p \rightarrow p\pi^+\pi^-$ in the 3.0 – 3.8 GeV photon energy range and 0.4 – 1.0 GeV²/c² range in the momentum transfer squared $-t$. Measurements were performed using the CLAS detector based at Jefferson Lab. The $p\pi^+\pi^-$ final state was selected by identifying the p and π^+ in the detector and reconstructing the π^- using the missing mass technique. Moments of the $\pi^+\pi^-$ angular distribution were first extracted from the data. Note that a detailed discussion of moments of angular distribution can be found in [51]. A partial wave expansion of the fitted moments was then performed to disentangle the different resonance spin contributions, and SDMEs were calculated from the resulting production amplitudes. An example plot showing the SDMEs calculated with CLAS for the P-wave contribution over the 3.2 – 3.4 GeV beam energy regime is shown in Figure 3.2. Note that SDMEs are plotted against the $\pi^+\pi^-$ invariant mass rather than $-t$.

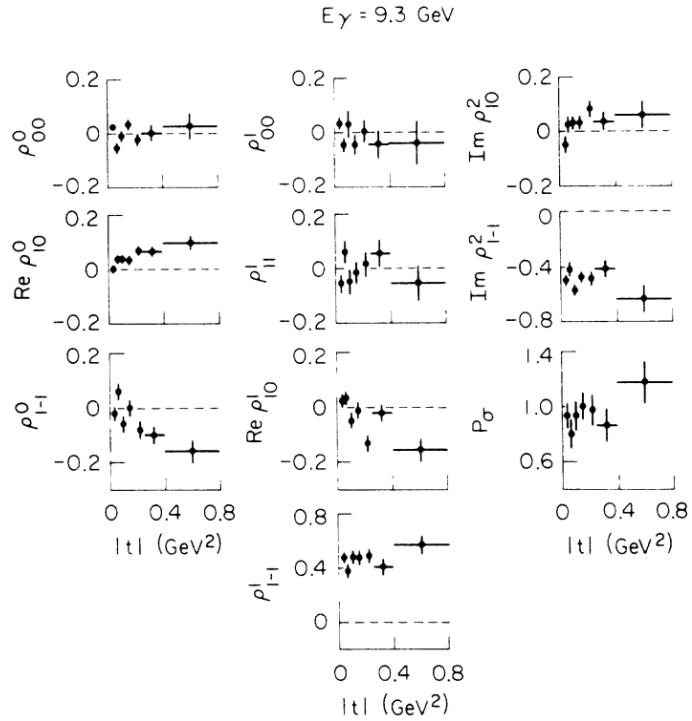


Figure 3.1: SDMEs in polarised $\rho(770)$ photoproduction reported by SLAC at a beam energy of 9.3 GeV. The six polarised and three polarisation independent SDMEs are plotted against the momentum transfer squared $-t$. The measured parity asymmetry P_σ is also shown in the bottom right plot. Figure taken from [50].

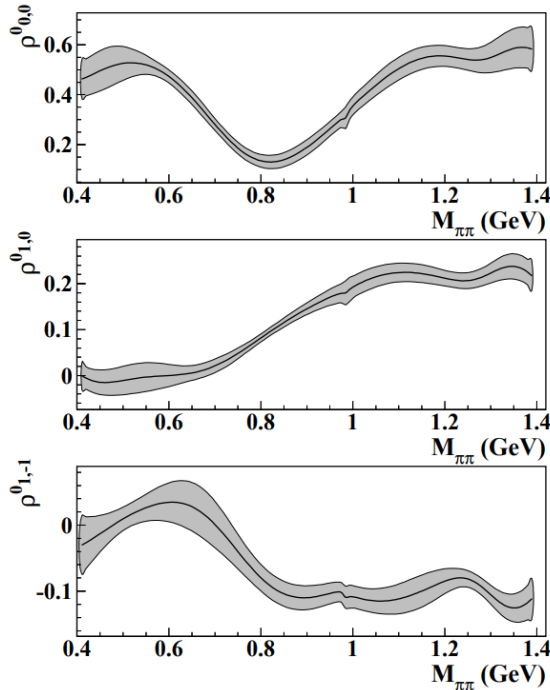


Figure 3.2: P-wave SDMEs in unpolarised photoproduction reported by CLAS. SDMEs were determined from fitted moments of angular distribution over the 3.2 – 3.4 GeV beam energy regime and $0.5 - 0.6 \text{ GeV}^2/c^2$ range in $-t$. Figure taken from [52].

3.2 Current theoretical model

A detailed model for the photoproduction of the three lightest vector mesons was developed by theorists at the Joint Physics Analysis Center (JPAC) [53]. They were able to use the model to predict the energy and momentum transfer dependence of the vector meson SDMEs. Figure 3.3 shows the SDMEs predicted by the JPAC model for the three lightest vector mesons. The model was formulated by performing a fit to the vector meson SDME measurements reported by SLAC (c.f. Section 3.1.1). The JPAC group based their model on Regge theory, which describes vector meson production at high energies as a process dominated by the exchange of Reggeons. Reggeons are defined as the poles of a Regge trajectory, and correspond to physical particles. The Regge trajectory is obtained by plotting the mass squared of the exchanged particle as a function of the total angular momentum, J . A more detailed summary of Regge theory is included in [29]. Only the leading order Regge trajectories are considered in the JPAC model, corresponding to the a_2 , f_2 , π and η exchanges. The natural parity Pomeron exchange is also considered, which is expected to dominate at high energies.

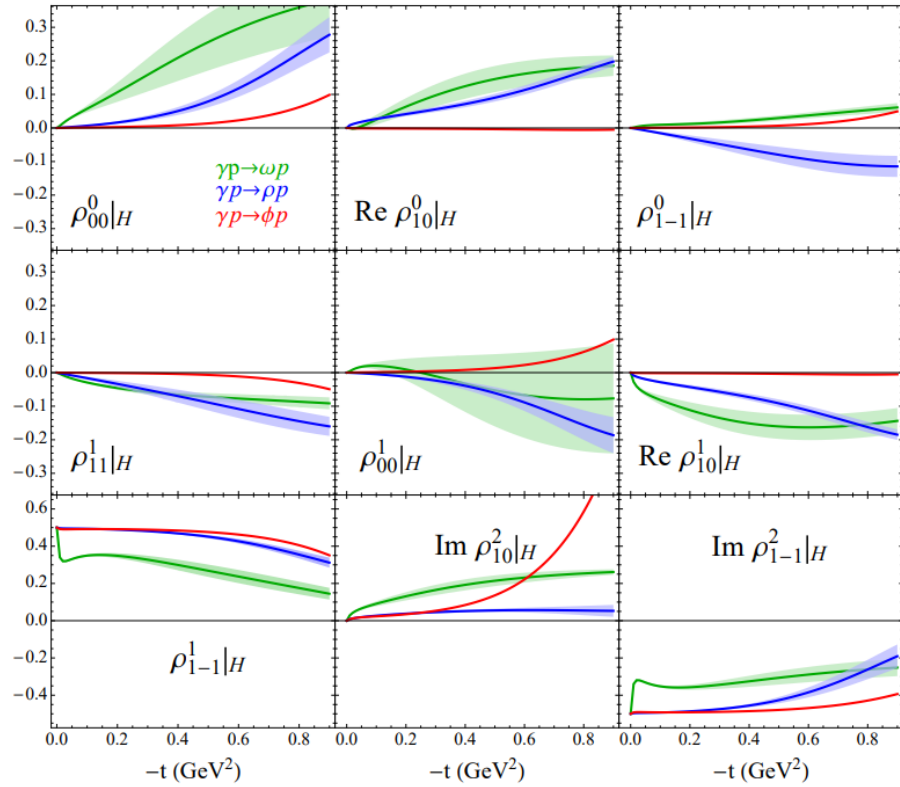


Figure 3.3: SDMEs predicted by the JPAC model for the photoproduction of the three lightest vector mesons with 8.5 GeV photons. Figure taken from [53].

In the JPAC model, the unpolarised SDMEs are determined in the Gottfried-Jackson frame as

$$\rho_{00}^0 = \frac{1}{N} \sum_{\lambda, \lambda'} M_{1,0} M_{1,0}^* , \quad (3.2)$$

$$\text{Re}\rho_{10}^0 = \frac{1}{2N} \text{Re} \sum_{\lambda, \lambda'} \left(M_{\lambda, \lambda'}^{1,1} - M_{\lambda, \lambda'}^{1,-1} \right) M_{\lambda, \lambda'}^{*1,0}, \quad (3.3)$$

$$\rho_{1-1}^0 = \frac{1}{N} \text{Re} \sum_{\lambda, \lambda'} M_{\lambda, \lambda'}^{1,1} M_{\lambda, \lambda'}^{*1,-1}, \quad (3.4)$$

where λ and λ' denote the helicities of the target and recoil nucleon respectively, and the M terms denote the s-channel helicity amplitudes. N is a normalisation factor given by

$$N = \frac{1}{2} \sum_{\lambda_\gamma, \lambda_V, \lambda, \lambda'} |M_{\lambda_\gamma, \lambda_V}|^2, \quad (3.5)$$

where λ_γ and λ_V denote the helicities of the incoming photon and photoproduced vector meson. SDMEs are determined in the helicity frame by a rotation of angle θ_q , the angle between the opposite direction of the recoil and the direction of the incoming photon,

$$\rho_{MM'}|_{GJ} = \sum_{\lambda_V, \lambda'_V} D_{M, \lambda_V}^1(\theta_q) \rho_{\lambda_V, \lambda'_V|H} D_{M', \lambda_V}^1(\theta_q). \quad (3.6)$$

The s-channel amplitudes are given by

$$M_{\lambda'_V, \lambda_\gamma}(s, t) = \sum_E M_{\lambda'_V, \lambda_\gamma}^E(s, t), \quad (3.7)$$

where the sum extends over the t-channel reggeons $E = \pi, \eta, \mathbb{P}, f_2, a_2$. Assuming a factorised form for each exchange,

$$M_{\lambda'_V, \lambda_\gamma}^E(s, t) = T_{\lambda'_V, \lambda_\gamma}^E(t) R^E(s, t) B_{\lambda'_V, \lambda_\gamma}^E(t), \quad (3.8)$$

where T^E and B^E denote the top and bottom vertices, describing the helicity transfer between the photon and vector meson and from the nucleon target to the recoil respectively. The coupling constants that JPAC extract by fitting the model to the SLAC data are encoded in these terms. This is discussed in detail in [53].

According to Regge theory, the energy dependence factorises into a power-law dependence given by $s^{\alpha_E(t)}$, where $\alpha_E(t)$ gives the relevant linear Regge trajectory ($\alpha_E(t) = \alpha_E(0) + \alpha'_E t$). The phase of the helicity amplitude is given by the signature factor $1 + e^{-i\pi\alpha_E(t)}$, which features in the definition of R^E ,

$$R^U(s, t) = \frac{1 + e^{-i\pi\alpha_U(t)}}{\sin\pi\alpha_U(t)} s^{\alpha_U(t)}, \quad (3.9)$$

$$R^N(s, t) = \frac{\alpha_N(t)}{\alpha_N(0)} \frac{1 + e^{-i\pi\alpha_N(t)}}{\sin\pi\alpha_N(t)} s^{\alpha_N(t)}, \quad (3.10)$$

where U and N denotes the unnatural (π, η) and natural (\mathbb{P}, f_2, a_2) exchanges respectively. The term \hat{s} is given by s/s_0 , with the energy scale given as $s_0 = 1 \text{ GeV}^2$.

By fitting this model to the SLAC data and extracting the relevant coupling constants, JPAC theorists were able to produce the SDME predictions shown in Figure 3.3. Both the dependence on the four-momentum transfer $-t$, and incoming photon energy are accounted for in the model. JPAC predictions of $\rho(770)$ SDMEs are compared with the results measured for this thesis in Section 8.1.

3.3 Summary

Although SDMEs have been measured previously in photoproduction for the $\pi^+\pi^-$ final state and $\rho(770)$ resonance, more data is clearly desirable. The only high energy measurement was performed by SLAC, where the available statistics were limited. Although SDMEs for the P-wave contribution to the $\pi^+\pi^-$ final state were determined with good statistical precision with CLAS, this was only achieved for a relatively narrow kinematic region. The measurement presented in this thesis takes advantage of the excellent statistics available with GlueX for the $\pi^+\pi^-$ final state to probe the energy, mass and momentum transfer dependence of SDMEs in more detail than any previous analysis of experimental data. This will provide the JPAC model with additional constraints, improving the accuracy of theoretical predictions and developing further our understanding of vector meson photoproduction. The following chapter explains how the GlueX detector is used to collect high quality photoproduction data from which SDMEs can be extracted.

Chapter 4

Experimental setup

This chapter provides an overview of the GlueX experiment, where the research for this work was performed. Figure 4.1 shows the experimental setup. The electron beam from the CEBAF accelerator is incident on a thin diamond radiator. This generates a linearly polarised photon beam from coherent bremsstrahlung, which is directed onto a proton (i.e. liquid hydrogen) target at the centre of the GlueX spectrometer. Outgoing neutral and charged particles are then detected using a combination of calorimetry, drift chambers and scintillating fibres. In the following, the GlueX beam line and detector subsystems are discussed in detail.

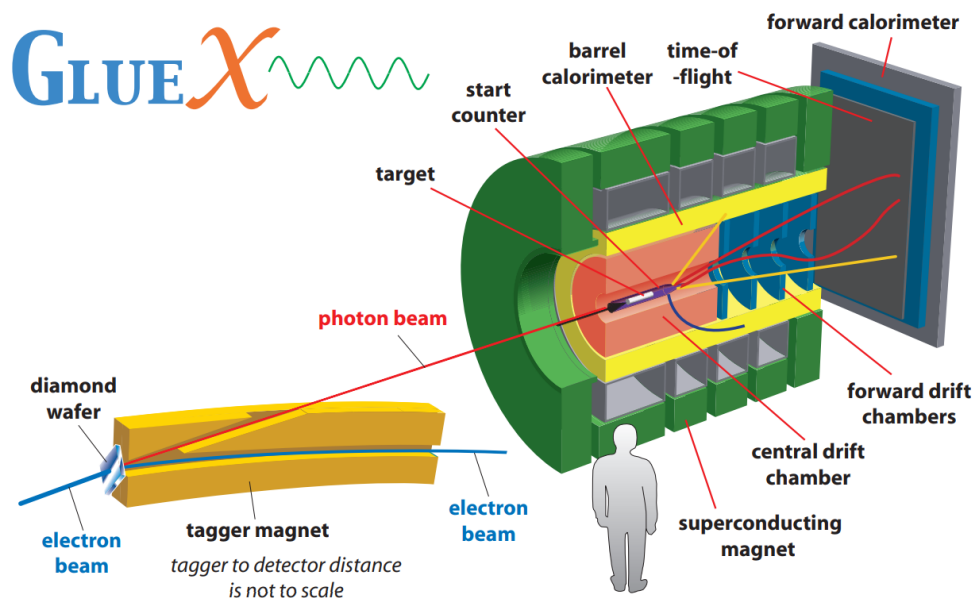


Figure 4.1: Schematic diagram of the important GlueX detector subsystems. Figure taken from [54].

4.1 CEBAF

The Continuous Electron Beam Accelerator Facility (CEBAF) is a continuous wave electron accelerator, delivering electrons with energies of up to 12 GeV. It has a total beam power of approximately 900 kW, corresponding to a current of around $100 \mu\text{A}$ [55]. The accelerator design comprises two anti-parallel linear accelerators (linac) connected by beam lines within steering magnets, as shown in Figure 4.2.

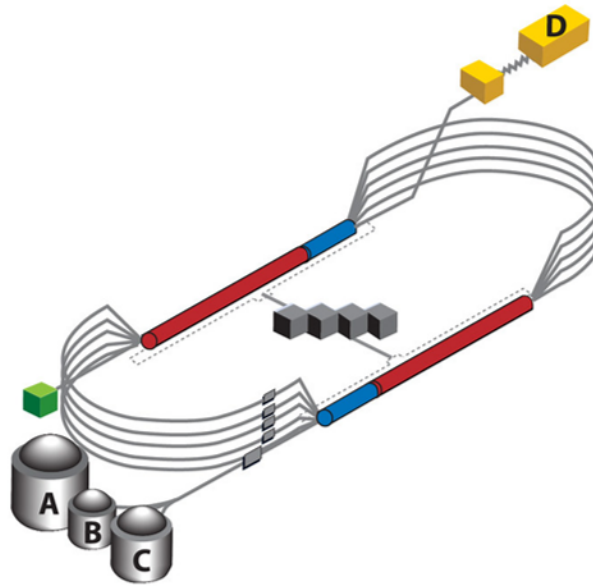


Figure 4.2: Schematic view of the CEBAF accelerator site. Figure taken from [56].

In the injection building, electron bunches are produced by directing a pulsed laser at a GaAs crystal [57]. Electrons are then injected into the north linac with a bunch frequency of either 499.0 MHz or 249.5 MHz [58], where each linac consists of 25 cryogenic modules [59]. Hall D receives 249.5 MHz bunches, corresponding to a bunch separation of 4.008 ns. Electrons are accelerated in each linac by an electromagnetic field generated by niobium cavities, super-cooled to 2 K using liquid helium [60]. At this temperature niobium becomes superconducting, which improves the efficiency of the acceleration process. The two linacs are connected by nine re-circulation arc beam lines within bending magnets for beam steering and focusing. With each full circulation of the race track configuration, electron energies increase by approximately 2.2 GeV [59]. After 5.5 passes, electrons are directed to the Hall D tagger hall, situated at the end of the north linac. Under normal running conditions between 150 nA and 180 nA of beam were delivered to Hall D during the Spring 2017 running period. Although maximum beam energies of 12 GeV are possible, the upper limit was reduced to 11.6 GeV during this period to improve accelerator stability.

4.2 Photon Beam

GlueX uses a linearly polarised beam for photoproduction experiments. Polarised photons are obtained by the method of coherent bremsstrahlung. Bremsstrahlung (breaking radiation) is radiation emitted in the form of photons by an electron as it decelerates in the electromagnetic field of an atomic nucleus [61]. Visual representations of the process are shown in Figures 4.3 and 4.4. The photon energy spectrum from bremsstrahlung follows a $1/E_\gamma$ distribution, as shown in Figure 4.5a.

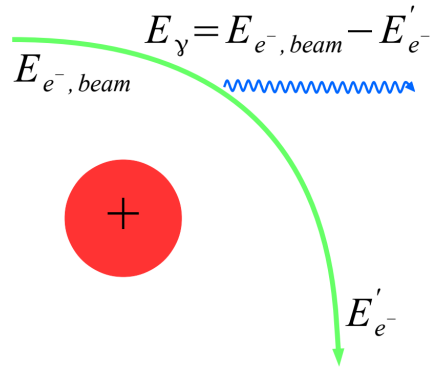


Figure 4.3: Diagram showing the production of bremsstrahlung radiation [62].

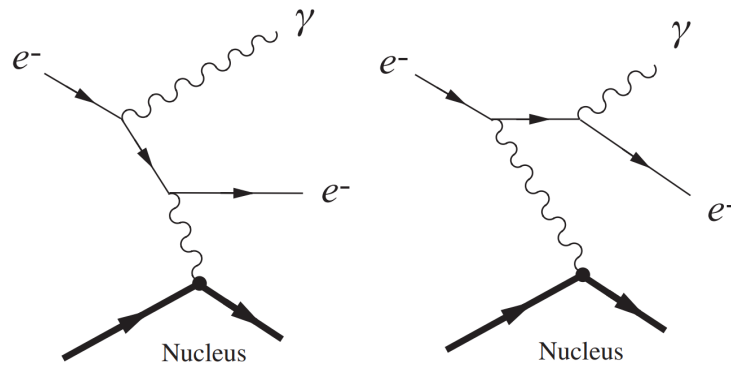


Figure 4.4: Dominant Feynman diagrams for the bremsstrahlung process (Figure taken from [63])

Coherent bremsstrahlung is analogous to Bragg scattering, a process where photons reflect from periodically spaced atoms to produce coherent scattered radiation. Similarly, coherent bremsstrahlung is produced when electrons are scattered from a medium consisting of periodically ordered atomic centres. One such medium is diamond. This is why the GlueX photon beam is produced by scattering electrons from a thin diamond wafer. A wafer orientation can be chosen that makes it possible for electrons to transfer their recoil momentum to the crystal lattice rather than a single atomic nucleus. When the recoil momentum transfer is equivalent to a multiple of the reciprocal lattice vector, the Bragg condition is satisfied and bremsstrahlung photons can interfere constructively. Photons originating from this process are linearly polar-

ised, and are referred to as *coherent bremsstrahlung*. A more detailed description of the coherent bremsstrahlung process can be found in [64]. Figure 4.5b shows the characteristic coherent bremsstrahlung energy spectrum. The $1/E_\gamma$ bremsstrahlung distribution underlies a series of peaks. These structures are characterised by an enhancement in the degree of linear polarisation. The most prominent peak is referred to as the *primary coherent peak*, and contains photons with the highest degree of polarisation. The steep decline to the right of the primary coherent peak is referred to as the *coherent edge*, and is used as a reference point to define the peak energy. The size of the coherent peak and degree of linear polarisation are limited by its energy relative to the incoming electron beam, but can be improved by collimation. The polarisation angle of coherent bremsstrahlung is determined by the orientation of the electric field vector of the photon beam. The polarisation angle, in addition to the peak energy can be controlled by finely tuning the diamond orientation relative to incoming electrons.

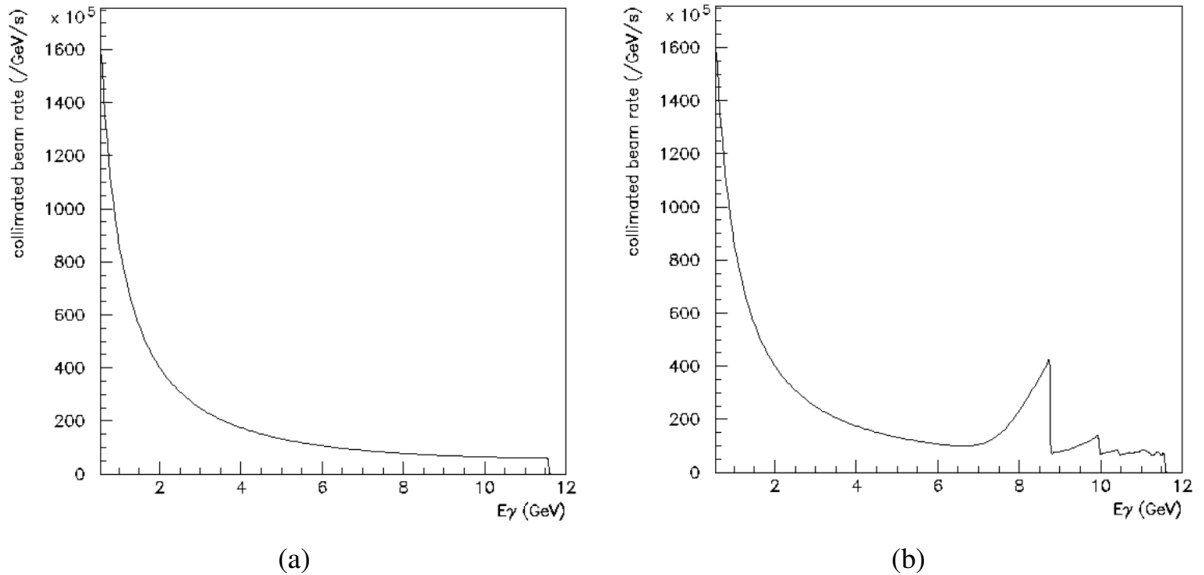


Figure 4.5: Photon energy spectra obtained (a) when an amorphous radiator is used and (b) when a diamond radiator is used. Each peak in (b) originates from the enhancement contribution of a different reciprocal lattice vector. Figure taken from [65].

At GlueX, the beam is obtained using coherent bremsstrahlung of electrons from CEBAF scattering off a $58 \mu\text{m}$ diamond wafer. The wafer is mounted on a goniometer in the Hall D tagger hall, 70 m upstream from the GlueX detector. By finely adjusting the diamond orientation, it is ensured that the primary coherent peak spans the energy range of 8.2 – 8.8 GeV. In this region, photons typically have a degree of linear polarisation of around 35%. Four different wafer orientations are used at GlueX, corresponding to two sets of orthogonal polarisation angles. This is done to reduce systematic uncertainties and to simplify the extraction of beam asymmetries.

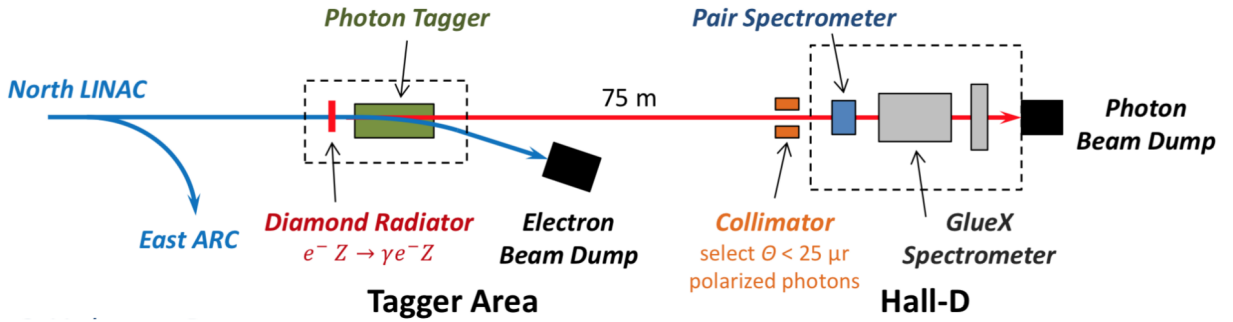


Figure 4.6: Schematic view of the GlueX beam line. Figure taken from [66].

4.2.1 Goniometer and radiators

The diamond wafer used to produce coherent bremsstrahlung is mounted on a multi-axis goniometer. The goniometer is used for fine tuning of the radiator orientation, and enables precise movement in two directions (x and y) and three rotations (roll, pitch, yaw). By carefully adjusting the diamond orientation, the beam polarisation can be optimised in the desired photon beam energy range. The centre of the goniometer features various diamond radiators, meaning a different radiator can be selected quickly to satisfy any changes in the experimental requirements. The goniometer is situated in a separate building to the main experimental hall, alongside the tagger hodoscope and microscope (see Section 4.2.2). This is located approximately 70 m downstream of main detector building. Positioning the radiator far away from the main experimental hall allows tight collimation of the photon beam (see Section 4.2.3). An amorphous aluminium radiator is also used for around 15 % of data taking. This radiator is mounted on a separate rail 61.5 cm downstream of the goniometer [67]. Using an amorphous radiator results in an unpolarised photon beam. Typically, the amorphous radiator is used for systematic and normalisation studies, or to determine the degree of linear polarisation via coherent bremsstrahlung shaping analysis [68]. However for this work, a majority of the analysed data were obtained over a wide photon energy range using the amorphous radiator since polarised photons are not required. Although systematic checks were performed using the diamond radiator to ensure results were consistent with those measured in polarised photoproduction, this was only possible over a relatively narrow beam energy range. This is because the energy range over which photons exhibit significant linear polarisation is typically restricted to the 8.2 – 8.8 GeV regime.

4.2.2 Photon Tagging

GlueX has two photon tagger systems; the tagger hodoscope (TAGH) and tagger microscope (TAGM). These components determine scattered electron energies from measurements of their spatial position after traversing a 1.5 T magnetic field. Since the electron beam energy is pre-

cisely known, the photon energy can be determined using the expression

$$E_\gamma = E_{e^-,beam} - E_{e^-,measured}. \quad (4.1)$$

After scattering from the diamond radiator, electrons are steered towards the tagging spectrometer by a dipole magnet. The Lorentz force induced by the magnet bends electrons on a curved trajectory, where the path curvature depends on the electron momentum. Since the magnetic field is well mapped, the electron energy can then be precisely determined from its position on a focal plane. These energy measurements are crucial for GlueX analyses, since knowing the energy of each photon triggering a reaction significantly improves reaction identification.

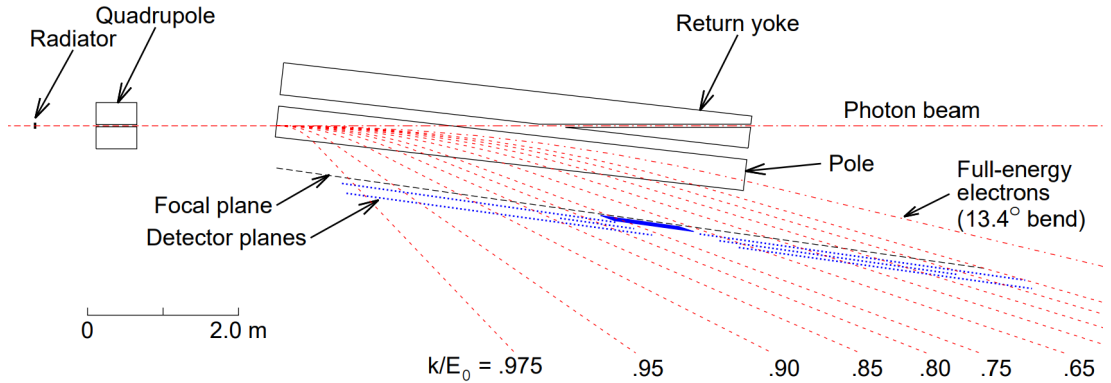


Figure 4.7: Diagram of the tagger hodoscope and microscope. Figure taken from [67].

The TAGH consists of 222 scintillator counters, sampling the range of photon energies spanning 25 – 97% of the full energy distribution [69]. A gap corresponding to the primary coherent peak region of 8.2 – 9.2 GeV is left open in the middle of this range. This energy regime is instead probed by the TAGM, comprising 102 columns of five scintillating fibres [67]. The finer granularity of this detector is necessary since the primary coherent peak contains the majority of linearly polarised photons. Both the TAGM and TAGH are able to achieve timing resolutions of around 200 ps [67]. This enables timing coincidences with the detector to identify the photon associated with each measured reaction. Electrons that pass through the diamond without interacting still have the full beam energy. These electrons are redirected into the beam dump by sweeping magnets to ensure the photon beam is not contaminated by charged particles.

4.2.3 Active Collimator

Coherent bremsstrahlung photons are typically produced under small forward angles. This means that beam collimation removes a large fraction of the unpolarised contribution and increases the degree of linear polarisation within the beam. The active collimator is situated 70 m downstream from the radiator. This distance optimises the divergence of the incoherent component, suppressing unpolarised photons while preserving a majority of the coherent contribution.

The collimator has a diameter of 5 mm and features 8 photon detectors for measuring the beam halo, from which the beam position is then inferred. This information is relayed to a feedback loop to control steering magnets in the electron beamline [67]. Drifts in the photon beam position are suppressed by this process, ensuring that the beam position is stable despite the very large collimation distance. Additionally, beam profilers can be inserted into the beamline to measure the beam position and size. Note that the detector components discussed in the following sections are all situated downstream of the collimator.

4.2.4 Triplet polarimeter

The Triplet Polarimeter (TPOL) measures the degree of linear polarisation of the photon beam. This component uses the angular dependence of triplet photoproduction on the degree of polarisation of impinging photons to obtain polarisation measurements. Triplet photoproduction describes the process where an electron-positron pair is produced by a photon recoiling from the Coulomb potential of an atomic electron. The electron is then ejected from the atom with a large polar angle, where the azimuthal angular distribution is related to the incident photon polarisation [70]. The TPOL consists of a $75\ \mu\text{m}$ thick beryllium foil target surrounded by a silicon strip detector. The strip detector is formed from 32 azimuthal sectors [70]. These measure the azimuthal distribution of recoil electrons using coincidences of detected electrons with pair spectrometer hits (see Section 4.2.5). The beam polarisation can then be determined from the measured distribution [71].

4.2.5 Pair spectrometer

The primary function of the pair spectrometer (PS) is to measure the photon energy spectrum and beam flux. The PS is situated at the entrance to hall D, and consists of a thin foil followed by a 1.8 T dipole magnet. The foil converts photons into electron-positron pairs by pair production. Lepton pairs are then separated by the dipole magnetic field and directed through a vacuum chamber on energy dependent trajectories. Lepton energies are then determined from their spatial position on the back-plane, equipped with two high granularity hodoscopes (PS-A/B) for high resolution energy measurements. These hodoscopes are formed from 290 scintillation counters read out by silicon photomultiplier tubes (SiPM) [72]. A coarse set of 16 scintillators (PSC-A/B) connected to photomultiplier tubes are situated behind each hodoscope. PSC counters have a timing resolution of 120 ps, making it possible to measure coincidences between the taggers and PS. This results in a substantial background reduction. Flux measurements require a precise determination of the PS analysing power. This is achieved using a combination of Monte Carlo simulations and experimental measurements.

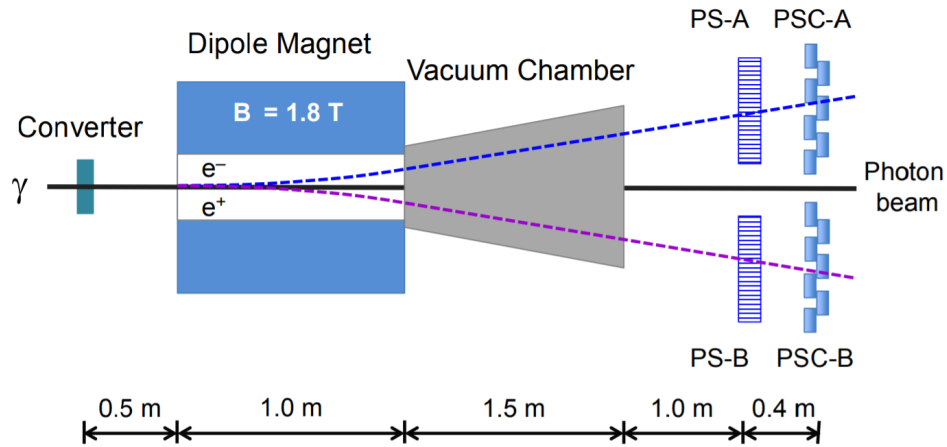


Figure 4.8: Schematic view of the GlueX pair spectrometer. Figure taken from [72].

4.2.6 Total Absorption Counter

As mentioned in Section 4.2.5, the analysing power of the PS must be determined to ensure that measurements of the photon flux are precise. In practice, this is achieved using the total absorption counter (TAC). The TAC is an SF-5 lead-glass calorimeter situated immediately upstream of the beam dump and directly within the photon beam path. It has a length of 40 cm and a width and height of 20 cm [73]. At low beam currents, the TAC is able to count the number of beam photons as a function of energy with an efficiency of nearly 100%. The TAC is removed under normal running conditions to protect it from radiation damage. However, dedicated routine TAC runs are performed under a low beam current to determine the efficiency of the PS.

4.3 Target

The GlueX photon beam is directed towards a liquefied hydrogen target at the centre of the main detector configuration. The 30 cm long cryogenic target is kept at a temperature of around 20 K and a pressure of around 1.31 bar. It has a conical shape, with a diameter of 2.42 cm at the entrance window that reduces to 1.56 cm at the exit window [74].

4.4 Solenoid magnet

The most important component of the GlueX spectrometer is the 2 T superconducting solenoid magnet. It is supercooled to 4.5 K using liquid helium and has an operating current of 1350 A. The solenoid has a length of 2 m and a diameter of 4.8 m [67]. It surrounds the tracking chambers, meaning charged particles follow a momentum dependent helical trajectory. This makes it possible to measure charged particle momenta since the magnetic field is known. Measurements confirm that the magnetic field map has been calculated to a high level of precision.

4.5 Start Counter

The innermost detector is the start counter (SC), consisting of 30 scintillator paddles that directly surround the target as shown in Figure 4.9. It covers approximately 90% of the solid angle. The main purpose of the SC is to help identify the correct beam bunch corresponding to each measured reaction. This requires excellent timing resolution, which the SC can provide by resolving events to a precision of less than 825 ps (FWHM). Furthermore, the SC provides limited particle identification by measuring the specific energy deposited (dE/dx) and particle time of flight.

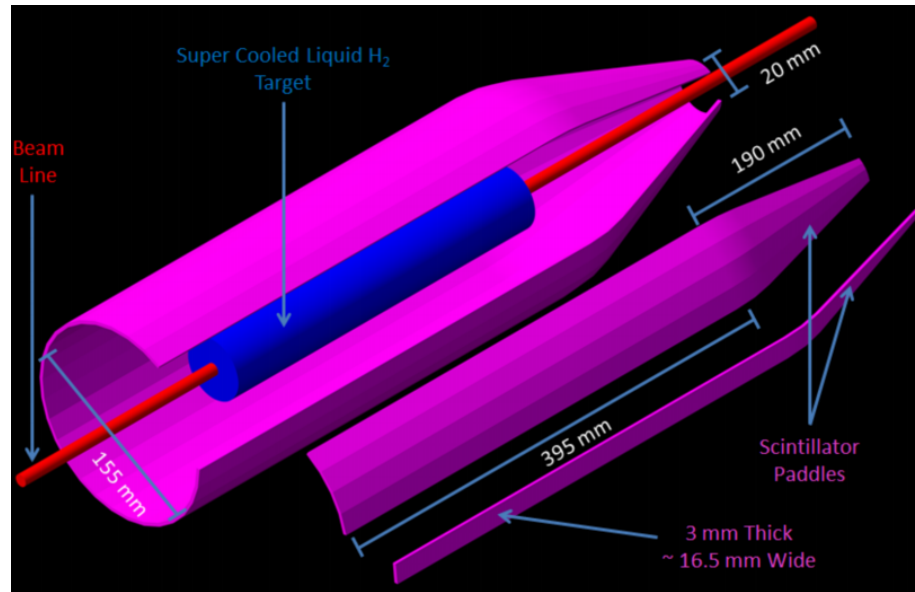


Figure 4.9: Schematic view of the GlueX Start Counter and target. Figure taken from [75].

4.6 Tracking

A superconducting solenoid magnet surrounds the GlueX detector set-up. This produces a 2 T magnetic field, causing charged particles to follow a momentum dependent trajectory after leaving the target. Particle tracking information is provided by two drift chambers, one in the forward region and another barrel-shaped chamber that surrounds the target. A momentum resolution of $\frac{\sigma_p}{p} \approx 1 - 5\%$ for charged particles is achievable with GlueX using this set-up [67].

A drift chamber is formed from multiple layers of anode wires contained within a gas filled chamber. Charged particles ionise the gas when they enter the chamber, and an electromagnetic field causes ions to drift towards wires. The electromagnetic field strength increases exponentially as the separation distance between the wire and ion decreases. This in turn creates more ion pairs, resulting in an avalanche effect that induces a measurable current in the wire.

4.6.1 Central drift chamber

The central drift chamber (CDC) is a cylindrical straw tube chamber containing 3522 anode wires enclosed within straw tubes filled with a gas mixture of 50% argon and 50% carbon dioxide. Tubes have a diameter of 1.55 cm and are arranged in 28 layers within a 1.5 m long active volume [76]. 12 of these layers are axial, while the remaining 16 layers have an alternating orientation of $\pm 6^\circ$ relative to the beam axis. The acceptance spans polar angles ranging from 6° to 168° [77], with optimal coverage between 29° and 131° [76]. Additionally, dE/dx measurements can be performed by measuring the energy loss in the gas filling the straw tubes. These measurements make it possible to easily distinguish low momentum protons from other particles (see Figure 4.11).

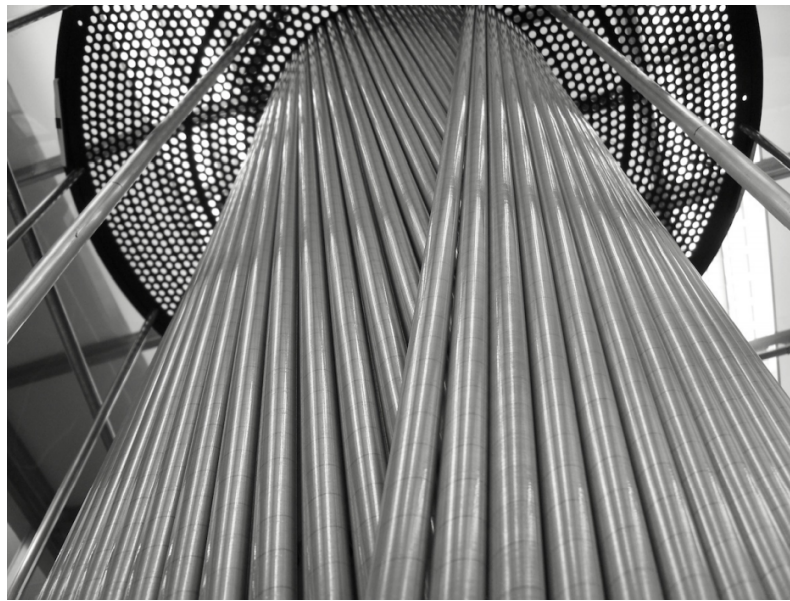


Figure 4.10: Straw tube arrangement visible in the CDC. Figure taken from [76].

4.6.2 Forward Drift Chambers

Charged particle tracks are measured in the forward region by an array of 24 disc-shaped planar drift chambers. Each drift chamber is oriented with an offset of 60° degrees relative to its neighbours [77]. These detectors are grouped into four separate configurations, where each chamber comprises a grid of 1 mm diameter anode wires [78]. Each disc is sandwiched between two layers of cathode strips with a relative orientation of 75° and 105° to the wires [77]. This set-up allows for the reconstruction of a single space point along the particle trajectory from each chamber and provides excellent multi-track separation for polar angles below 20° .

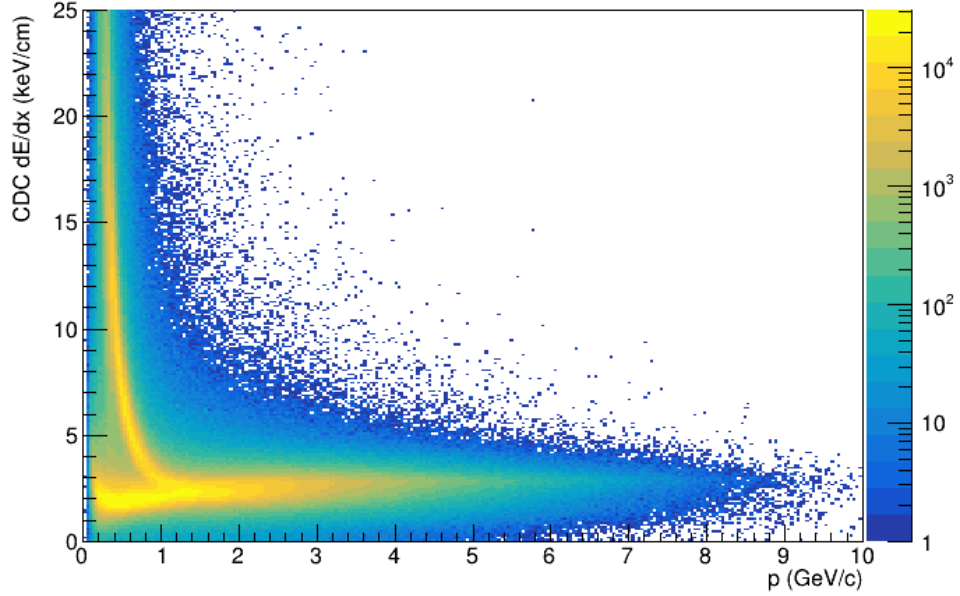


Figure 4.11: CDC $\frac{dE}{dx}$ plotted versus the momenta of positively charged particles. The upper band corresponds to protons while the lower band corresponds mostly to pions. Evidently, lower momentum protons are easily distinguishable due to their higher energy disposition.

4.7 Calorimetry

The GlueX spectrometer features two electromagnetic calorimeters; one in the forward region and another surrounding the drift chambers. Electromagnetic calorimeters infer particle energy measurements from the electromagnetic showers produced by charged particles or photons. These showers are proportional to the incident particle energy, and cause scintillation which is then converted into an electronic signal. The total energy of a particle can only be measured if it is stopped inside the detector. For this reason, materials with high atomic number Z are used. These materials have a high stopping power for charged particles and photons.

4.7.1 Barrel Calorimeter

The barrel calorimeter (BCAL) is a cylindrical sampling calorimeter consisting of 48 detector modules. Each module has a trapezoidal cross section, with a height of 22.2 cm and a length 390 cm. These 48 modules collectively form a barrel, with an inner diameter of 130 cm and an outer diameter of 180 cm. Detector modules are formed from matrices of lead sheets interwoven with scintillating-fibre, where each module incorporates 185 layers of 0.5 mm lead sheets and 184 layers of 1 mm plastic fibres [79]. Scintillating-fibres run parallel to the cylindrical axis of the BCAL, where light is delivered to SiPMs by small light guides at either end of each module. With this design, the BCAL is able to measure electromagnetic showers with polar angles ranging from 11° – 126° , azimuthal angles from 0° – 360° and energies between 0.05 and several

GeV. The energy resolution of the BCAL is given by $\frac{\sigma_E}{E} = \frac{5.2\%}{\sqrt{E(\text{GeV})}} \oplus 6\%$, where the \oplus symbol specifies that the terms are summed in quadrature, for neutral particles between 0.5 GeV and 2.5 GeV. The first term is statistical, describing the limitations arising from sampling fluctuation and photo-electron statistics. The second term accounts for mechanical imperfections, shower leakage, variations in detector calibrations, time instability and material effects [79]. The BCAL also has a timing resolution of around 200 ps for high energy pions ($E > 1$ GeV) and 150 ps for 1 GeV electromagnetic showers [79]. The excellent timing resolution makes it possible to perform time of flight measurements for particle identification.

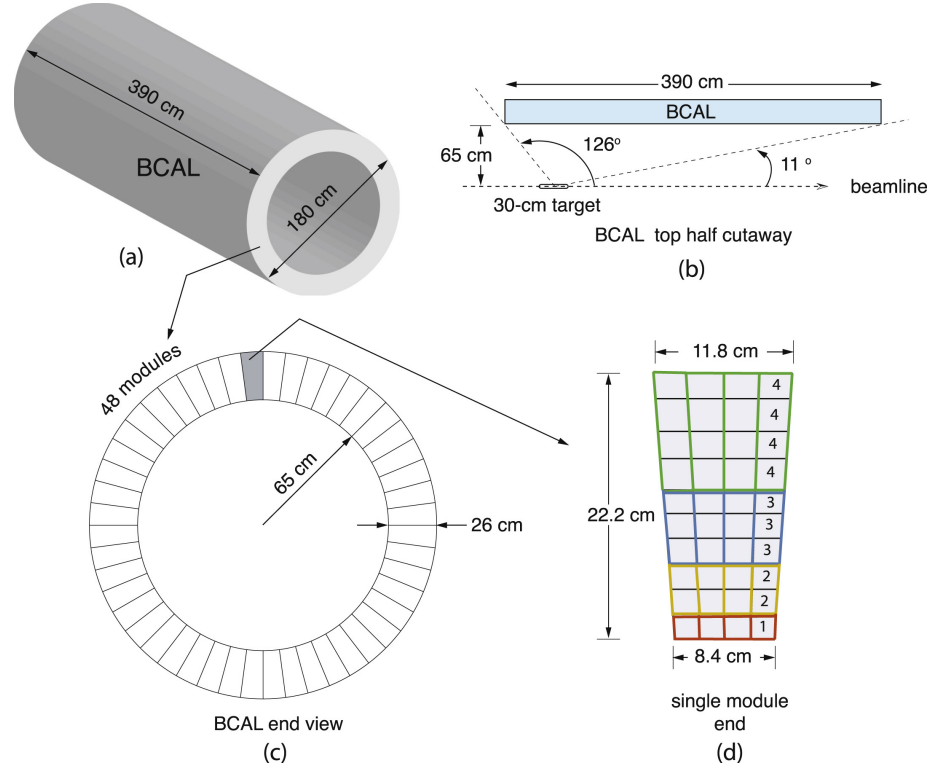


Figure 4.12: Schematics of the BCAL detector. (a) general view of the module configuration. (b) BCAL polar angle coverage. (c) cross section view of (a). (d) read-out matrix. Figure taken from [79].

4.7.2 Forward Calorimeter

The forward calorimeter (FCAL) is situated behind the Time-of-Flight detector, and comprises 2800 lead glass blocks arranged in a circular array. Blocks have dimensions of $4 \times 4 \times 45 \text{ cm}^3$ [80], and each one is coupled to a photomultiplier tube to provide readout. The central nine blocks are removed to allow the beam component that did not interact to pass through. With this design, the FCAL is able to measure electromagnetic showers with polar angles ranging from 1° – 11° and energies between 0.1 GeV and several GeV. The energy resolution of the FCAL is given by $\frac{\sigma_E}{E} = \frac{5.6\sqrt{\text{GeV}}}{\sqrt{E(\text{GeV})}} \oplus 3.5\%$ [67]. It has a position resolution of around $\frac{6.4 \text{ mm}}{\sqrt{E}}$ and a timing resolution of about 0.4 ns [80]. Since there is a large separation distance of 560 cm

between the target and FCAL, the FCAL still has particle identification capabilities despite not having the best time resolution.

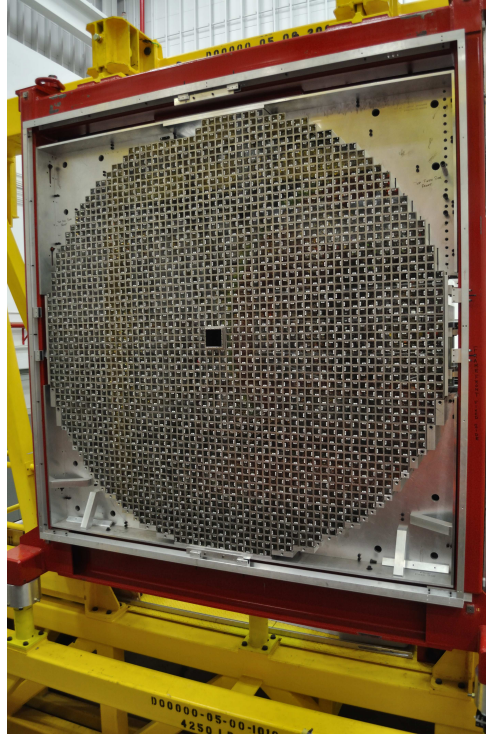


Figure 4.13: Photo of the FCAL detector in hall D. Figure taken from [81].

4.8 Time-of-Flight Detector

The Time-of-Flight detector (TOF) is used for particle identification, and is situated just before the FCAL. It is formed from a wall of scintillation bars with a gap left in the centre to allow the beam component that did not interact to pass through. Each scintillator is coupled to one of 176 photomultiplier tubes [80] to provide readout. The TOF is separated from the interaction point by a distance of 5.5 m, covering a polar angular range of 0.6° – 13° . The large separation distance and excellent timing resolution (90 – 95 ps [80]) ensure that particle identification can be achieved to a very high level of precision. The 2D histogram of calculated Lorentz factor β versus particle momentum is shown in Figure 4.15. Bands corresponding to different particle types are easily distinguishable for lower particle momenta. Evidently, the TOF provides good π/K and π/p separation for particle momenta less than 2 GeV and 4 GeV respectively.

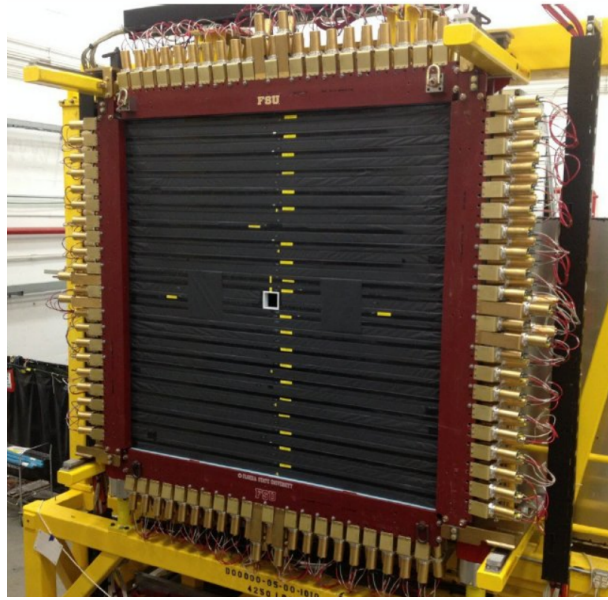


Figure 4.14: Photo of the TOF wall in hall D. Figure taken from [82]

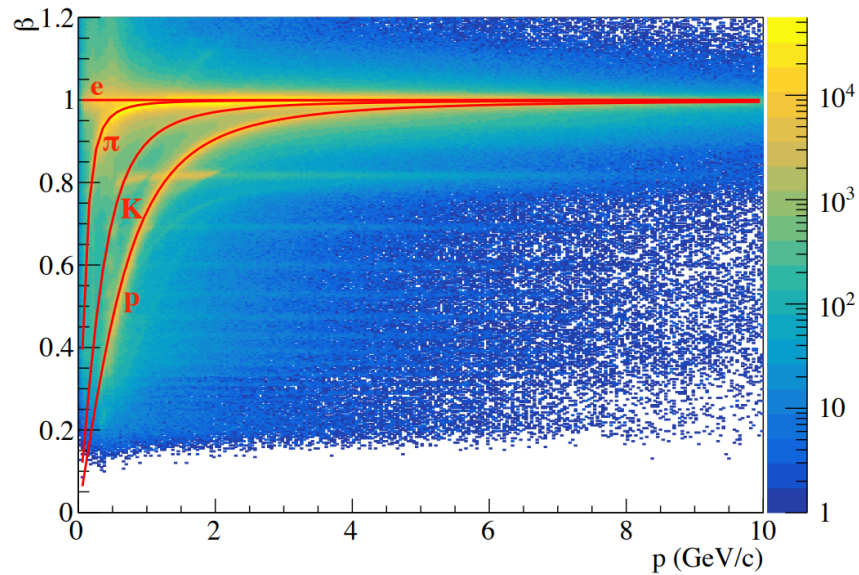


Figure 4.15: Lorentz factor β plotted against momentum for various particles. The theoretical curves for each particle are plotted in red. Bands corresponding to each particle are clearly distinguishable for momenta less than 2 GeV. A series of faint bands are seen to converge to values of $\beta < 1$. These result from events reconstructed with an incorrect beam bunch (c.f. Section 5.7.1), meaning β is not calculated correctly. These events are removed by the exclusivity criterion and random subtraction detailed in Section 5.7. Figure taken from [62].

4.9 Data acquisition and trigger

The GlueX experiment features a streaming data acquisition (DAQ) and trigger system. This means the signals measured by detector components are continuously digitised and written to a pipeline. When an event satisfies the predefined selection criteria, the trigger selects the relevant portion in the pipeline to be stored. These selection criteria were designed to accept a majority of high energy hadronic interactions and minimise the background rate from electromagnetic and low energy hadronic interactions. Readout is then translated into complete events and stored locally on tape in a format suitable for physics analysis.

The entire DAQ system is implemented using the CEBAF data acquisition system (CODA) framework. A more detailed description of this framework can be found in [83]. Flash-Analog-to-Digital-Converters (FADCs) digitise signals from the BCAL and FCAL with a 250 MHz sampling rate [67]. Digitised signals are then stored in a pipeline, where important properties such as the integral and pulse height are determined. These quantities are eventually converted into complete physics events by the event builder (EB) if trigger conditions are satisfied. They are read out by 55 Versa Module Eurocard (VME) crates. Each crate has a maximum readout capability of 200 MB/s, and is coupled to a crate readout controller (ROC) with a typical data rate of 20 – 70 MB/s under normal running conditions. Physics events are then constructed from this data by the event builder. The resulting data are in a format suitable for physics analysis, and are written to tape by the event recorder (ER). In total, the DAQ stored about 900 TB of raw data on tape during the spring 2017 beam time.

Table 4.1: Summary of trigger conditions for the Spring 2017 beam time. The first two entries describe physics triggers, while the two additional triggers were used for flux measurements and efficiency studies.

trigger condition	FCAL rings masked
$E_{FCAL} + 0.5 \cdot E_{BCAL} > 0.5 \text{ GeV}$, $E_{FCAL} > 0 \text{ GeV}$	2
$E_{BCAL} > 1.2 \text{ GeV}$	0
PS coincidence	0
Random trigger 100 Hz	0

During the spring 2017 run period a minimum bias trigger was used, meaning that the recorded event rate for hadronic reactions was kept as high as possible. In general, events were recorded when the energy deposited in the calorimeters exceeded a certain threshold. The total deposited energy was determined by performing energy sum calculations on the signals stored in the pipeline. The two inner-most FCAL rings are masked from the trigger. This is due to the high event rates they experience resulting from their close proximity to the beam line. The Spring 2017 trigger conditions are summarised in Table 4.1 [84]. The PS trigger infers flux meas-

measurements from timing coincidences in both spectrometer arms. The random trigger is used to improve the accuracy of efficiencies and acceptances in detector simulations. It has a fixed rate of 100 Hz, where the recorded events are used to add a background of random coincidences to simulations. Over the Spring 2017 beam time, the approximate total trigger rate was 40 kHz, corresponding to a data rate of around 600 MB/s [67].

4.10 Summary

The GlueX beamline and detector were designed specifically for measuring hadronic reactions in polarised photoproduction. These measurements are performed in an energy regime where previously only limited data were available. The spectrometer configuration has excellent momentum and energy resolution for both neutral and charged final state particles. This set-up provides an optimal environment for studying the spectroscopy of hadrons, and is expected to eventually enable the mapping of the exotic hybrid meson spectrum. This would be a crucial step towards understanding the fundamental nature of QCD and the strong force. The following chapter demonstrates how the particle identification capabilities of the GlueX detector are utilised to maximise the yield of data corresponding to the $\pi^+\pi^-p$ final state topology.

Chapter 5

Event selection and analysis

Various steps were necessary to prepare the data recorded by the detector for physics analysis. Calibrations were applied, and particle four-momenta needed to be reconstructed. Data was also skimmed to remove backgrounds and reduce the overall file size, and a kinematic fit was performed for each physics event. The following chapter explains the steps outlined above in detail.

5.1 Dataset

The data used in this analysis were obtained over the Spring 2017 beam time between February 4 and March 9, 2017. Data were recorded in separate runs to facilitate data handling. Each run lasted around two hours, where the data for each run were saved over multiple files to ensure the file size did not exceed 20 GB. Raw data were recorded in EVIO [85], a format developed for data acquisition with CODA. 347 runs were identified as physics quality, meaning the detector and beam were stable throughout the run and no issues were encountered with the DAQ.

Each run was performed using one of two radiators, a $30\ \mu\text{m}$ amorphous aluminium or $58\ \mu\text{m}$ diamond radiator, where the diamond radiator was positioned according to one of four possible orientations. A 100 nA beam current was delivered by CEBAF for the first part of beam time. From run 30796 onwards, the current was increased to 150 nA. Table 5.1 shows the total number of triggers recorded for each diamond orientation and with the amorphous radiator. It should be noted that a majority of the analysis presented in this thesis was performed on amorphous data only. The amorphous dataset that was analysed consisted of 45 runs. Polarised SDMEs were also measured in a separate analysis to provide a cross check with SDMEs previously published by GlueX [86]. For this measurement, the full Spring 2017 polarised data set was analysed. This data set consisted of 281 diamond radiator runs.

Table 5.1: Number of recorded triggers for each diamond orientation and the amorphous radiator

diamond-orientation	number of triggers	
	100 nA beam current	150 nA beam current
0°	5.8e9	4.6e9
90°	5.8e9	5.2e9
-45°	5.6e9	4.6e9
45°	5.7e9	4.3e9
amo	4.1e9	3.9e9

5.2 Calibrations

Precise measurement of angles, times and energies are required to construct the four-vectors for detected particles and associate them with the correct trigger event. These come from a combination of hit location, deposited charge and event time, and are derived from the data recorded by time-to-digital converters (TDCs) and charge-to-digital converters (QDCs), which must be calibrated in order to convert digital signals into reliable physical quantities. Beyond those standard calibrations, the GlueX spectrometer also requires more specialised calibrations to account for effects such as the gravitational sagging of drift chamber wires.

These calibrations involve many steps, and were performed immediately after data taking. The calibration constants from the previous run period were used as starting parameters. With GlueX, calibrations are performed by experts and shared with the whole collaboration. An overview of the important steps is provided in the following.

5.2.1 Timing calibrations

The GlueX reference time is derived from the CEBAF radio frequency (RF) clock, which generates 499 MHz timing signals. These timing signals are then read out at the TOF crate.

The GlueX detectors are generally comprised of a large number of channels. Most incorporate both TDCs and QDCs, with the exception of the CDC and FCAL which have QDC only readout. Note that QDCs also provide timing readout, but with poorer resolution than TDCs. The QDCs and TDCs needed to be synchronised for each channel within a detector, and this was achieved with a timing alignment. The overall detector reference time was then aligned to the RF clock. A time walk correction was also applied to the TDC signals. This corrects for the dependency of the timing signal on the signal pulse amplitude in leading edge discriminators. The effect of the timing calibration is demonstrated in Figure 5.1, which shows the tagger timing signal measured relative to the RF clock before and after applying the calibration. The signal is plotted against the corresponding detector channel number for the TAGH and TAGM in the top and bottom left plots respectively. A histogram of the timing signal is shown in the bottom right, while the top left plot shows the signal versus photon energy. For the signal histogram, we expect to see a

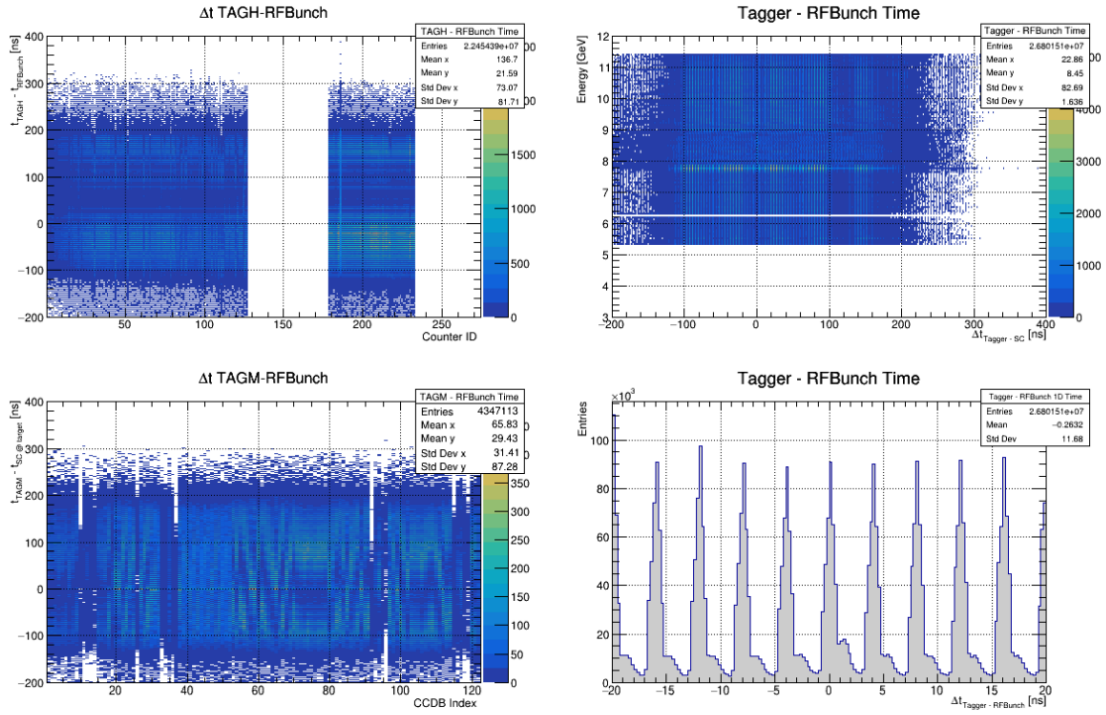
dominant peak at 0 ns corresponding to prompt photons, with a series of smaller peaks to either side separated by 4.008 ns (i.e. the accelerator beam bunch frequency). Before applying the calibration none of the peaks were well defined and the central peak was not seen to dominate. However, after applying the calibration the correct behaviour was observed.

A few detector specific calibrations were also required. The time differences between signals coming from both ends of a TOF paddle were calibrated to ensure the particle position along the length of the paddle could be determined [88]. An additional timing calibration was also applied to the BCAL, which made it possible to determine the z position of particle showers. This calibration was performed by matching signals originating from the upstream and downstream readout [79]. Most of the timing calibrations were performed once for the whole run period. The PS, tagger and TOF calibrations were more sensitive to factors such as temperature and atmospheric pressure. It was therefore necessary to perform these on a run by run basis

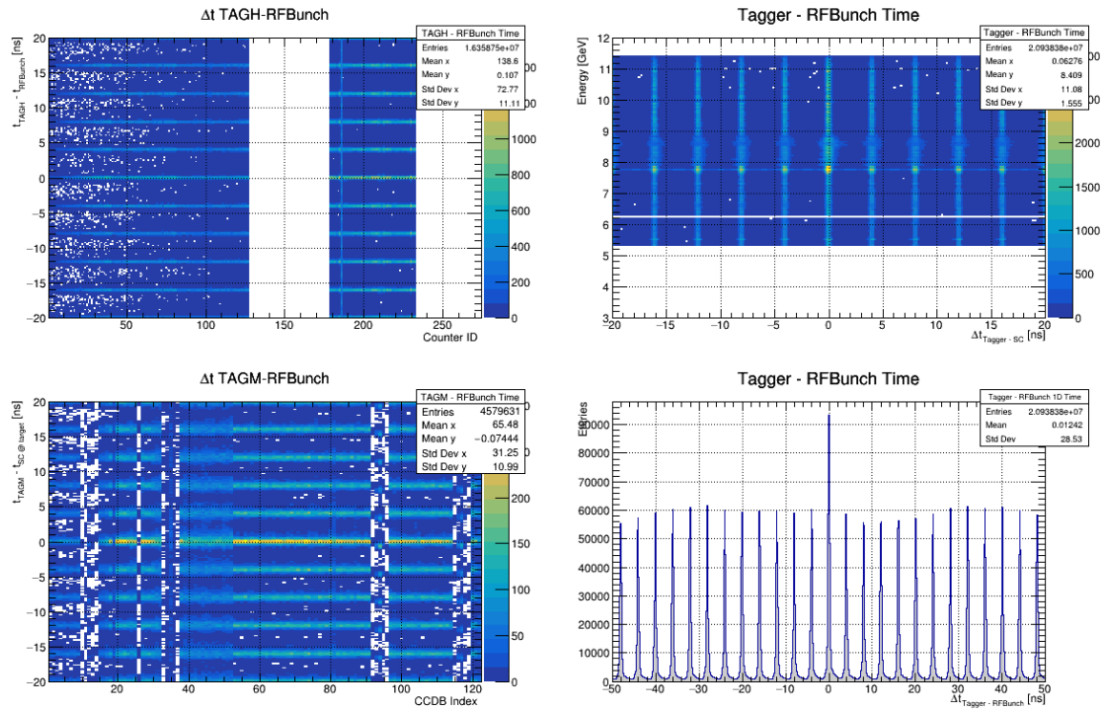
5.2.2 Gain calibrations

Gain calibrations were necessary for the CDC, BCAL and FCAL to relate the charge collected in each detector channel to the deposited energy. Gains were calibrated for the BCAL and FCAL using $\pi^0 \rightarrow \gamma\gamma$ decay events. Since the mass of the π^0 is known, the calibration can be achieved by adjusting the gain such that the $\gamma\gamma$ invariant mass peak coincides with the π^0 PDG mass of $135 \text{ MeV}/c^2$ [79]. Gain calibrations were applied for the beam time as a whole on a channel-by-channel basis. Several iterations of gain calibrations were required to ensure the $\pi^0 \rightarrow \gamma\gamma$ invariant mass peak was correctly positioned with a minimised width. Shower based non-linearity corrections were then applied to the data when gain calibrations were complete. Figure 5.2 demonstrates the improvement in the $\pi^0 \rightarrow \gamma\gamma$ invariant mass peak position resulting from gain calibrations. The red lines denote Gaussian fits to the π^0 peak. These fits were used to extract the peak width and mean, which are indicated in each plot legend. The data were divided into four subsets according to photon cluster energy. These energies are indicated in the plot titles. A calibration from the previous beam time was used to produce the plots shown in (a). Although the peak was already centred on a value close to the π^0 PDG mass, an up to date calibration clearly results in an improvement in the peak mean and width as shown in (b).

The CDC is used for particle identification, which it achieves by measuring the energy deposited by a charged particle in a thin medium. The CDC was calibrated using minimum ionising particles, which deposit constant energy in the detector. It was necessary to perform these calibrations on a run-by-run basis, since they are sensitive to temperature and pressure changes within the detector.

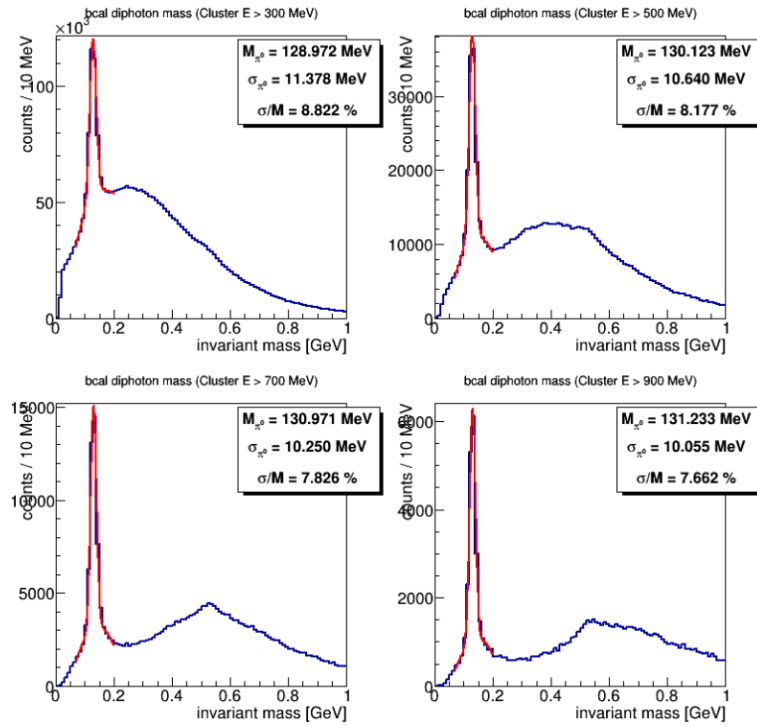


(a) before calibration

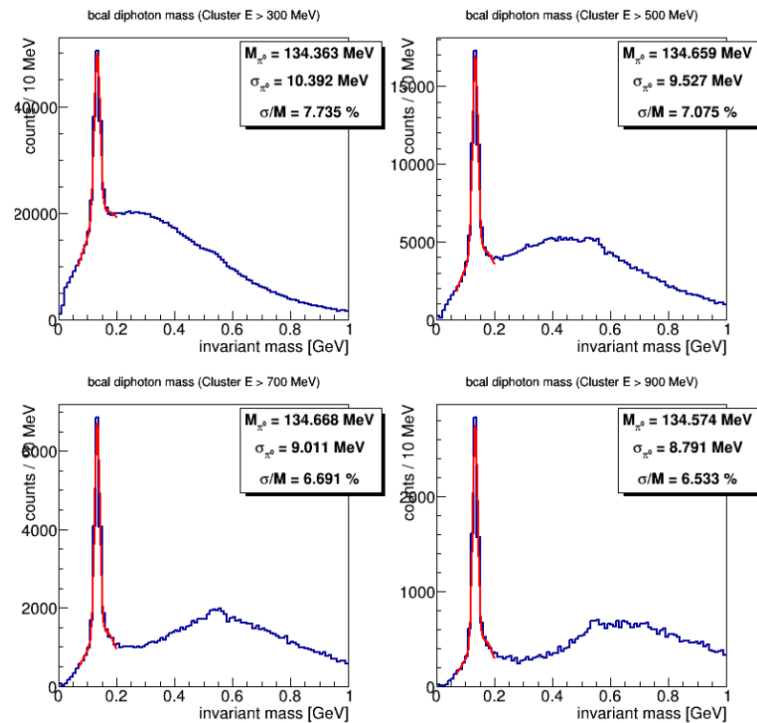


(b) after calibration

Figure 5.1: Plots showing the timing signal relative to the RF clock before (a) and after (b) applying timing calibrations for run 30999. The top and bottom left plots show the signal plotted against channel number for the TAGH and TAGM respectively. The top right plot shows the signal plotted versus photon energy, while the bottom right plot shows the signal distribution. Figure taken from [87].



(a) before calibration



(b) after calibration

Figure 5.2: Plots showing the $\gamma\gamma$ invariant mass measured by the BCAL before (a) and after (b) applying gain calibrations on the π^0 mass and width for run 30999. The blue line shows the measured invariant mass distribution while the Gaussian fit to the π^0 is shown by the red line. The data were divided into four subsets according to the photon cluster energy denoted in each plot title. Figure taken from [89].

5.2.3 Additional calibrations

Additional calibrations were required for certain detector components. The wire chamber alignment was calibrated using data collected without a magnetic field. Charged particles move on straight tracks when there is no magnetic field. This makes it possible to correct for gravitational sagging of wires from their nominal positions [77]. An iterative time-to-distance calibration was also applied to the CDC. This accounts for the drift time of charge within a straw tube.

5.3 Event reconstruction

The final state particles resulting from each measured reaction were identified using combined information from all detector components. Neutral particle energies were determined by identifying clusters in the calorimeters and measuring the total energy. For charged particles, wire chamber hits were matched with clusters identified in the calorimeters and hits in the scintillation counters, making it possible to reconstruct particle tracks in a process called *tracking*. Since the magnetic field in the detector is known, particle momenta measurements can be inferred from the associated track curvature (c.f. Section 4.6).

The tracking process involves three steps. For the first step, track segments were formed by linking hits within FDC packages and adjacent CDC rings. A fit was then applied to these segments to form track candidates. These candidates were used as starting parameters for the second stage. A Kalman filter [90, 91] tracking algorithm was then used to identify the track parameters at the point of closest approach to the beam line. The algorithm starts from the outside of the detector and steps towards the centre, where the track parameters are updated after each step. Energy loss, multiple scattering and the magnetic field within the detector were all accounted for by the Kalman filter. All track candidates with momentum greater than $0.8 \text{ GeV}/c$ were fitted with a pion hypothesis, while the remaining tracks were assumed to be protons. For the final step, tracks were matched to the scintillation counters or calorimeters to determine the start time. This allows the drift time to be taken into account, meaning the track can be refitted with a proton, electron, pion and kaon hypothesis [67].

Since event reconstruction is such a computationally expensive procedure, it was coordinated for the whole collaboration. The results were then saved in hddm (Hall-D Data Model) files. The file size was reduced by excluding unnecessary hit information and only including higher level track information. In doing so, the size of the full data set was reduced from 900 TB to 120 TB.

5.4 Skimming and kinematic fitting

The amount of data was already reduced significantly by the event reconstruction process. However, the data size was still too large, meaning it could not be analysed efficiently. In order to further reduce the data size, data was *skimmed* at Jefferson Lab. This involved splitting the data into separate subsets according to specific event criteria. Data were then stored in ROOT trees [92], a data storage format developed by CERN specifically for handling data from nuclear and particle physics experiments.

A $p\pi^+\pi^-$ skim was used for this analysis. This means events with at least one negative and two positive tracks were saved to the output ROOT trees, since these are consistent with the desired final state topology. Up to three additional tracks were also allowed in each event. This ensured that good events containing additional false tracks (e.g. resulting from detector noise) were still preserved. Multiple tagger hits were recorded for each event, meaning there were multiple candidate beam photons. Only candidate photons with an associated time between -18.036 ns and 18.036 ns relative to the event reference time were preserved to reduce the background of random tagger coincidences (c.f. Section 5.7.1). The resulting photon timing distribution is shown in Figure 5.10. This cut was chosen to be wide since side bands in the distribution that consist exclusively of randoms were required to subtract the background of randoms from beneath the prompt photon peak. This background subtraction is discussed in more detail in Section 5.7.1. All possible combinations of beam photons and final state particles were then treated as separate events.

Preliminary particle identification cuts were applied to further reduce the data size and the number of background events in the skim file. These are summarised in Table 5.2. Note that when applying timing cuts, the time measured by the best available detector subsystem was used. The subsystem with the best timing resolution was the BCAL, followed by the TOF, FCAL and SC in order of decreasing resolution. Events with missing energy less than -3 GeV or greater than 3 GeV were also removed. Note that this cut was tightened in the final selection (c.f. Section 5.7.4).

Protons were distinguished from other particles by cutting on the energy loss, dE/dx , in the CDC. Δt is the difference in time between a measured track and the time calculated for a specific particle hypothesis. It is defined as

$$\Delta t = t_{track} - \left(t_{RF} + \frac{z_{track} - z_{target}}{c} \right), \quad (5.1)$$

where t_{track} is the time of the track at its origin, z_{track} denotes the z position of the track at its origin, z_{target} is the z position of the target centre, c is the speed of light and t_{RF} is the overall reference time as measured by the RF clock. t_{RF} was measured under the assumption that the

reaction occurred in the target centre. Note that the mass dependence is incorporated in t_{track} , since this is calculated during reconstruction for different particle hypotheses.

Table 5.2: Summary of particle identification cuts applied during the data skim. Note that in the final column, p denotes the measured particle momentum along the x axis.

PID	BCAL/RF Δt (ns)	TOF/RF Δt (ns)	FCAL /RF Δt (ns)	SC/RF Δt (ns)	CDC dE/dx (keV/cm)
π^+	± 1.0	± 0.5	± 2.0	± 2.5	$dE/dx < \exp(-7.0p + 3.0) + 6.2$
π^-	± 1.0	± 0.5	± 2.0	± 2.5	$dE/dx < \exp(-7.0p + 3.0) + 6.2$
p	± 1.0	± 0.6	± 2.0	± 2.5	$dE/dx > \exp(-4.0p + 2.25) + 1.0$

After applying the cuts described above, there were multiple candidate photons associated with each measured final state. A kinematic fit [93] was performed for every possible combination. The kinematic fit applies four-momentum conservation constraints, and also requires that all particle tracks originated from the same vertex position. The χ^2 of the kinematic fit indicates how well the event matches the final state hypothesis based on the kinematics and detector resolutions. It can be thought of as a measure of how much the particle kinematics had to be modified in order to satisfy the vertex and four-momentum constraints. The kinematic fit provides new four-vectors that satisfy the fit constraints for each particle. In this analysis, kinematically fitted four-vectors were used instead of measured four-vectors in order to improve the overall resolution.

5.5 Detector simulations

An accurate parameterisation of the detector configuration is usually required to perform an analysis of GlueX data. Properties of the set up such as detector geometries, resolutions and reconstruction probabilities need to be well understood. This is made possible with *hdgeant4* [94], a software package based on the widely used *Geant4* [95] simulation framework. Events were generated using external *event generators* with *hdgeant4*. The generated position and momentum final state four-vectors were passed through the simulation, which tracks each particle through the detector and emulates particle interactions with the detector medium. This produced output that could then be analysed in the same way as real data.

With *hdgeant4*, the simulated efficiencies were found to be slightly better than for real data. This made it necessary to *smear* the simulated output such that the generated data was more realistic. The simulated timing and energy distributions were convoluted with carefully determined Gaussian functions. Random trigger coincidences were also folded into the output. This made tracking efficiencies more realistic. In practice, these were distorted by noise and background events.

Running conditions were constantly changing over the Spring 2017 beam time. For most analyses, it is important that this is properly accounted for in simulation since it drives many characteristics of the collected data. This was achieved by matching run dependent variables such as photon flux and coherent peak orientation to real data. This ensured that the proportion of the simulated output corresponding to each polarisation setting was consistent with what was collected in practice. Additionally, run dependent calibrations were applied to the simulations to ensure they were realistic.

The trigger conditions used during data taking were also reproduced in simulation software. This was implemented during the reconstruction of simulated data. Emulation of trigger conditions was particularly useful, as it made it possible to study the effects of different trigger configurations on an event-by-event basis.

5.6 Additional corrections

Additional corrections were necessary to account for a miscalibration of the photon tagger and a small rotational offset observed between the GlueX detector and the lab coordinate system. These corrections were motivated by the SDME analysis, and were applied after the event reconstruction and skimming.

5.6.1 Tagger correction

Figure 5.3 shows the missing energy (c.f. Section 5.7.4) distribution measured for events corresponding to the reaction $\gamma p \rightarrow p\pi^+\pi^-$. Since the reaction of interest is fully exclusive, one would always expect to see a distribution with a peak centred on zero. However, a photon energy dependent shift from zero was observed. This shift was not reproduced in the simulated data used for the acceptance correction, where missing energy distributions are seen to peak on zero as expected. The observed shift was a result of a miscalibration of the photon tagger energy scale.

Since a cut was applied on the missing energy, and the agreement between reconstructed and simulated data distributions was poor, it was necessary to correct for the mis-calibration of the tagger. This was important as it ensured the acceptance correction was applied effectively (c.f. Chapter 6). In order to determine the tagger correction, the missing energy distributions were produced for each individual TAGH and TAGM channel. Each distribution was then fitted with a Gaussian function. This made it possible to produce correction plots for the TAGM and TAGH by plotting the tagger channel versus the corresponding Gaussian mean. Three separate plots were produced; one for the TAGM, one for TAGH channels 0-155 and another for channels 155 onwards. The resulting plots are shown in Figure 5.4. Note that the vertical error bars in these plots were inferred from the corresponding Gaussian fit.

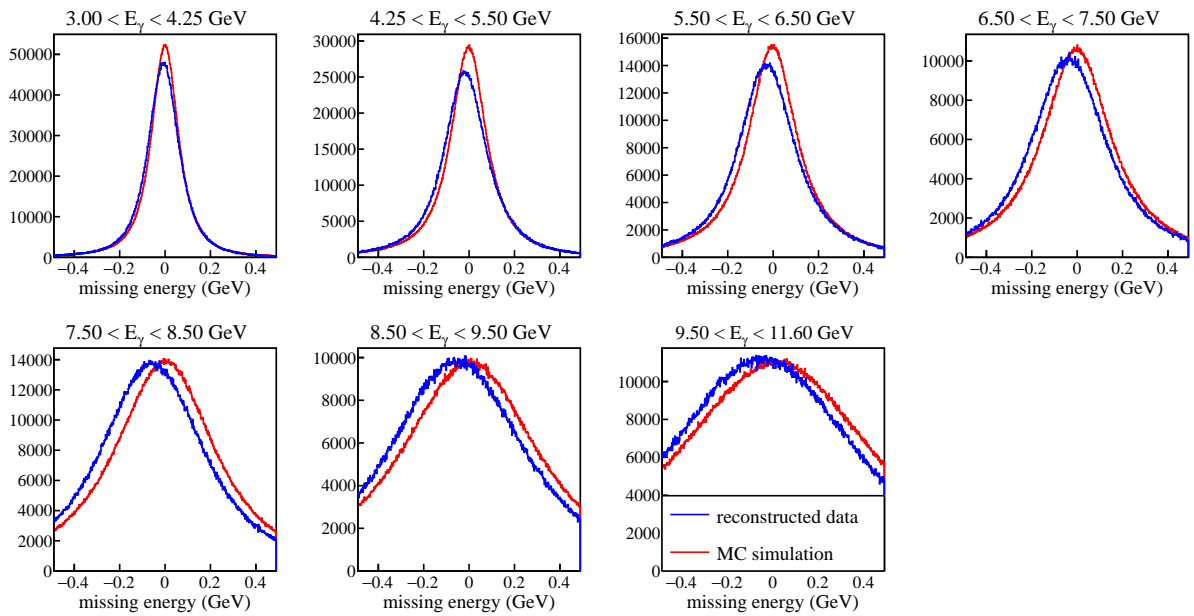


Figure 5.3: Missing energy distributions plotted for different E_γ ranges. The blue and red lines show the distributions for reconstructed and simulated data respectively.

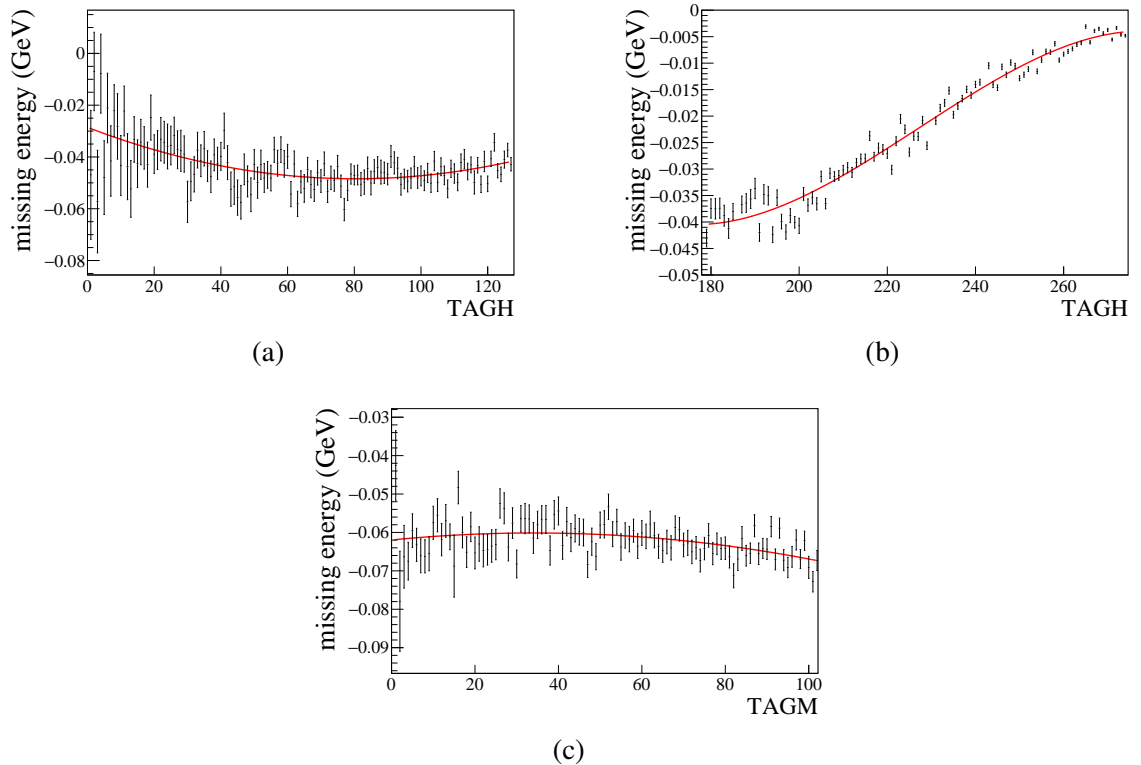


Figure 5.4: Correction plots produced for the TAGH (a), (b) and TAGM (c). The mean missing energy is plotted against the corresponding tagger channel number. (a) and (b) show the calibration plots for the low and high energy TAGH channels respectively. The red line denotes a polynomial fit, which is used to evaluate the shift and correct for the tagger miscalibration.

The next step was to fit each plot with a 2 or 3 degree polynomial. The resulting fits describe the photon energy shift. The shift was then evaluated for each tagger channel and subtracted from the measured photon energy. Figure 5.5 shows the missing energy distributions after applying the correction. The peaks are seen to align with zero, and a good agreement is observed between reconstructed and simulated data.

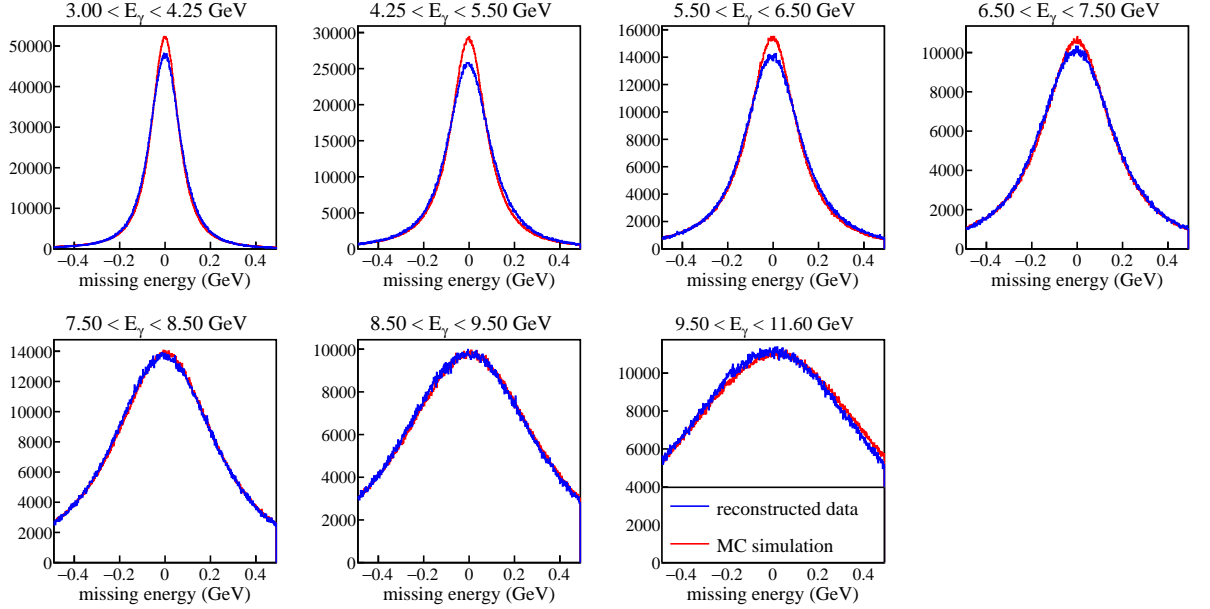


Figure 5.5: Missing energy distributions plotted for different E_γ ranges after applying the tagger correction.

5.6.2 Beam correction

The GlueX reconstruction and analysis framework assumes the incoming beam photon only has momentum along the z -axis with no transverse component. However, when the beam momentum was reconstructed from the three exclusive final state particle tracks, the reconstructed transverse momentum components were seen to correlate with the photon energy. This effect is shown in Figure 5.6, and is indicative of a small rotational offset between the GlueX detector and the lab coordinate system.

A correction was applied to account for the tilt of the beam axis. This involved studying the missing transverse momentum components as a function of the TAGM or TAGH channel number. The missing momentum can be defined as

$$\text{missing } p = p_{\text{target}} + p_\gamma - p_{\pi^+} - p_{\pi^-} - p_{\text{coil}}. \quad (5.2)$$

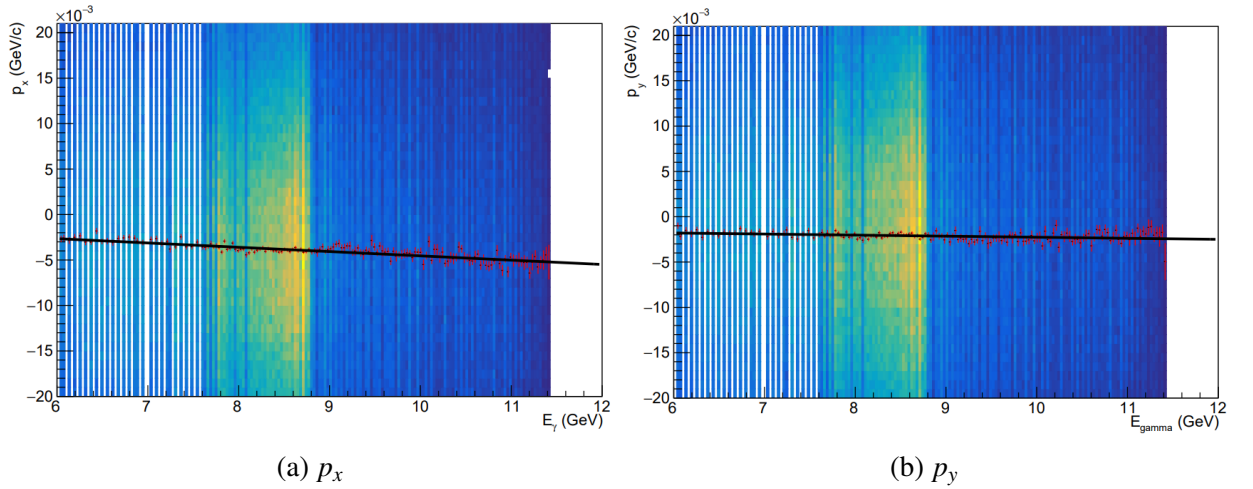


Figure 5.6: Transverse components of the beam momentum reconstructed from the final state plotted against the photon energy. Figure taken from [96].

Since we measure an exclusive final state, distributions of the missing momentum components along the x and y axes should show a peak centred on zero with a drop off on either side due to finite detector resolutions. Due to the apparent tilt of the beam axis, this was not seen to be the case, as shown in Figure 5.7. Peak centroids were shifted from zero, with a photon energy dependent magnitude.

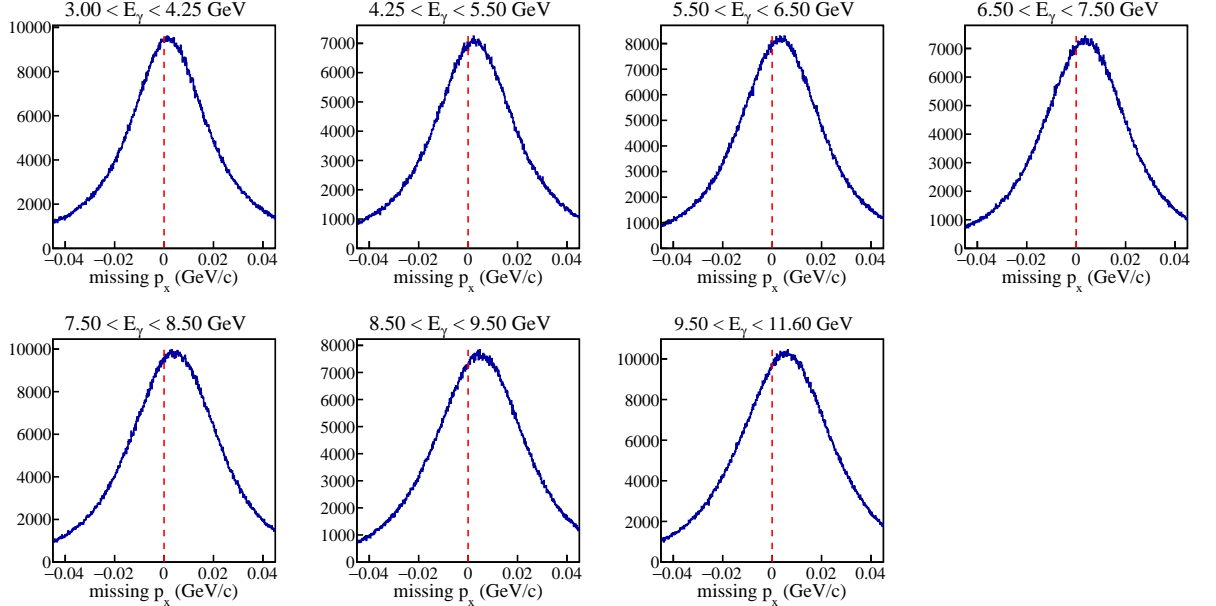


Figure 5.7: Missing p_x distributions plotted for different E_γ ranges.

In order to determine the beam correction, the missing momentum distributions in x and y were produced for each individual TAGH and TAGM channel. Each distribution was then fitted with a Gaussian function. The tagger channel was plotted against the corresponding Gaussian mean. Two separate plots were produced for both transverse axes; one for the TAGM and one for the

TAGH. The resulting plots are shown in Figure 5.8, where the vertical error bars were inferred from the corresponding Gaussian fit. The next step was to fit each plot with a 3 degree polynomial. The resulting fits describe the shifts in p_x and p_y as a function of the tagger channel number. The shift was then determined from the associated fit for each tagger channel and subtracted from the relevant transverse momentum component of the measured beam photon. Figure 5.9 shows the corrected missing momentum distributions. Clearly the distribution peaks are now all consistent with zero, showing that the correction was successful.

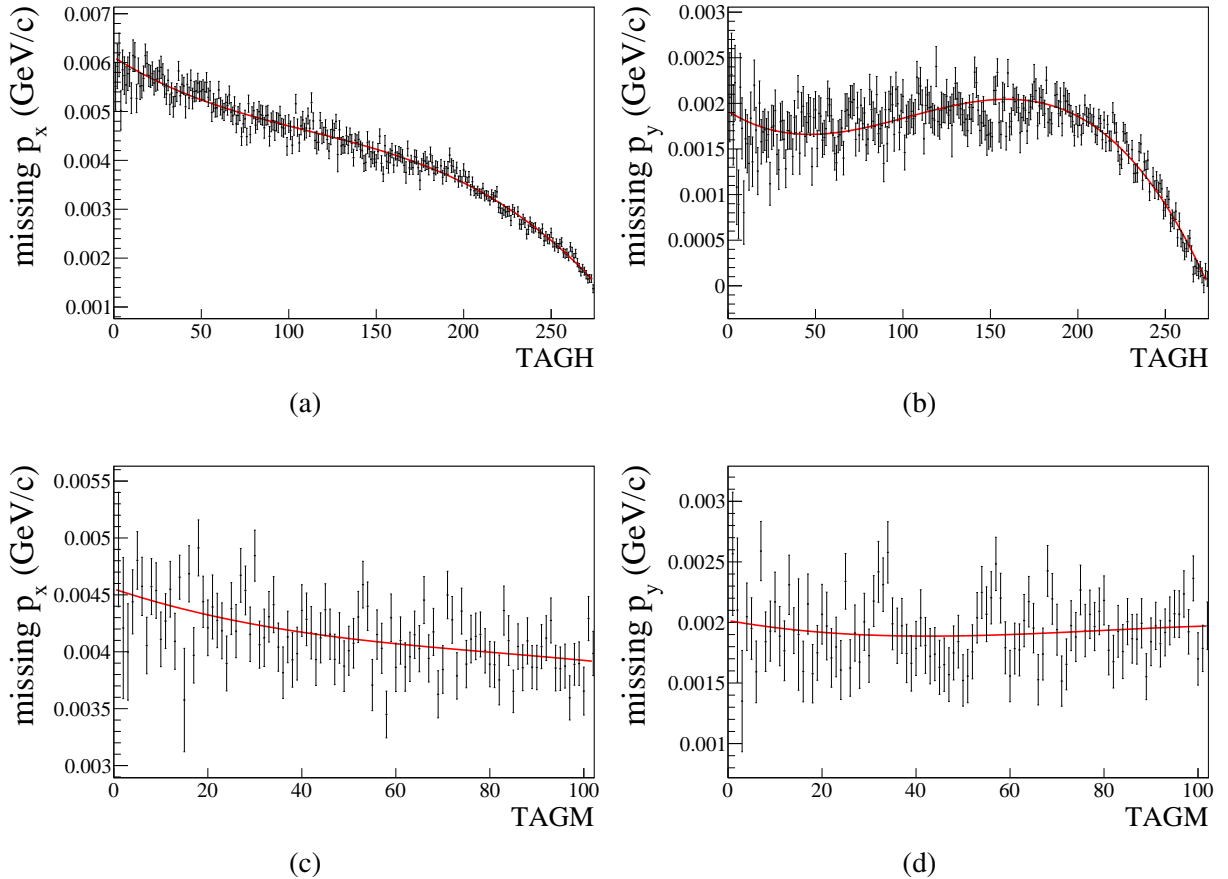


Figure 5.8: Beam correction plots produced for the TAGH ((a) and (b)) and TAGM ((c) and (d)). On the left (right), the mean missing p_x (p_y) is plotted against the corresponding tagger channel number. The red line shows a fit to the data, which was then used to evaluate the shift and correct for the beam tilt.

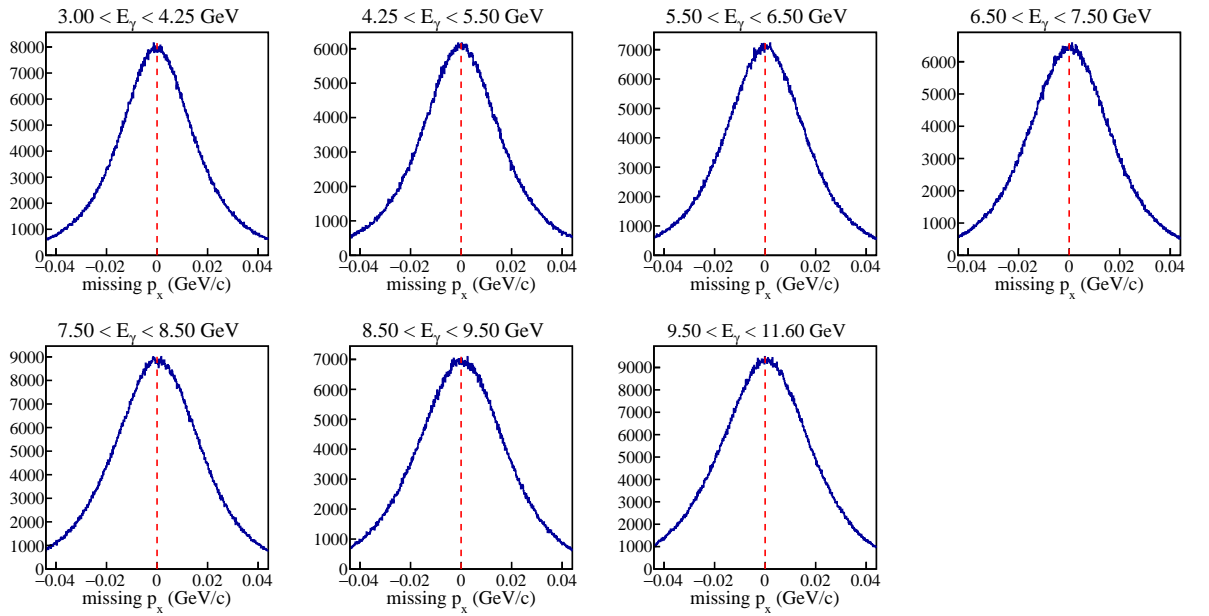


Figure 5.9: Missing p_x distributions plotted for different E_γ ranges after correcting for the beam axis tilt.

5.7 Final selection

After the steps described above had been performed, skim files were obtained that contained reconstructed data in the form of ROOT trees. In order to further reduce the background of events that do not match the exclusive $p\pi^+\pi^-$ final state topology, a series of cuts were applied to the skimmed data. These cuts are described in the following.

5.7.1 Tagger accidentals

It is important to match each of the measured final states with its associated beam photon. This was achieved using timing coincidence measurements between the SC and TAGH/TAGM. Due to the high beam flux and limited timing resolution, there were typically around 60-80 coincidences associated with each final state. Even after the full event selection had been applied, it was still possible to have multiple tagger hits associated with a recorded final state. Clearly, it is only possible for a single beam photon to trigger an event. The other associated coincidences are referred to as the *random background* or *tagger accidentals*. To account for the background of random coincidences, an accidental subtraction was applied to the photon timing spectrum.

The CEBAF electron beam has a bunch structure with a time separation of 4.008 ns between each bunch. This bunch structure is visible in Figure 5.10, which shows the timing spectrum of $\pi^+\pi^-p$ events. The central peak is referred to as the *prompt* peak. It is formed from beam photons that triggered the recorded physics event and a background of random coincidences.

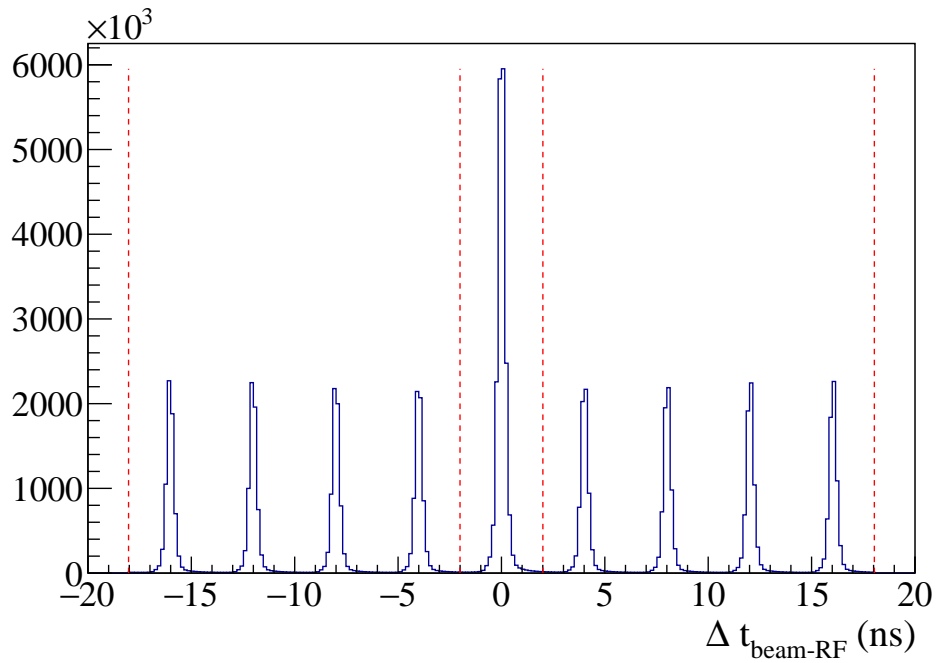


Figure 5.10: Histogram showing the time difference between each photon tagger hit and the time stamp provided by the CEBAF RF clock. The dashed lines annotate the prompt (centre) and side band (left and right) regions.

The four peaks to the left and right of the prompt peak result from beam bunches that arrive before or after the bunch which is in coincidence with the recorded event (i.e. the bunch that is responsible for the prompt peak). The two regions spanned by these peaks consist exclusively of events resulting from accidental timing coincidences, and are referred to as *side bands*. The accidental subtraction was applied by weighting events in the random peaks by $-\frac{1}{8}$, since there are four peaks in each side band. Events from the prompt peak were then assigned a weight of 1. All histograms required for the analysis were then filled using these weights. This statistically removed the background of random coincidences from the prompt peak.

The side band subtraction method assumes that the contribution from random coincidences in each of the side band peaks is the same as the contribution beneath the prompt peak. However, in practice this was not seen to be the case. A run dependent scaling factor [97] was determined by experts at Jefferson Lab to account for the discrepancy. The scaling factor was seen to vary between values of 1.0 and 1.6 depending on the run. The precision of the side band subtraction was then improved by multiplying timing weights in the side band region by the relevant scaling factor.

5.7.2 Reaction vertex

Cut limits were imposed on the position of the reconstructed reaction vertex to ensure that each measured final state originated from within the target cell. These limits are given by,

$$52 \text{ cm} < z < 78 \text{ cm} \quad (5.3)$$

where z denotes the z position of the kinematically fitted combined event vertex in the GlueX lab frame. Figure 5.15 shows the z distribution before and after the full event selection is applied. The upstream and downstream windows are visible at around 50 cm and 84 cm. Clearly the chosen cut limits were effective in removing events that did not originate from between these windows.

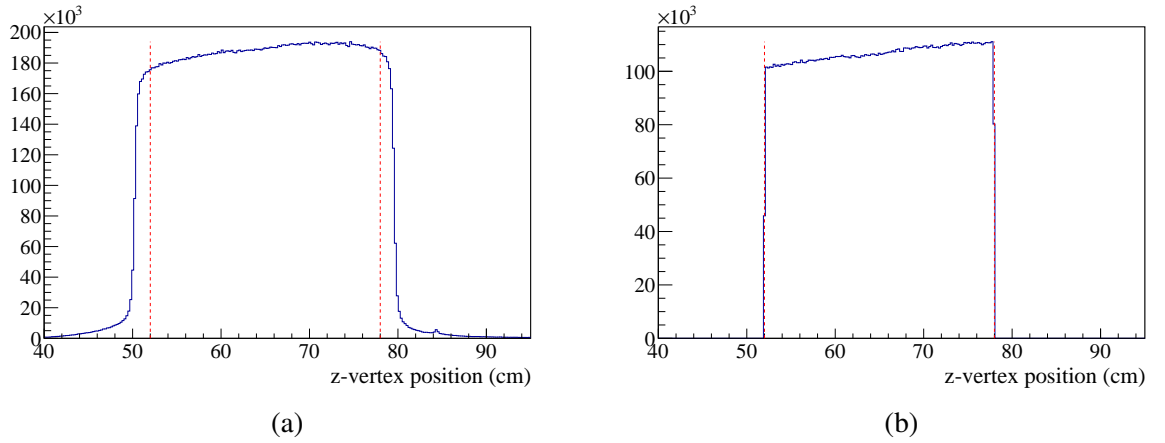


Figure 5.11: Histograms showing the z coordinate of the reaction vertex before (a) and after (b) the full event selection had been applied. The chosen cut limits are denoted by the red lines.

5.7.3 Missing mass squared

The missing mass squared of the reaction is defined as

$$\text{missing mass squared} = (P_\gamma + P_{\text{target}} - P_p - P_{\pi^+} - P_{\pi^-})^2 \quad (5.4)$$

where P_γ , P_{target} , P_p , P_{π^+} and P_{π^-} are the four-momenta of the incident photon, target proton, recoil proton, π^+ and π^- respectively. Since the reaction was measured in a fully exclusive final state, energy and momentum conservation require that the missing mass squared equates to $0 \text{ GeV}^2/c^4$. However, in practice a continuum of values for the measured missing mass squared are possible since detector resolutions are finite. For an exclusive reaction such as dipion photoproduction, one would expect a missing mass squared distribution with a peak at 0, and a symmetric drop-off at either side. Figure 5.12 shows the measured missing mass distribution before any additional cuts were applied to the skimmed, reconstructed data. No unexpected

structures are visible in the distribution. This suggests that the background contributions originating from missing or misidentified final state particles were already relatively low. Since the statistics available for the reaction of interest were excellent, it was decided that the final event selection should be very conservative. An upper limit of $0.02 \text{ GeV}^2/c^4$ on the magnitude of the missing mass squared was therefore imposed to further reduce background contributions. Note that the missing mass squared is strongly correlated to the χ^2 of the kinematic fit. A cut on the χ^2/NDF will therefore implicitly cut on the missing mass. This means that the missing mass cut only removed a small number of events, and can be thought of as supplementary to the kinematic fit cut. It should also be noted that the cut was applied using the measured missing mass squared, rather than the missing mass squared from the kinematic fit. This is because the four-momentum conservation constraints implemented by the fit ensure that every event has zero missing mass.

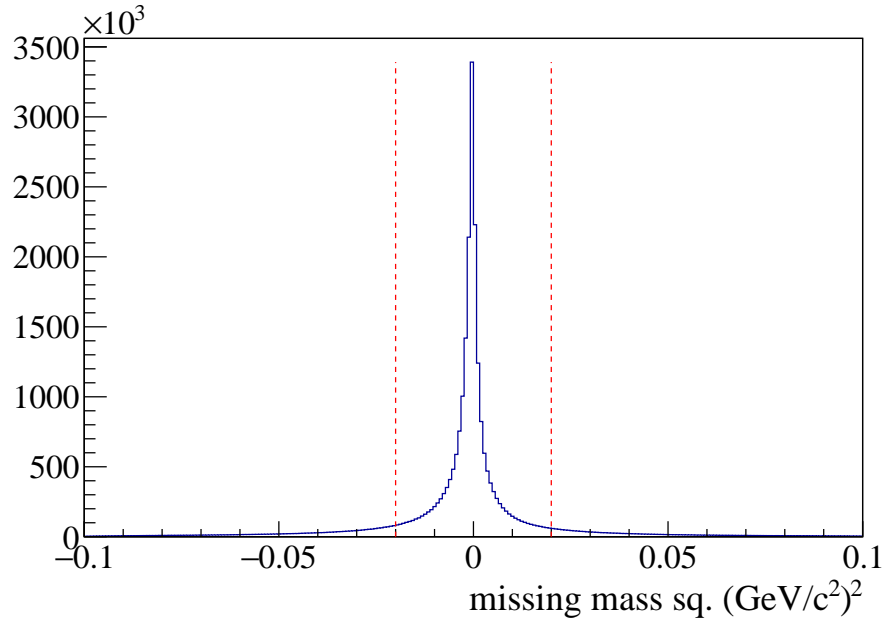


Figure 5.12: Histogram showing the missing mass squared for measured $\gamma p \rightarrow \rho \pi^- \pi^+$ events before any additional cuts had been applied. The chosen cut limits are denoted by the red lines.

5.7.4 Missing energy

The missing energy of the reaction is given by

$$\text{missing energy} = E_\gamma + E_{\text{target}} - E_p - E_{\pi^+} - E_{\pi^-}, \quad (5.5)$$

where E_γ , E_{target} , E_p , E_{π^+} and E_{π^-} are the total energies of the incident photon, target proton, recoil proton, π^+ and π^- respectively. Since the reaction is fully exclusive, conservation of energy requires that the missing energy equates to 0 GeV. As before, this is not always measured

in practice since detector resolutions are finite. Figure 5.13a shows the measured missing energy distribution for the reaction of interest. Clearly, there is only a small amount of missing energy. The distribution peaks at 0 GeV, with no additional structures visible. This indicates that the event sample was already quite clean. The distribution is seen to be slightly asymmetric, however this was corrected by applying a χ^2/NDF cut, as shown in Figure 5.13b. In order to further reduce backgrounds originating from missing or misidentified final state particles, events where the magnitude of the missing energy exceeds 0.5 GeV were cut away. This removes around 20% of events from the skimmed data sample. Similar to the missing mass squared cut, the measured rather than kinematically fitted missing energy were used to implement the cut. The missing energy inferred from the kinematic fit always equates to zero due to four-momentum conservation constraints.

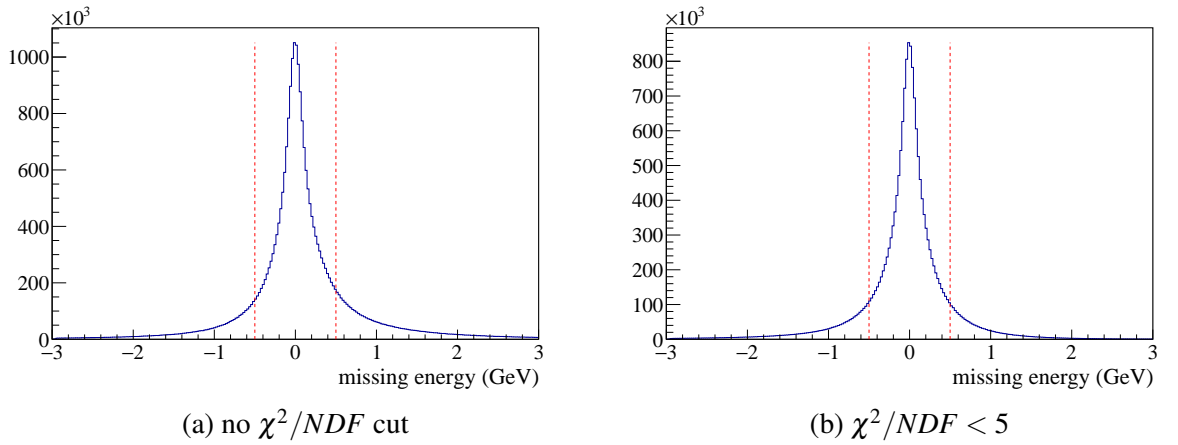


Figure 5.13: Histogram showing the missing energy for measured $\gamma p \rightarrow p\pi^-\pi^+$ final states (a) before any final selection cuts and (b) after applying the restriction $\chi^2/NDF < 5$. The chosen cut limits are denoted by the red lines.

5.7.5 Particle identification

Additional particle identification was applied in the final event selection. The minimum specific energy loss in the CDC for the recoil proton was restricted with the following function,

$$\frac{dE}{dx} > \exp(4p + 3.2) + 1 \text{ keV/cm}, \quad (5.6)$$

where p is the recoil proton momentum in units of GeV/c. The cut is illustrated in Figure 5.14. This restriction limited the possibility of misidentifying a K^+ .

5.7.6 Kinematic fit

The χ^2 per number of degrees of freedom (χ^2/NDF) from the kinematic fit after applying the full event selection is shown in Figure 5.15a. An additional peak was visible in the res-

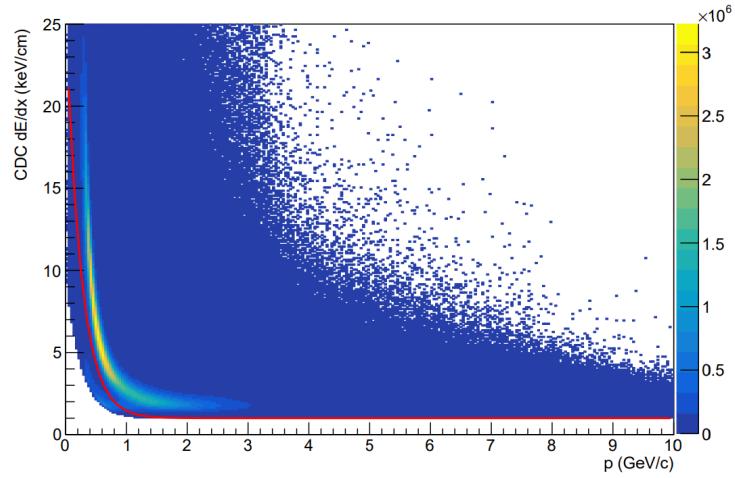


Figure 5.14: dE/dx measured for particle tracks in the CDC. The bright yellow band corresponds to reconstructed protons, while the red line denotes the particle ID cut specified by Equation (5.6).

ulting dipion invariant mass spectrum (see Figure 5.15b) at around $0.37 \text{ GeV}/c^2$. This was a result of the $\phi(1020)$ resonance decaying to K^+K^- , where the kaons were falsely identified as pions. Although the peak was located far below the mass of the $\rho(770)$, leakage into the $0.60 - 0.88 \text{ GeV}/c^2$ signal region may still be possible. Different χ^2/NDF cuts were studied to try and remove the $\phi \rightarrow K^+K^-$ background. Cutting on the kinematic fit χ^2/NDF tightens any vertex and four-momentum constraints. This improves the yield of exclusive final states and mitigates the possibility of falsely identifying final state particles. Figure 5.15b shows the effect of different χ^2/NDF cuts on the peak. Evidently, the $\chi^2/NDF < 5$ cut removes almost all of the background, and was therefore included in the final selection.

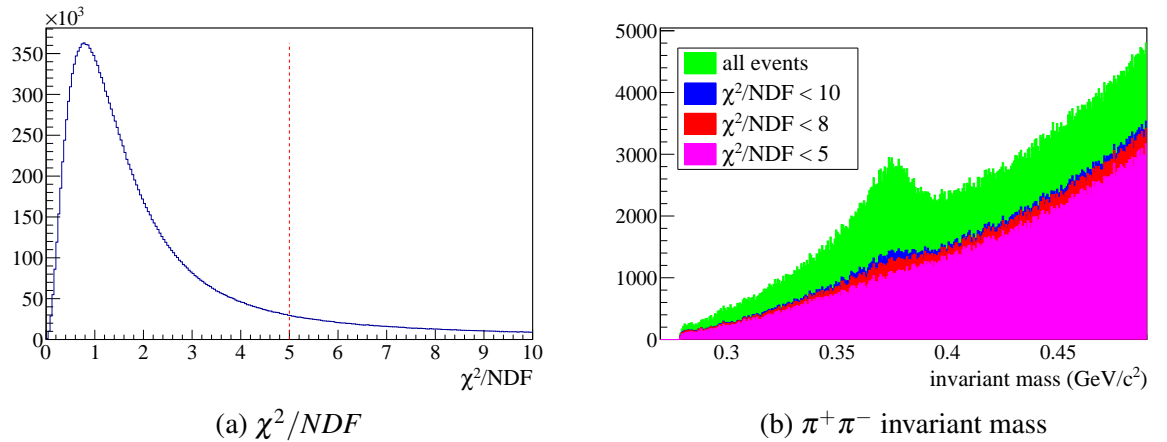


Figure 5.15: Suppression of misidentified $\phi(1020) \rightarrow K^+K^-$ with kinematic fit cuts. (a) shows the kinematic fit χ^2/NDF distribution before any of the final selection cuts were applied. (b) shows the low mass tail of the dipion invariant mass spectrum for various χ^2/NDF cuts.

5.7.7 Anti Δ^{++} cut

At low beam energies, the kinematic separation between the $\rho(770)$ and baryon resonances becomes poorer. The dominant excitation is the Δ^{++} . The primary decay mode of the Δ^{++} baryon resonance is $\pi^+ p$, with the reaction proceeding as $\gamma p \rightarrow \Delta^{++} \pi^- \rightarrow p \pi^+ \pi^-$. The final state is identical to the one expected from $\rho(770)$ decay. Figure 5.16 shows the $\pi^+ p$ invariant mass distribution for $E_\gamma < 4.25$ GeV. A peak corresponding to the $\Delta^{++}(1232)$ resonance is clearly observed. SDMEs were extracted by performing a maximum likelihood fit to experimental data using Equation (2.32) as a probability distribution function (PDF). Equation (2.32) only describes the angular distribution of vector meson decay products. It was therefore necessary to remove as much baryon contamination as possible.

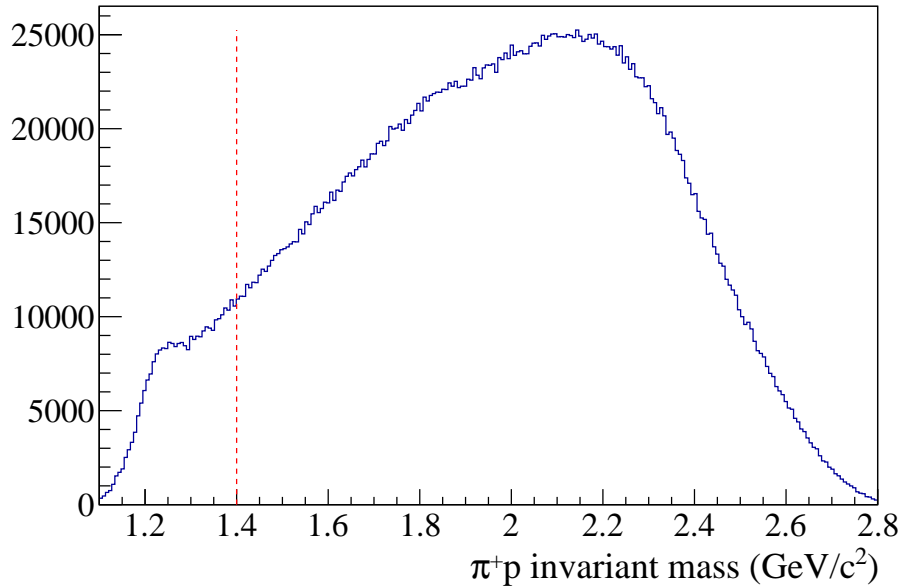


Figure 5.16: $\pi^+ p$ invariant mass distribution measured at low beam energy ($E_\gamma < 4.25$ GeV). The red line denotes the cut used to remove the $\Delta^{++}(1232)$ contribution.

The Δ^{++} background contribution was suppressed by removing events with $M_{\pi^+ p} < 1.4$ GeV/ c^2 , where the $\pi^+ p$ invariant mass is inferred from the kinematic fit. In order to be as conservative as possible, this cut was applied over the full beam energy range.

5.8 Binning

The statistics available for the $p \pi^+ \pi^-$ final state with GlueX were excellent. In order to make the most of the data, results were extracted in finely spaced bins over multiple dimensions in phase space using three different binning schemes.

In the first binning scheme, SDMEs were extracted from bins in the Mandelstam variable, t ,

which describes the four-momentum transfer squared to the recoil proton,

$$t = (p_{p_{\text{target}}} - p_{p_{\text{recoil}}})^2. \quad (5.7)$$

Since t is negative, $-t$ is used for plotting and binning. This variable effectively describes the mass of the virtual hadron exchanged between the beam photon and target in the production reaction. This makes it a natural choice of binning variable, and makes it possible to study the dependence of the production mechanism on the reaction kinematics. Eighteen logarithmically spaced bins in $-t$ were defined. Since the acceptance for cold protons with GlueX is poor, the lower limit for bins in $-t$ was chosen to be $0.1 \text{ GeV}^2/c^2$. This binning configuration complements the shape of the $-t$ distribution seen in data, shown in Figure 5.17.

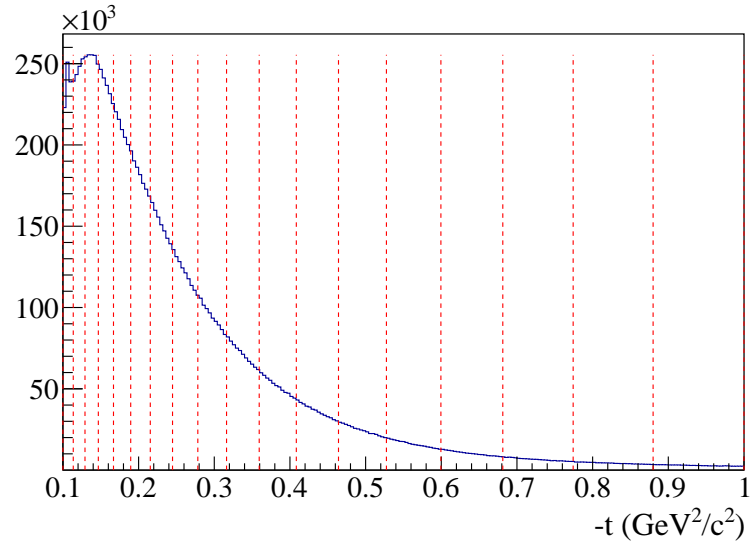


Figure 5.17: $-t$ distribution measured in data after applying the full event selection. The bin limits are denoted by the red lines.

Since the decay distribution was expected to depend on the energy regime of the reaction, results were also extracted in seven different beam energy ranges in the first binning scheme. Bins with varying widths were defined to ensure the statistics in each of the studied E_γ ranges were similar. A visual representation of the binning in E_γ is shown in Figure 5.18. Binning in the photon energy shows the extent to which the studied reaction conserves helicity in the s-channel as a function of E_γ . In turn, this offers some insight into the production mechanism and hadron exchange responsible for the measured final state.

The second binning scheme was very similar to the one described above, the only difference being that seven bins in the dipion invariant mass were also defined. The $\rho(770)$ is a broad resonance, with significant non-resonant background beneath the peak, in addition to mixing with the $\omega(782)$ resonance. Moreover, baryon resonances are likely to contribute in the lower E_γ regime. Binning in the $M_{\pi^+\pi^-}$ is a good way of studying the effect that these backgrounds

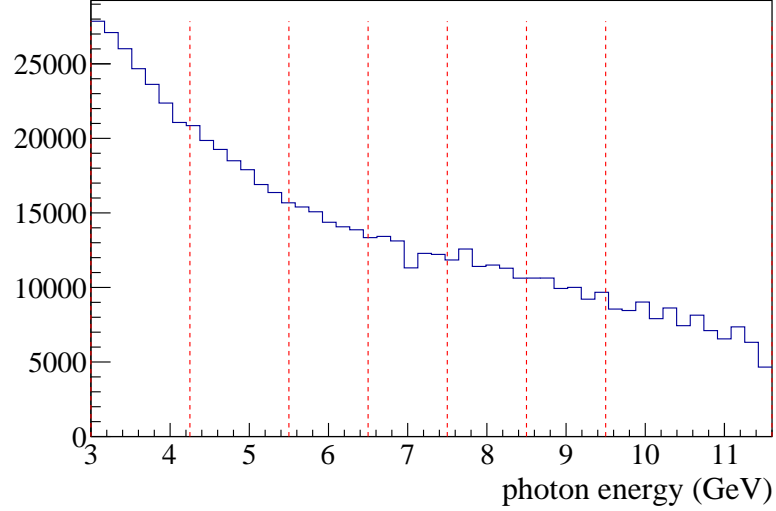


Figure 5.18: Beam energy distribution for data collected with an amorphous radiator.

have on the extracted SDMEs. $M_{\pi^+\pi^-}$ bins were chosen to have varying widths to ensure the statistics in each bin were approximately the same. The scheme is annotated in the dipion invariant mass distribution shown in Figure 5.19. The upper and lower limits in $M_{\pi^+\pi^-}$ were chosen to be $0.88 \text{ GeV}/c^2$ and $0.60 \text{ GeV}/c^2$ respectively. The $\rho(770)$ was seen to comfortably dominate in this region, as shown in Figure 5.19.

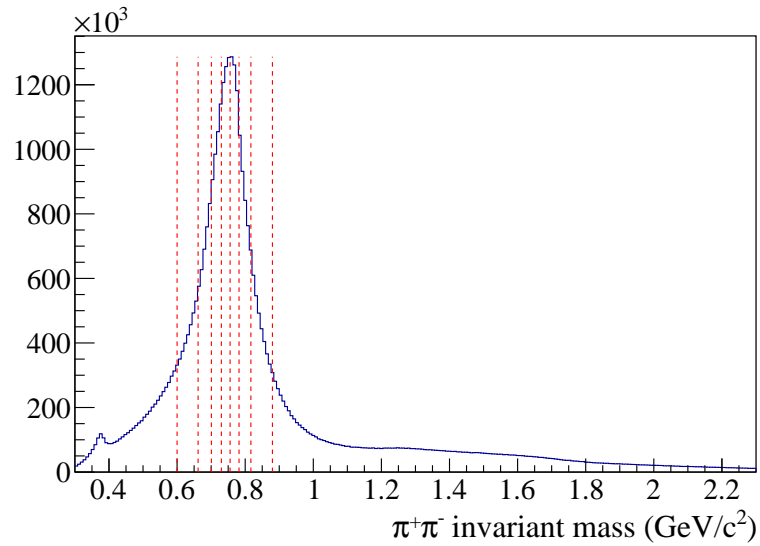


Figure 5.19: Invariant mass distribution of the dipion system over the $\rho(770)$ peak. Bin edges are annotated by the dashed lines.

A third binning scheme was constructed to study the mass dependence of the extracted results in more detail. In this scheme, the same beam energy binning configuration was defined as in the first two schemes. However, a finer binning arrangement for the $\pi^+\pi^-$ invariant mass

was used to more carefully probe the mass dependence of results, with fourteen equally spaced bins defined over the $0.60 - 0.88 \text{ GeV}/c^2$ mass range. Moreover, data were split into six different ranges in $-t$ spanning the $0.1 - 1.0 \text{ GeV}^2/c^2$ region. This meant that backgrounds could be studied in more detail, since different resonances were expected to dominate over different regions in $-t$.

5.9 Summary

After the data recorded by the detector had been reconstructed, calibrated and skimmed by experts at Jefferson Lab, additional cuts were applied to select the $p\pi^+\pi^-$ final state and remove backgrounds. These cuts are summarised in Table 5.3, while Figure 5.20 shows a visual representation of the entire analysis flow. Modifications of the chosen cut limits were studied to evaluate the cut stability and determine systematic uncertainties. These studies are described in Section 7.1. In the following chapter, the extraction of SDMEs from the prepared data is presented.

Table 5.3: Summary of cuts applied in the final selection.

cut	lower limit	upper limit	cut	lower limit	upper limit
vertex z (cm)	52	78	CDC dE/dx (keV/cm)	$\exp(4p + 3.2) + 1$	none
missing mass squared (GeV^2/c^4)	-0.02	0.02	kinematic fit χ^2/NDF	none	5
missing energy (GeV)	-0.5	0.5	π^+p invariant mass (GeV/c^2)	1.4	none

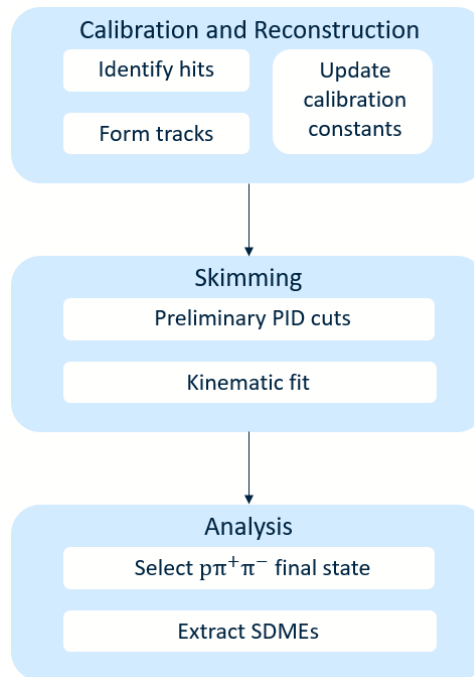


Figure 5.20: Flowchart showing the sequence of analysis steps required to extract physics observables from raw GlueX data. The calibration, reconstruction and skimming steps were performed at Jefferson lab by experts. The analysis, which includes the tagger and beam corrections summarised in Section 5.6, were performed locally.

Chapter 6

Observable extraction

After following the steps outlined in the previous chapter, a clean sample of events corresponding to the $p\pi^+\pi^-$ final state was obtained. This meant that SDMEs could then be extracted from the data by studying the angular distributions of particles in each event.

The reaction of interest was studied in the helicity system, shown in Figure 2.5. The reaction kinematics were analysed using the helicity frame angles, ϕ and θ , of the π^+ measured for events in fixed ranges of the photon energy, $\pi^+\pi^-$ invariant mass and $-t$. The ϕ and θ distributions of decaying vector mesons in unpolarised photoproduction are described by the intensity function given by Equation (2.33). This function contains three fit parameters (SDMEs) and two variables (ϕ and θ). In this work, the three SDMEs were extracted with an extended maximum likelihood fit. This was achieved using a Markov chain Monte Carlo (MCMC) based parameter estimation. Each SDME was then estimated by extracting the mean from the corresponding posterior distribution, where the final statistical uncertainty was determined from the distribution width. Finally, each of the extracted SDMEs following from the MCMC chain were used as starting parameters for a second extended maximum likelihood fit using ROOT's MINUIT2 algorithm [98]. In this chapter, these analysis steps are explained in detail.

6.1 Extended maximum likelihood fit

SDMEs were extracted from Equation (2.33) by determining the set of parameters that maximised the calculated log-likelihood. This was achieved using an extended maximum likelihood fit [99]. In order to perform the fit, it was necessary to construct a likelihood function. The construction of the likelihood is described in the following.

The probability of an event characterised by the decay angles θ_i and ϕ_i measured by a specific

experiment can be defined as

$$P_i = \frac{\sigma(\theta_i, \phi_i) \eta(\theta_i, \phi_i)}{\int d\Omega \sigma(\theta, \phi) \eta(\theta, \phi)}, \quad (6.1)$$

where $\eta(\theta, \phi)$ is the acceptance of the experiment and $\sigma(\theta, \phi)$ is the measured cross section given by

$$\sigma(\theta, \phi) = A \cdot W(\theta, \phi). \quad (6.2)$$

Here, A is an overall normalisation factor and $W(\theta, \phi)$ is the decay angular distribution defined in Equation (2.33). For an experiment of fixed duration, the total number of measured events N follows a Poisson distribution with an expectation value \bar{N} . This distribution is taken into account by the extended likelihood function

$$\mathcal{L} = \frac{e^{-\bar{N}} \bar{N}^N}{N!} \prod_{i=1}^N P_i, \quad (6.3)$$

which can be simplified to

$$\mathcal{L} = \frac{e^{-\bar{N}} \bar{N}^N}{N!} \prod_{i=1}^N \sigma(\theta_i, \phi_i) \eta(\theta_i, \phi_i) \quad (6.4)$$

by considering the value of \bar{N} with the total number of events given by the denominator in Equation (6.1). Sums are more computationally simple to handle than products. It was therefore the logarithm of the likelihood that was maximised to match the measured angular distribution $\sigma(\theta_i, \phi_i)$,

$$\ln \mathcal{L} = \sum_{i=1}^N \ln \sigma(\theta_i, \phi_i) + \sum_{i=1}^N \ln \eta(\theta_i, \phi_i) - \ln N! - \int d\Omega \sigma(\theta, \phi) \eta(\theta, \phi) \quad (6.5)$$

The second and third terms in Equation (6.5) are constant and do not depend on the fit parameters and were therefore omitted from the fit. The first term describes the events recorded in the detector, while the integral for the experimental acceptance is given by the last term. This corrects for acceptance effects introduced by the detector, and was evaluated by summing over all events in a sample of simulated data that was generated with flat angular dependence. Note that generated Monte Carlo events were passed through the full detector simulation and reconstruction.

The complete extended log-likelihood function can now be written as

$$\ln \mathcal{L} = \sum_{i=1}^N t_i \ln \sigma(\theta_i, \phi_i) - \int d\Omega \sigma(\theta, \phi) \eta(\theta, \phi), \quad (6.6)$$

where t_i are the timing weights defined in Section 5.7.1. Including these weights ensured that events where the associated beam photon originates from the background of tagger randoms were properly subtracted. The extended likelihood function can be maximised by optimising

a set of SDMEs along with the normalisation factor A to achieve the best possible agreement between $\sigma(\theta, \phi)$ and the measured data. This was achieved using an MCMC. The determined SDMEs were then defined as the starting parameters for a second extended maximum likelihood that used MINUIT instead of MCMC.

6.2 Markov chain Monte Carlo

Markov chain Monte Carlo is a parameter estimation method ideally suited for problems with high dimensionality. The parameter space is explored numerically by stepping through likelihood space. This is achieved by changing one or more parameters with each step and then recalculating the likelihood. A decision is then made on whether or not the new set of parameters is accepted based on the initial and recalculated likelihood. The set of parameters from each step form a chain, from which parameter estimates can be extracted. The key feature of MCMC is that each new set of parameters in the chain is dependent only on the set defined in previous step. This makes it possible to avoid local minima in the negative log-likelihood. A more detailed explanation of Markov chain Monte Carlo methods can be found in [100].

6.2.1 Bayes' theorem

One of the key concepts underlying MCMC methods is Bayes' theorem. The theorem can be expressed as

$$P(\theta|Z)P(Z) = P(Z|\theta)P(\theta). \quad (6.7)$$

$P(\theta|Z)$ is the conditional probability of measuring a set of parameters, θ , given a specific dataset, Z . This is often referred to as the *posterior probability*. The posterior probability is the component of interest in Bayes' theorem, since it describes the probability that a specific set of parameters, θ , is responsible for the observed data, Z . $P(Z)$ is the probability of measuring the dataset, Z . It does not play an important role in this analysis, and has no effect on the final result. $P(Z|\theta)$ is equivalent to the likelihood \mathcal{L} defined in Equation (6.6) for the extended maximum likelihood fit. It describes the probability of measuring a dataset, Z , given a specific set of parameters, θ . $P(\theta)$ is referred to as the *prior probability*, and describes the probability of a given set of parameters θ within the model. The prior probability introduces a subjective component to the formalism since it is constructed under the assumption that a given model correctly describes the problem, and that the posterior distribution can be described by a specific shape which is often constrained within a set of hypothesised limits.

6.2.2 Metropolis-Hastings algorithm

The MCMC method used for the parameter estimation in this analysis is the *Metropolis-Hastings algorithm* [101], [102]. The algorithm can be summarised in four key steps [100].

1. A set of start parameters θ^0 is chosen
2. A candidate is selected for the next step in the chain θ' , according to a *proposal distribution* $q(\theta'|\theta^n)$, where θ^n is the set of parameters at the current step. For the analysis presented in this thesis, a Gaussian distribution centred on the parameter value of the current step is used as the proposal distribution. The width of this distribution is controlled by defining a step size. This is discussed in more detail in Section 6.2.3.
3. The *acceptance probability* is determined. This is the probability of going from θ^n to θ' , and is calculated based on a *prior distribution*. For the analysis presented in this thesis, a uniform distribution with upper and lower limits corresponding to 1 and -1 respectively is used for the prior distribution. Note that the range [-1,1] includes all physically allowed values for each of the SDMEs. The acceptance probability is defined as

$$\alpha(\theta'|\theta^n) = \min \left\{ \frac{P(\theta'|Z)q(\theta^n|\theta')}{P(\theta^n|Z)q(\theta'|\theta^n)}, 1 \right\}. \quad (6.8)$$

$\pi(\theta')$ is the *posterior distribution* of the proposed candidate θ' , and can be expressed using terms from Equation (6.7). This means Equation (6.8) can be rewritten as

$$\alpha(\theta'|\theta^n) = \min \left\{ \frac{P(Z|\theta')P(\theta')q(\theta^n|\theta')}{P(Z|\theta^n)P(\theta^n)q(\theta'|\theta^n)}, 1 \right\}. \quad (6.9)$$

The acceptance probability now only depends on the likelihood of measuring the dataset Z , given parameters θ' and θ^n , the *prior distribution* and the *proposal distribution*, all of which are either calculable or explicitly defined by the analyser.

4. θ' is accepted with probability $\alpha(\theta'|\theta^n)$. The current set of parameters θ^n is added to the chain again if θ' is rejected. Return to step 2.

The resulting Markov chain has the distribution $P(\theta|Z)$, meaning it describes the probability distribution for the set of parameters given the input dataset Z .

Figure 6.1 shows a visualisation of the Metropolis-Hastings algorithm. A set of start parameters θ^0 is chosen and a new step in parameter space is proposed. The acceptance probability for the step is calculated using a uniform *prior distribution*, with upper and lower limits Ub and Lb . The likelihood increases for the first two steps which are then accepted, meaning the new sets of parameters are added to the chain. The likelihood decreases in the third step, but the step is

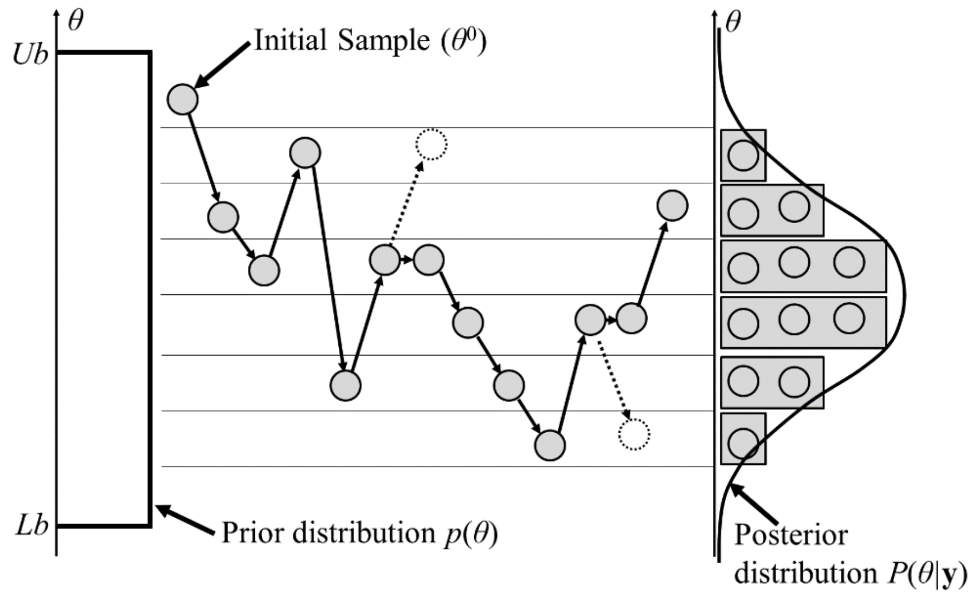


Figure 6.1: Illustration of the Metropolis-Hastings algorithm. Figure taken from [103].

still accepted and the new set of parameters is added to the chain. The likelihood increases for the fourth and fifth steps, which are automatically accepted. In the sixth step the likelihood decreases, the step is rejected and the current set of parameters are added to the chain again. This process then continues for a predetermined number of steps, after which the *posterior distribution* can be obtained by histogramming the accepted parameters. The posterior distribution will more accurately describe the likelihood distribution of the parameters for longer chains. The set of parameters that fits the data best can then be estimated from posterior distributions (e.g. mean or mode), and the associated uncertainty can be derived from the distribution width.

The Metropolis-Hastings algorithm was implemented using the RooStats [104] package within the `brufit` [105] analysis framework. MCMC steps were proposed using an approach based on the covariance matrix of an initial sequential proposal chain. This approach is explained in the next section. The starting parameters for all three SDMEs were set to zero and a uniform prior probability was defined over the $[-1, 1]$ range, which includes all allowed values for the SDMEs. The SDMEs determined from the mean of each final posterior distribution were then used as starting parameters for a MINUIT fit to extract final results. Since these starting parameters are already within the region of the global minimum, there is no possibility that the MINUIT fit will unintentionally extract parameters corresponding to a local minimum. The final parameters will always be closer to the true minimum relative to what was extracted with MCMC. The uncertainties associated with MINUIT fitting were often seen to be unphysical, as demonstrated in Figure 6.2a. Statistical uncertainties were therefore determined from the widths of posterior distributions from the MCMC.

6.2.3 Covariance matrix step proposal method

Initially, a simple sequential proposal (SP) adaption of the Metropolis-Hastings algorithm was used to sample the parameter space. This algorithm performs each MCMC step in a single dimension in parameter space before re-calculating the likelihood, where the remaining parameters are kept constant. The step is then accepted or rejected in accordance with the criteria outlined in the previous section, and a new step is proposed in one of the other parameter dimensions. This method ignores correlations between parameters. Moreover, the SP algorithm requires fine tuning of the step size to maximise efficiency and ensure the global minimum is found. After each step, the next parameter value in the chain is sampled from a Gaussian distribution centred on the current value. The width of the Gaussian is related to the step size, and needs to be tuned to ensure the proposal acceptance rate is around 20%. The proposal acceptance is defined as

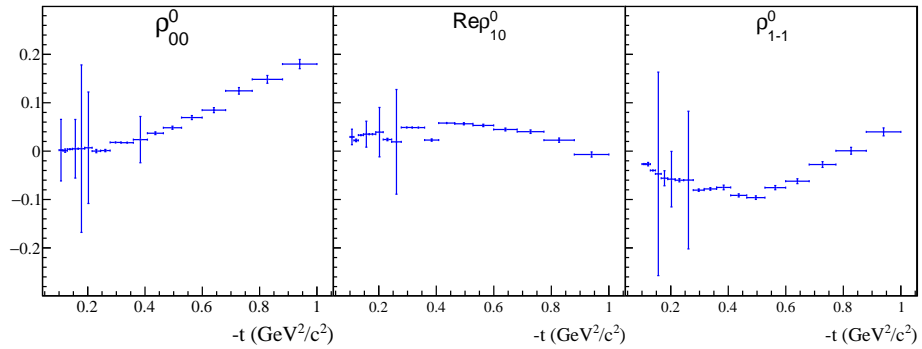
$$\text{acceptance} = \frac{\text{number of accepted steps}}{\text{total number of proposed steps}}. \quad (6.10)$$

If the proposal acceptance is too high then the chain may have spent too much time sampling regions where the evaluated likelihood was low, meaning the parameter space has not been properly explored. If the acceptance is too low, a greater number of steps will clearly be necessary to achieve the desired number of accepted steps, making the parameter extraction more computationally intensive. The proposal acceptance is related to the statistics available for each individual fit. A complex binning scheme was used in this analysis with various different ranges in E_γ , $M_{\pi\pi}$ and $-t$ defined for independent MCMC fits. This made it time consuming to determine the optimal step size for each individual fit.

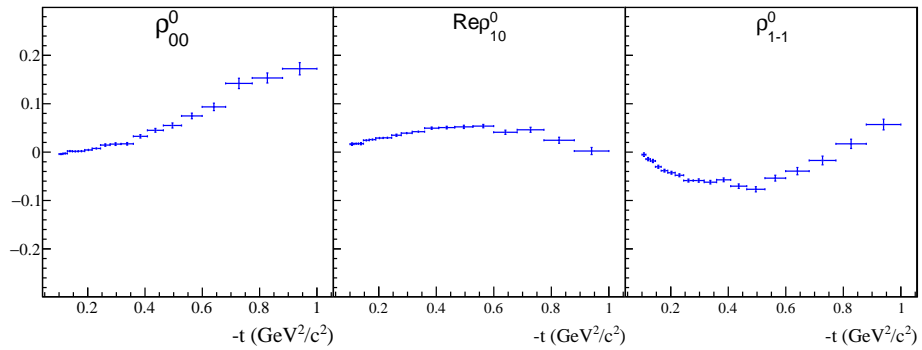
A step proposal method based on the covariance matrix of a SP chain [106] was used to try and avoid the complications detailed above. The first step involves initialising an SP chain for a given number of steps. For every thousand steps in the SP chain the proposal acceptance rate is determined. If the calculated acceptance is between a set of limits defined by the user then the chain is allowed to continue. If the acceptance is determined to be outwith these limits, a normalisation parameter is modified to either reduce or increase the step size and the chain is reset. This step is performed recursively until the proposal acceptance is within the user-defined window, ensuring that the step size is optimal. After the SP chain has terminated, it is used to calculate a covariance matrix. This matrix encodes correlations between parameters, in addition to the widths of posterior distributions for individual parameters. Finally, the covariance matrix is used to define a step proposal function for a second MCMC chain. For this chain, all fit parameters are varied simultaneously in each step using a proposal function that incorporates knowledge of parameter correlations. Since the proposal acceptance is automatically optimised and parameter correlations are taken into account, this step proposal method is much more efficient than the conventional SP approach.

6.2.4 Comparison with a MINUIT based parameter estimation

It was necessary to use an MCMC based parameter extraction to avoid local minima in the negative log-likelihood. The importance of this approach is demonstrated in Figures 6.2a and 6.2b. Figure 6.2a shows an example of SDMEs extracted using MINUIT, where the starting parameters were all set to zero. Bin-to-bin fluctuations that are inconsistent with the magnitude of the plotted uncertainties are visible in the data. It is likely that these fits either converged in local rather than global minima, or did not converge at all. Furthermore, many of the statistical uncertainties were clearly overestimated by the fit. With MINUIT, the error matrix is determined from the matrix of second derivatives in the likelihood of the extracted parameters, where the second derivatives are estimated using a numerical approximation. When this approximation fails, the resulting uncertainties are often unphysical, leading to inflated error bars such as those shown in Figure 6.2a.



(a)



(b)

Figure 6.2: SDMEs measured over the 6.5 – 7.5 GeV photon energy range using a MINUIT (a) and MCMC (b) based parameter estimation.

Figure 6.2b shows the result measured when an MCMC based parameter extraction is performed. The fluctuations that were present in the results shown in Figure 6.2a are no longer visible, suggesting that the MCMC is effective in locating the global minimum for every fit. The statistical uncertainties in this plot were determined from the widths of posterior distributions, and are clearly more realistic than the uncertainties plotted in Figure 6.2a.

6.3 Results

Figures 6.3 to 6.5 summarise the performance of a single MCMC fit. Figure 6.3 shows the so-called *trace plots* from the initial SP chain. The accepted parameter values are plotted against the corresponding step to visualise the evolution of the MCMC chain. Although posteriors are more likely to resemble the true probability distributions for longer chains, the process will become more computationally intensive as the number of steps increases. A chain length of 3500 steps was chosen for the SP, which was sufficient for accurately mapping out the likelihood space while ensuring the time overhead was manageable. Initially the chain was unstable due to the choice of starting parameters. Since these are unlikely to be consistent with the true SDMEs, the proposal acceptance rate will usually be high to begin with as the parameters accepted at each step gradually converge towards the true solution. It was therefore necessary to discard the first 800 steps to minimise the effect of the chosen start parameters on the final result. This is standard practice, and is referred to as *burn in*. The resulting covariance matrix was then reliable enough to construct a step proposal function for the second MCMC chain. Since the first chain had already converged on a stable set of parameters, the second chain did not require as many steps. Furthermore, the covariance matrix approach allowed the parameter space to be explored more efficiently. The second chain was therefore chosen to be 1000 steps long, with a burn in of 80.

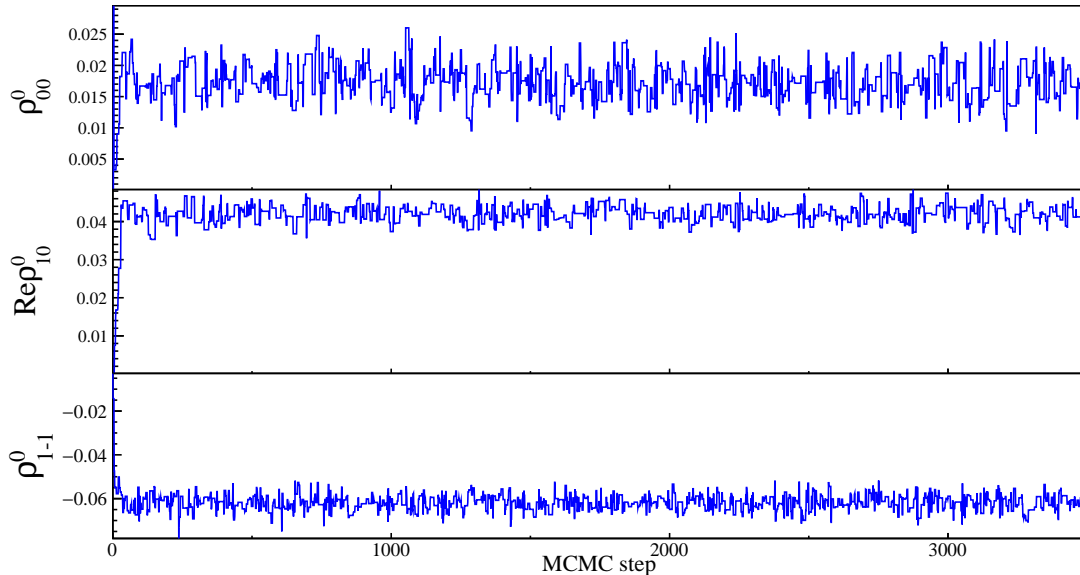


Figure 6.3: Step timeline plots for the $6.5 - 7.5 \text{ GeV } E_\gamma$ and $0.32 - 0.36 \text{ GeV}^2/c^2 -t$ bin

Figure 6.4 shows the 1D and 2D posterior distributions for all three parameters from the second Markov chain. No strong correlations are observed between any of the fit parameters. Plots such as these are commonly referred to as *corner plots*. Corner plots offer a convenient way of identifying correlated parameters and visualising the spreads of posterior distributions.

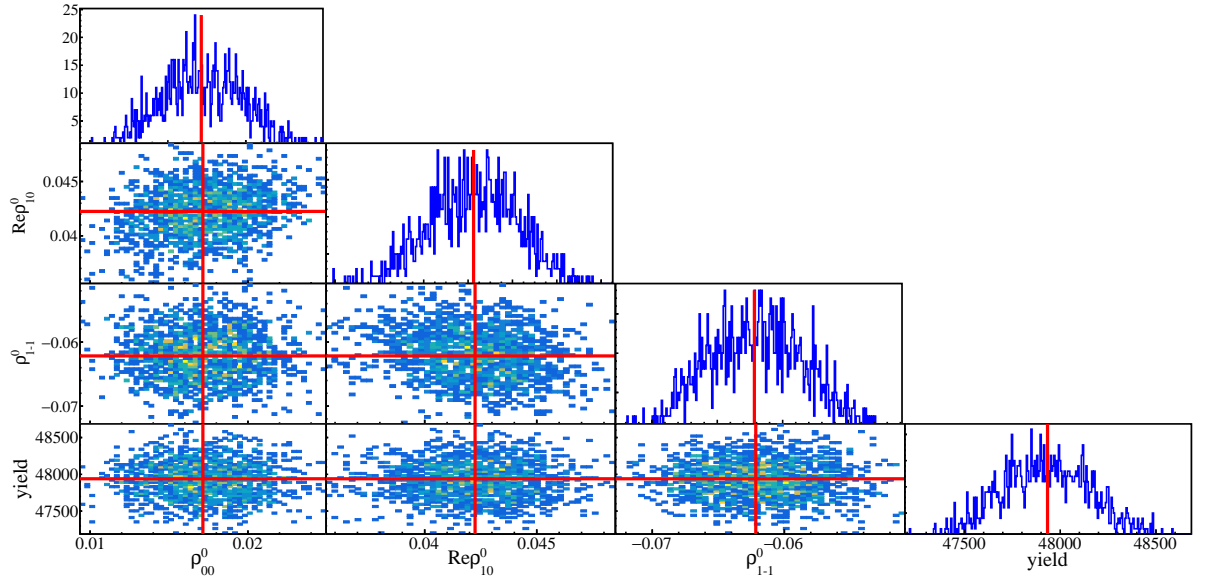


Figure 6.4: Corner plot for the $6.5 - 7.5 \text{ GeV } E_\gamma$ and $0.32 - 0.36 \text{ GeV}^2/c^2 -t$ bin. The solid red lines denote the means of the relevant posterior distributions.

The quality of the fit can be evaluated by weighting the Monte Carlo sample used for the acceptance correction with the extracted SDMEs. The unweighted Monte Carlo sample is generated with a flat angular dependence, and is produced with an accurate model of detector acceptances provided by the `hdgeant4` simulation. The angular distributions from data can then be compared with distributions from the weighted Monte Carlo. A good agreement between both distributions indicates that the extracted SDMEs are effective in describing the experimental data, suggesting that SDMEs have been estimated correctly. Comparisons of weighted Monte Carlo and reconstructed data angular distributions are shown in Figure 6.5. The data and associated statistical uncertainties are shown in black, while the weighted Monte Carlo is shown in red. Distributions are seen to agree well for both π^+ decay angles, indicating that the fit had performed well.

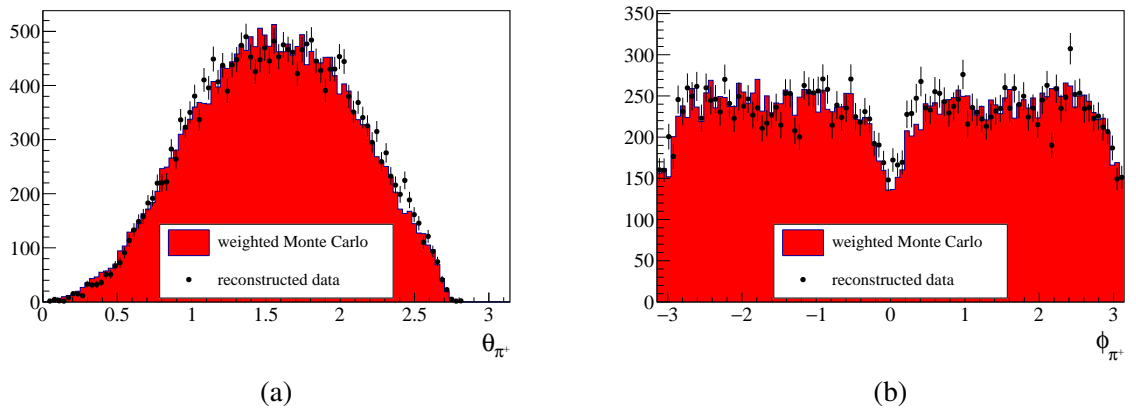


Figure 6.5: Projections of θ (a) and ϕ (b) from experimental data (black) and the acceptance weighted fit results (red) for the $6.5 - 7.5 \text{ GeV } E_\gamma$ and $0.32 - 0.36 \text{ GeV}^2/c^2 -t$ bin.

6.4 Summary

In this chapter, an overview of the parameter estimation method used to obtain the final results presented in Chapter 8 was given. It was demonstrated that SDMEs can be extracted from data using the Metropolis-Hastings MCMC algorithm to obtain starting parameters for a MINUIT fit. The plots shown in Section 6.3 indicate that MCMC fits were performing well. In the following chapter, validation studies are presented that confirm the reliability of the chosen parameter extraction method. The calculation of systematic uncertainties deriving from the stability of the chosen cut variables is also summarised.

Chapter 7

Determination of systematic uncertainties

Detailed studies were performed to identify any systematic effects arising from various aspects of the analysis. The findings were then used to calculate systematic uncertainties. These studies are summarised in the following sections.

7.1 Event selection

A cut based event selection was applied to reduce the data size, improve the yield of exclusive $\gamma p \rightarrow \pi^+ \pi^- p$ events and mitigate baryon contamination. Cuts are applied both during the data skim at Jefferson Lab, and locally in the final selection. These cuts are summarised in Sections 5.4 and 5.7. The stability of the final selection was studied by varying the chosen limits for each of the cuts specified in Chapter 5 and repeating the observable extraction. Four different variations were defined for each cut, except for the cut on the CDC energy loss. For this particular cut, only a single variation was necessary. This meant the entire analysis chain needed to be re-performed 21 times. The cut variations that were used are specified in Table 7.1. Each was designed to cover a reasonable range over which the cut limits could have been placed.

Table 7.1: Modifications to the event selection that were used for cut stability studies. The cuts used in the final SDME extraction are shown in red.

setup	cut varied	limit	setup	cut varied	limit
1	$\chi_{kin.}^2./NDF$	3	15	$ E_{miss} $	0.70 GeV
2	$\chi_{kin.}^2./NDF$	4	16	M_{π^+p}	1.50 GeV/ c^2
3	$\chi_{kin.}^2./NDF$	5	17	M_{π^+p}	1.45 GeV/ c^2
4	$\chi_{kin.}^2./NDF$	6	18	M_{π^+p}	1.40 GeV/ c^2
5	$\chi_{kin.}^2./NDF$	7	19	M_{π^+p}	1.35 GeV/ c^2
6	$ M_{miss}^2 $	0.012 GeV ² / c^4	20	M_{π^+p}	1.30 GeV/ c^2
7	$ M_{miss}^2 $	0.016 GeV ² / c^4	21	CDC $\frac{dE}{dx}$	$\exp(4p + 3.20) + 1$ (keV/cm)
8	$ M_{miss}^2 $	0.020 GeV ² / c^4	22	CDC $\frac{dE}{dx}$	$\exp(4p + 2.25) + 1$ (keV/cm)
9	$ M_{miss}^2 $	0.024 GeV ² / c^4	23	vertex z	54 – 76 cm
10	$ M_{miss}^2 $	0.028 GeV ² / c^4	24	vertex z	53 – 77 cm
11	$ E_{miss} $	0.30 GeV	25	vertex z	52 – 78 cm
12	$ E_{miss} $	0.40 GeV	26	vertex z	51 – 79 cm
13	$ E_{miss} $	0.50 GeV	27	vertex z	50 – 80 cm
14	$ E_{miss} $	0.60 GeV			

The Barlow test as defined in [107] was used to identify systematic deviations and determine whether they were significant. For each cut, the chosen limits are varied and SDMEs are re-measured. After each measurement the associated variable σ_B is calculated as

$$\sigma_B = \sqrt{|\sigma^2 - \sigma'^2|}, \quad (7.1)$$

where σ denotes the uncertainty as reported by the fit for the baseline setting and σ' is the reported error for the variation. Note that the baseline setting is given by the default event selection used to extract the final results presented in Section 8.1. A significance is then defined for each variation as

$$\frac{\rho - \rho'}{\sigma_B}, \quad (7.2)$$

where ρ is the result extracted using the baseline event selection and ρ' is the result for the specific variation under study. The denominator σ_B accounts for the sample of events shared between the baseline measurement and the measurement performed to obtain ρ' , ensuring that correlations between the two data samples are taken into consideration. According to Barlow, a significance value between 1 and -1 is indicative of an insignificant variation in results. A

value greater than 4 or less than -4 suggests the discrepancy can be explained by a statistically significant systematic effect. One would expect to see a trend of significant values across the analysed $-t$ range if a systematic effect is present. Even if the determined significance values are consistently between 1 and -1, a continuous trend over a large range in $-t$ is still indicative of a systematic effect.

The significance region between 1 and 4 is left to judgement. This introduces a subjective element to the test, whereby a decision needs to be made on the metric adopted for identifying systematic deviations. For this work, significance values of ± 2 define a set of boundaries. When the significance is seen to be consistently outwith these limits, the deviation is accredited to a systematic effect. This benchmark was chosen to be stricter than other GlueX analyses [86, 108], where values of ± 4 were used. However, the statistics available with GlueX for dipion photoproduction are excellent, meaning uncertainties are more likely to be driven by systematic effects. This makes it necessary to adopt a conservative approach towards determining the systematics of the measurement.

7.1.1 Kinematic fit χ^2/NDF cut

The cut on the χ^2/NDF of the kinematic fit (c.f. Section 5.4) is one of the most important cuts applied in the event selection. It was therefore necessary to study the associated systematics very carefully. The baseline cut limit for the χ^2/NDF was 5. Four additional cuts were also studied, two of which were looser and two wider (Table 7.1, setups 1-5). The analysis was then repeated for each of the additional cuts. This was performed over the $0.60 - 0.88 \text{ GeV}/c^2$ range in $M_{\pi\pi}$, for each of the seven E_γ bins individually. The results for the $3.00 - 4.25 \text{ GeV}$ E_γ bin are shown in Figure 7.1.

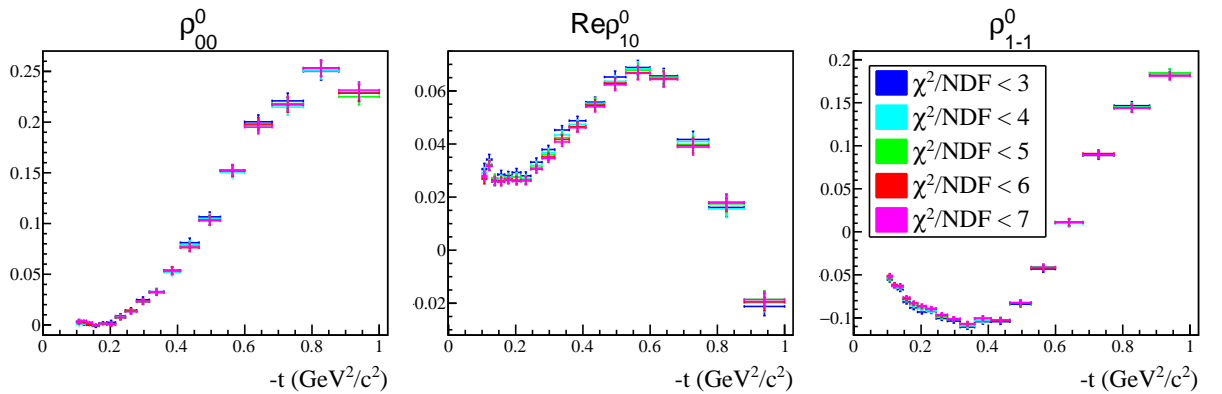


Figure 7.1: SDMEs measured over the $0.60 - 0.88 \text{ GeV}/c^2$ $M_{\pi\pi}$ range for the $3.00 - 4.25 \text{ GeV}$ E_γ bin. The results extracted using a range of χ^2/NDF cuts are shown.

Although the results measured for each cut mostly agree within error bars, it is clear that SDMEs are systematically shifted as the cut is tightened. After performing the Barlow test, the signifi-

ance plot shown in Figure 7.2 is obtained. Systematic shifts are clearly seen in $\text{Re}\rho_{10}^0$ and ρ_{1-1}^0 , where a majority of the tests performed for the tightest χ^2/NDF cut give significance values that are continuously greater than 2 or less than -2. The naive assumption might be that a tighter

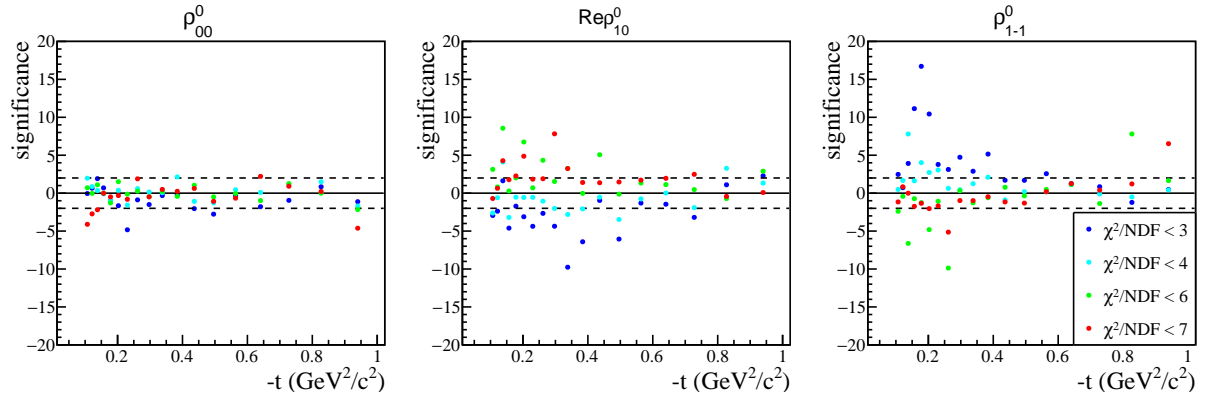


Figure 7.2: The Barlow test significance is plotted for each $-t$ bin and each cut variation for the 3.00 – 4.25 GeV E_γ range. Note that the kinematic fit χ^2/NDF cut significance plots for all of the studied photon energy ranges are included in Appendix A.1.1.

cut on the kinematic fit χ^2/NDF will always improve the final result. One reason why this is untrue is that the modelled detector resolutions are imperfect. Although this is not a significant issue for events with a high χ^2 , the kinematic fitter becomes more sensitive to mismodelled detector resolutions at low χ^2 . Moreover, a subtle disagreement is observed between the χ^2/NDF distributions from reconstructed and simulated data, as demonstrated in Figure 7.3. This may

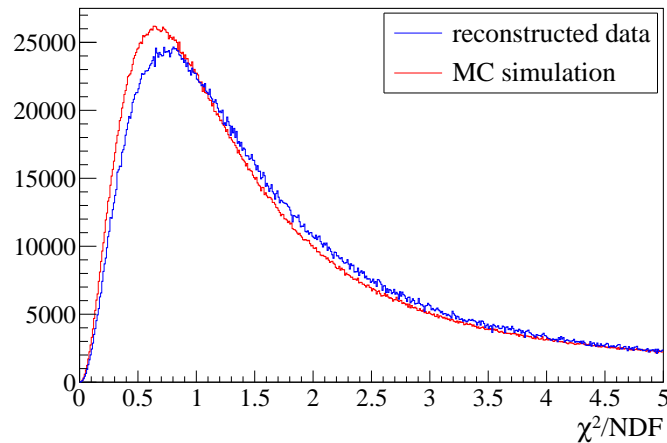


Figure 7.3: Comparison of normalised χ^2/NDF distributions for reconstructed and simulated data over the 3.00 – 4.25 GeV E_γ energy range.

also result from the simulated detector resolutions being slightly inaccurate. Furthermore, the experimentally measured data contains background resonances with an identical final state to the $\rho(770)$ which are not accounted for in the simulation. The agreement between reconstructed and simulated data is seen to improve as χ^2/NDF increases. The discrepancy becomes more

diluted when a wider cut range is used since the overall agreement improves. This could result in stronger systematic effects when cuts at low χ^2/NDF are used, since the acceptance correction may fail due to the poor agreement between reconstructed and simulated data.

Systematic deviations arising from the choice of χ^2/NDF cut limits were seen to become less significant with increasing E_γ . Figure 7.4 summarises the results of the Barlow test for the 9.5 – 11.6 GeV E_γ regime. Although systematic trends are still visible, it is evident that these

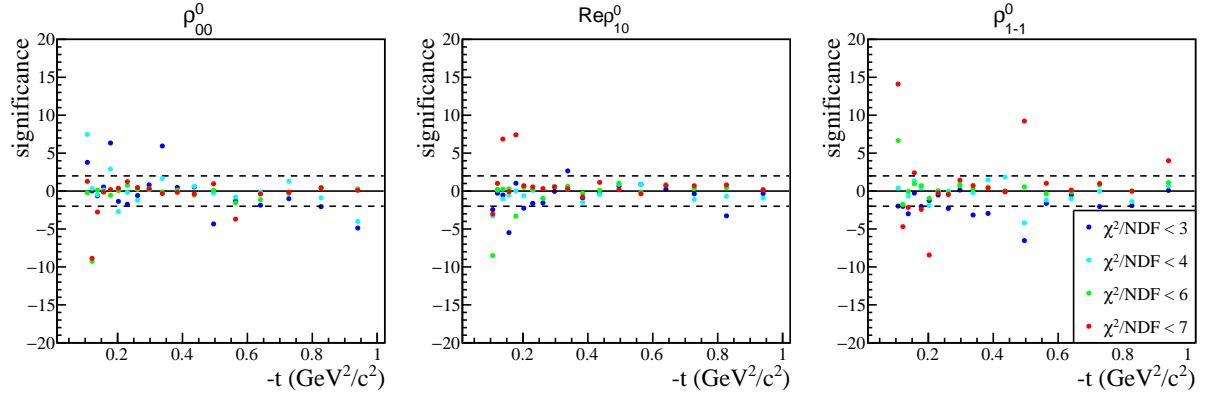


Figure 7.4: The Barlow test significance is plotted for each $-t$ bin and each cut variation for the 9.5 – 11.6 GeV E_γ range.

are no longer statistically significant since the majority of tests give significance values lying between 2 and -2. Although the reason for the observed dependence of the cut stability on E_γ is unknown, it is accounted for by determining systematic uncertainties for each E_γ range independently.

Since the Barlow test shows that there is a systematic effect related to the χ^2/NDF cut, it was necessary to determine the associated systematic uncertainty. This was defined as the standard deviation, σ_{sd} , of results in each $-t$ bin for all cut variations. When σ_B from Equation (7.1) is redefined as

$$\sigma_B = \sqrt{|\sigma^2 - \sigma'^2 - \sigma_{sd}^2|} \quad (7.3)$$

and the significance plot shown in Figure 7.5 is reproduced, most of the systematic deviations become insignificant. This demonstrates that the observed systematic effect is well accounted for by the calculated systematic uncertainties. For this reason, the standard deviation was used as a representation of the systematic uncertainty for each of the cuts that follow whenever a systematic effect is observed.

It was necessary to independently determine the systematic uncertainties for the results presented in Section 8.2 due to the change in binning configuration. The same four cuts (Table 7.1, setups 1-5) were used to perform the Barlow test in each of the $-t$, E_γ and $M_{\pi^+\pi^-}$ bins. Figure 7.6 shows the Barlow significance plotted in the 3.00 – 4.25 GeV E_γ and 0.10 – 0.15 GeV $^2/c^2$ $-t$ regime for each of the four cut variations. A systematic effect is clearly observed, however it

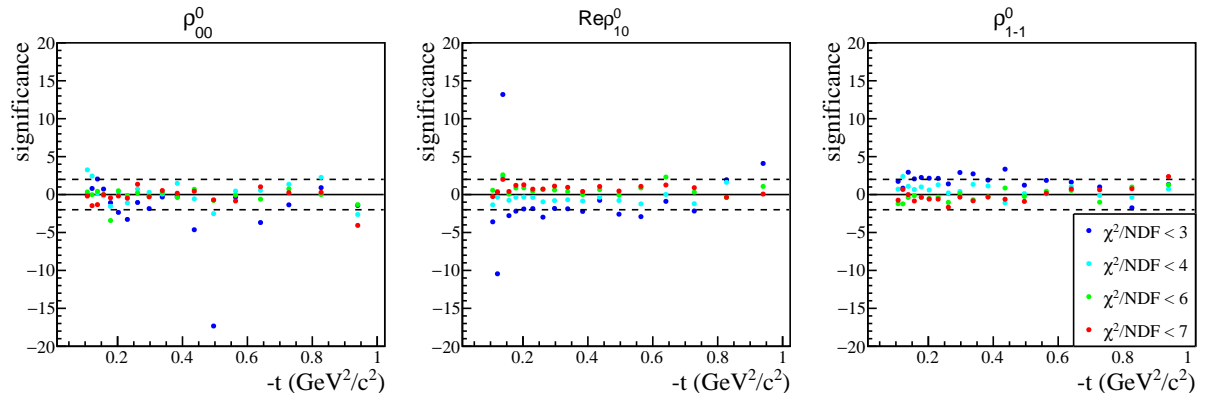


Figure 7.5: The Barlow test significance is plotted for each $-t$ bin and each cut variation for the $3.00 - 4.25$ E_γ range, where the definition of the Barlow significance has been modified to account for systematic uncertainties.

is seen to become less significant for the highest $-t$ bins, as shown in Figure 7.7. The associated systematic uncertainty is determined for the full $-t$ range using the standard deviation as before. It is likely that the observed improvement with increasing $-t$ is a result of lower statistics in the high $-t$ regime, meaning the systematic effect becomes less statistically significant.

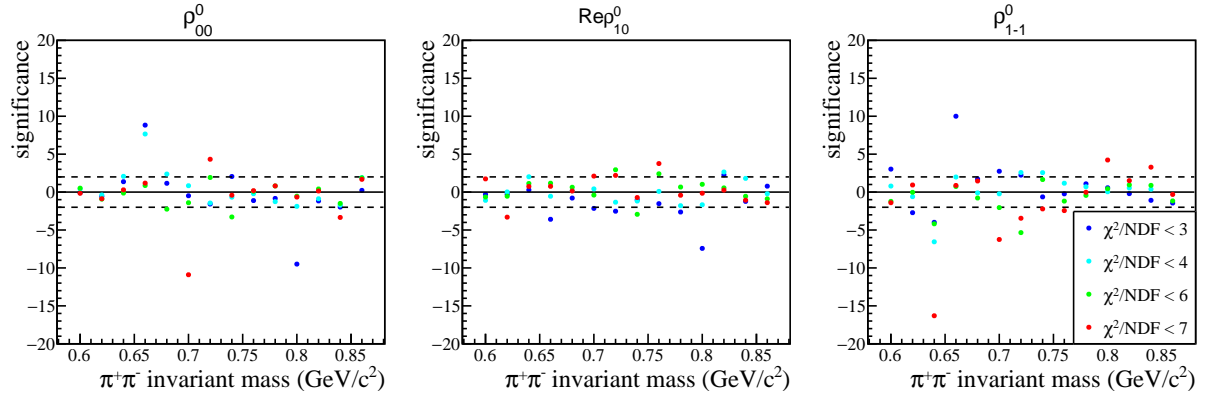


Figure 7.6: The Barlow test significance is plotted for each dipion mass bin and each cut variation for the $3.00 - 4.25$ E_γ and $0.10 - 0.15$ GeV^2/c^2 $-t$ ranges. Note that the kinematic fit χ^2/NDF cut significance plots for all of the studied $-t$ ranges are included in Appendix A.1.2 for the lowest studied photon energy range.

7.1.2 Missing mass squared cut

A loose cut is placed on the missing mass squared of the measured variables. This can be thought of as supplementary to the cut placed on the kinematic fit, which already applies four-momentum conservation constraints. Since it only removes a small number of events, no statistically significant systematic effects were expected. Nevertheless, the Barlow test was performed using two tighter cuts and two looser cuts (Table 7.1, setups 6-10) for each of the studied E_γ ranges. The results for the $3.00 - 4.25$ E_γ regime are summarised in Figure 7.8. Only five data points

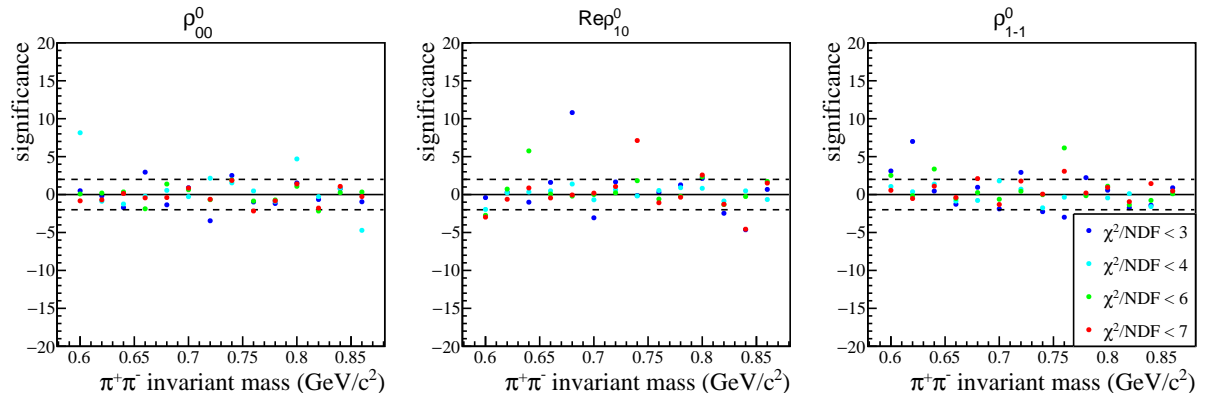


Figure 7.7: The Barlow test significance is plotted for each dipion mass bin and each cut variation for the $3.00 - 4.25 \text{ GeV } E_\gamma$ and $0.68 - 1.00 \text{ GeV}^2/c^2 -t$ ranges.

seem to indicate a systematic effect. Since the remaining data points all have significance values between 2 and -2, it was assumed that the five failed tests were outliers. The missing mass squared cut was seen to be stable over the full $3.0 - 11.6 \text{ GeV } E_\gamma$ range, meaning no contribution from the cut to the overall systematic uncertainty was considered. Similarly, the cut is seen to be stable when the alternative binning scheme is used, over the full $-t$ and E_γ ranges. An example Barlow significance plot for this binning scheme is shown in Figure 7.9.

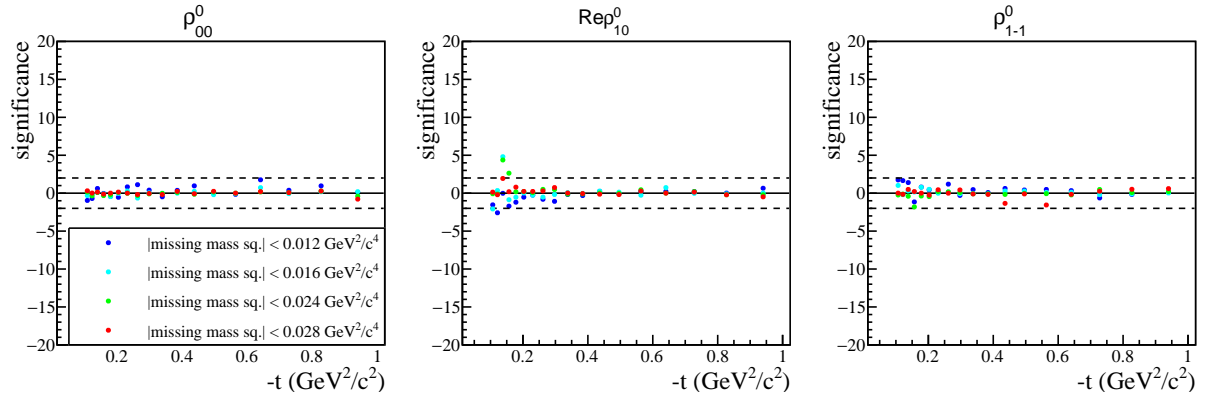


Figure 7.8: The Barlow significance is plotted for each $-t$ bin and each missing mass squared cut variation for the $3.00 - 4.25 \text{ GeV } E_\gamma$ range.

7.1.3 Missing energy cut

The Barlow test was performed to determine the influence of the missing energy cut stability on the SDME extraction. The cut variations shown by setups 12-15 in Table 7.1 were used, two of which were tighter and two of which were looser than the baseline setting of $|E_{\text{miss}}| < 0.5 \text{ GeV}$. The Barlow significance is plotted for the $3.00 - 4.25 \text{ GeV } E_\gamma$ range in Figure 7.10.

A particularly strong systematic effect is observed at low $-t$ for $\text{Re}\rho_{10}^0$ and ρ_{1-1}^0 . Note that similar to the kinematic fit χ^2/NDF cut, the systematic effect become more diluted with increasing

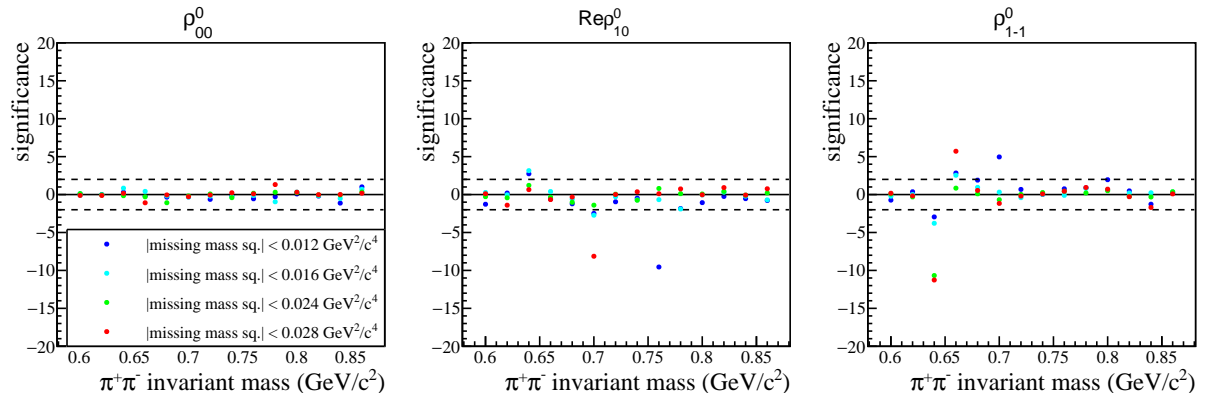


Figure 7.9: The Barlow significance is plotted for each $M_{\pi^+\pi^-}$ bin and each missing mass squared cut variation for the 3.00 – 4.25 $\text{GeV } E_\gamma$ and 0.10 – 0.15 $\text{GeV}^2/c^2 -t$ ranges.

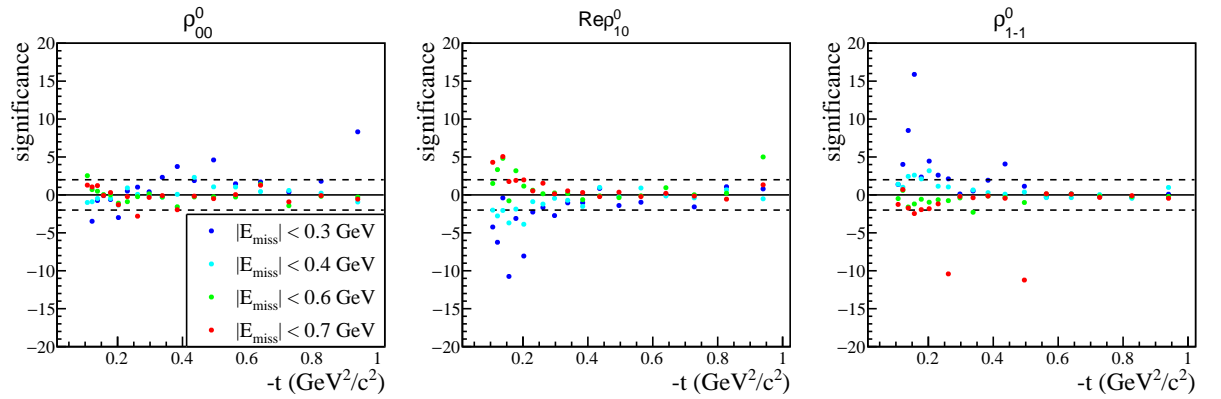


Figure 7.10: The Barlow significance is plotted for each $-t$ bin and each missing energy cut variation for the 3.00 – 4.25 $\text{GeV } E_\gamma$ range. Note that the missing energy cut significance plots for all of the studied photon energy ranges are included in Appendix A.2.1.

E_γ , as demonstrated in Figure 7.11. Nevertheless, a systematic uncertainty associated with the stability of the missing energy cut for each E_γ was determined using the standard deviation as before.

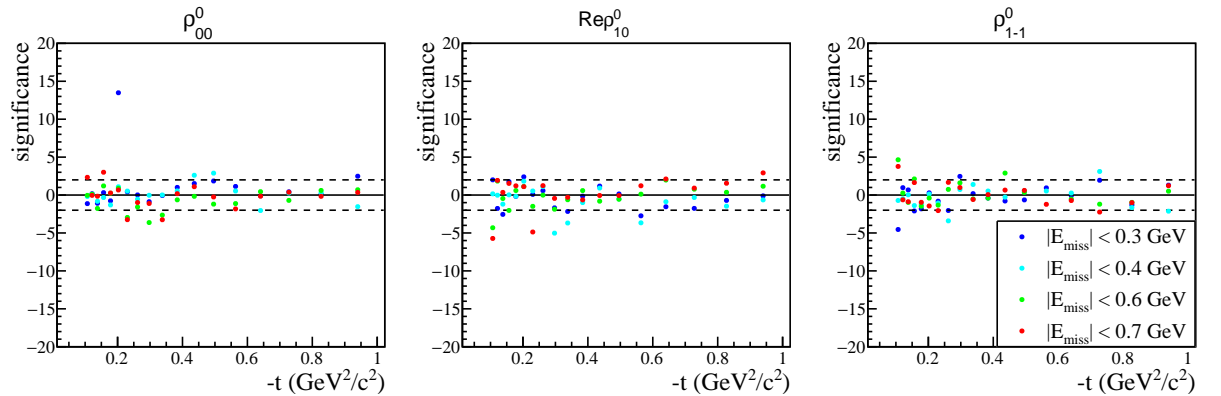


Figure 7.11: The Barlow significance is plotted for each $-t$ bin and each missing energy cut variation for the 9.5 – 11.6 $\text{GeV } E_\gamma$ range.

A systematic effect is also observed when the Barlow test is performed for the binning scheme used in Section 8.2. Figure 7.12 shows the Barlow significance plotted for the 3.00 – 4.25 GeV E_γ and 0.10 – 0.15 GeV $^2/c^2$ $-t$ regime. A series of failed tests originating from the $|E_{miss}| < 0.3$ GeV cut are observed in $\text{Re}\rho_{10}^0$ for a continuous region in $-t$. However, the effect is seen to become statistically insignificant in the 0.68 – 1.00 GeV $^2/c^2$ $-t$ range, as shown in Figure 7.13. Again, this can probably be explained by the poorer statistical precision of measurements performed in the higher $-t$ ranges.

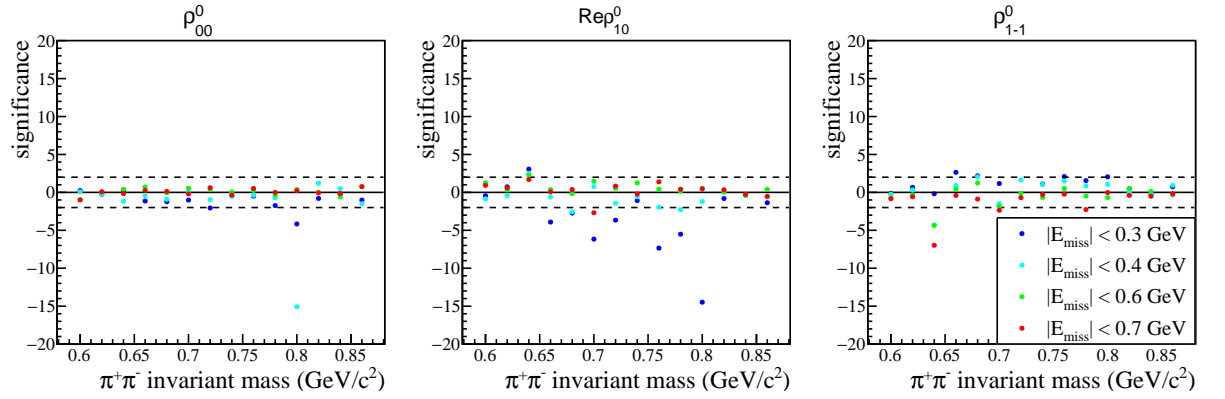


Figure 7.12: The Barlow significance is plotted for each $M_{\pi^+\pi^-}$ bin and each missing energy cut variation for the 3.00 – 4.25 GeV E_γ and 0.10 – 0.15 GeV $^2/c^2$ $-t$ ranges. Note that the missing energy cut significance plots for all of the studied $-t$ ranges are included in Appendix A.2.2 for the lowest studied photon energy range.

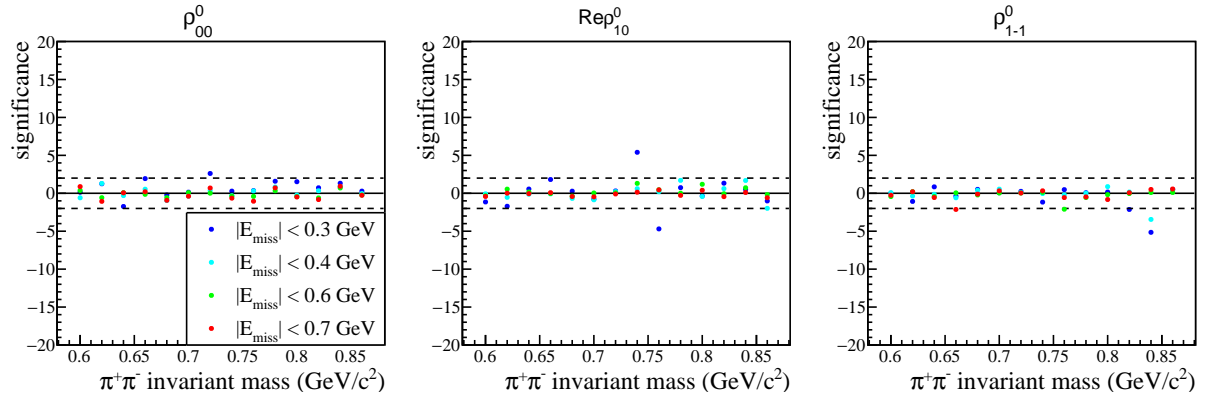


Figure 7.13: The Barlow significance is plotted for each $M_{\pi^+\pi^-}$ bin and each missing energy cut variation for the 3.00 – 4.25 GeV E_γ and 0.68 – 1.00 GeV $^2/c^2$ $-t$ ranges.

7.1.4 Delta mass cut

Although the studied final state predominantly results from $\rho(770)$ mesons decaying to $\pi^+\pi^-$, there are still contributions from baryon resonances that cannot be removed. The primary baryonic contribution comes from the $\Delta^{++}(1232)$ resonance. This background is mitigated by placing a cut on the π^+p invariant mass. The Barlow test is performed using the four cut variations given by setups 16-20 in Table 7.1 to study the systematics associated with this cut. The results for the 3.00 – 4.25 GeV regime in E_γ are shown in Figure 7.14.

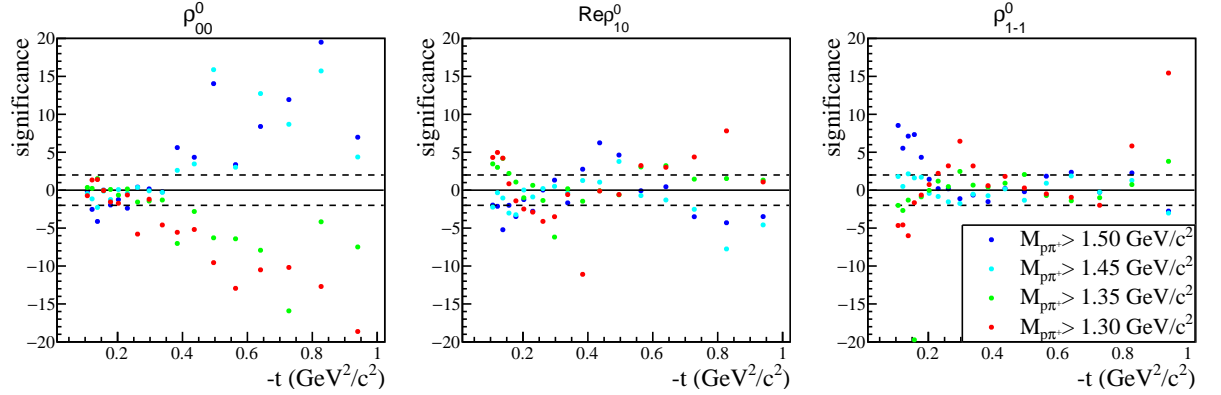


Figure 7.14: The Barlow significance is plotted for each $-t$ bin and each π^+p invariant mass cut variation for the 3.00 – 4.25 GeV E_γ range. Note that the π^+p invariant mass cut significance plots for all of the studied photon energy ranges are included in Appendix A.1.1.

Evidently, the delta mass cut is the dominant source of systematic uncertainty in this photon energy regime. Strong systematic effects are observed in all three SDMEs, where tests give significance values greater than 2 or less than -2 for continuous regions in $-t$. It was therefore necessary to consider the π^+p cut in the overall systematic uncertainty calculation.

It is likely that the observed systematic effect can be explained by contamination from higher mass baryons decaying to π^+p . Figure 7.15 shows the π^+p invariant mass spectrum over the 3.00 – 4.25 GeV E_γ and 0.60 – 1.00 GeV²/c² $-t$ range. A peak originating from Δ^{++} decays is visible at around 1.8 GeV. Note that this peak is most prominent at high $-t$, and a significant reduction in baryon contamination is observed for low $-t$, as shown in Figure 7.15a. This observation is consistent with the systematic effect shown in Figure 7.14 for the ρ_{00}^0 , which becomes stronger with increasing $-t$.

Although the π^+p invariant mass cut is the dominant source of error for low photon energies, Figure 7.16 shows that the observed systematic effect becomes less significant for high E_γ . This is to be expected, since contributions from baryon decays are known to become less significant with increasing E_γ .

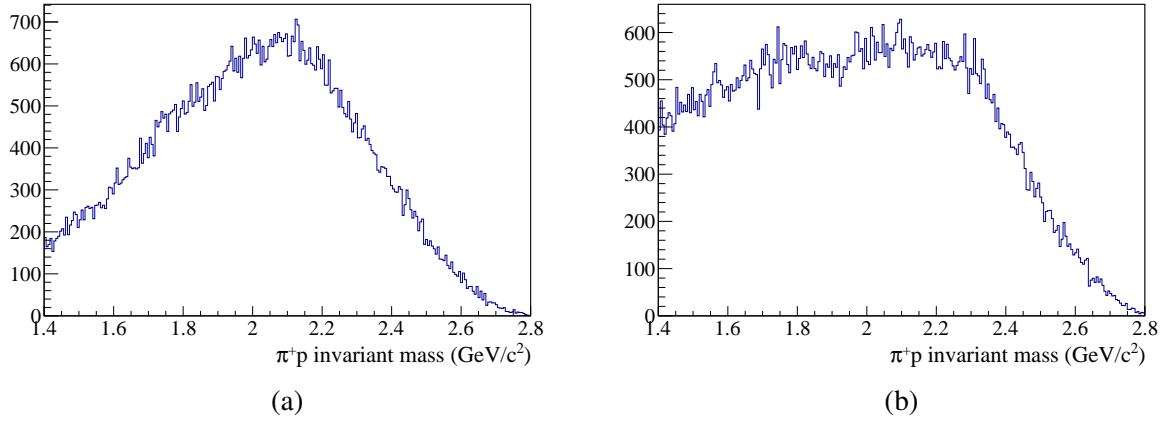


Figure 7.15: Histograms showing the $\pi^+ p$ invariant mass over the 3.00 – 4.25 GeV photon energy regime for the (a) 0.10 – 0.11 GeV^2/c^2 and (b) 0.6 – 1.0 GeV^2/c^2 ranges in $-t$.

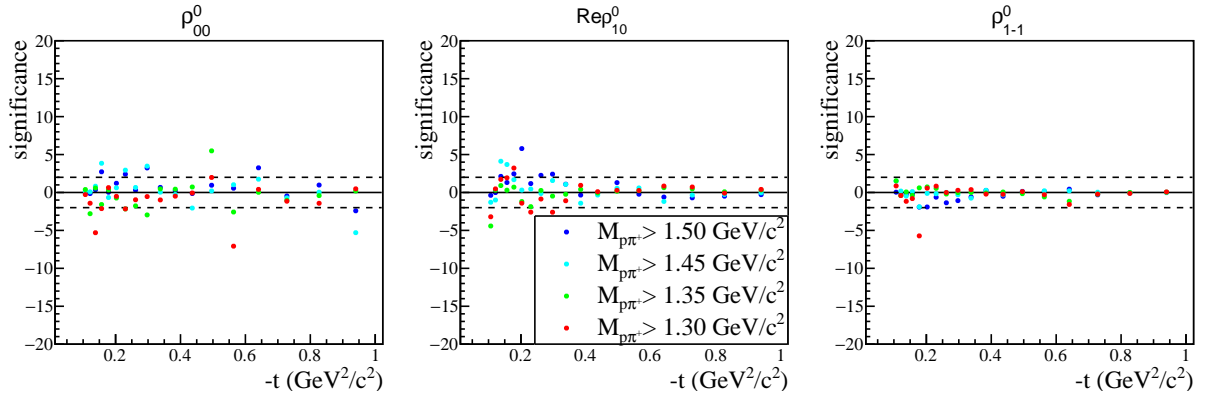


Figure 7.16: The Barlow significance is plotted for each $-t$ bin and each $\pi^+ p$ invariant mass cut variation for the 9.5 – 11.6 GeV E_γ range.

Since the stability of the $\pi^+ p$ mass cut is seen to be highly dependent on $-t$, it was important to study the associated systematics for the third binning scheme shown in Section 5.8, where SDMEs are extracted over six different $-t$ ranges. In Figure 7.17, the Barlow significance is plotted over the 3.00 – 4.25 GeV E_γ and 0.10 – 0.15 GeV^2/c^2 $-t$ regime using the four $M_{\pi^+ p}$ cut variations given by setups 16-20 in Table 7.1. Strong systematic effects are seen in $\text{Re}\rho_{10}^0$ and ρ_{1-1}^0 , but not in ρ_{00}^0 . This is expected, since baryonic contributions are not as strong for low $-t$. The available statistics become poorer for the higher $-t$ bins and the systematic effects observed in $\text{Re}\rho_{10}^0$ and ρ_{1-1}^0 become less statistically significant, as shown in Figures 7.17 and 7.19. However, for the highest $-t$ bins a strong systematic effect emerges in ρ_{00}^0 as shown in Figure 7.19. Here, the tests for the $M_{\pi^+ \pi^-} > 1.5 \text{ GeV}$ and $M_{\pi^+ \pi^-} > 1.3 \text{ GeV}$ cuts fail for prolonged, continuous regions in $M_{\pi^+ \pi^-}$. Again, this is likely to be a result of larger contributions from baryon decays at high $-t$.

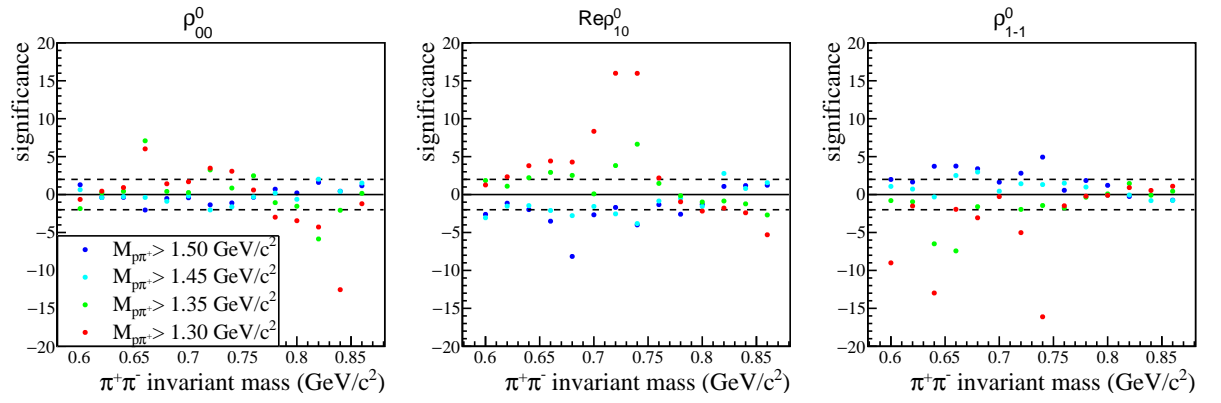


Figure 7.17: The Barlow significance is plotted for each $M_{\pi^+\pi^-}$ bin and each π^+p invariant mass cut variation for the 3.00 – 4.25 GeV E_γ and 0.10 – 0.15 GeV²/c² $-t$ ranges. Note that the π^+p invariant mass cut significance plots for all of the studied $-t$ ranges are included in Appendix A.3.2 for the lowest studied photon energy range.

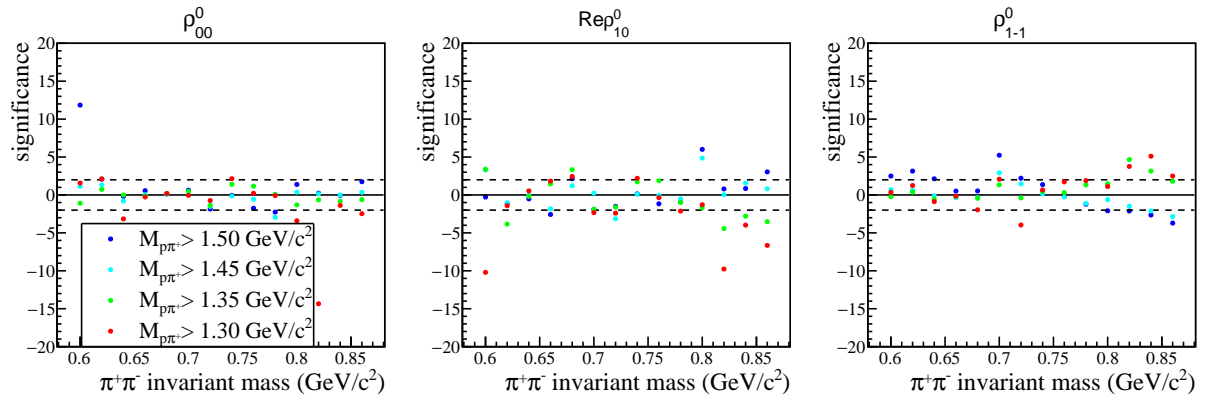


Figure 7.18: The Barlow significance is plotted for each $M_{\pi^+\pi^-}$ bin and each π^+p invariant mass cut variation for the 3.00 – 4.25 GeV E_γ and 0.22 – 0.32 GeV²/c² $-t$ ranges.

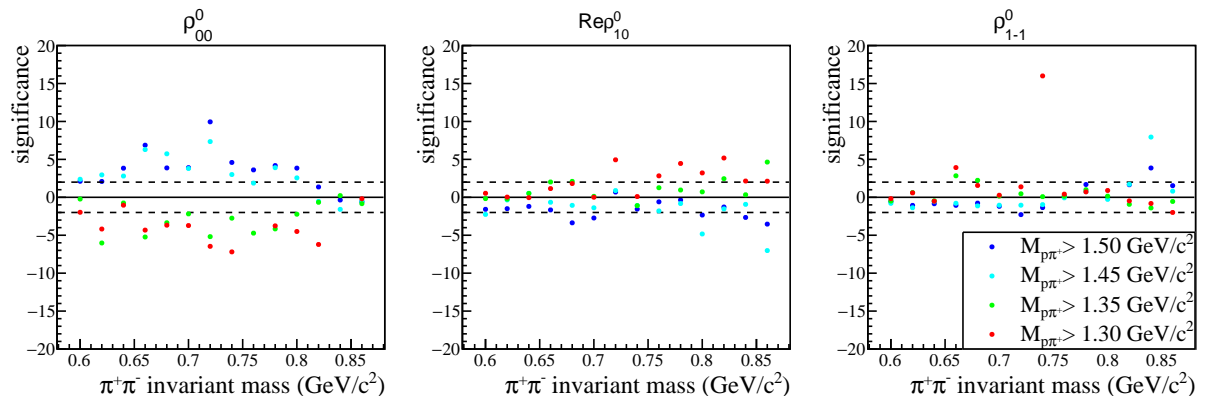


Figure 7.19: The Barlow significance is plotted for each $M_{\pi^+\pi^-}$ bin and each π^+p invariant mass cut variation for the 3.00 – 4.25 GeV E_γ and 0.68 – 1.00 GeV²/c² $-t$ ranges.

7.1.5 Particle identification cut

A restriction is applied on the specific energy loss of the recoil proton in the CDC as a function of its momentum. This limits the possibility of misidentifying a positive kaon. The cut is summarised in Section 5.7.5. This is by far the loosest cut defined in the event selection, and only changes the data by a fraction of a percent. It was therefore not expected to have any significant effect on the systematics. In order to verify this, the SDME extraction was performed over the 3.00 – 4.25 GeV E_γ range using the following cut on the proton energy loss,

$$\frac{dE}{dx} > \exp(4p + 2.25) + 1, \quad (7.4)$$

where p is the recoil proton momentum. This is the cut applied during the data skimming process, and is much looser than the cut defined in Section 5.7.5. The Barlow significance is then plotted for each $-t$ bin, where the baseline setting is defined using the cut from Section 5.7.5. The result is shown in Figure 7.20. As expected, no significant systematic effect is observed and only a single test fails. Since most of the other data points are approximately consistent with zero, this test is assumed to be an outlier.

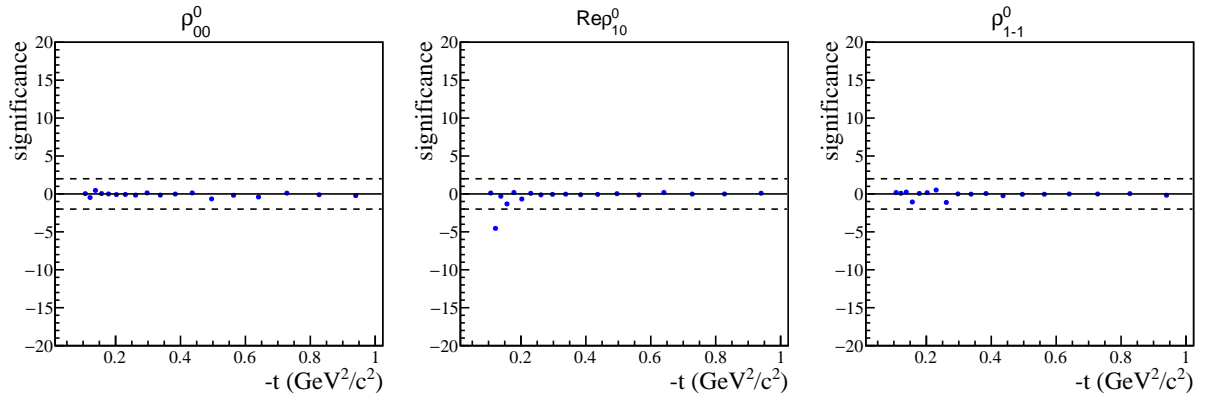


Figure 7.20: The Barlow significance is plotted for each $-t$ bin over the 3.00 – 4.25 GeV E_γ range using a single particle ID cut variation.

7.1.6 Vertex cut

SDMEs were measured in five equally spaced bins spanning the full range of the cut applied on the z co-ordinate of the reaction vertex. The results are summarised in Figure 7.21.

No obvious systematic trends are observed. The pull distributions in Figure 7.22 were formed by calculating the pull for each $-t$ bin and each vertex bin, giving a total of 90 histogram entries for each SDME. The pull is defined as

$$\frac{\rho_{\text{measured}} - \rho_{\text{true}}}{\delta_{\text{measured}}}, \quad (7.5)$$

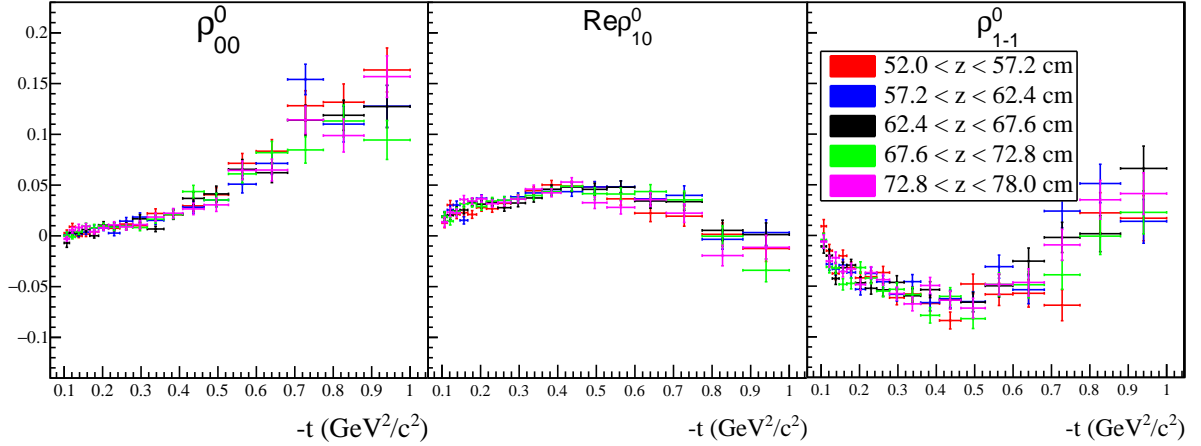


Figure 7.21: SDMEs measured for five bins in the reaction vertex, over the 7.5 – 8.5 GeV E_γ range and 0.60 – 0.88 GeV/ c^2 dipion mass range.

where ρ_{true} is the result measured over the full vertex range, $\rho_{measured}$ is the result measured for a specific vertex bin and $\delta_{measured}$ is the associated statistical uncertainty. Gaussian fits are applied to each of the pull distributions. The widths, σ , are seen to be consistent with 1 for each SDME, while the means are all consistent with 0. This also indicates that there is no contribution to the systematic uncertainty from the stability of the vertex cut.

The Barlow test was also used to diagnose any systematic effects arising from the stability of the chosen vertex cut limits. This was performed for each of the seven E_γ bins. As shown in Figure 7.23, no systematic trends are seen, and a majority of the data points have a figure of merit between 2 and -2 for each of the cut variations indicated in the plot legend. Although a few tests fail, these points are assumed to be outliers. One would expect a systematic effect arising from the cut stability to affect SDMEs over a continuous region in $-t$. However, most of the failed tests seem to occur in isolated $-t$ bins, while the nearest neighbours exhibit significance values lying between -2 and 2. The cut is also seen to be stable when the Barlow test is performed for the alternative binning scheme presented in Section 5.8 across each of the studied E_γ and $-t$ ranges and over the majority of $M_{\pi^+\pi^-}$ bins.

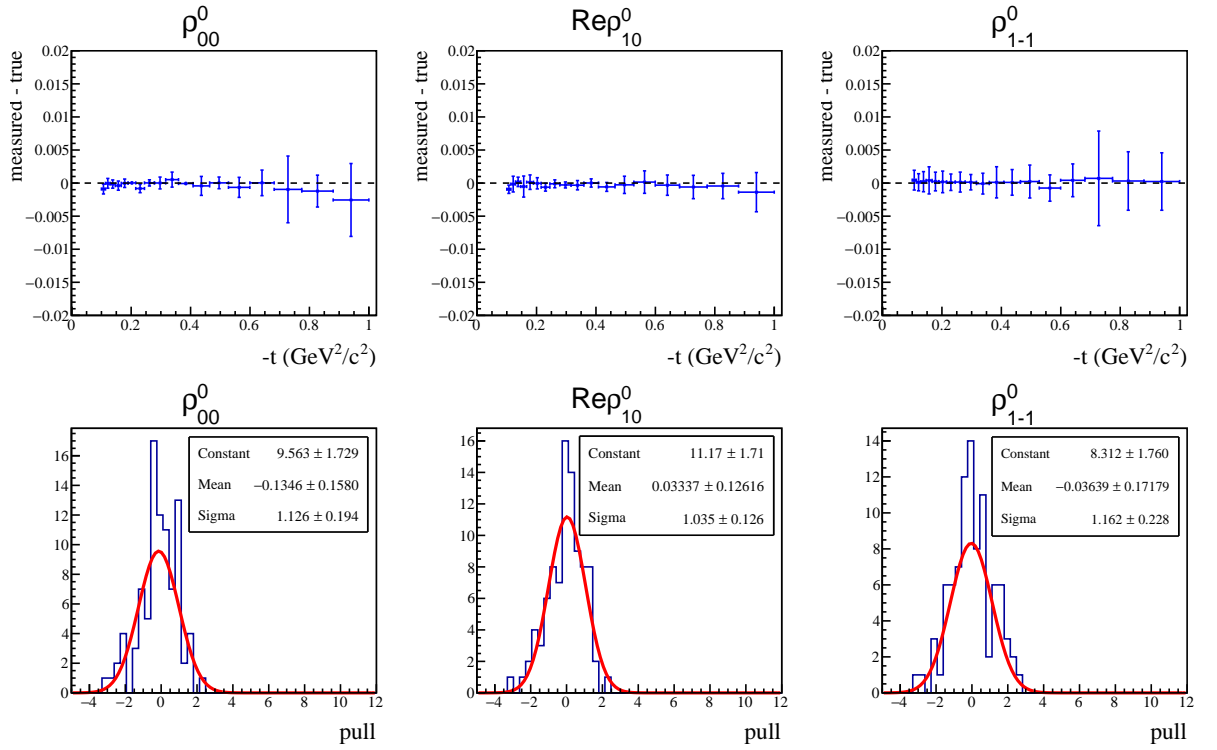


Figure 7.22: Summary of study with SDME fits binned in the reaction vertex. ‘measured - true’ is the mean difference between the results extracted over the full z cut range and the results extracted in each of the five z bins. The error bars are given by the standard deviation of the mean difference.

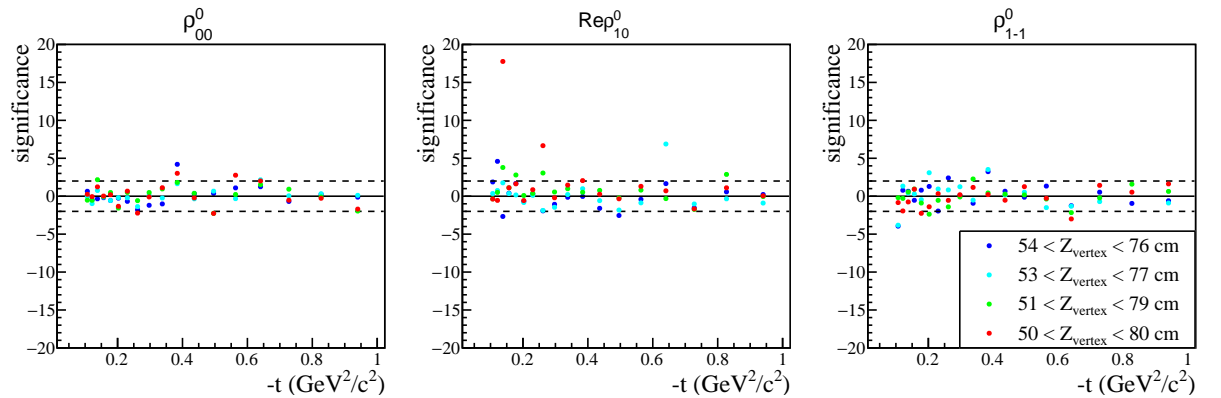


Figure 7.23: The Barlow significance is plotted for each $-t$ bin and each vertex cut variation for the $3.00 - 4.25 \text{ GeV } E_\gamma$ range.

7.2 Validation of results

Studies of toy data were performed to validate the final results and statistical uncertainties presented in Chapter 8. Large samples of Monte Carlo data corresponding to the $p\pi^+\pi^-$ final state were generated with flat angular dependence for each of the eighteen $-t$ ranges used to perform SDME fits. These samples were passed through the full `hdgeant4` simulation, ensuring that detector resolution and acceptance effects were correctly modelled. The $\pi^+\pi^-$ invariant

mass distribution for each $-t$ bin was modelled with a Breit-Wigner signal distribution, with a mean of $0.757 \text{ GeV}/c^2$ and a width of $0.146 \text{ GeV}/c^2$. The $-t$ distribution was modelled with an exponential curve of the form e^{-bt} , where a $-t$ slope parameter of $b = 6 \text{ c}^2/\text{GeV}^2$ was used. Although the generated $-t$ distribution did not perfectly match what was observed experimentally (c.f. Figure 7.24), it serves as a good approximation when binning finely in $-t$.

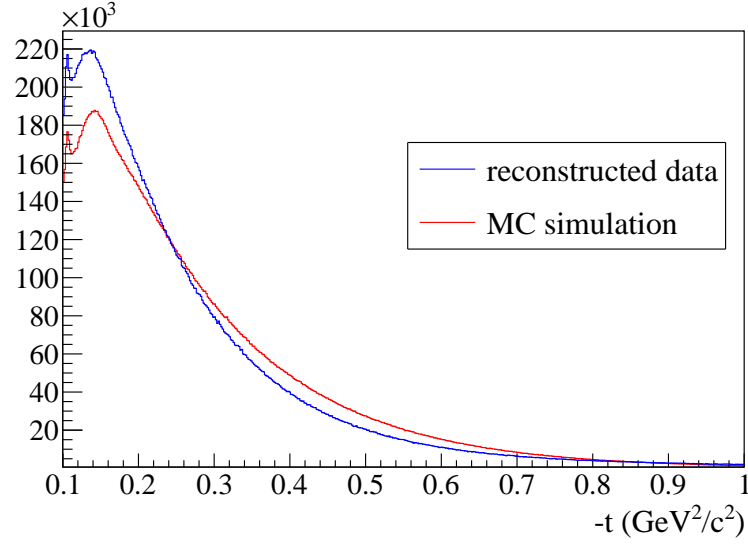


Figure 7.24: Comparison of $-t$ distributions observed in reconstructed and simulated data (normalised).

SDMEs were imposed on the flat simulated data on an event-by-event basis using a modified version of Equation (2.31), given by

$$W^0(\cos \theta, \phi) = \frac{t_i}{N} \frac{3}{4\pi} \left(\left(\frac{1}{2}(1 - \rho_{00}^0) + \frac{1}{2}(3\rho_{00}^0 - 1)\cos^2 \theta - \sqrt{2}\text{Re} \rho_{10}^0 \sin 2\theta \cos \phi - \rho_{1-1}^0 \sin^2 \theta \cos 2\phi \right) \right), \quad (7.6)$$

where t_i is the timing weight associated with the i^{th} event, used to subtract the background of random tagger coincidences (c.f. Section 5.7.1), N is a normalisation factor, and all other symbols have the same meanings as those defined in Section 2.2.1. The values for the SDMEs defined in Equation (7.6) were inferred from measurements performed on experimental data (c.f. Section 8). The values for W^0 calculated for each event were then used to define the acceptance probability for a rejection sampling algorithm. This involved generating a random number between 0 and 1 using the Mersenne Twister 19937 generator [109] from the C++ standard library. The event was then rejected if the generated number was greater than the value calculated for W^0 . Figure 7.25 compares the θ and ϕ distributions in the resulting toy data with the corresponding distributions observed in experimental data. The toy model clearly does a good job of reproducing the experimentally measured distributions.

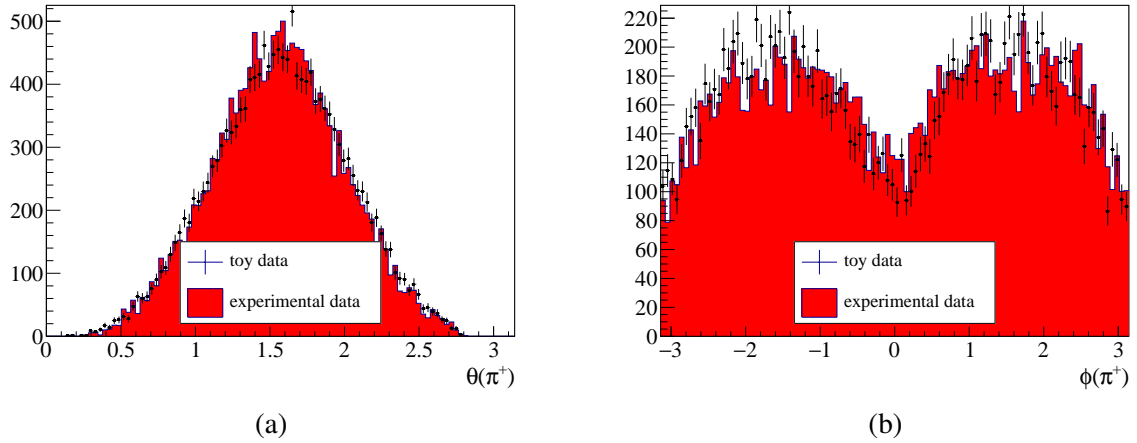


Figure 7.25: Comparison showing normalised θ (a) and ϕ (b) distributions from experimental and toy data over the $0.10 - 0.11 \text{ GeV}^2/c^2$ range in $-t$.

The toy data and original flat Monte Carlo samples were divided into between 100 and 500 statistically independent samples depending on the $-t$ bin. It was ensured that the number of events in each sample was approximately the same as both what was determined from experimental data, and what was used for the acceptance correction in the final analysis. Since it was necessary to ensure the statistics were consistent with the experimental and simulated data used for the final SDME extraction, generating a large enough amount of Monte Carlo to study the full photon energy and $\pi^+\pi^-$ invariant mass range would not have been feasible. As such, Monte Carlo was only generated over the $6.5 - 7.5 \text{ GeV}$ range in the photon energy and $0.60 - 0.66 \text{ GeV}/c^2$ range in the dipion invariant mass to provide a representative study.

Toy data were then treated in the exact same way as experimental data to perform over one hundred independent toy SDME fits for each $-t$ bin, where the acceptance correction was applied in each fit using the flat Monte Carlo samples. The resulting pull was calculated for each individual SDME from each fit as

$$\text{pull} = \frac{\text{measured } \rho - \text{true } \rho}{\Delta(\text{measured } \rho)}, \quad (7.7)$$

where Δ denotes the uncertainty reported by the fit. This made it possible to produce pull distributions for each of the studied $-t$ bins and each of the three SDMEs. Pull distributions were fitted with Gaussian functions and the means and widths were extracted, as shown in Figure 7.26. One would expect pull distributions to be centred on 0 if there is no intrinsic bias associated with the fitting procedure. Similarly, one would expect the extracted widths to be consistent with 1 for normally distributed statistical uncertainties that have been correctly propagated. A width greater (less) than 1 implies that statistical uncertainties have underestimated (overestimated).

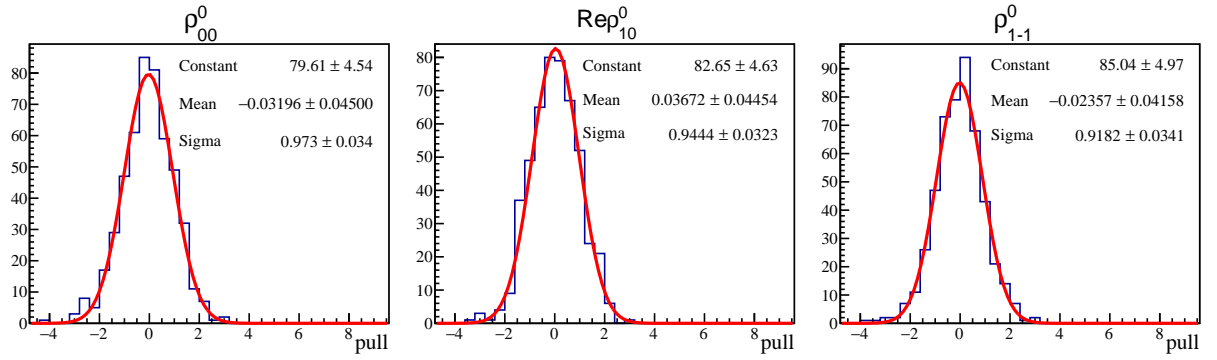


Figure 7.26: Pull distributions determined from toy studies over the $0.28 - 0.32 \text{ GeV}^2/c^2$ range in $-t$. Gaussian fits are denoted by the red lines. The final parameters reported by the fit are also indicated for each SDME.

Figure 7.27 shows the final extracted Gaussian mean plotted for each $-t$ bin, where the error bars were inferred from the results of each of the associated Gaussian fits. The systematic uncertainties determined from the cut stability studies presented in the previous section are shown by the faint blue bands. The errors calculated for each of the three unstable cuts are summed in quadrature and expressed in units of $\Delta(\text{measured } \rho)$, the statistical uncertainty reported by the fit in each $-t$ bin. The majority of the plotted means are consistent with 0. Although discrepancies are exhibited by a few data points in the $-t > 0.7 \text{ GeV}^2/c^2$ and $-t < 0.26 \text{ GeV}^2/c^2$ regions, these shifts are relatively small considering the magnitude of the statistical uncertainties. The errors originating from the three unstable cuts (missing energy, kinematic fit χ^2/NDF and $\pi^+ p$ invariant mass) are generally seen to be the dominant source of systematic uncertainty. It is not surprising that pull means are shifted from 0 in the low $-t$ regime, where statistical uncertainties are much smaller and the calculated pull is more sensitive to subtle systematic effects. Similar to what was found in the previous section, ρ_{1-1}^0 is seen to be the SDME with the smallest associated systematic uncertainty.

Figure 7.28 shows the pull widths plotted for each $-t$ bin. The extracted widths were generally seen to be slightly larger than 1, indicating that the statistical uncertainties were underestimated. This could originate from the statistics in the flat Monte Carlo samples used to perform acceptance corrections, which were not accounted for in the calculation of statistical uncertainties. However, the effect is seen to be very small, and it was decided that a re-calculation of the uncertainties would not be necessary.

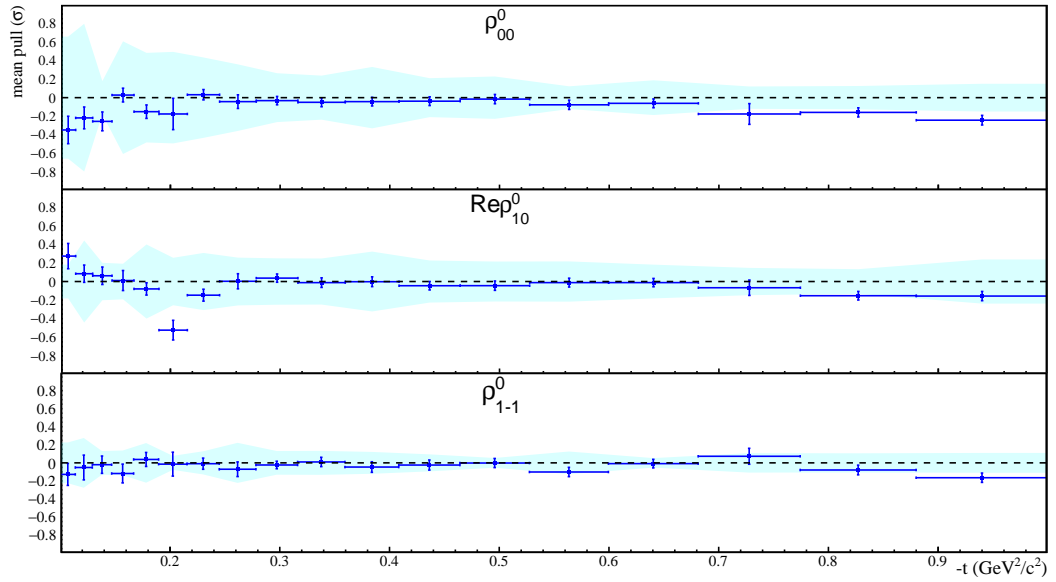


Figure 7.27: Means extracted from pull distributions for each SDME and each $-t$ bin. The systematic uncertainties derived from the cut stability studies presented in Section 7.1 are denoted by the faint blue band.

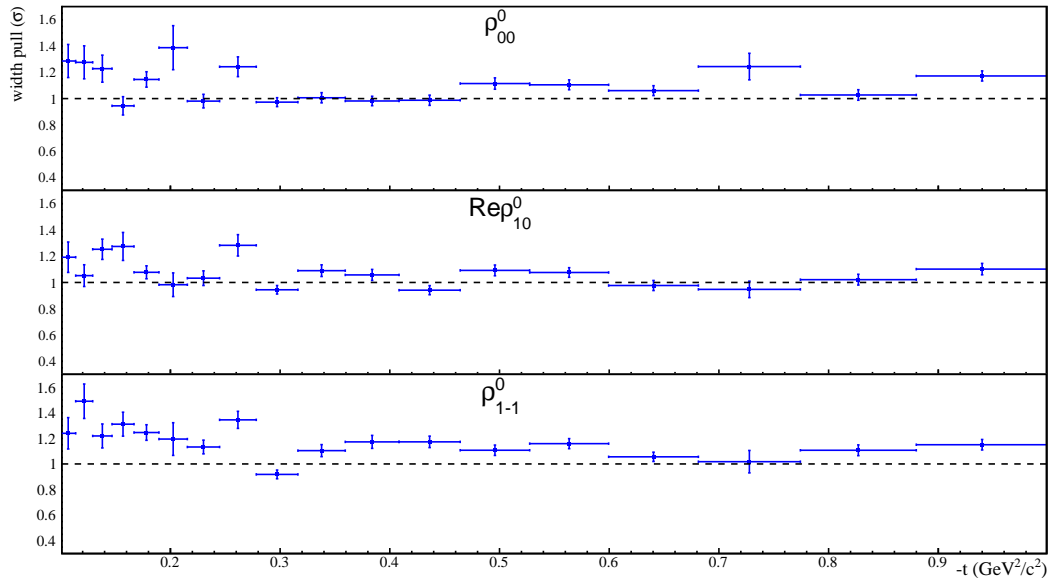


Figure 7.28: Widths extracted from pull distributions for each SDME and each $-t$ bin.

7.3 Summary

The studies presented in this chapter made it possible to estimate the systematic uncertainties associated with final results. The magnitude of systematic errors were seen to be dependent on both the photon energy and $-t$. The dominant systematic error was seen to originate from the stability of the chosen limits for three of the cuts described in Section 5.7. The largest systematic uncertainty at low beam energies originated from the $p\pi^+$ invariant mass cut, however the contribution from this cut to the overall uncertainty was seen to become less significant

at higher photon energies where there is a cleaner kinematic separation between baryons and mesons. There were also systematic effects associated with the missing energy and kinematic fit cuts. Since the kinematic fit applies energy conservation constraints to remove the background of misidentified final states, it is likely that the effects observed for these two cuts are correlated. Although there was a small error contribution associated with the overall fitting procedure, as demonstrated in Section 7.2, this was generally seen to be insignificant when compared with the systematic uncertainty from the cut stability. The ρ_{00}^0 was seen to be the most sensitive of the three SDMEs to systematic effects, while the ρ_{1-1}^0 had the smallest associated systematic error. The reason for this is still unknown. It is encouraging to note that in most cases, the calculated systematic errors were either smaller or similar in magnitude to the statistical uncertainties. In the next chapter, the SDMEs extracted using various binning configurations are presented along with the associated statistical uncertainties.

Chapter 8

Results

In the following, the SDMEs extracted using each of the three binning schemes detailed in Section 5.8 are presented. In the first binning scheme SDME fits are performed in eighteen logarithmically spaced bins in $-t$ over the $0.60 - 0.88 \text{ GeV}/c^2$ range in the $\pi^+\pi^-$ invariant mass, split into seven sub ranges in the photon energy. The second binning scheme is similar to the first, the only difference being that data are also divided into seven sub ranges in the $\pi^+\pi^-$ invariant mass. The measurements performed using these two schemes are presented in Section 8.1. Results from the final binning scheme are shown in Section 8.2, where SDME fits are performed in fourteen equally spaced bins in the $\pi^+\pi^-$ invariant mass and the data are split into six sub ranges in $-t$ and seven sub ranges in the photon energy. Comparisons with results measured in different experiments are included, and a comparison with the prediction of the JPAC theoretical model for $\rho(770)$ photoproduction is also shown. Moreover, a comparison with polarised SDMEs measured with GlueX over the $8.2 - 8.8 \text{ GeV}$ photon energy range is presented to reinforce the viability of the analysis presented in this thesis.

The results obtained using each of the three binning schemes are available in tabulated format on request from the author (j.fitches.1@research.gla.ac.uk), or from the following members of the Glasgow Nuclear and Hadron Physics group who also participated in this work; Derek Glazier (derek.glazier@glasgow.ac.uk), Peter Hurck (peter.hurck@glasgow.ac.uk) and Kenneth Livingston (kenneth.livingston@glasgow.ac.uk).

8.1 $-t$ dependence

Figures 8.1 to 8.3 show SDMEs measured over the $0.60 - 0.88 \text{ GeV}/c^2$ $\pi^+\pi^-$ invariant mass range for seven sub-ranges in photon energy spanning the full GlueX beam energy range of $3.0 - 11.6 \text{ GeV}$. SDMEs are extracted in eighteen logarithmically spaced bins in $-t$. All of the plotted uncertainties are statistical, originating from the width of posterior distributions in

MCMC fits. The systematic uncertainties are plotted separately in Figures 8.4 to 8.6. All results are in good agreement with earlier SLAC measurements [50], even though the beam energy regimes that were studied are not entirely consistent with what was used in this analysis. Moreover, the statistical precision of the GlueX measurement is clearly superior to that of SLAC.

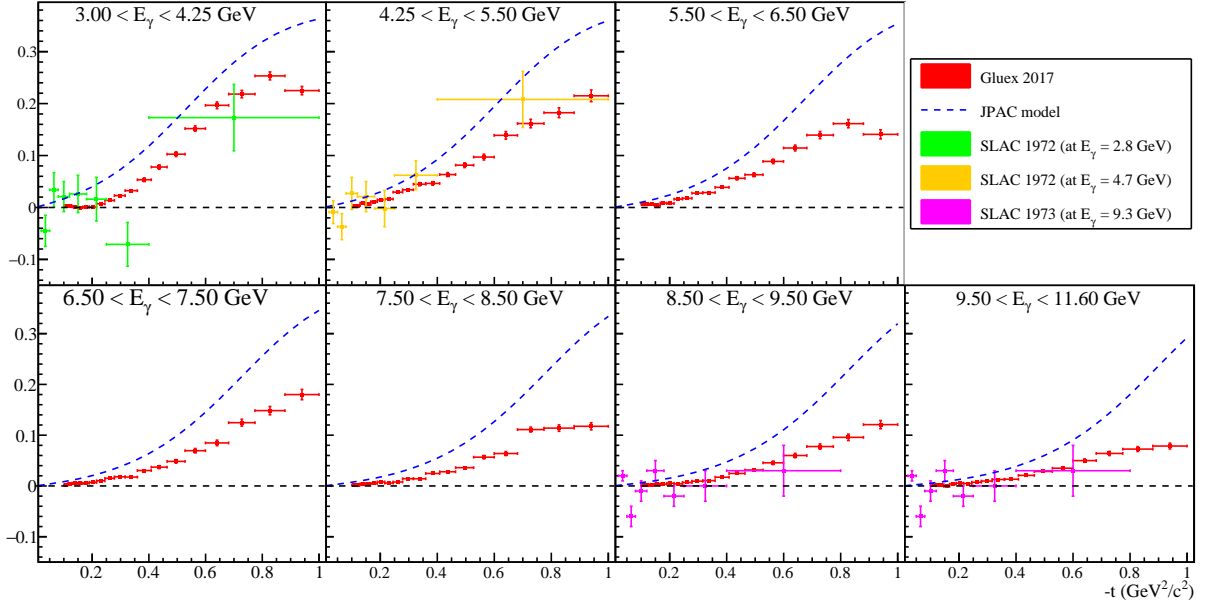


Figure 8.1: ρ_{00}^0 measured in eighteen logarithmically spaced bins in $-t$ over the $0.60 - 0.88 \text{ GeV}/c^2$ $\pi^+\pi^-$ invariant mass range. Results are presented for various beam energy regimes. SLAC measurements [50] of $\rho(770)$ SDMEs are also included for the relevant energy ranges, and the prediction of the current JPAC model [53] for the $\rho(770)$ is shown by the dashed blue line.

The results suggest an agreement with the model of s-channel helicity conservation in the limit of small $-t$. Deviations from s-channel helicity conservation are predicted by Regge theory [53]. These are accounted for in the JPAC model for $\rho(770)$ photoproduction. The prediction of the JPAC model is also shown in Figures 8.1 to 8.3, and the SDMEs measured with GlueX follow the predicted deviations from zero up to around $-t = 0.4 \text{ GeV}^2/c^2$. The prediction of the JPAC model becomes invalid above this point since it uses an expansion in powers of $\sqrt{-t}/m_V$ where $m_V = 0.77 \text{ GeV}/c^2$ is the mass of the vector meson. It should be noted that the JPAC curves are obtained from Regge fits to the SLAC data, not to the SDME measurements presented in this thesis. Predictions are obtained at photon energies that differ from the energy regimes studied by SLAC through extrapolation.

The extracted SDMEs are seen to have more structure at low beam energies, and become flatter as the beam energy increases. This is expected, since the contribution from the pomeron exchange becomes more significant as the photon energy increases. The pomeron exchange is helicity non-flip, which dilutes deviations from s-channel helicity conservation driven by other production mechanisms.

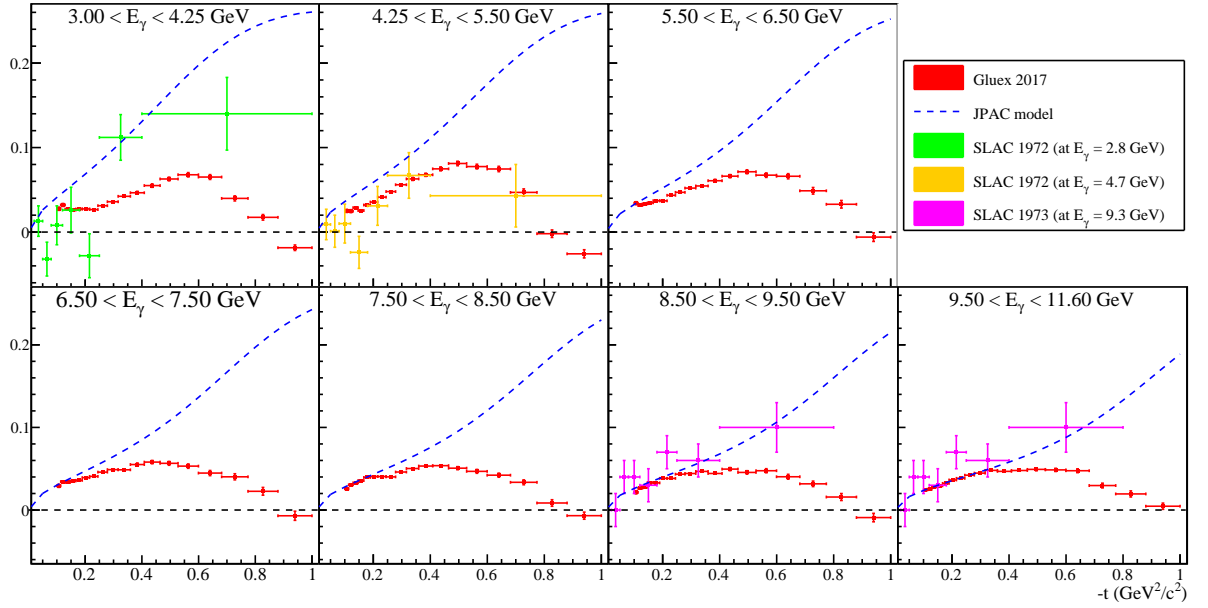


Figure 8.2: $\text{Re} \rho_{10}^0$ measured in eighteen bins in $-t$ over the $0.60 - 0.88 \text{ GeV}/c^2$ $\pi^+\pi^-$ invariant mass range.

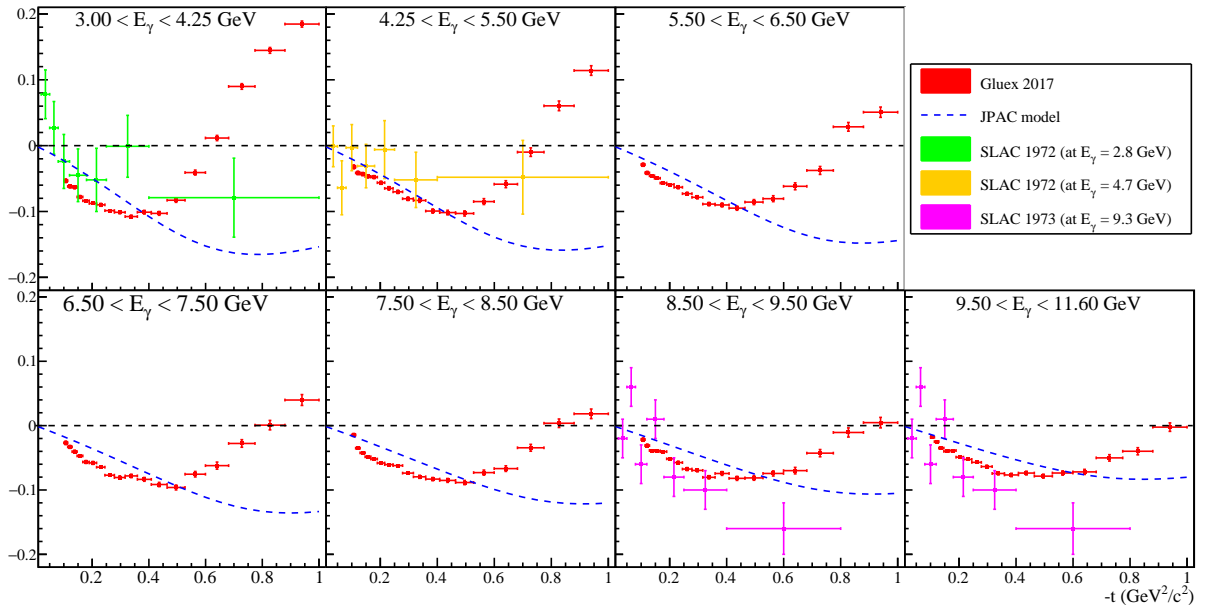


Figure 8.3: ρ_{1-1}^0 measured in eighteen bins in $-t$ over the $0.60 - 0.88 \text{ GeV}/c^2$ $\pi^+\pi^-$ invariant mass range.

Figures 8.4 to 8.6 show the systematic uncertainties associated with the results presented in Figures 8.1 to 8.3. The systematic errors were inferred from the cut stability studies outlined in Section 7.1, since the dominant error was seen to originate from the stability of the chosen cut limits. The systematic uncertainties calculated for each of the three unstable cuts (kinematic fit χ^2/NDF , $p\pi^+$ invariant mass, missing energy) were summed in quadrature. Some of these errors, particularly from the missing energy and kinematic fit cuts, are likely to be correlated.

Combining the three contributions in quadrature is therefore not entirely valid, so it should be noted that the systematic uncertainties plotted in Figures 8.4 to 8.6 are included for visualisation purposes only.

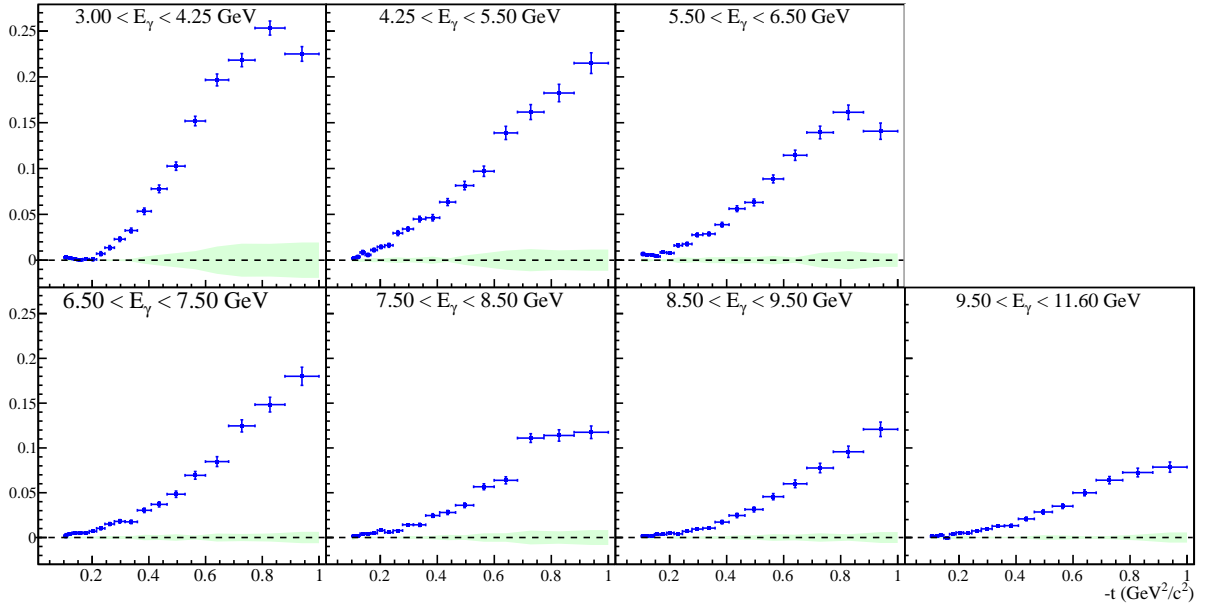


Figure 8.4: ρ_{00}^0 measured in eighteen bins in $-t$ over the $0.60 - 0.88 \text{ GeV}/c^2$ $\pi^+\pi^-$ invariant mass range. The estimated systematic uncertainty is denoted by the light green band.

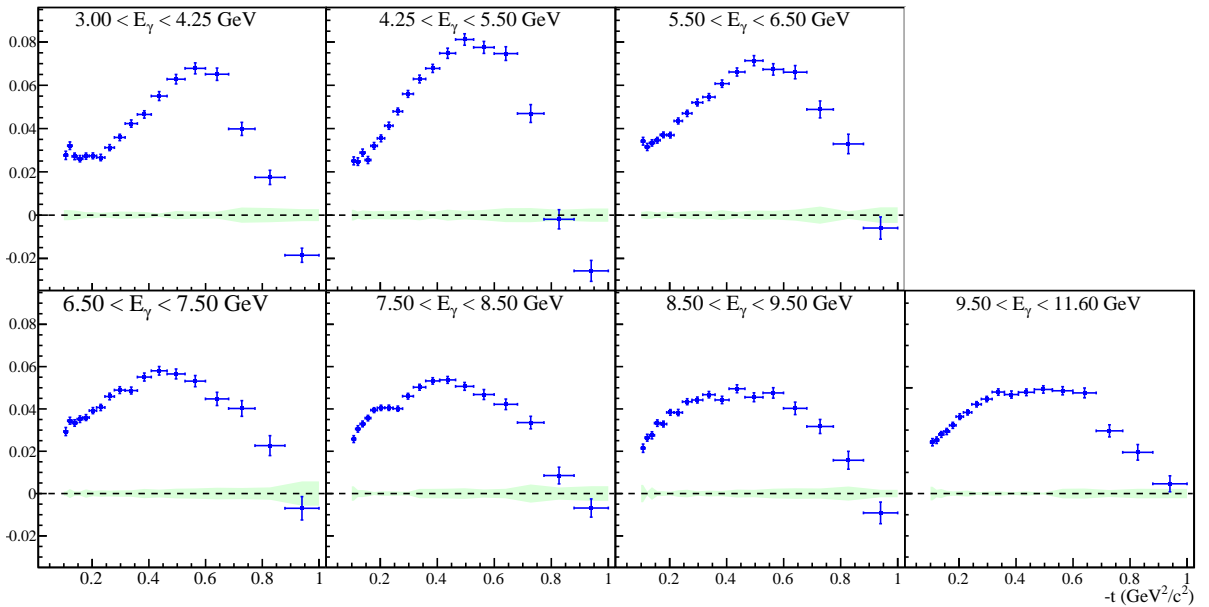


Figure 8.5: $\text{Re} \rho_{10}^0$ measured in eighteen bins in $-t$ over the $0.60 - 0.88 \text{ GeV}/c^2$ $\pi^+\pi^-$ invariant mass range. The estimated systematic uncertainty is denoted by the light green band.

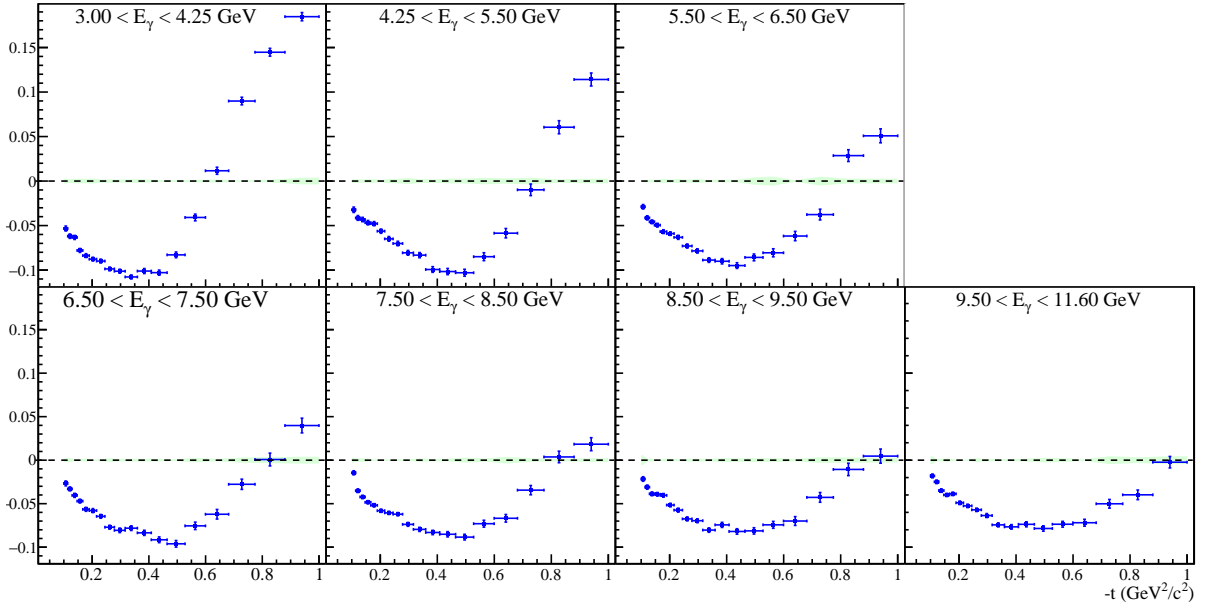


Figure 8.6: ρ_{1-1}^0 measured in eighteen bins in $-t$ over the $0.60 - 0.88 \text{ GeV}/c^2$ $\pi^+\pi^-$ invariant mass range. The estimated systematic uncertainty is denoted by the light green band.

ρ_{00}^0 has the largest systematic uncertainty. This uncertainty is dependent on the reaction kinematics, where errors are larger at low energy and high $-t$. This is expected, since this kinematic region suffers the largest contribution from baryon backgrounds. This results in a large systematic error originating from the π^+p invariant mass cut, which was designed to remove Δ^{++} decays. $\text{Re}\rho_{10}^0$ and ρ_{1-1}^0 are less sensitive to variations in the cut limits. The systematics associated with these SDMEs are seen to be generally independent of the reaction kinematics.

Figures 8.7 to 8.13 show the SDMEs extracted in the same seven beam energy sub-ranges, using the same binning scheme in $-t$. Measurements are also performed in seven different $\pi^+\pi^-$ invariant mass bins spanning the $0.60 - 0.88 \text{ GeV}/c^2$ mass range. The measured results are seen to be strongly dependent on the $\pi^+\pi^-$ invariant mass. This mass dependence is discussed in more detail in Section 8.2.

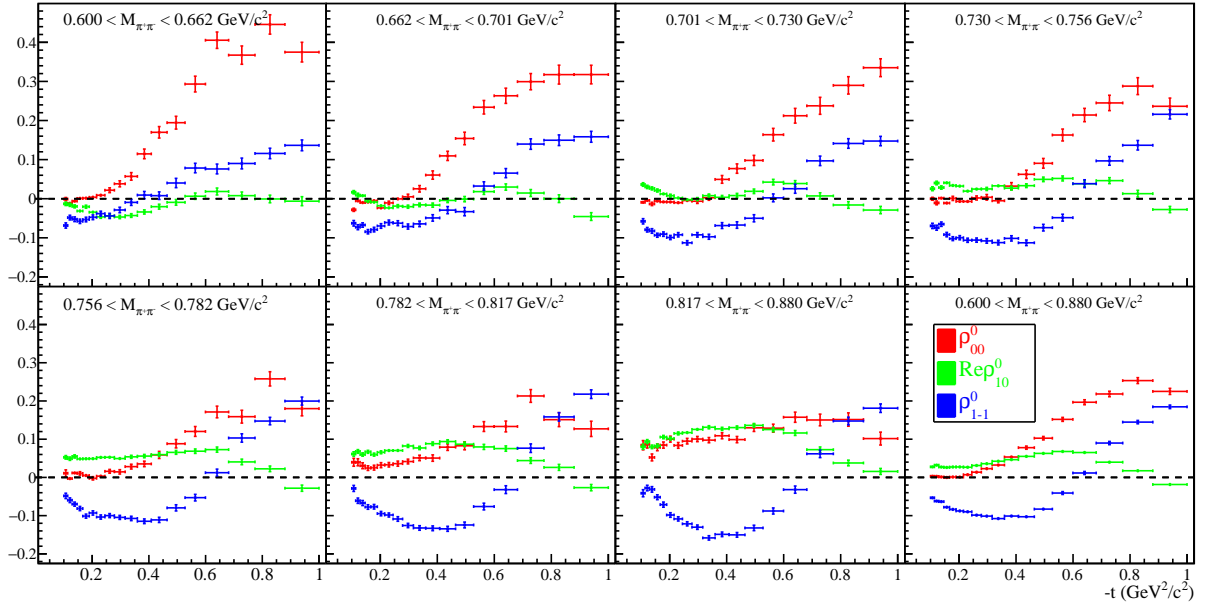


Figure 8.7: All three SDMEs are plotted in eighteen bins in $-t$ and seven sub-ranges of the $\pi^+\pi^-$ invariant mass over the 3.00 – 4.25 GeV beam energy range. Note that the bottom right plot shows the SDMEs extracted over the full 0.60 – 0.88 GeV/ c^2 dipion mass range.

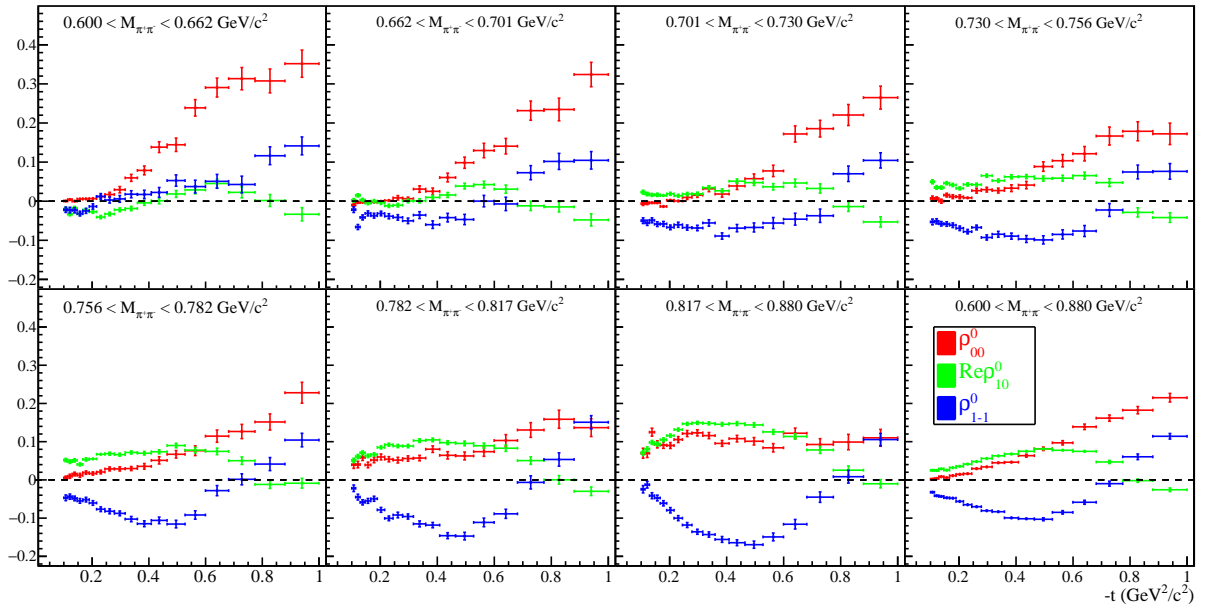


Figure 8.8: All three SDMEs are plotted in eighteen bins in $-t$ and seven sub-ranges of the $\pi^+\pi^-$ invariant mass over the 4.25 – 5.50 GeV beam energy range.

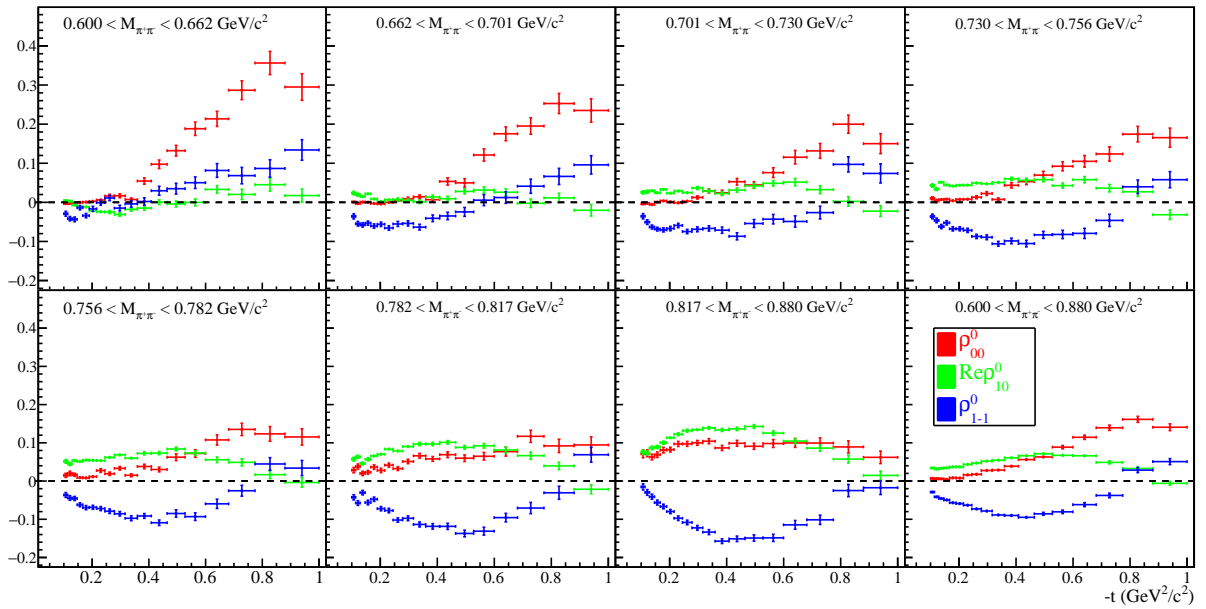


Figure 8.9: All three SDMEs are plotted in eighteen bins in $-t$ and seven sub-ranges of the $\pi^+\pi^-$ invariant mass over the 5.5 – 6.5 GeV beam energy range.

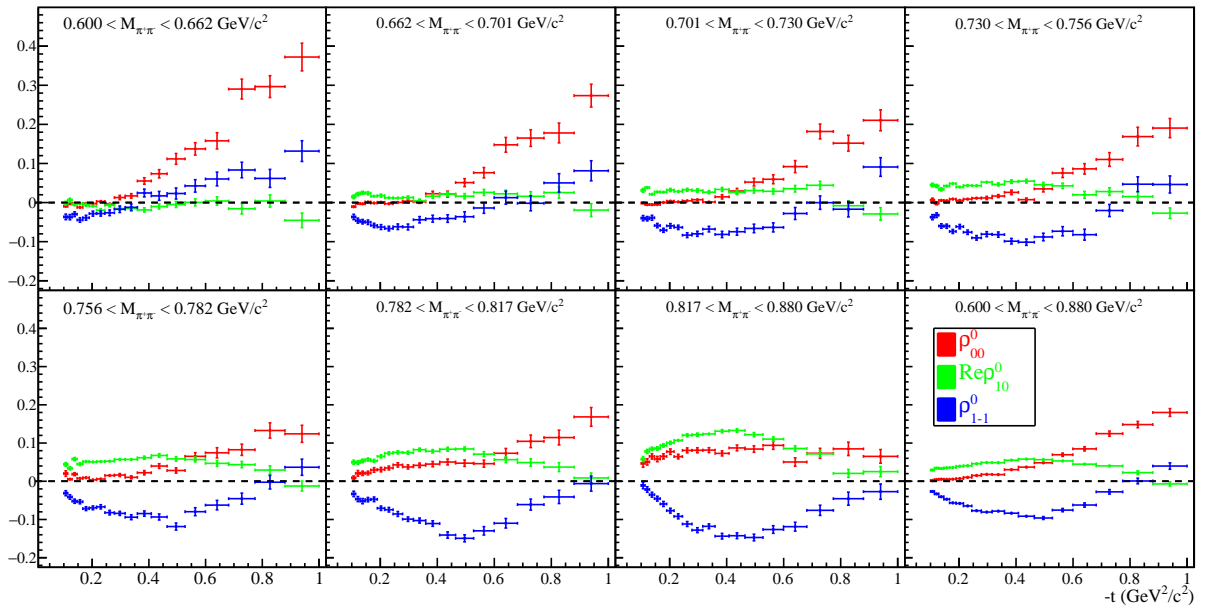


Figure 8.10: All three SDMEs are plotted in eighteen bins in $-t$ and seven sub-ranges of the $\pi^+\pi^-$ invariant mass over the 6.5 – 7.5 GeV beam energy range.

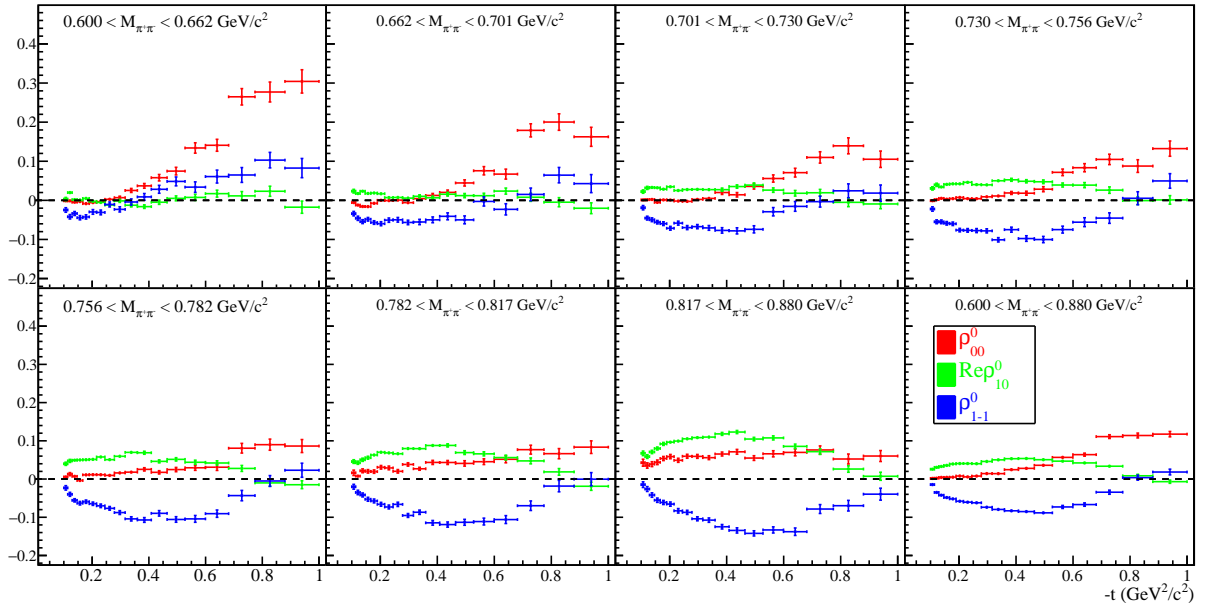


Figure 8.11: All three SDMEs are plotted in eighteen bins in $-t$ and seven sub-ranges of the $\pi^+\pi^-$ invariant mass over the 7.5 – 8.5 GeV beam energy range.

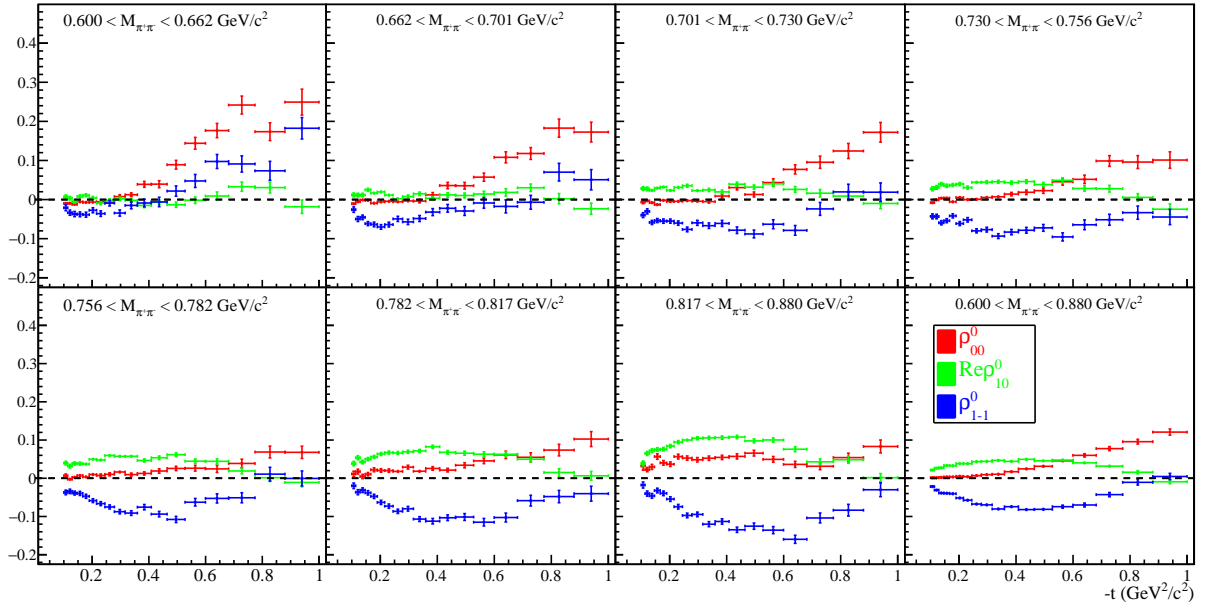


Figure 8.12: All three SDMEs are plotted in eighteen bins in $-t$ and seven sub-ranges of the $\pi^+\pi^-$ invariant mass over the 8.5 – 9.5 GeV beam energy range.

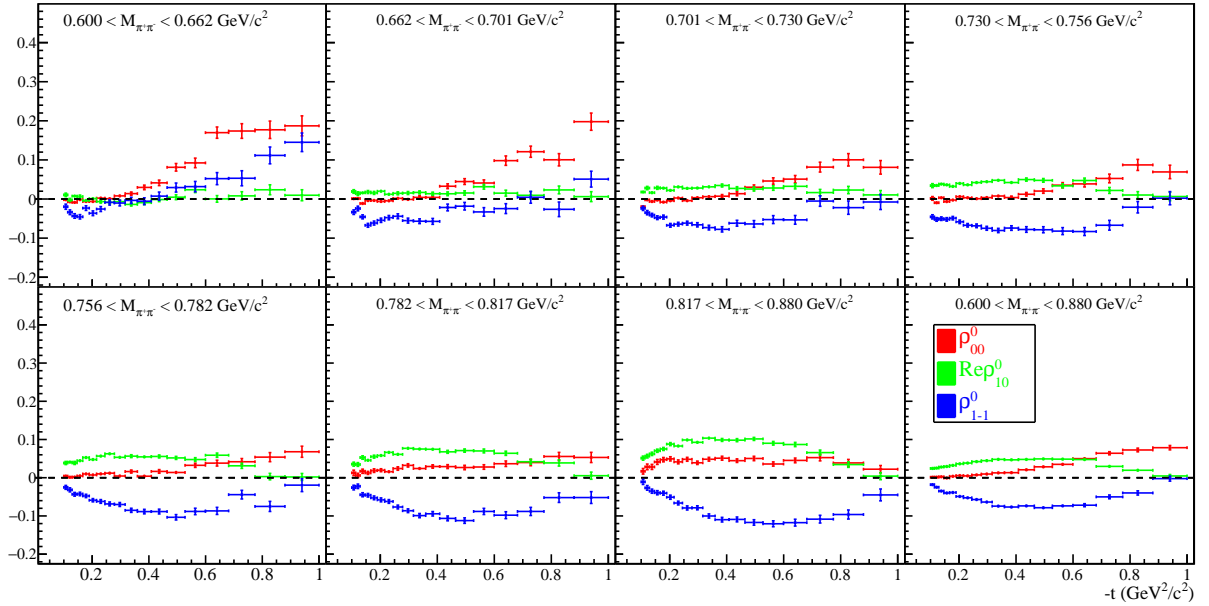


Figure 8.13: All three SDMEs are plotted in eighteen bins in $-t$ and seven sub-ranges of the $\pi^+\pi^-$ invariant mass over the 9.5 – 11.6 GeV beam energy range.

8.1.1 Comparison with GlueX results

SDMEs in $\pi^+\pi^-$ photoproduction were measured by A. Austregesilo [86] in an independent analysis of GlueX data. This measurement was performed over the coherent peak region of the beam energy spectrum (8.2 – 8.8 GeV), using data recorded with a diamond radiator during the Spring 2017 beam time. The coherent peak is characterised by an enhancement in linearly polarised photons, meaning the six polarisation dependent SDMEs could also be extracted. There were also some important differences in the analysis methodology used by Austregesilo compared with what was used for this thesis. Austregesilo performed SDME fits within the AmpTools [110] analysis framework, while `brufit` was used for the work presented here. Moreover, the parameter estimation was performed without an MCMC. Results were extracted using MINUIT only, and the statistical uncertainties were obtained via Bootstrapping [111].

Results were extracted using the same data set and compared with the polarised and unpolarised SDMEs measured by Austregesilo. This was performed as a cross check to evaluate the methodology used in this work, and to determine whether the final results were reproducible using an independent analysis approach. The same selection criteria as those specified in Section 5.7 were used and an additional cut was placed on the photon energy to isolate the coherent peak. A maximum likelihood fit was performed using Equation (2.32) as a PDF instead of Equation (2.33), meaning the polarisation dependent SDMEs could also be extracted. The resulting comparison is shown in Figure 8.14. An excellent agreement is observed, indicating that SDME measurements can be consistently reproduced in independent analyses of the same data.

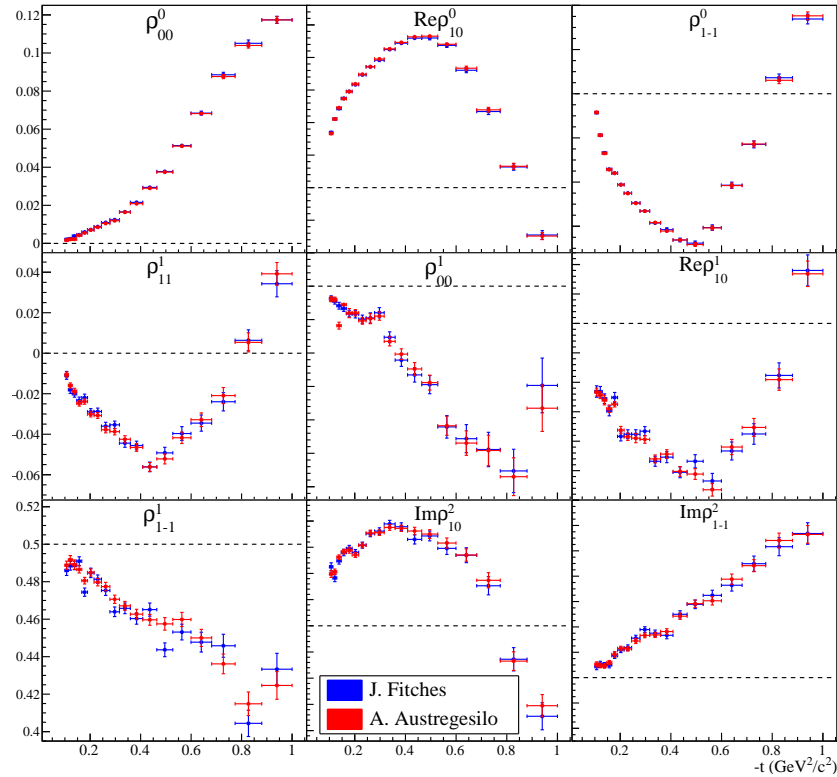


Figure 8.14: SDMEs measured for polarised $\rho(770)$ photoproduction in two independent analyses of the same data-set. A dashed horizontal line is drawn at 0 in each plot to show the prediction of the s-channel helicity conservation model, assuming a natural parity exchange.

8.2 $\pi^+\pi^-$ invariant mass dependence

Figures 8.7 to 8.13 demonstrate that SDMEs are strongly dependent on the $\pi^+\pi^-$ invariant mass. This is likely to result from interference between the $\rho(770)$ and the mass dependent background from non resonant S-wave production (c.f. Section 2.1). Other possible backgrounds that may contribute are the broad $f_0(500)$ S-wave resonance, and a small contribution from the $\omega(782)$ vector meson. Currently, no models exist that describe the mass dependence of the $\rho(770)$ decay distribution. The JPAC model describes a stable ρ with a mass of $0.775 \text{ GeV}/c^2$. However, in practice the $\rho(770)$ mass is seen to depend on the production mechanism as a result of interference with Drell processes.

In order to study the mass dependence in greater detail, results were extracted using the third binning scheme outlined in Section 5.8. SDME fits were performed in fourteen bins in the $\pi^+\pi^-$ invariant mass, shown in Figure 8.15, over various ranges in the photon energy and momentum transfer. The measured SDMEs are shown in Figures 8.16 to 8.18. It is interesting to note that while the results extracted in the lowest three $-t$ ranges ($0.10 - 0.32 \text{ GeV}^2/c^2$) are generally in good agreement, significant discrepancies are visible for SDMEs measured over the higher $-t$ ranges. This suggests that the P-wave assumption may only be valid for $-t < 0.32 \text{ GeV}^2/c^2$,

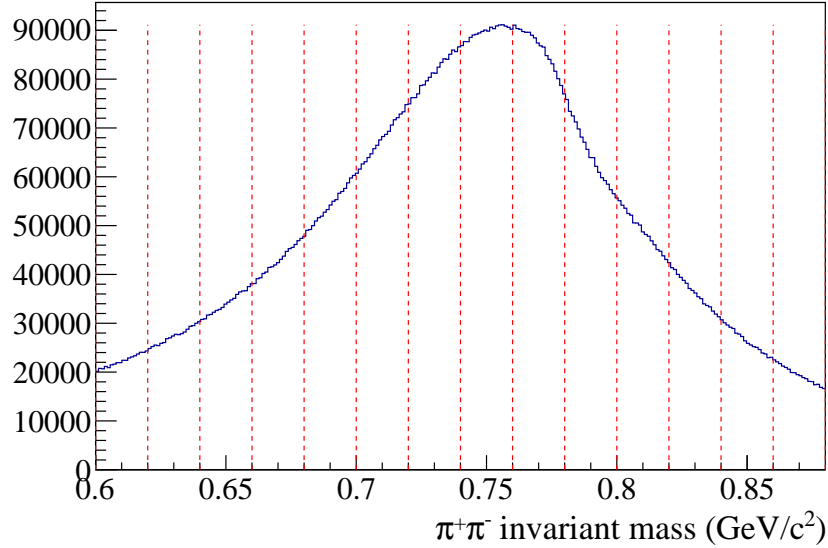


Figure 8.15: $\pi^+\pi^-$ invariant mass distribution, where the binning scheme used is annotated by the vertical dashed lines. When fitted with a Breit-Wigner function, the resonance was found to have a mass of $0.749 \text{ GeV}/c^2$ and a width of $0.141 \text{ GeV}/c^2$.

while a more complete model of the angular distribution is required to correctly extract SDMEs for higher values of $-t$. The structures visible in SDMEs measured over the highest studied $-t$ ranges are vastly different from what is observed for the lower sub ranges in $-t$. As the photon energy increases, this discrepancy is seen to become less significant. This is likely to result from baryon contamination, since the baryonic contribution is known to become more significant at lower beam energies and high $-t$.

8.2.1 Comparison with CLAS results

CLAS published SDME measurements in unpolarised $\pi^+\pi^-$ photoproduction in 2009 [52]. Results were extracted over the $3.6 - 3.8 \text{ GeV}$ photon energy regime in six $0.1 \text{ GeV}^2/c^2$ wide bins in $-t$ spanning the $0.4 - 1.0 \text{ GeV}^2/c^2$ range. The analysis was also binned in the $\pi^+\pi^-$ invariant mass to study the mass dependence. The fitting procedure differed from the method presented in Chapter 6 in that SDMEs were inferred from a moment analysis [51] of the photo-produced mesons.

SDME fits were performed using a similar binning scheme as CLAS to evaluate the agreement between GlueX and CLAS measurements. The same cut selection as before (c.f. Section 5.7) was applied, with an additional cut on the photon energy to match what was used in the CLAS analysis. The data were also split using the same six ranges in $-t$ as CLAS. The statistics available with GlueX over the $3.6 - 3.8 \text{ GeV}$ photon energy range were poor, so it was not possible to bin as finely as CLAS over the $\pi^+\pi^-$ invariant mass. The measured SDMEs are shown in

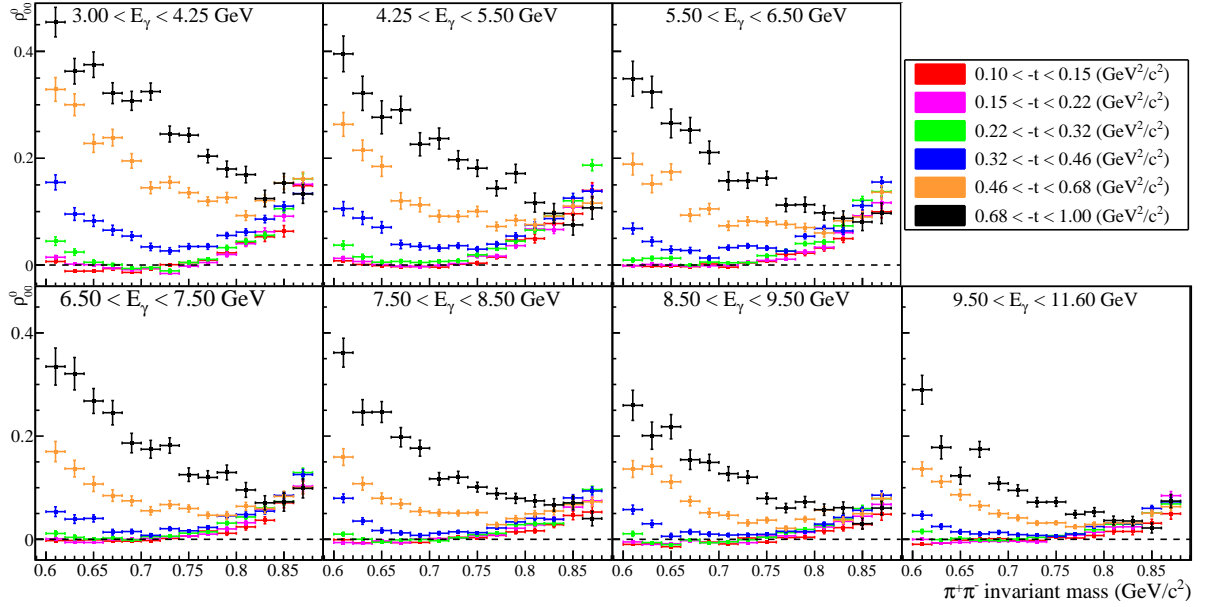


Figure 8.16: ρ_{00}^0 measured in fourteen $\pi^+\pi^-$ invariant mass bins for various photon energy regimes. Results are extracted over six different ranges in $-t$. These ranges are indicated in the plot legend.

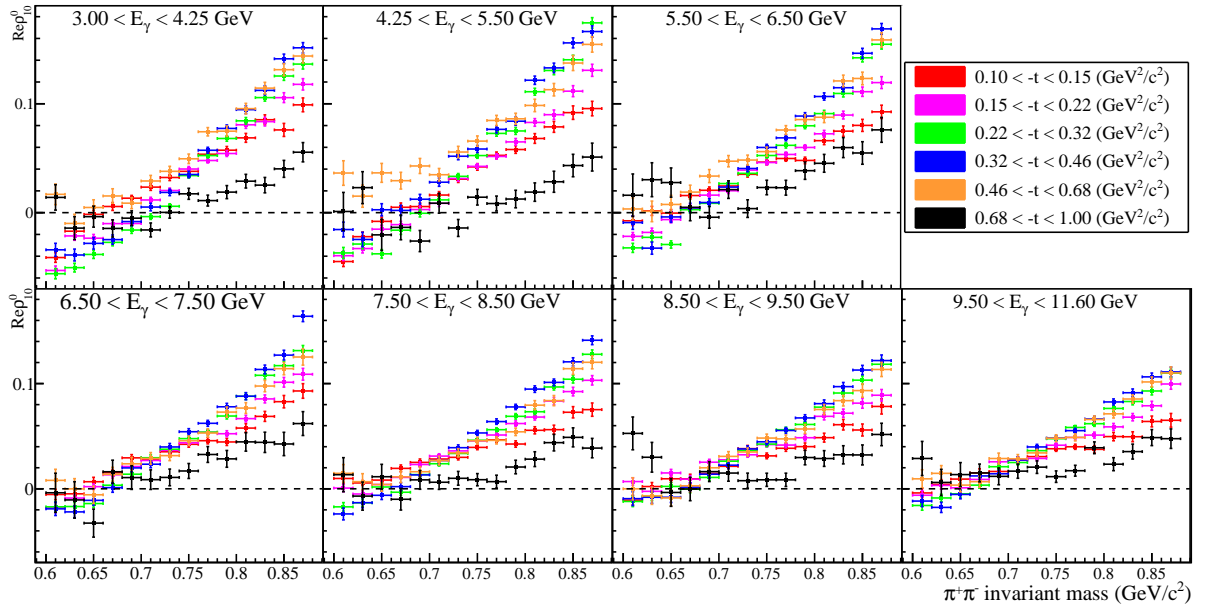


Figure 8.17: $\text{Re}\rho_{10}^0$ measured in fourteen $\pi^+\pi^-$ invariant mass bins for various photon energy regimes. Results are extracted over six different ranges in $-t$.

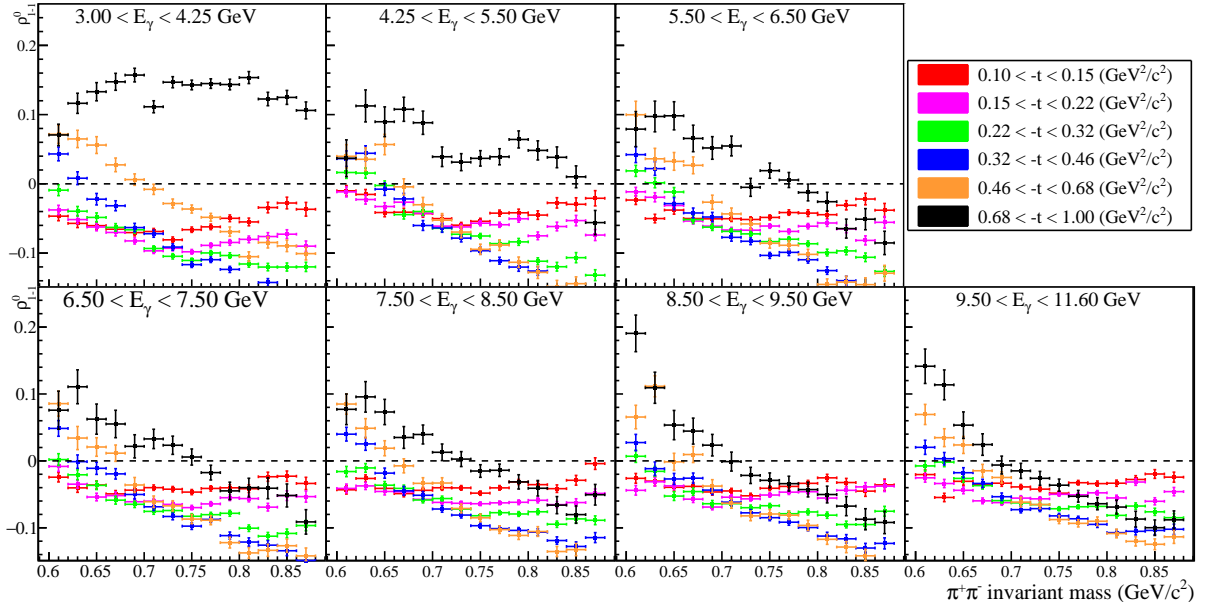


Figure 8.18: ρ_{1-1}^0 measured in fourteen $\pi^+\pi^-$ invariant mass bins for various photon energy regimes. Results are extracted over six different ranges in $-t$.

Figures 8.19 to 8.24 along with the CLAS results. It should be noted that the apparent smoothness of the CLAS data can be explained by the fitting procedure used. A model describing partial wave amplitudes was formulated by fitting the moments of angular distribution extracted by the analysers, and SDMEs were then determined by model-based calculations. Moreover, the uncertainties plotted in the CLAS data are systematic, originating from the difference in the moments obtained using four different extraction methods.

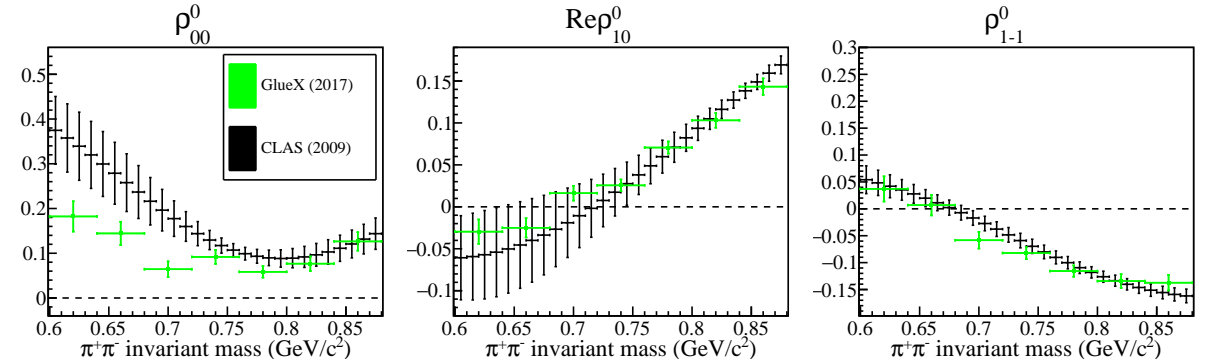


Figure 8.19: SDMEs measured in seven $\pi^+\pi^-$ invariant mass bins over the 3.6 – 3.8 GeV beam energy range and $0.4 - 0.5 \text{ GeV}^2/c^2$ $-t$ range. The SDMEs measured by CLAS are shown in black.

The CLAS results and the measurements performed with GlueX are generally in good agreement for the $\text{Re}\rho_{10}^0$ and ρ_{1-1}^0 SDMEs. A reasonable agreement is seen for ρ_{00}^0 at low $-t$. For the highest $-t$ bins a significant deviation in ρ_{00}^0 is seen between the CLAS and GlueX results. The ρ_{00}^0 was seen to be the most sensitive of the three SDMEs to systematic errors. This is discussed

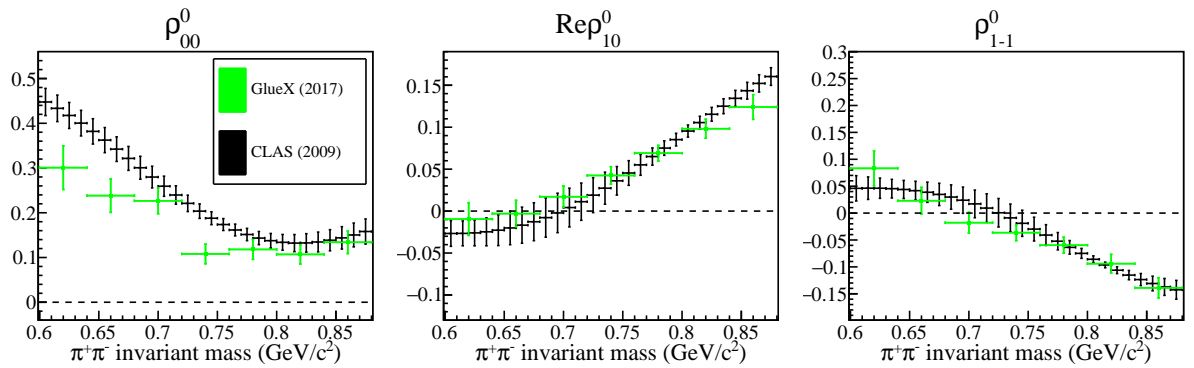


Figure 8.20: SDMEs measured in seven $\pi^+\pi^-$ invariant mass bins over the 3.6 – 3.8 GeV beam energy range and 0.5 – 0.6 GeV²/c² $-t$ range.

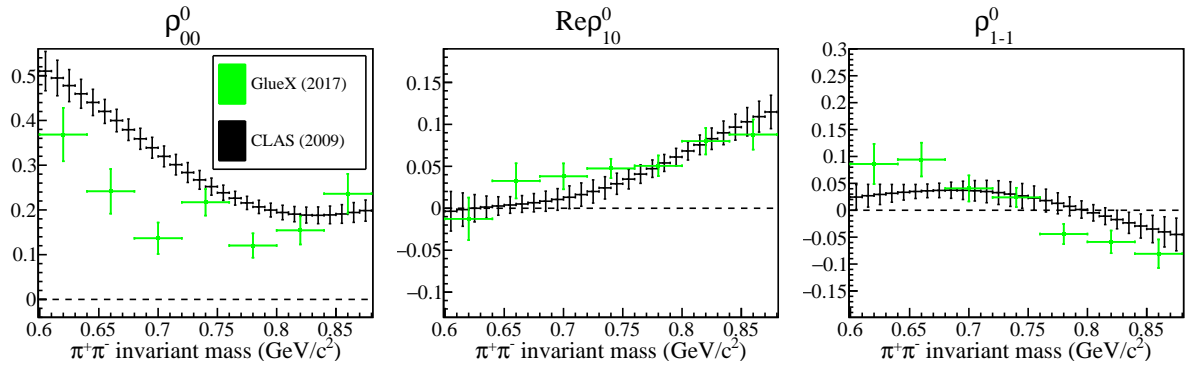


Figure 8.21: SDMEs measured in seven $\pi^+\pi^-$ invariant mass bins over the 3.6 – 3.8 GeV beam energy range and 0.6 – 0.7 GeV²/c² $-t$ range.

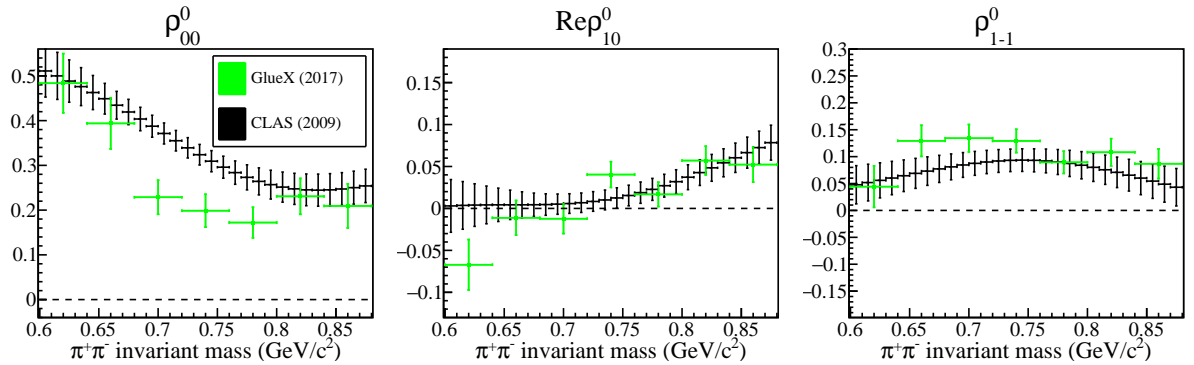


Figure 8.22: SDMEs measured in seven $\pi^+\pi^-$ invariant mass bins over the 3.6 – 3.8 GeV beam energy range and 0.7 – 0.8 GeV²/c² $-t$ range.

in Section 7.1. In the 3.6 – 3.8 GeV beam energy regime, the dominant source of systematic uncertainty was introduced by the cut on the π^+p invariant mass. This is demonstrated in Figure 7.14. The π^+p invariant mass cut was designed to remove the background originating from Δ^{++} resonances decaying to π^+p . Although this cut was effective in removing the $\Delta^{++}(1232)$ background, the production of higher mass Δ^{++} resonances is possible in this photon energy regime, especially at high $-t$. Moreover, there may also be contributions from Δ^0 and N^* res-

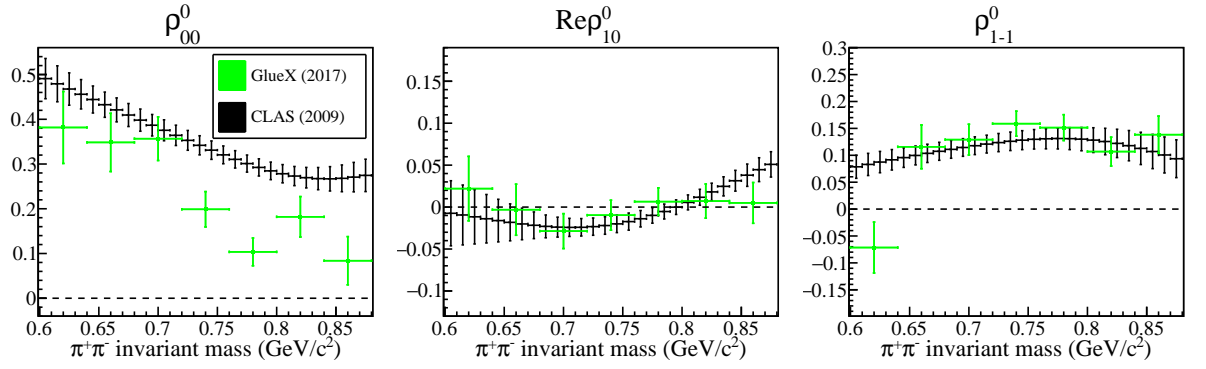


Figure 8.23: SDMEs measured in seven $\pi^+\pi^-$ invariant mass bins over the 3.6 – 3.8 GeV beam energy range and $0.8 - 0.9 \text{ GeV}^2/c^2$ $-t$ range.

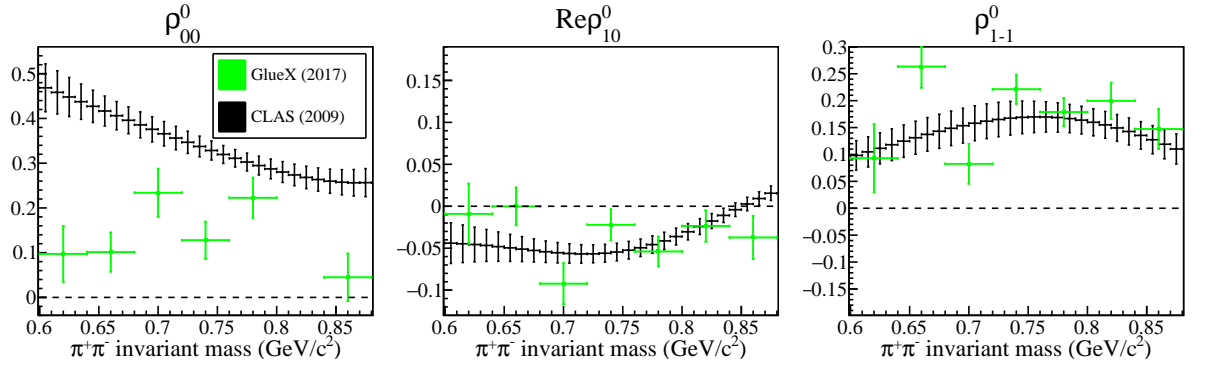


Figure 8.24: SDMEs measured in seven $\pi^+\pi^-$ invariant mass bins over the 3.6 – 3.8 GeV beam energy range and $0.9 - 1.0 \text{ GeV}^2/c^2$ $-t$ range.

onances decaying to $\pi^- p$. With CLAS, SDMEs were calculated from partial wave amplitudes derived from fitted moments of angular distribution. This allowed CLAS to disentangle the different angular momentum components that contributed to the measured decay distribution. They performed systematic studies that determined the contribution from reflections of baryon decays on the $\pi^+\pi^-$ system to have a negligible effect on the extracted partial wave amplitudes. SDMEs were therefore calculated from the P-wave signal alone, while the background from non P-wave resonances was effectively removed. For the work presented in this thesis, SDMEs were extracted by performing a fit to Equation (2.33). This formalism describes the angular distribution of P-wave decay products alone. The observed decay distribution is therefore assumed to originate from P-wave resonances, while the non P-wave background is not accounted for. Although this may be a valid approximation at low $-t$, it may not be the case at high $-t$ where the non-resonant S-wave and baryonic backgrounds become more significant. Nevertheless, it is encouraging to note that a significant disagreement is only observed over a narrow region of phase space, and that both sets of results are fairly consistent overall.

Chapter 9

Conclusion

For the work presented in this thesis, SDMEs were measured in unpolarised $\pi^+\pi^-$ photoproduction with excellent statistics. The statistical precision of these measurements surpasses what was achievable with previous experiments by several orders of magnitude. The best available data prior to this measurement was published by SLAC, shown in Figures 8.1 to 8.3. The statistics available to SLAC were relatively poor, meaning the $-t$ dependence of the extracted SDMEs was seen to be approximately flat. It is encouraging to see that the measurements performed with GlueX are generally in excellent agreement with the data published by SLAC. Moreover, additional structures become visible in GlueX data since the achievable resolution in $-t$ is far superior to what was possible with SLAC.

The JPAC theory group developed a model for $\rho(770)$ photoproduction based on Regge theory by performing a fit to the SLAC data. The results obtained with GlueX describe SDMEs in $\rho(770)$ photoproduction to a first approximation, and are seen to agree well with the predictions of the JPAC model at low $-t$. The JPAC model becomes invalid for $-t \gtrsim 0.5 \text{ GeV}^2/c^2$, leading to a discrepancy with the GlueX results. The high statistics measurements reported in this thesis will further constrain the JPAC model. This will lead to more accurate predictions and a more robust description of vector meson photoproduction mechanisms.

The JPAC model also predicts the energy dependence of $\rho(770)$ SDMEs. Larger deviations from the s-channel helicity conservation model are predicted at low photon energies, where a more significant contribution from the helicity flip f_2 exchange is expected. Smaller deviations from s-channel helicity conservation are predicted by JPAC at higher beam energies following from the helicity non-flip pomeron exchange, which dominates in the high energy regime. In this work, SDMEs were measured over an energy regime that was more extensive than what had been studied in any previous analysis of $\pi^+\pi^-$ photoproduction data. This makes it possible to test the energy dependence predicted by the JPAC model in great detail. The GlueX measurements are seen to follow the energy dependence of the JPAC prediction very closely. By studying the

energy dependence of the dipion photoproduction process, much can be learned about the relative strengths of the f_2 and pomeron exchange mechanisms. The results obtained in this work may even make it possible for theorists to disentangle the f_2/\mathbb{P} coupling ratio.

The measured SDMEs were also seen to be highly dependent on the $\pi^+\pi^-$ invariant mass. No mass dependence is currently predicted by the JPAC model, which describes a stable $\rho(770)$ with a fixed mass of $0.775 \text{ GeV}/c^2$. There are a number of possible explanations for the mass dependence observed in GlueX measurements. The background beneath the $\rho(770)$ peak is complex, and can be characterised by a significant contribution from non-resonant S-wave production processes. These processes are mass dependent, and interfere with the P-wave signal from the ρ . This motivates the need for a more detailed model of the Drell background, which is currently poorly understood. One could potentially account for the non-resonant S-wave background using a similar approach to CLAS. With CLAS, moments of angular distribution were extracted from photoproduced mesons and expanded to determine the partial wave amplitudes. These amplitudes were then used to calculate SDMEs. This method disentangles the different angular momentum components of the decay distribution, meaning P-wave and S-wave contributions can be separated. Although this is more computationally challenging, future analyses of the $\rho(770)$ should utilise this approach to ensure a more complete angular description of the decay is defined in the fit. There are also some indications in the GlueX results that baryon resonances overlapping with the measured $\pi^+\pi^-$ system are partly responsible for the mass dependence. JPAC theorists are currently developing a model for $\pi^+\pi^-$ photoproduction that includes baryon resonances. It will be interesting to compare the predictions of the new model with the results presented in this thesis to determine the extent to which the mass dependence can be explained by baryon contamination.

The results presented in this thesis are currently being prepared for publication. SDMEs in unpolarised $\pi^+\pi^-$ photoproduction have never been measured in such an extensive kinematic region, and the extracted results are more statistically precise than any previous measurement to date. This will provide valuable input for vector meson photoproduction models, ultimately helping GlueX to achieve its primary physics objective of mapping out the spectrum of exotic hybrid meson states.

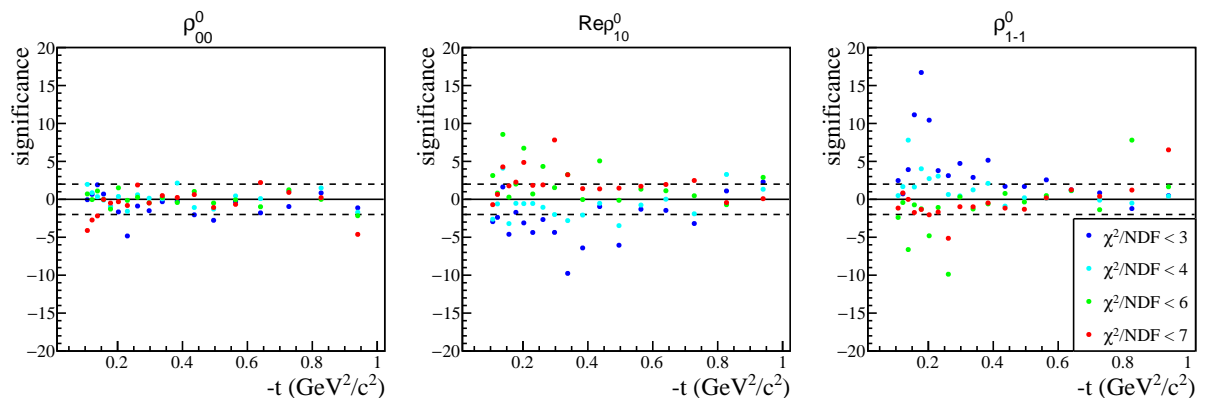
Appendix A

Additional Barlow significance plots

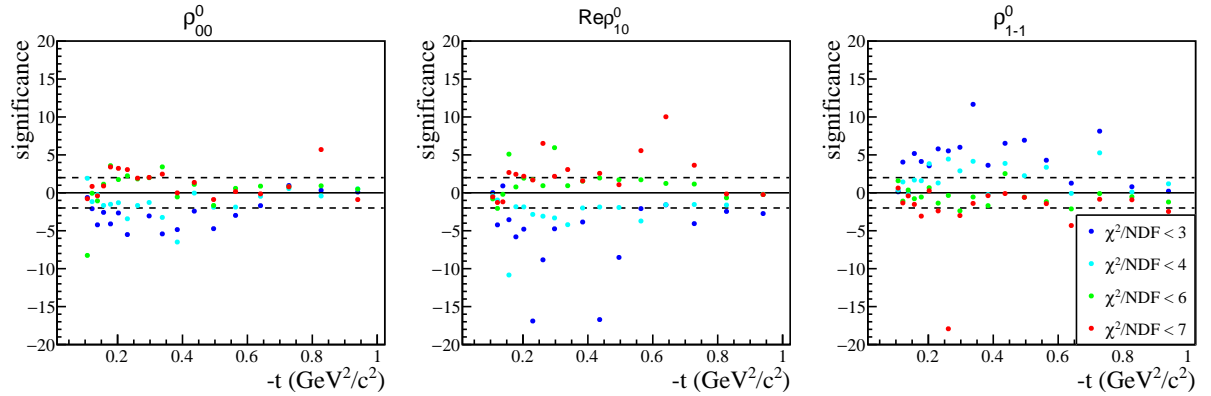
In Section 7.1, plots of the Barlow significance were produced to identify systematic effects. These were chosen to be representative, and only a small selection were included for brevity. In the following, significance plots for each of the studied beam energy ranges will be presented for the three cuts that were determined to be unstable. Plots produced using the Barlow significance versus $\pi^+\pi^-$ invariant mass, where the significance is shown as a function of the dipion invariant mass, are also included. Individual plots for each of the studied $-t$ ranges are shown for the 3.00 – 4.25 GeV photon energy bin only, since systematic effects were seen to be the most prominent over this energy range.

A.1 Kinematic fit χ^2/NDF cut

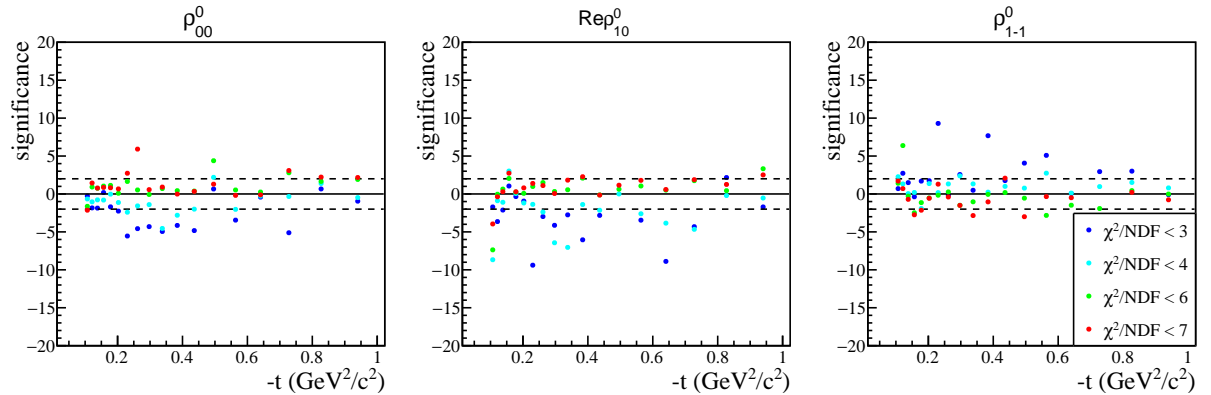
A.1.1 Significance versus $-t$



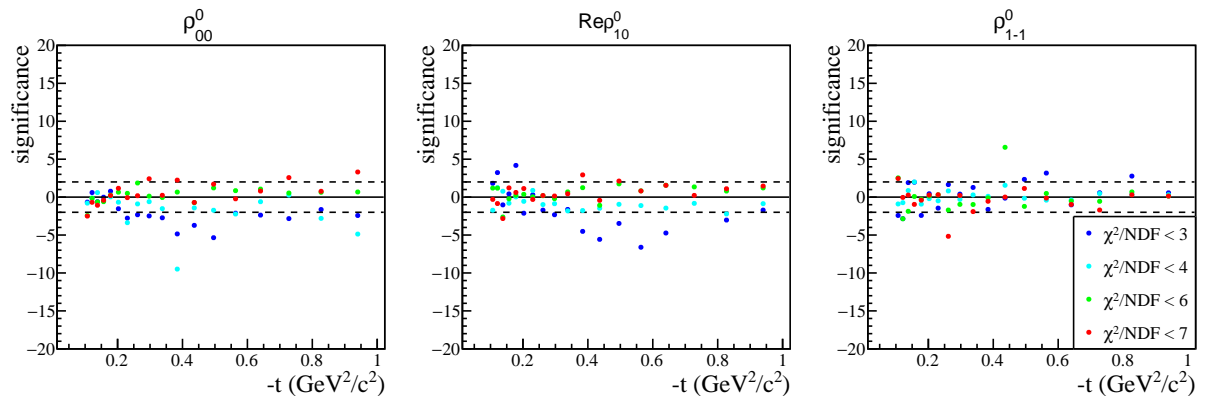
The Barlow significance is plotted for each $-t$ bin and each kinematic fit χ^2/NDF cut variation for the 3.00 – 4.25 GeV E_γ range.



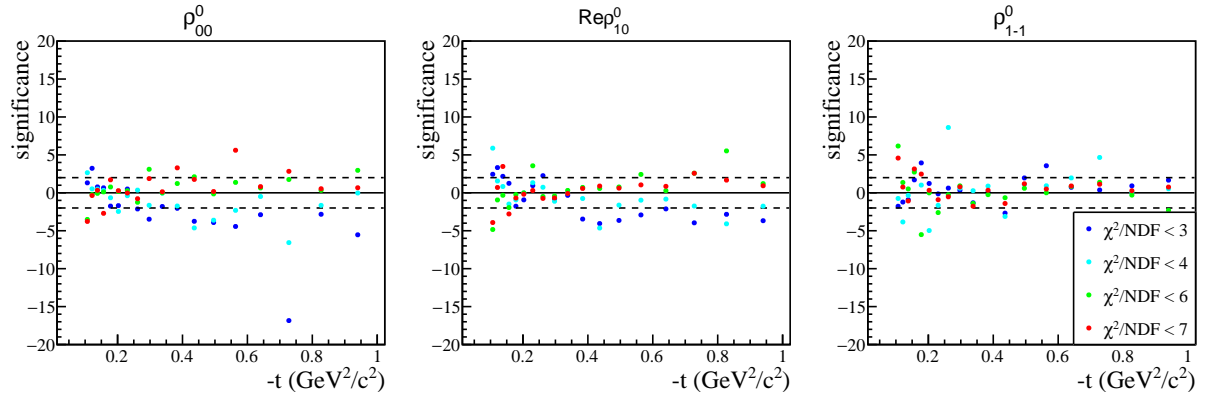
The Barlow significance is plotted for each $-t$ bin and each kinematic fit χ^2/NDF cut variation for the 4.25 – 5.50 GeV E_γ range.



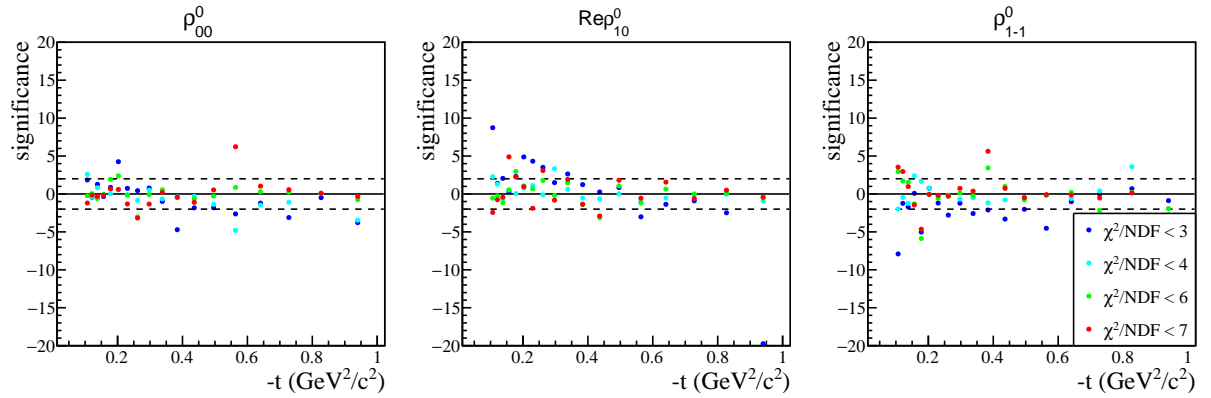
The Barlow significance is plotted for each $-t$ bin and each kinematic fit χ^2/NDF cut variation for the 5.5 – 6.5 GeV E_γ range.



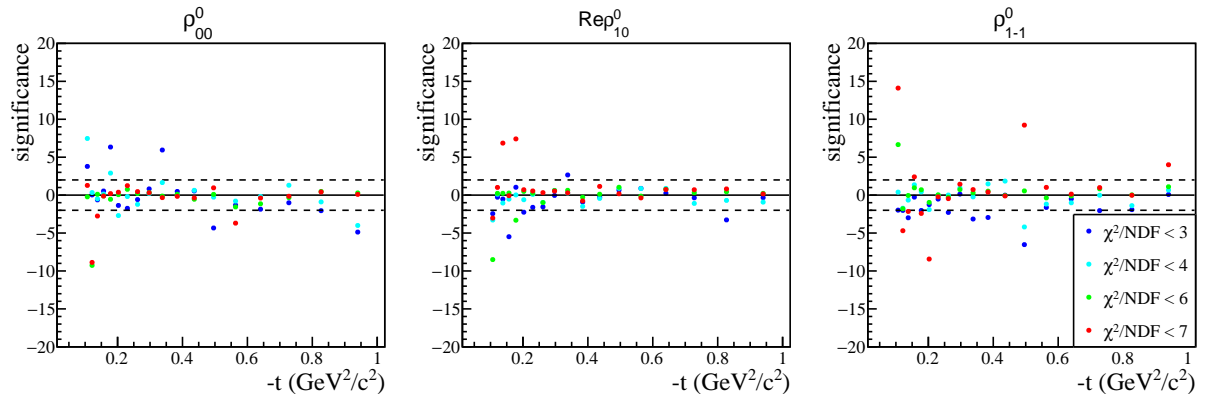
The Barlow significance is plotted for each $-t$ bin and each kinematic fit χ^2/NDF cut variation for the 6.5 – 7.5 GeV E_γ range.



The Barlow significance is plotted for each $-t$ bin and each kinematic fit χ^2/NDF cut variation for the 7.5 – 8.5 GeV E_γ range.

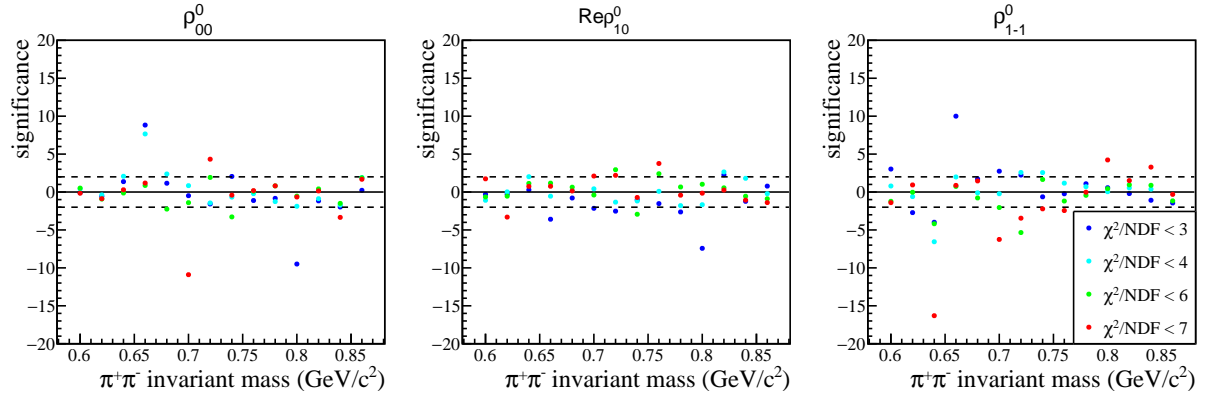


The Barlow significance is plotted for each $-t$ bin and each kinematic fit χ^2/NDF cut variation for the 8.5 – 9.5 GeV E_γ range.

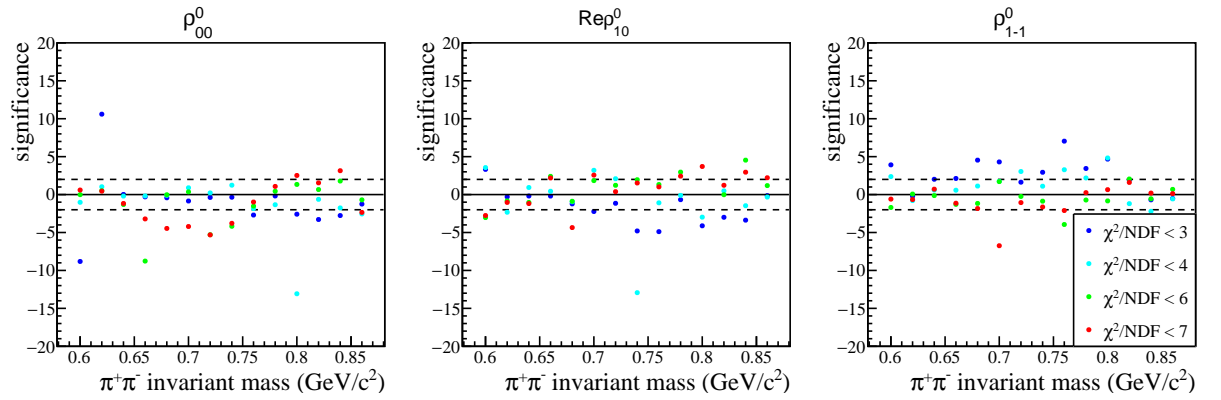


The Barlow significance is plotted for each $-t$ bin and each kinematic fit χ^2/NDF cut variation for the 9.5 – 11.6 GeV E_γ range.

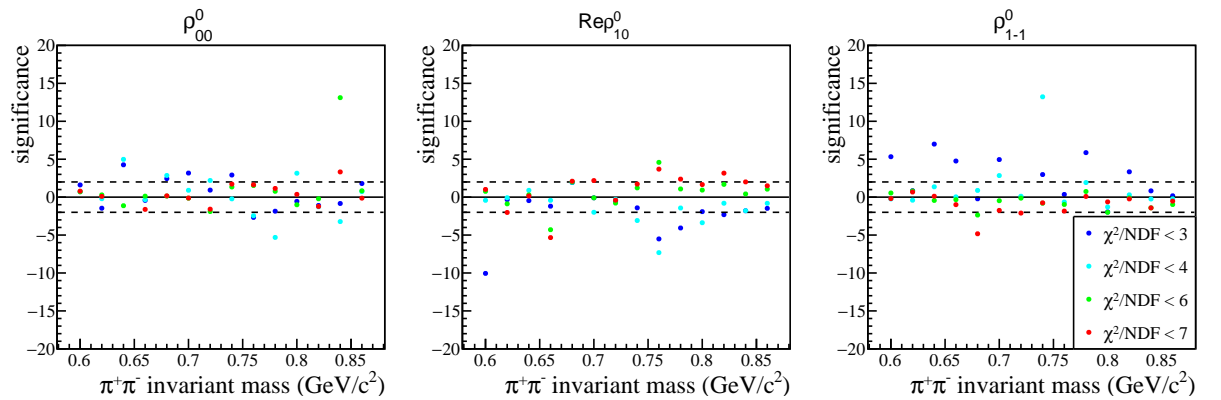
A.1.2 Significance versus $\pi^+\pi^-$ invariant mass



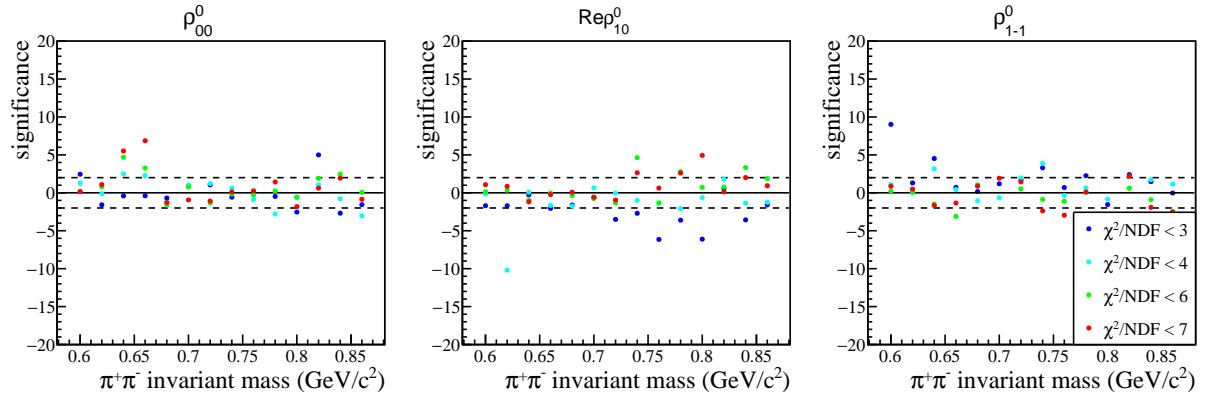
The Barlow significance is plotted for each $M_{\pi\pi}$ bin and each kinematic fit χ^2/NDF cut variation over the 3.00 – 4.25 GeV range in E_γ and 0.10 – 0.15 GeV^2/c^2 range in $-t$.



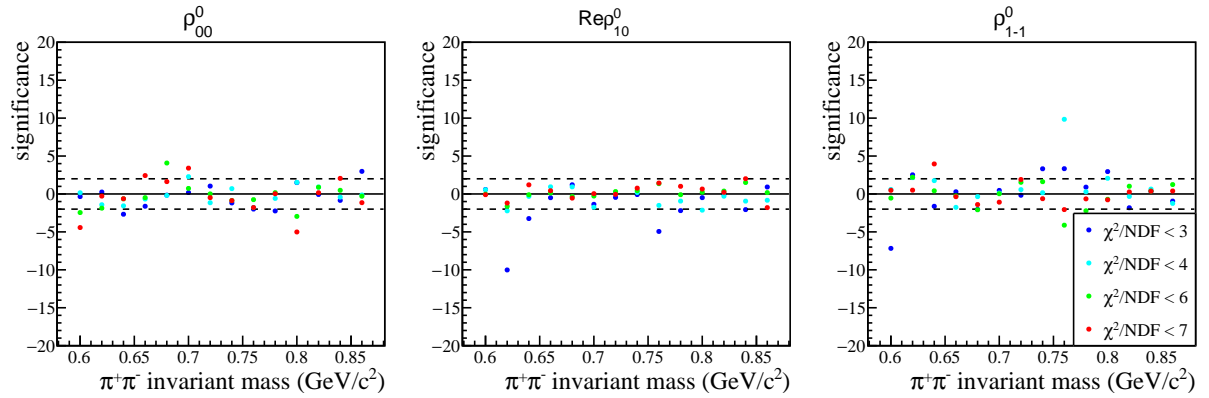
The Barlow significance is plotted for each $M_{\pi\pi}$ bin and each kinematic fit χ^2/NDF cut variation over the 3.00 – 4.25 GeV range in E_γ and 0.15 – 0.22 GeV^2/c^2 range in $-t$.



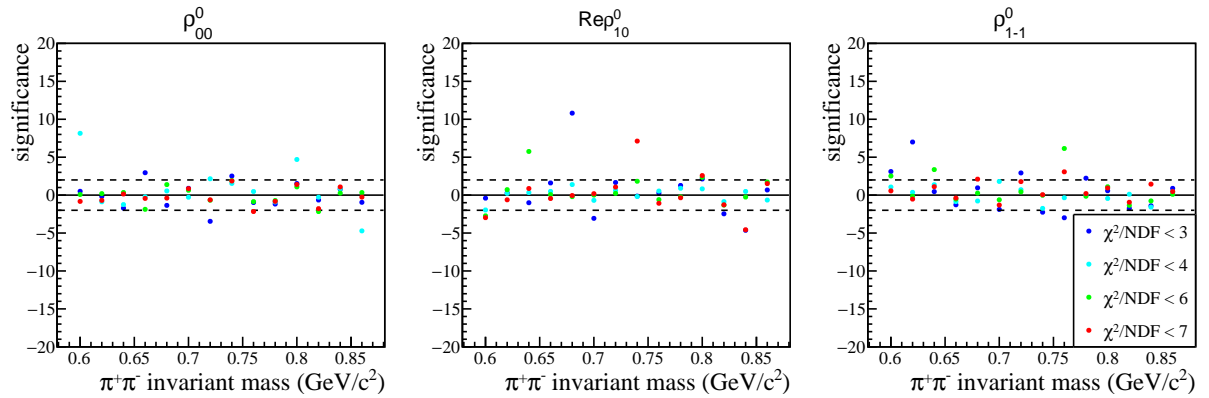
The Barlow significance is plotted for each $M_{\pi\pi}$ bin and each kinematic fit χ^2/NDF cut variation over the 3.00 – 4.25 GeV range in E_γ and 0.22 – 0.32 GeV^2/c^2 range in $-t$.



The Barlow significance is plotted for each $M_{\pi\pi}$ bin and each kinematic fit χ^2/NDF cut variation over the 3.00 – 4.25 GeV range in E_γ and 0.32 – 0.46 GeV^2/c^2 range in $-t$.



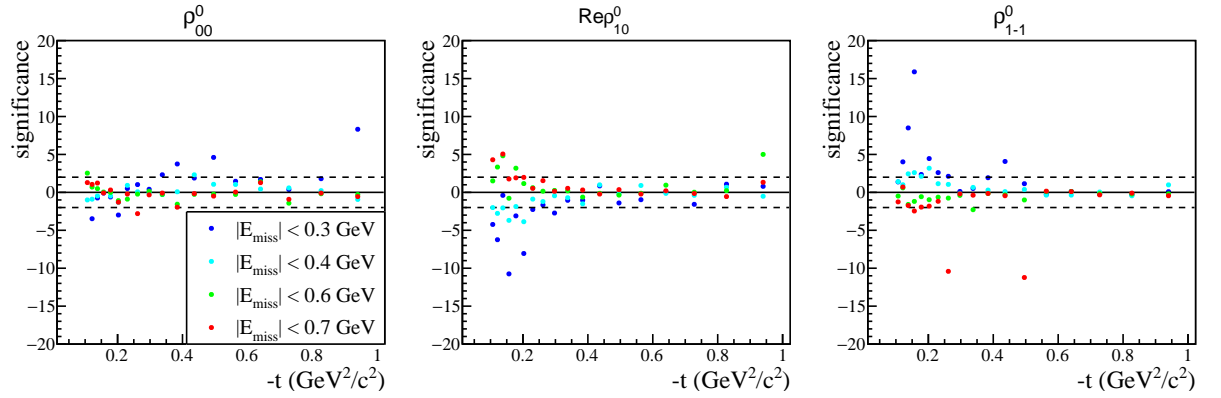
The Barlow significance is plotted for each $M_{\pi\pi}$ bin and each kinematic fit χ^2/NDF cut variation over the 3.00 – 4.25 GeV range in E_γ and 0.46 – 0.68 GeV^2/c^2 range in $-t$.



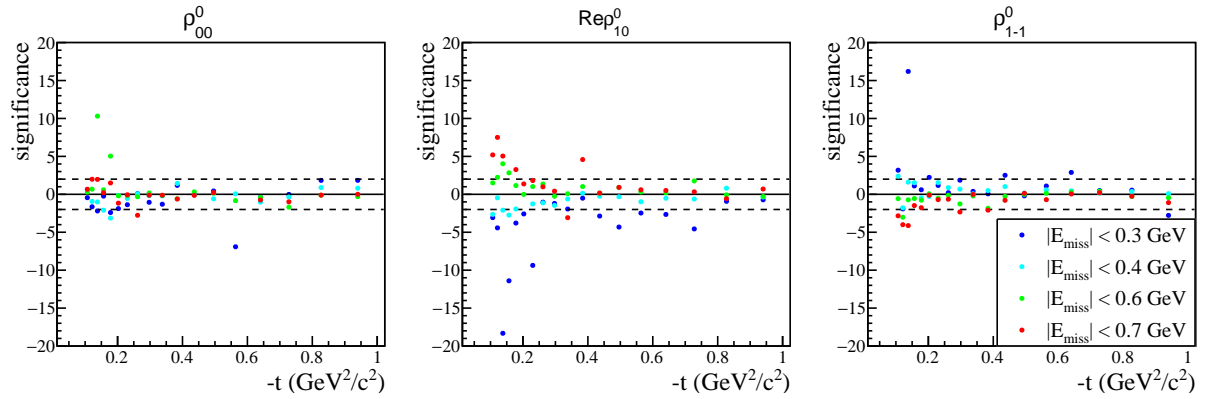
The Barlow significance is plotted for each $M_{\pi\pi}$ bin and each kinematic fit χ^2/NDF cut variation over the 3.00 – 4.25 GeV range in E_γ and 0.68 – 1.00 GeV^2/c^2 range in $-t$.

A.2 Missing energy cut

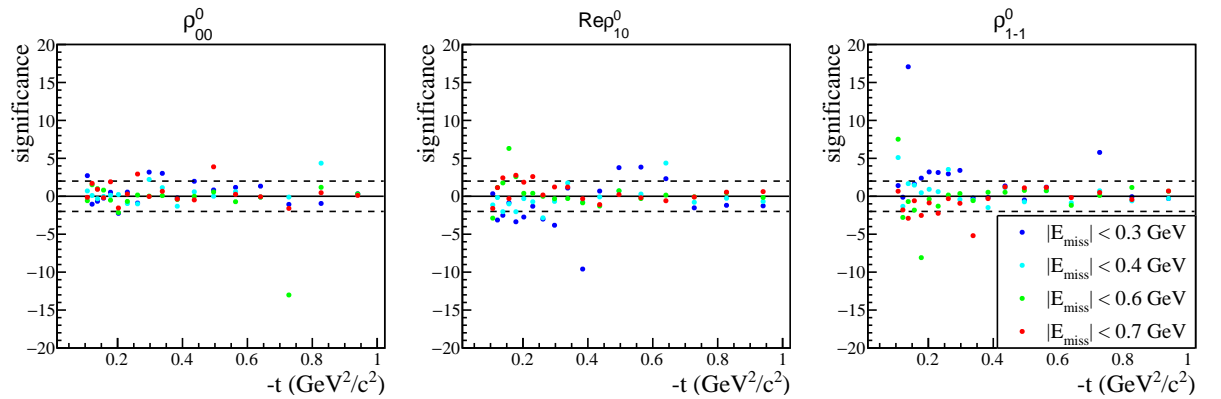
A.2.1 Significance versus $-t$



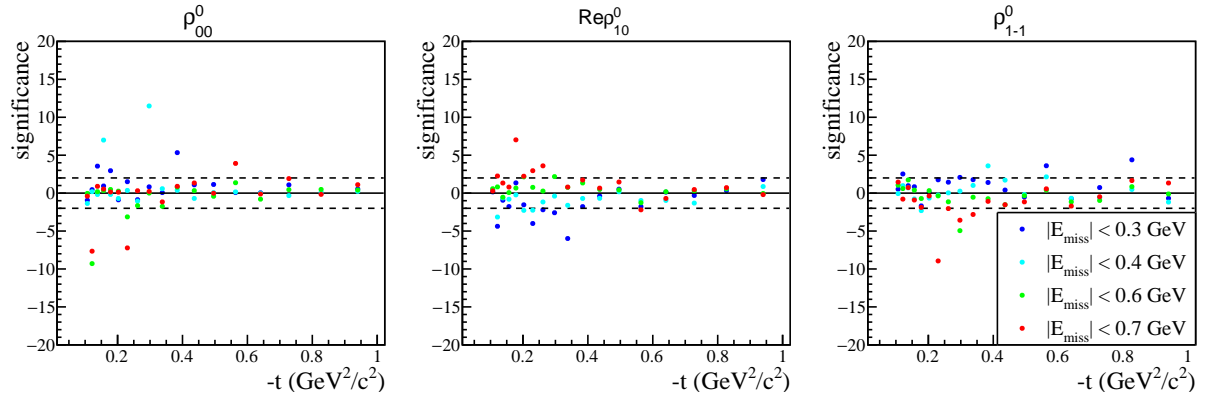
The Barlow significance is plotted for each $-t$ bin and each missing energy cut variation for the $3.00 - 4.25$ GeV E_γ range.



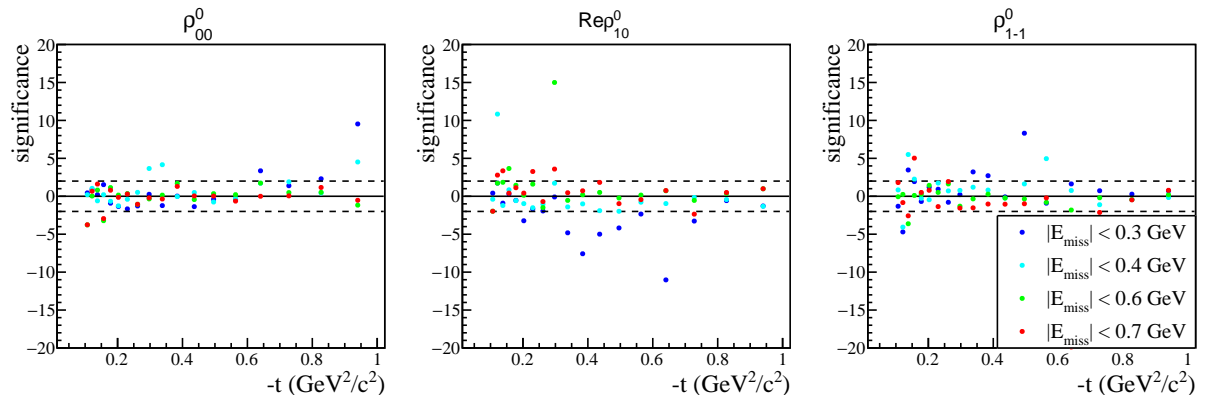
The Barlow significance is plotted for each $-t$ bin and each missing energy cut variation for the $4.25 - 5.50$ GeV E_γ range.



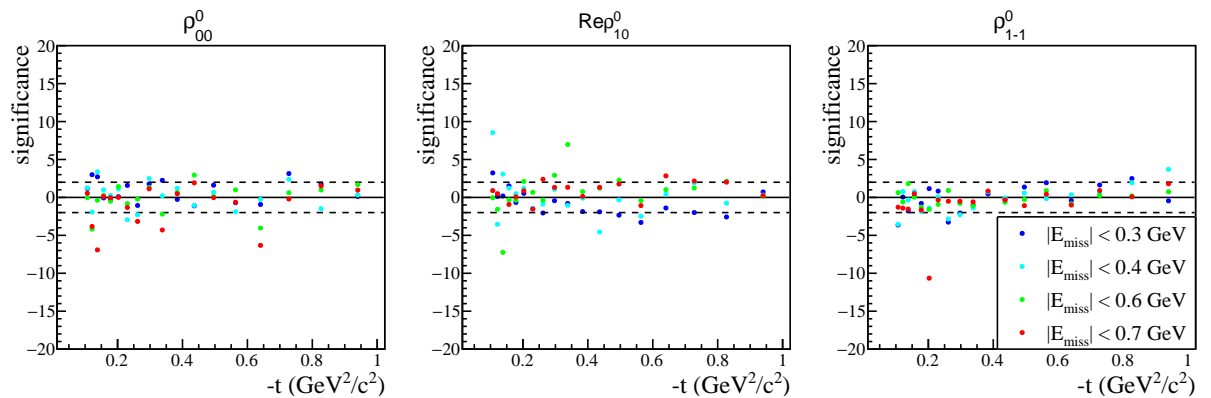
The Barlow significance is plotted for each $-t$ bin and each missing energy cut variation for the $5.5 - 6.5$ GeV E_γ range.



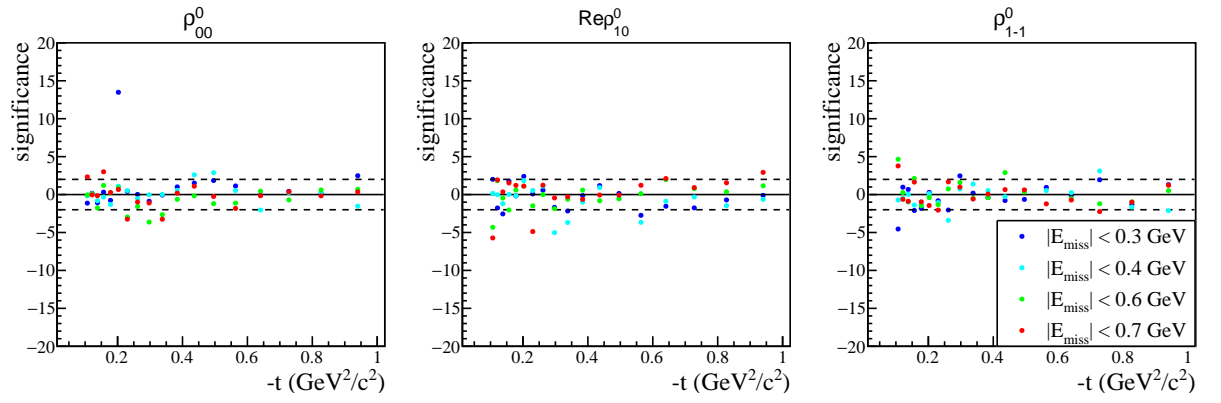
The Barlow significance is plotted for each $-t$ bin and each missing energy cut variation for the $6.5 - 7.5 \text{ GeV } E_\gamma$ range.



The Barlow significance is plotted for each $-t$ bin and each missing energy cut variation for the $7.5 - 8.5 \text{ GeV } E_\gamma$ range.

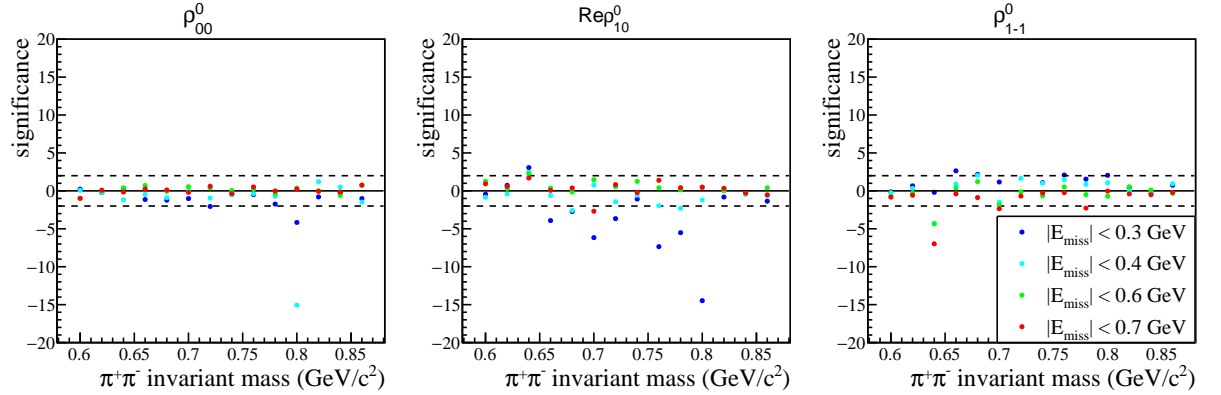


The Barlow significance is plotted for each $-t$ bin and each missing energy cut variation for the $8.5 - 9.5 \text{ GeV } E_\gamma$ range.

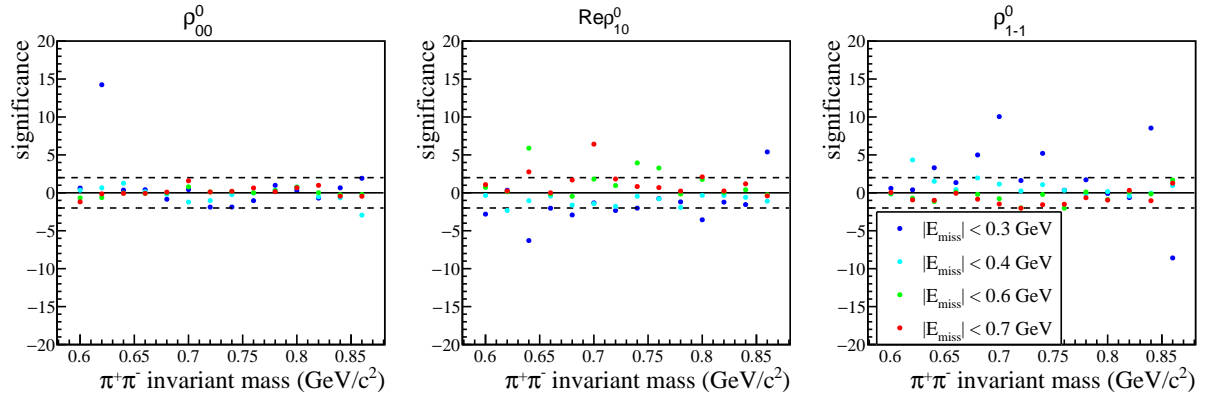


The Barlow significance is plotted for each $-t$ bin and each missing energy cut variation for the $9.5 - 11.6 \text{ GeV } E_\gamma$ range.

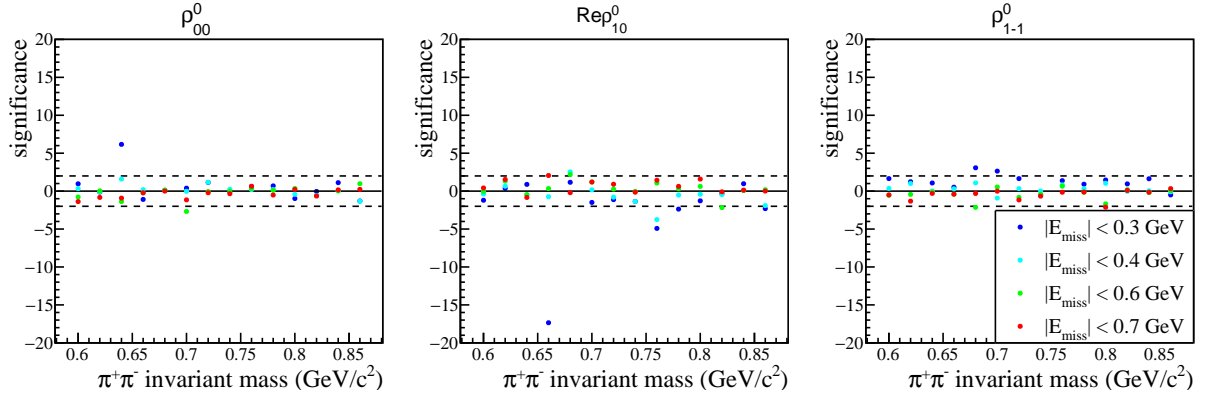
A.2.2 Significance versus $\pi^+\pi^-$ invariant mass



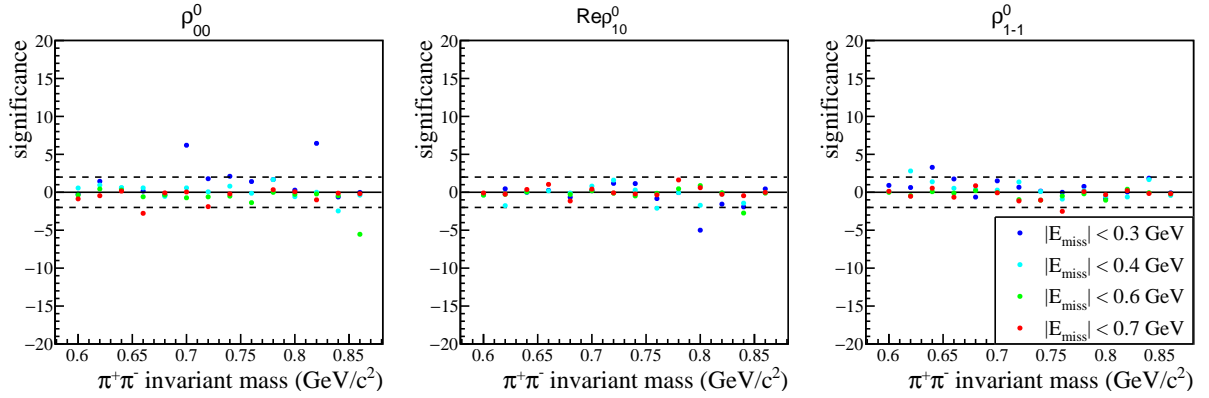
The Barlow significance is plotted for each $M_{\pi\pi}$ bin and each missing energy cut variation over the $3.00 - 4.25 \text{ GeV}$ range in E_γ and $0.10 - 0.15 \text{ GeV}^2/c^2$ range in $-t$.



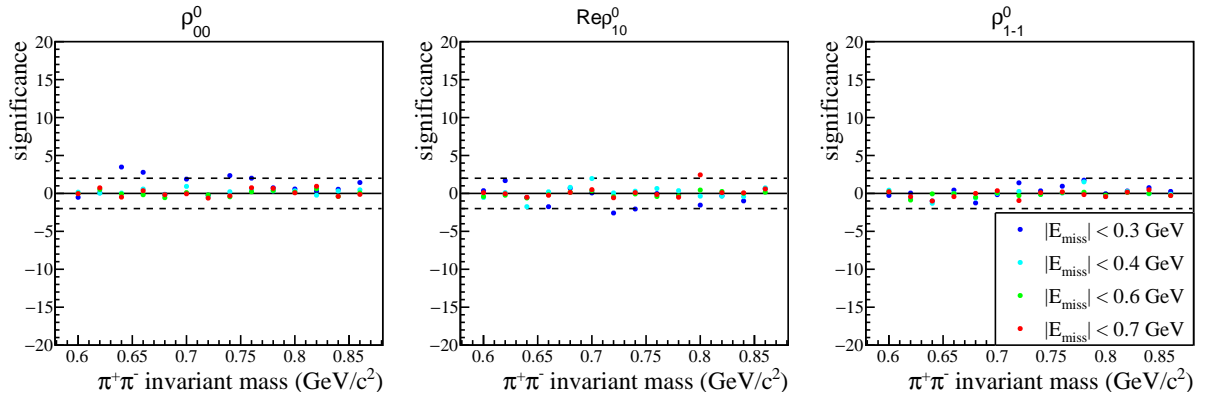
The Barlow significance is plotted for each $M_{\pi\pi}$ bin and each missing energy cut variation over the $3.00 - 4.25 \text{ GeV}$ range in E_γ and $0.15 - 0.22 \text{ GeV}^2/c^2$ range in $-t$.



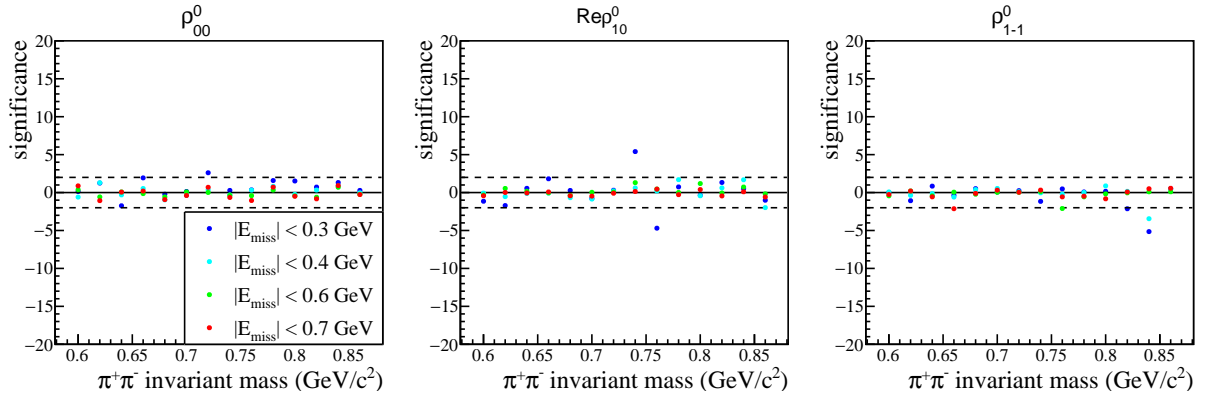
The Barlow significance is plotted for each $M_{\pi\pi}$ bin and each missing energy cut variation over the 3.00 – 4.25 GeV range in E_γ and 0.22 – 0.32 GeV^2/c^2 range in $-t$.



The Barlow significance is plotted for each $M_{\pi\pi}$ bin and each missing energy cut variation over the 3.00 – 4.25 GeV range in E_γ and 0.32 – 0.46 GeV^2/c^2 range in $-t$.



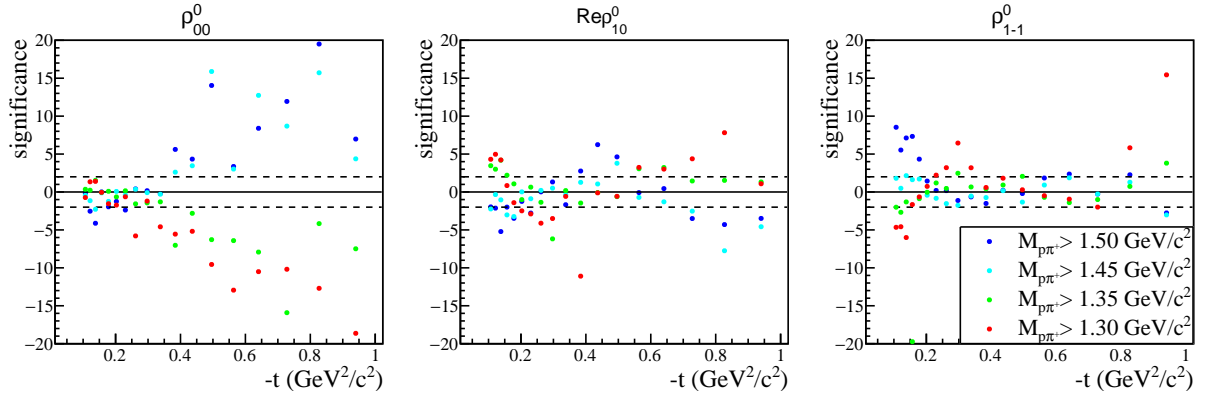
The Barlow significance is plotted for each $M_{\pi\pi}$ bin and each missing energy cut variation over the 3.00 – 4.25 GeV range in E_γ and 0.46 – 0.68 GeV^2/c^2 range in $-t$.



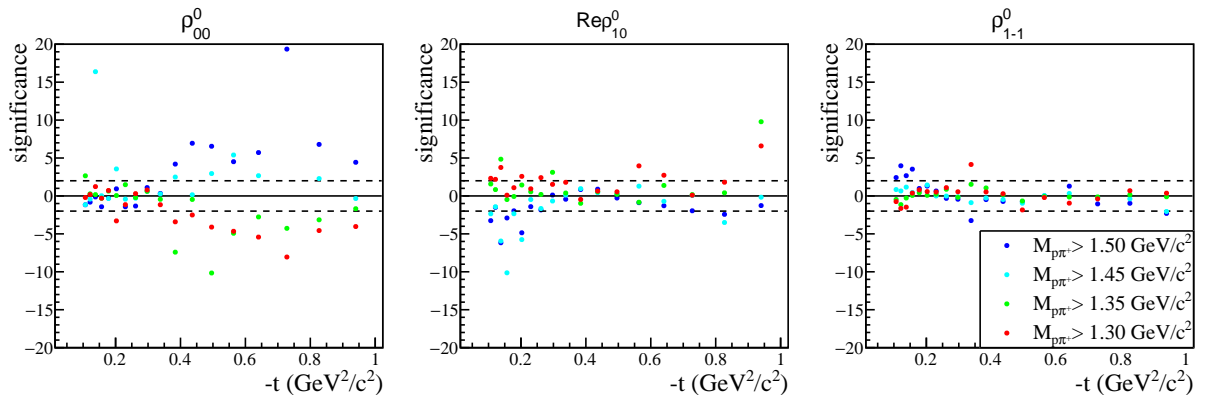
The Barlow significance is plotted for each $M_{\pi\pi}$ bin and each missing energy cut variation over the 3.00 – 4.25 GeV range in E_γ and 0.68 – 1.00 GeV^2/c^2 range in $-t$.

A.3 $\pi^+ p$ invariant mass cut

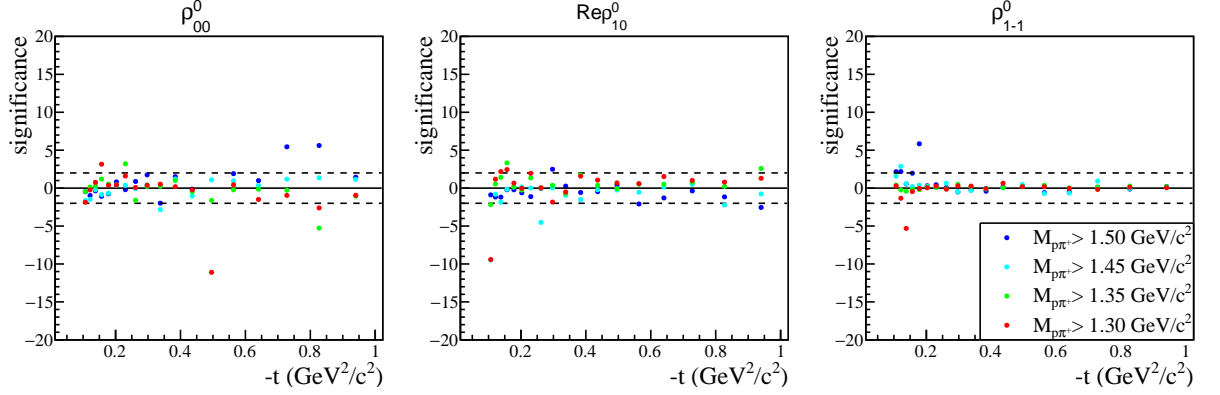
A.3.1 Significance versus $-t$



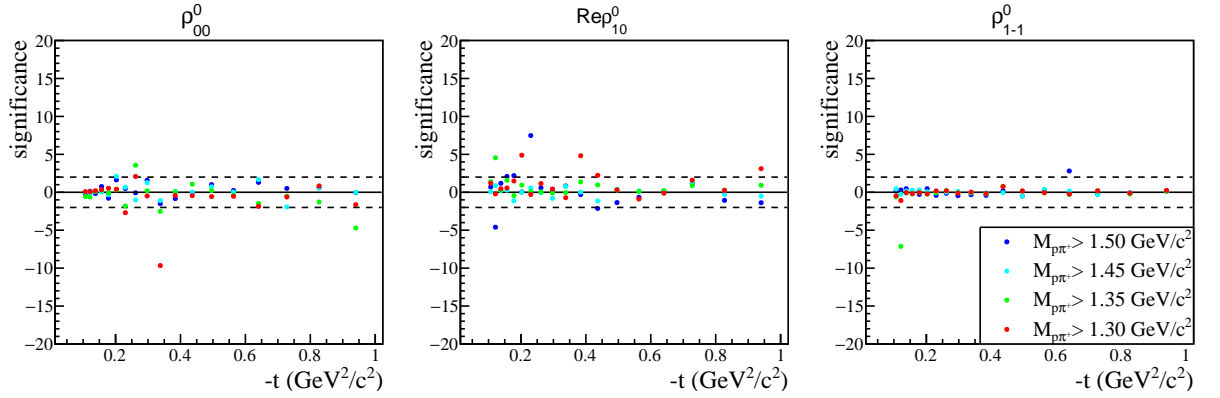
The Barlow significance is plotted for each $-t$ bin and each $p\pi^+$ invariant mass cut variation for the 3.00 – 4.25 GeV E_γ range.



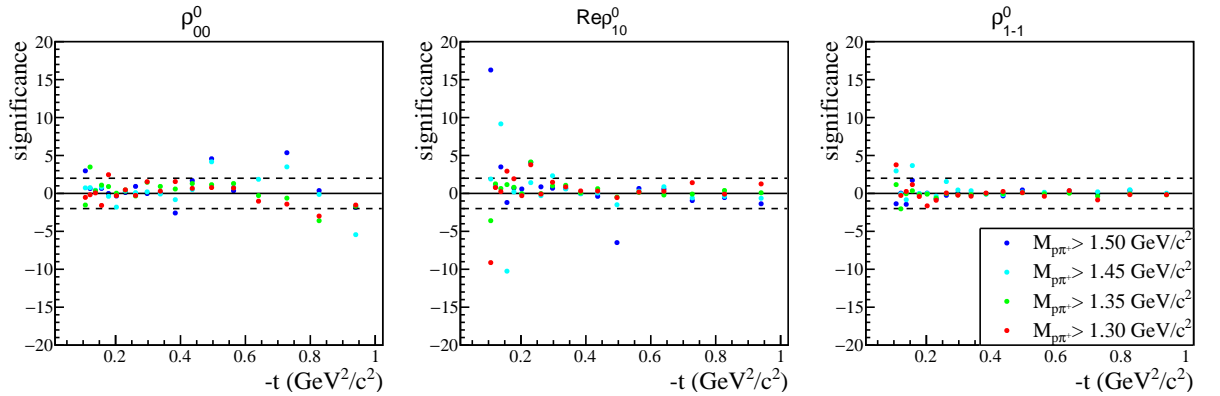
The Barlow significance is plotted for each $-t$ bin and each $p\pi^+$ invariant mass cut variation for the 4.25 – 5.50 GeV E_γ range.



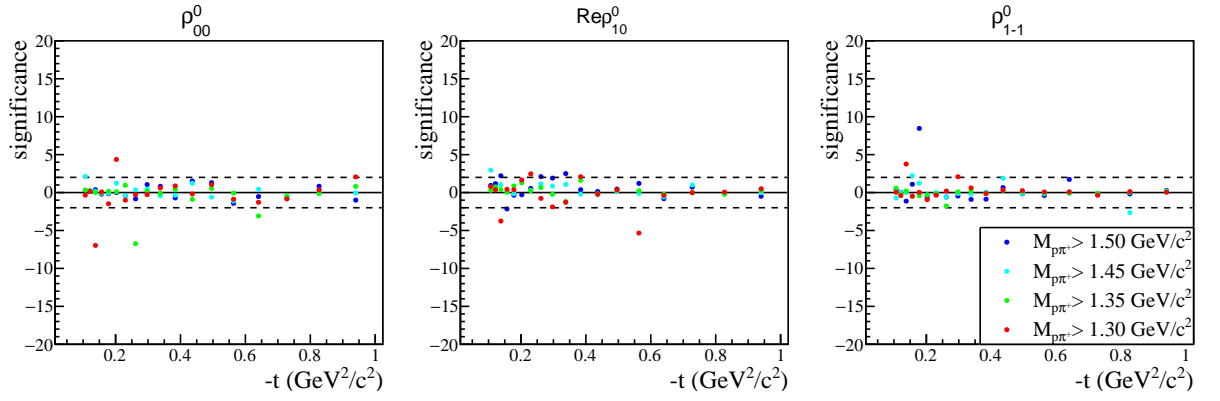
The Barlow significance is plotted for each $-t$ bin and each $p\pi^+$ invariant mass cut variation for the 5.5 – 6.5 GeV E_γ range.



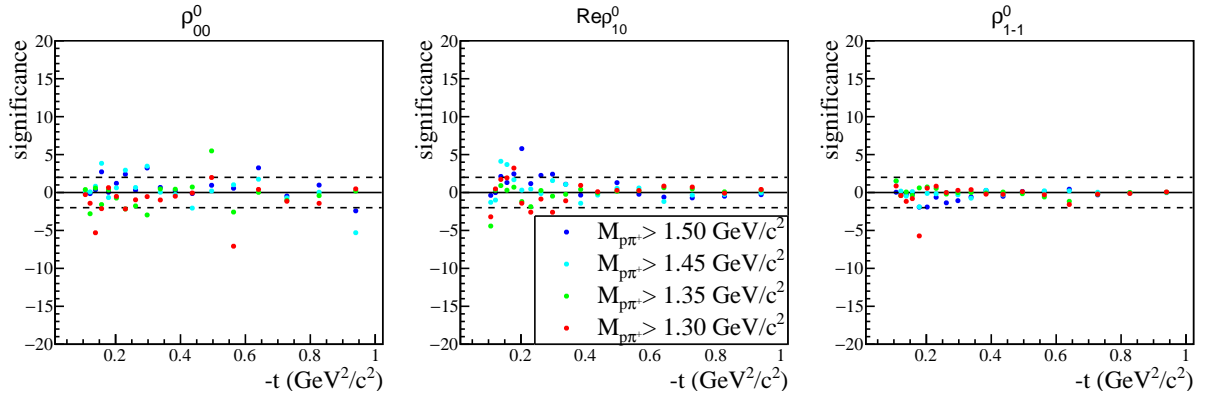
The Barlow significance is plotted for each $-t$ bin and each $p\pi^+$ invariant mass cut variation for the 6.5 – 7.5 GeV E_γ range.



The Barlow significance is plotted for each $-t$ bin and each $p\pi^+$ invariant mass cut variation for the 7.5 – 8.5 GeV E_γ range.

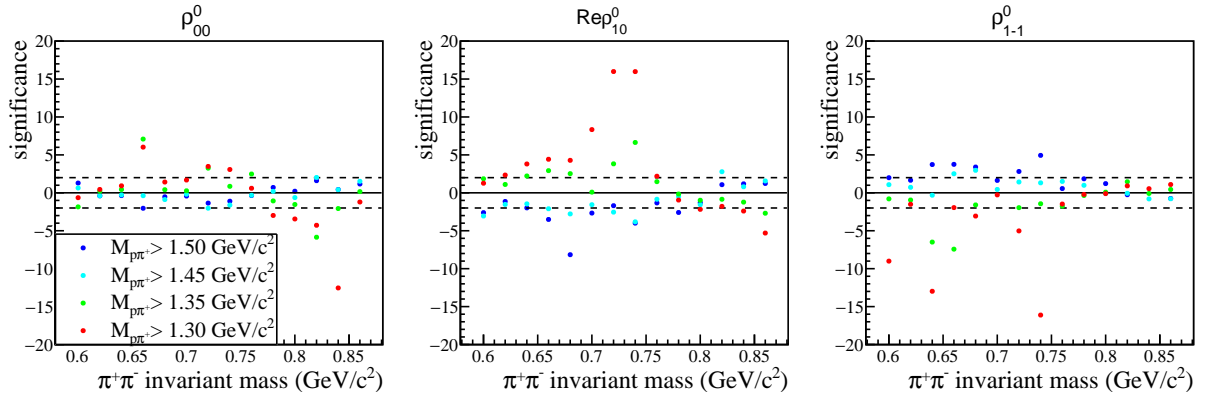


The Barlow significance is plotted for each $-t$ bin and each $p\pi^+$ invariant mass cut variation for the 8.5 – 9.5 E_γ range.

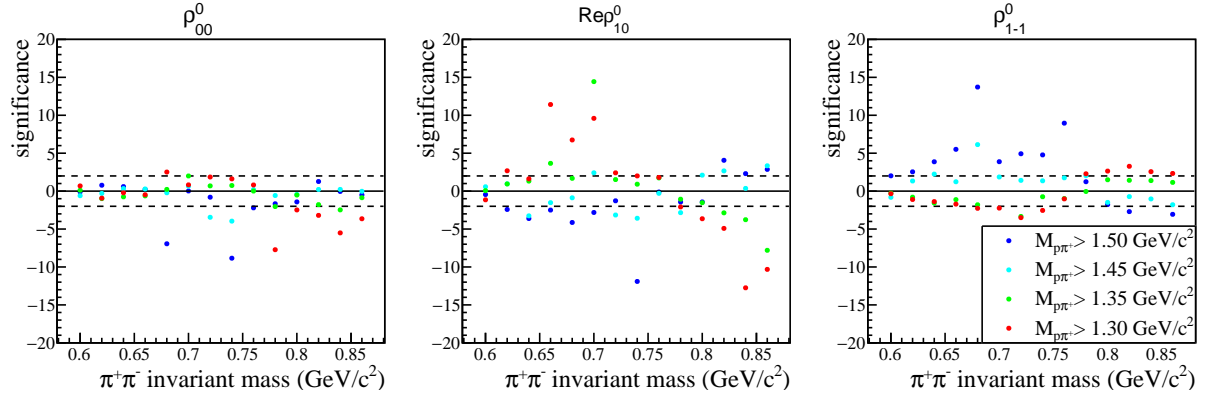


The Barlow significance is plotted for each $-t$ bin and each $p\pi^+$ invariant mass cut variation for the 9.5 – 11.6 E_γ range.

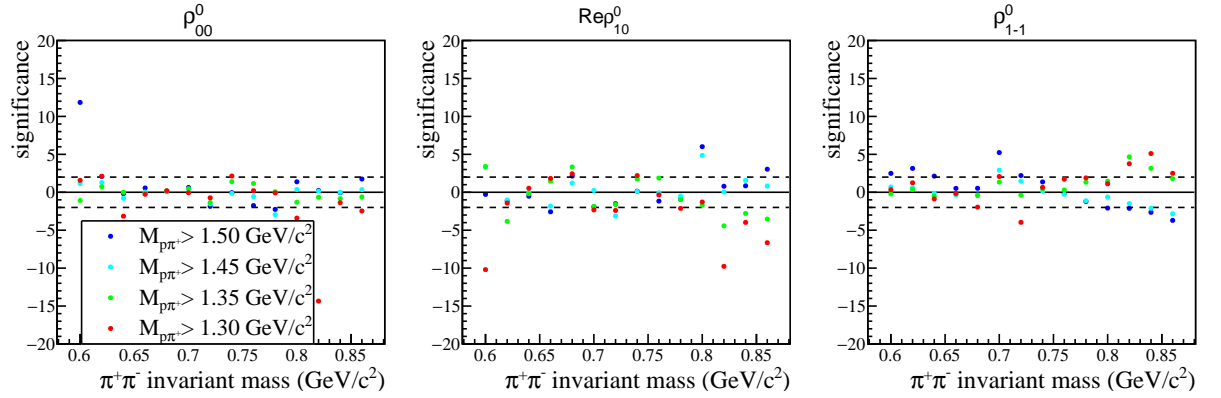
A.3.2 Significance versus $\pi^+\pi^-$ invariant mass



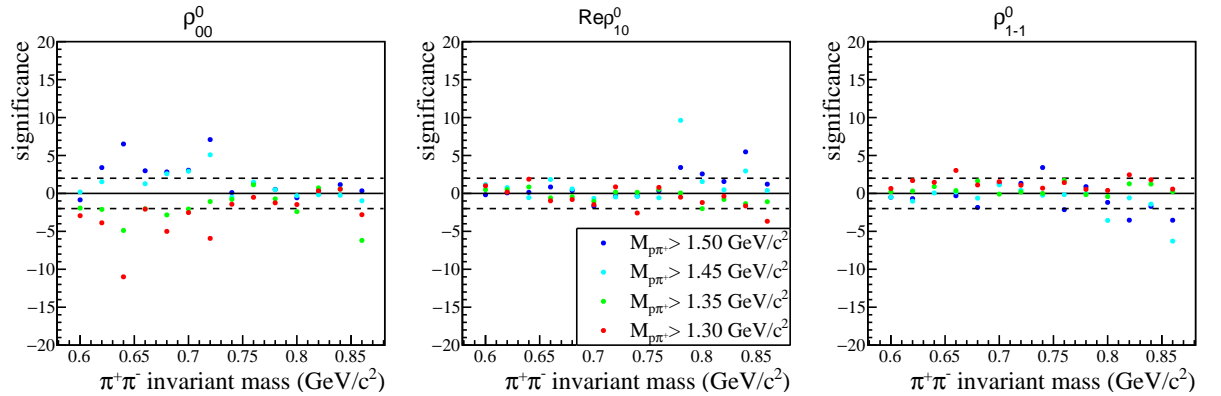
The Barlow significance is plotted for each $M_{\pi\pi}$ bin and each $p\pi^+$ invariant mass cut variation over the 3.00 – 4.25 E_γ and 0.10 – 0.15 GeV^2/c^2 range in $-t$.



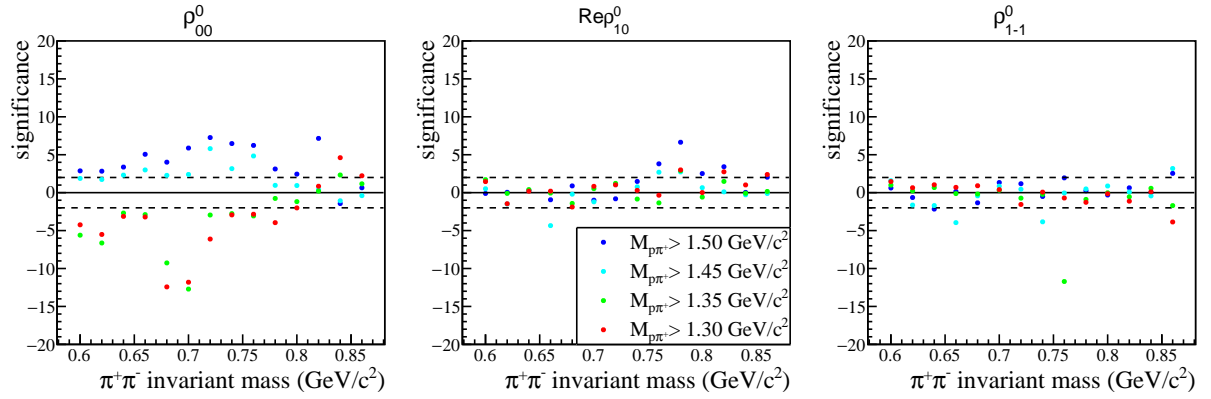
The Barlow significance is plotted for each $M_{\pi\pi}$ bin and each $p\pi^+$ invariant mass cut variation over the 3.00 – 4.25 GeV range in E_γ and 0.15 – 0.22 GeV^2/c^2 range in $-t$.



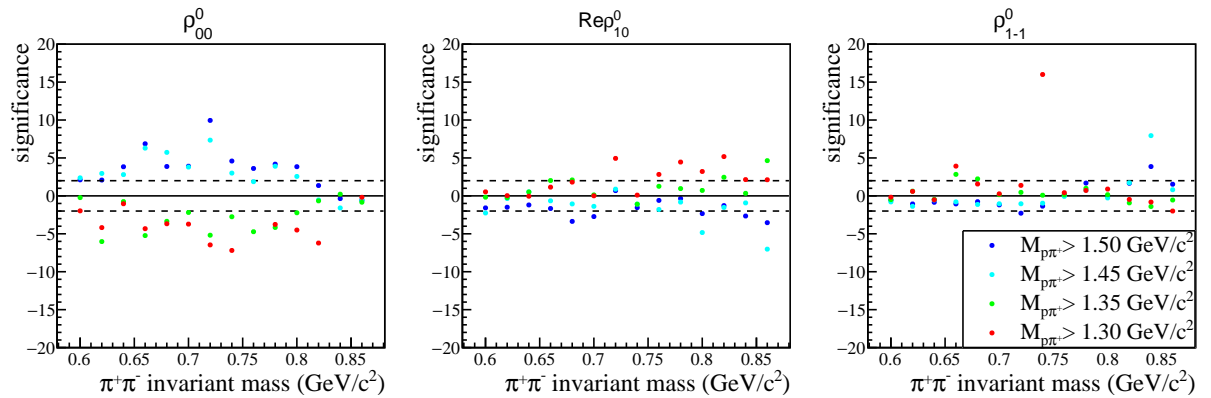
The Barlow significance is plotted for each $M_{\pi\pi}$ bin and each $p\pi^+$ invariant mass cut variation over the 3.00 – 4.25 GeV range in E_γ and 0.22 – 0.32 GeV^2/c^2 range in $-t$.



The Barlow significance is plotted for each $M_{\pi\pi}$ bin and each $p\pi^+$ invariant mass cut variation over the 3.00 – 4.25 GeV range in E_γ and 0.32 – 0.46 GeV^2/c^2 range in $-t$.



The Barlow significance is plotted for each $M_{\pi\pi}$ bin and each $p\pi^+$ invariant mass cut variation over the 3.00 – 4.25 GeV range in E_γ and 0.46 – 0.68 GeV^2/c^2 range in $-t$.



The Barlow significance is plotted for each $M_{\pi\pi}$ bin and each $p\pi^+$ invariant mass cut variation over the 3.00 – 4.25 GeV range in E_γ and 0.68 – 1.00 GeV^2/c^2 range in $-t$.

Bibliography

- [1] Sheldon L. Glashow. Partial-symmetries of weak interactions. *Nuc. Phys.*, 22(4):579–588, 1961. doi:[https://doi.org/10.1016/0029-5582\(61\)90469-2](https://doi.org/10.1016/0029-5582(61)90469-2).
- [2] Steven Weinberg. A model of leptons. *Phys. Rev. Lett.*, 19:1264–1266, Nov 1967. doi:10.1103/PhysRevLett.19.1264.
- [3] Abdus Salam. Weak and Electromagnetic Interactions. *Conf. Proc. C*, 680519:367–377, 1968. doi:10.1142/9789812795915_0034.
- [4] Murray Gell-Mann. Symmetries of baryons and mesons. *Phys. Rev.*, 125:1067–1084, Feb 1962. doi:10.1103/PhysRev.125.1067.
- [5] P.W. Higgs. Broken symmetries, massless particles and gauge fields. *Phys. Lett.*, 12(2):132–133, 1964. doi:[https://doi.org/10.1016/0031-9163\(64\)91136-9](https://doi.org/10.1016/0031-9163(64)91136-9).
- [6] Rym Bouchendira, Pierre Cladé, Saïda Guellati-Khélifa, François Nez, and François Biraben. New determination of the fine structure constant and test of the quantum electrodynamics. *Phys. Rev. Lett.*, 106(8), feb 2011. doi:10.1103/physrevlett.106.080801.
- [7] Sunil Mukhi and Probir Roy. Developments in high energy theory. *Pramana*, 73:3–60, 2009, arXiv:0905.1793 [physics.pop-ph]. doi:10.1007/s12043-009-0093-9.
- [8] Klaus Rabbertz. *Jet Physics at the LHC: The Strong Force beyond the TeV Scale*, volume 268 of *Springer Tracts in Modern Physics*. Springer, Berlin, 2017. doi:10.1007/978-3-319-42115-5.
- [9] E. Rutherford. Collision of α particles with light atoms. IV. An anomalous effect in nitrogen. *Phil. Mag. Ser. 6*, 37:581–587, 1919. doi:10.1080/14786431003659230.
- [10] J. Chadwick. Possible Existence of a Neutron. *Nature*, 129:312, 1932. doi:10.1038/129312a0.
- [11] J. Chadwick. The Existence of a Neutron. *Proc. Roy. Soc. Lond. A*, 136(830):692–708, 1932. doi:10.1098/rspa.1932.0112.

- [12] C. M. G. Lattes, H. Muirhead, G. P. S. Occhialini, and C. F. Powell. Processes Involving Charged Mesons. *Nature*, 159:694–697, 1947. doi:10.1038/159694a0.
- [13] Hideki Yukawa. On the Interaction of Elementary Particles I. *Proc. Phys. Math. Soc. Jap.*, 17:48–57, 1935. doi:10.1143/PTPS.1.1.
- [14] Murray Gell-Mann. The Eightfold Way: A Theory of strong interaction symmetry. March 1961. doi:10.2172/4008239.
- [15] J. Ashman, et al. A measurement of the spin asymmetry and determination of the structure function g_1 in deep inelastic muon-proton scattering. *Phys. Lett. B*, 206(2):364–370, 1988. doi:https://doi.org/10.1016/0370-2693(88)91523-7.
- [16] M. Ablikim, et al. Observation of a charged charmoniumlike structure in $e^+e^- \rightarrow \pi^+\pi^- j/\psi$ at $\sqrt{s}=4.26$ GeV. *Phys. Rev. Lett.*, 110:252001, Jun 2013. doi:10.1103/PhysRevLett.110.252001.
- [17] M. Ablikim, et al. Observation of a charged $(D\bar{D}^*)^\pm$ mass peak in $e^+e^- \rightarrow \pi d\bar{d}^*$ at $\sqrt{s} = 4.26$ GeV. *Phys. Rev. Lett.*, 112:022001, Jan 2014. doi:10.1103/PhysRevLett.112.022001.
- [18] R. Aaij, et al. Observation of a narrow pentaquark state, $P_c(4312)^+$, and of the two-peak structure of the $P_c(4450)^+$. *Phys. Rev. Lett.*, 122(22), June 2019. doi:10.1103/physrevlett.122.222001.
- [19] B. Aubert, et al. Observation of a broad structure in the $\pi^+\pi^- j/\psi$ mass spectrum around 4.26 GeV/ c^2 . *Phys. Rev. Lett.*, 95:142001, Sep 2005. doi:10.1103/PhysRevLett.95.142001.
- [20] Vincent Mathieu, Nikolai Kochelev, and Vicente Vento. The Physics of Glueballs. *Int. J. Mod. Phys. E*, 18:1–49, 2009, arXiv:0810.4453 [hep-ph]. doi:10.1142/S0218301309012124.
- [21] W. Ochs. The Status of Glueballs. *J. Phys. G*, 40:043001, 2013, arXiv:1301.5183 [hep-ph]. doi:10.1088/0954-3899/40/4/043001.
- [22] D. Alde, et al. Evidence for a 1^+ exotic meson. *Phys. Lett. B*, 205(2):397–400, 1988. doi:https://doi.org/10.1016/0370-2693(88)91686-3.
- [23] G. S. Adams, et al. Observation of a new $j^{pc} = 1^{-+}$ exotic state in the reaction $\pi^- p \rightarrow \pi^+\pi^-\pi^- p$ at 18 GeV/ c . *Phys. Rev. Lett.*, 81:5760–5763, Dec 1998. doi:10.1103/PhysRevLett.81.5760.

- [24] G.S. Adams, et al. Confirmation of the $1+$ meson exotics in the 0 system. *Phys. Lett. B*, 657(1):27–31, 2007. doi:<https://doi.org/10.1016/j.physletb.2007.07.068>.
- [25] M. G. Alekseev, et al. Observation of a $J^{Pc} = 1^{-+}$ exotic resonance in diffractive dissociation of $190 \text{ GeV}/c$ π^{-} into $\pi^{-}\pi^{-}\pi^{+}$. *Phys. Rev. Lett.*, 104:241803, Jun 2010. doi:10.1103/PhysRevLett.104.241803.
- [26] M. Aghasyan, et al. Light isovector resonances in $\pi^{-}p \rightarrow \pi^{-}\pi^{-}\pi^{+}p$ at $190 \text{ GeV}/c$. *Phys. Rev. D*, 98:092003, Nov 2018. doi:10.1103/PhysRevD.98.092003.
- [27] R. L. Workman et al. Review of Particle Physics. *PTEP*, 2022:083C01, 2022. doi:10.1093/ptep/ptac097.
- [28] P. Söding. On the apparent shift of the rho meson mass in photoproduction. *Phys. Lett.*, 19(8):702–704, 1966. doi:[https://doi.org/10.1016/0031-9163\(66\)90451-3](https://doi.org/10.1016/0031-9163(66)90451-3).
- [29] P. D. B. Collins. Regge theory and particle physics. *Phys. Rept.*, 1:103–234, 1971. doi:10.1016/0370-1573(71)90007-X.
- [30] Arthur Bolz, et al. Photoproduction of $\pi^{+}\pi^{-}$ pairs in a model with tensor-pomeron and vector-odderon exchange. *JHEP*, 01:151, 2015, arXiv:1409.8483 [hep-ph]. doi:10.1007/JHEP01(2015)151.
- [31] Murray Gell-Mann and Fredrik Zachariasen. Form factors and vector mesons. *Phys. Rev.*, 124:953–964, Nov 1961. doi:10.1103/PhysRev.124.953.
- [32] Otto Nachtmann. Pomeron physics and QCD. In *Ringberg Workshop on New Trends in HERA Physics 2003*, pages 253–267, 2004, arXiv:hep-ph/0312279. doi:10.1142/9789812702722_023.
- [33] U. Fano. Description of states in quantum mechanics by density matrix and operator techniques. *Rev. Mod. Phys.*, 29:74–93, Jan 1957. doi:10.1103/RevModPhys.29.74.
- [34] K. Schilling, P. Seyboth, and Guenter E. Wolf. On the Analysis of Vector Meson Production by Polarized Photons. *Nucl. Phys. B*, 15:397–412, 1970. doi:10.1016/0550-3213(70)90070-2.
- [35] M. Jacob and G. C. Wick. On the General Theory of Collisions for Particles with Spin. *Annals Phys.*, 7:404–428, 1959. doi:10.1016/0003-4916(59)90051-X.
- [36] Alexander Austregesilo. Spin-density matrix elements for vector meson photoproduction at GlueX. *AIP Conf. Proc.*, 2249(1):030005, 2020, arXiv:1908.07275 [nucl-ex]. doi:10.1063/5.0008585.

- [37] K. Gottfried and John David Jackson. On the Connection between production mechanism and decay of resonances at high-energies. *Nuovo Cim.*, 33:309–330, 1964. doi:10.1007/BF02750195.
- [38] M. E. Rose and B. T. Feld. Elementary Theory of Angular Momentum. *Physics Today*, 10(11):30–30, 11 1957. doi:10.1063/1.3060162.
- [39] G. Cohen-Tannoudji, Ph. Salin, and A. Morel. A simple formulation of high-energy exchange models in terms of direct-channel amplitudes. *Nuovo Cim. A*, 55(3):412–422, 1968. doi:10.1007/BF02857563.
- [40] F.J. Gilman, J. Pumplin, A. Schwimmer, and L. Stodolsky. Helicity conservation in diffraction scattering. *Phys. Lett. B*, 31(6):387–390, 1970. doi:https://doi.org/10.1016/0370-2693(70)90203-0.
- [41] J. A. Z. Zarling. *Measurement of pseudoscalar beam asymmetry for $\pi^- \Delta^{++}$ photoproduction on the proton at $E_\gamma=8.5$ GeV with the gluex experiment.* PhD thesis, Indiana University, July 2019.
- [42] Yoichiro Nambu. Possible existence of a heavy neutral meson. *Phys. Rev.*, 106:1366–1367, Jun 1957. doi:10.1103/PhysRev.106.1366.
- [43] Robert Hofstadter. Electron scattering and nuclear structure. *Rev. Mod. Phys.*, 28:214–254, Jul 1956. doi:10.1103/RevModPhys.28.214.
- [44] William R. Frazer and Jose R. Fulco. Effect of a pion-pion scattering resonance on nucleon structure. *Phys. Rev. Lett.*, 2:365–368, Apr 1959. doi:10.1103/PhysRevLett.2.365.
- [45] J. J. Sakurai. Theory of strong interactions. *Annals Phys.*, 11:1–48, 1960. doi:10.1016/0003-4916(60)90126-3.
- [46] A. Salam and J. C. Ward. Vector field associated with the unitary theory of the Sakata model. *Nuovo Cim.*, 20:419–421, 1961. doi:10.1007/BF02781760.
- [47] Y. Ne’eman. Derivation of strong interactions from a gauge invariance. *Nucl. Phys.*, 26(2):222–229, 1961. doi:https://doi.org/10.1016/0029-5582(61)90134-1.
- [48] A. R. Erwin, R. March, W. D. Walker, and E. West. Evidence for a $\pi - \pi$ resonance in the $i = 1, j = 1$ state. *Phys. Rev. Lett.*, 6:628–630, Jun 1961. doi:10.1103/PhysRevLett.6.628.
- [49] D. Stonehill, et al. Pion-pion interaction in pion production by $\pi^+ - p$ collisions. *Phys. Rev. Lett.*, 6:624–625, Jun 1961. doi:10.1103/PhysRevLett.6.624.
- [50] J. Ballam, et al. Vector-meson production by polarized photons at 2.8, 4.7, and 9.3 GeV. *Phys. Rev. D*, 7:3150–3177, June 1973. doi:10.1103/PhysRevD.7.3150.

- [51] Vincent Mathieu. Moments of Angular Distribution in Two Mesons Photoproduction. *AIP Conf. Proc.*, 2249(1):030020, 2020, arXiv:1909.09473 [hep-ph]. doi:10.1063/5.0008590.
- [52] M. Battaglieri et al. Photoproduction of $\pi^+\pi^-$ meson pairs on the proton. *Phys. Rev. D*, 80:072005, 2009, arXiv:0907.1021 [hep-ex]. doi:10.1103/PhysRevD.80.072005.
- [53] V. Mathieu, et al. Vector Meson Photoproduction with a Linearly Polarized Beam. *Phys. Rev. D*, 97(9):094003, 2018, arXiv:1802.09403 [hep-ph]. doi:10.1103/PhysRevD.97.094003.
- [54] M. Dugger et al. A study of decays to strange final states with GlueX in Hall D using components of the BaBar DIRC. 8 2014, arXiv:1408.0215 [physics.ins-det].
- [55] Michael Spata. 12 GeV CEBAF Initial Operational Experience and Challenges. In *9th International Particle Accelerator Conference*, 6 2018. doi:10.18429/JACoW-IPAC2018-WEYGBD1.
- [56] Jefferson Lab. CEBAF at 12 GeV schematic. <https://www.flickr.com/photos/jeffersonlab/12599705145>. last access 08/11/2022.
- [57] R. Suleiman, et al. High current polarized electron source. *AIP Conf. Proc.*, 1970(1):050007, 2018. doi:10.1063/1.5040226.
- [58] Tomasz Plawski, et al. CEBAF Photo Gun RF System. In *29th International Linear Accelerator Conference*, page MOPO115, 2018. doi:10.18429/JACoW-LINAC2018-MOPO115.
- [59] A. Freyberger. Commissioning and Operation of 12 GeV CEBAF. In *6th International Particle Accelerator Conference*, page MOXGB2, 2015. doi:10.18429/JACoW-IPAC2015-MOXGB2.
- [60] Charles E. Reece. Continuous wave superconducting radio frequency electron linac for nuclear physics research. *Phys. Rev. Accel. Beams*, 19:124801, Dec 2016. doi:10.1103/PhysRevAccelBeams.19.124801.
- [61] H. Bethe and W. Heitler. On the Stopping of fast particles and on the creation of positive electrons. *Proc. Roy. Soc. Lond. A*, 146:83–112, 1934. doi:10.1098/rspa.1934.0140.
- [62] P. Pauli. *Lambda(1520) measurements at the GlueX experiment*. PhD thesis, University of Glasgow, August 2020.

- [63] B.R. Martin and G. Shaw. *Particle Physics*. Manchester Physics Series. Wiley, Manchester, 2016.
- [64] U. Timm. Coherent bremsstrahlung of electrons in crystals. *Fortsch. Phys.*, 17:765–808, 1969.
- [65] R. Jones. Hall d coherent bremsstrahlung rate calculator. <http://zeus.phys.uconn.edu/halld/cobrems/ratetool.cgi>. last access 08/11/2022.
- [66] S. Adhikari et al. Strange Hadron Spectroscopy with a Secondary KL Beam at GlueX. July 2017, arXiv:1707.05284 [hep-ex].
- [67] S. Adhikari et al. The GLueX beamline and detector. *Nucl. Instrum. Meth. A*, 987:164807, 2021, arXiv:2005.14272 [physics.ins-det]. doi:10.1016/j.nima.2020.164807.
- [68] F.A Natter, P Grabmayr, T Hehl, R.O Owens, and S Wunderlich. Monte carlo simulation and analytical calculation of coherent bremsstrahlung and its polarisation. *Nuc. Instrum. Meth.*, 211(4):465–486, 2003. doi:[https://doi.org/10.1016/S0168-583X\(03\)01420-4](https://doi.org/10.1016/S0168-583X(03)01420-4).
- [69] A. Barnes. *Development of the Tagger Microscope and Analysis of Spin Density Matrix Elements in $\gamma p \rightarrow \phi p$ for the GlueX Experiment*. PhD thesis, University of Connecticut, May 2017.
- [70] M. Dugger et al. Design and construction of a high-energy photon polarimeter. *Nucl. Instrum. Meth. A*, 867:115–127, 2017, arXiv:1703.07875 [physics.ins-det]. doi:10.1016/j.nima.2017.05.026.
- [71] S. Adhikari et al. Measurement of the photon beam asymmetry in $\vec{\gamma}p \rightarrow K^+\Sigma^0$ at $E_\gamma = 8.5$ GeV. *Phys. Rev. C*, 101(6):065206, 2020, arXiv:2003.08038 [nucl-ex]. doi:10.1103/PhysRevC.101.065206.
- [72] F. Barbosa et al. Pair spectrometer hodoscope for hall d at jefferson lab. *Nucl. Instr. and Meth. A*, 795:376–380, 2015. doi:<https://doi.org/10.1016/j.nima.2015.06.012>.
- [73] GlueX Collaboration. Total absorption counter. https://halldweb1.jlab.org/wiki/index.php/Total_Absorption_Counter. last access 21/09/2022.
- [74] C. D. Keith. Hall D LH2 cryotarget. https://halldweb1.jlab.org/wiki/images/b/b8/Halld_Target_Table.pdf. last access 21/09/2022.
- [75] E. Pooser et al. The GlueX start counter detector. *Nucl. Instr. and Meth. A*, 927:330342, May 2019. doi:10.1016/j.nima.2019.02.029.

- [76] N.S. Jarvis et al. The central drift chamber for gluex. *Nucl. Instr. and Meth. A*, 962:163727, May 2020. doi:10.1016/j.nima.2020.163727.
- [77] M. J. Staib. *Calibrations for charged particle tracking and measurements of ω photoproduction with the GlueX detector*. PhD thesis, Carnegie Mellon University, Sep 2017.
- [78] L. Pentchev, et al. Studies with cathode drift chambers for the GlueX experiment at Jefferson Lab. *Nucl. Instrum. Meth. A*, 845:281–284, 2017. doi:10.1016/j.nima.2016.04.076.
- [79] Tegan D. Beattie et al. Construction and Performance of the Barrel Electromagnetic Calorimeter for the GlueX Experiment. *Nucl. Instrum. Meth. A*, 896:24–42, 2018, arXiv:1801.03088 [physics.ins-det]. doi:10.1016/j.nima.2018.04.006.
- [80] GlueX collaboration. Technical construction report. Technical Report GlueX-doc-2511-v6, 2017.
- [81] GlueX Collaboration. Forward calorimeter. <https://gluexweb.jlab.org/content/photo/fcal-front>. last access 20/09/2022.
- [82] A. Ostrovidov. TOF status. Technical Report GlueX-doc-3030, 2016.
- [83] S. Boyarinov et al. The CLAS12 Data Acquisition System. *Nucl. Instrum. Meth. A*, 966:163698, 2020. doi:10.1016/j.nima.2020.163698.
- [84] GlueX Collaboration. Spring 2017 trigger summary. https://halldweb.jlab.org/wiki/index.php/Spring_2017_Trigger_Summary. last access 29/09/2022.
- [85] Jefferson Lab EVIO. <https://data.jlab.org/drupal/evio>. last access 11/01/2023.
- [86] A. Austregesilo, N. Jarvis, and C. Meyer. Measurement of spin-density matrix elements in $\rho(770)$ production with a linearly-polarized photon beam at $E_\gamma=8.2-8.8$ GeV. *Phys. Rev. C*, 2023 (in preperation).
- [87] T. Britton Calibration Browser. https://halldweb.jlab.org/data_monitoring/CalibBrowser.html. last access 12/01/2023.
- [88] Benedikt Zihlmann. Gluex time of flight calibration. Technical Report GlueX-doc-2767, 2017.
- [89] T. Britton and K. Mizutani Plot Browser. https://halldweb.jlab.org/data_monitoring/Plot_Browser.html. last access 12/01/2023.

- [90] R. E. Kalman. A New Approach to Linear Filtering and Prediction Problems. *Bas. Eng.*, 82(1):35–45, 03 1960. doi:10.1115/1.3662552.
- [91] R. E. Kalman and R. S. Bucy. New Results in Linear Filtering and Prediction Theory. *Bas. Eng.*, 83(1):95–108, 03 1961. doi:10.1115/1.3658902.
- [92] Rene Brun and Fons Rademakers. Root an object oriented data analysis framework. *Nuc. Instrum. Meth. A*, 389(1):81–86, 1997. doi:https://doi.org/10.1016/S0168-9002(97)00048-X.
- [93] P. Mattione. Least squares kinematic fitting of physics reactions. Technical Report GlueX-doc-2112-v5, 2016.
- [94] GlueX Collaboration. hdgeant4. <https://github.com/JeffersonLab/HDGeant4>. last access 29/09/2022.
- [95] S. Agostinelli, et al. Geant4-a simulation toolkit. *Nuc. Instrum. Meth. A*, 506(3):250–303, 2003. doi:https://doi.org/10.1016/S0168-9002(03)01368-8.
- [96] C. Meyer. A. Austregesilo, N. Jarvis. Measurement of spin-density matrix elements in $\rho(770)$ production with a linearly-polarized photon beam at $E_\gamma=8.2-8.8$ GeV. Analysis Note GlueX-doc-5576, 2023.
- [97] B. Zihlmann. Tagger accidentals and scaling. Technical Report GlueX-doc-4122, 2019.
- [98] M. Hatlo, et al. Developments of mathematical software libraries for the LHC experiments. *IEEE Trans. Nucl. Sci.*, 52:2818–2822, 2005. doi:10.1109/TNS.2005.860152.
- [99] R. Barlow. Extended maximum likelihood. *Nuc. Instrum. Meth. A*, 297(3):496–506, 1990. doi:https://doi.org/10.1016/0168-9002(90)91334-8.
- [100] Massimiliano Bonamente. *Statistics and Analysis of Scientific Data*. Springer, New York, 2017. doi:doi:10.1007/978-1-4939-6572-4.
- [101] Metropolis N. et al. Equation of state calculations by fast computing machines. *Chem. Phys.*, 21(6):1087–1092, 1953, <https://doi.org/10.1063/1.1699114>. doi:10.1063/1.1699114.
- [102] W. K. Hastings. Monte Carlo sampling methods using Markov chains and their applications. *Biometrika*, 57(1):97–109, 04 1970. doi:10.1093/biomet/57.1.97.
- [103] Jaewook Lee, Woosuk Sung, and Joo-Ho Choi. Metamodel for efficient estimation of capacity-fade uncertainty in li-ion batteries for electric vehicles. *Energies*, 8(6):5538–5554, 2015. doi:10.3390/en8065538.

- [104] G. Schott L. Moneta*, K. Cranmer and W. Verkerke. The RooStats project. *Proceedings of Science*, 93:057, 2010. doi:<https://doi.org/10.22323/1.093.0057>.
- [105] D. I. Glazier. brufit. <https://github.com/dglazier/brufit>. last access 31/01/2023.
- [106] R. Wishart. *Analysis of Three Body Decays in Quasi-Real Photoproduction*. PhD thesis, University of Glasgow, 2023 (thesis in preperation).
- [107] R. Barlow. Systematic errors: Facts and fictions. In *Conference on Advanced Statistical Techniques in Particle Physics*, pages 134–144, 7 2002, arXiv:hep-ex/0207026.
- [108] S. Adhikari et al. Measurement of spin density matrix elements in $\Lambda(1520)$ photoproduction at 8.2–8.8 GeV. *Phys. Rev. C*, 105(3):035201, 2022, arXiv:2107.12314 [nucl-ex]. doi:10.1103/PhysRevC.105.035201.
- [109] Makoto Matsumoto and Takuji Nishimura. Mersenne twister: A 623-dimensionally equidistributed uniform pseudo-random number generator. *ACM Trans. Model. Comput. Simul.*, 8(1):330, jan 1998. doi:10.1145/272991.272995.
- [110] Matthew Shepherd, Ryan Mitchell, Justin Stevens, and Alex Austregesilo. mashephe/amptools: Version 0.13.0 release, February 2022. doi:10.5281/zenodo.6047744.
- [111] B. Efron and R.J. Tibshirani. *An Introduction to the Bootstrap (1st ed.)*. Chapman and Hall/CRC, 1994. doi:<https://doi.org/10.1201/9780429246593>.